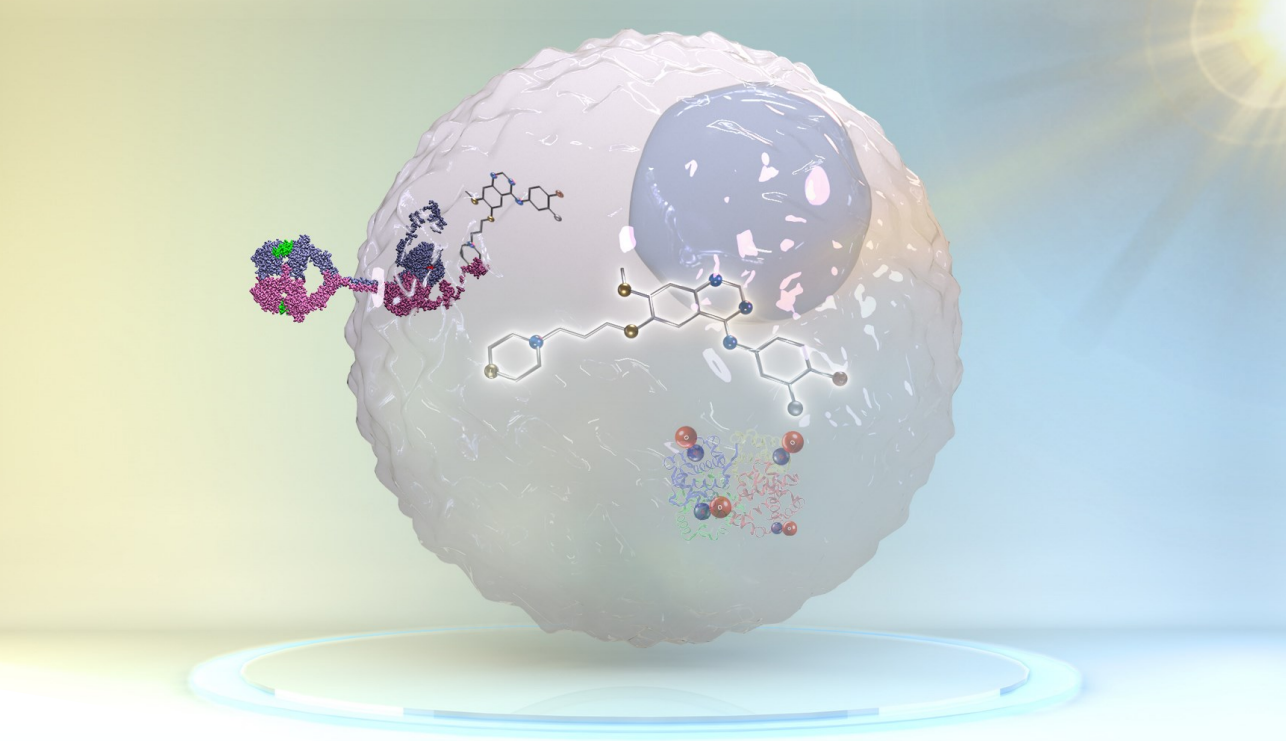

In Vitro Photobehavior of Tyrosine Kinase Inhibitors in Solution and within Skin Cells

Doctoral Thesis

Meryem El Ouardi El Hamidy

Supervised by:

Prof. Miguel Ángel Miranda Alonso
Dr. Inmaculada Andreu Ros

Valencia, March 2024

Instituto de Tecnología Química (ITQ), Universitat Politècnica de València-Consejo Superior de Investigaciones Científicas (UPV-CSIC)
Departamento de Química, Universitat Politècnica de València (UPV)
Unidad Mixta de Investigación UPV – Instituto de Investigación Sanitaria (IIS) La Fe, Hospital La Fe

In Vitro Photobehavior of Tyrosine Kinase Inhibitors in Solution and within Skin Cells

by

Meryem El Ouardi

DOCTORAL THESIS
International PhD Mention

Supervised by

Prof. Miguel Ángel Miranda Alonso

Dr. Inmaculada Andreu Ros

Valencia, March 2024

D. MIGUEL ÁNGEL MIRANDA ALONSO, catedrático de universidad de la Universitat Politècnica de València, y Dña. INMACULADA ANDREU ROS, profesora titular de universidad de la Universitat Politècnica de València.

CERTIFICAN:

Que la presente tesis doctoral, titulada: "*In Vitro* Photobehavior of Tyrosine Kinase Inhibitors in Solution and within Skin Cells" ha sido desarrollada por MERYEM EL OUARDI EL HAMIDY bajo su dirección, en el Instituto de Tecnología Química (ITQ), Universitat Politècnica de València-Consejo Superior de Investigaciones Científicas (UPV-CSIC), el Departamento de Química de la Universitat Politècnica de València y en la Unidad Mixta de Investigación UPV – Instituto de Investigación Sanitaria (IIS) La Fe, Hospital la Fe, para optar al grado de doctora en Química por la Universitat Politècnica de València.

Fdo. D. Miguel Ángel Miranda Alonso

Fdo. Dña. Inmaculada Andreu Ros

Agradecimientos

Las palabras no pueden describir la gratitud que siento al finalizar esta etapa tan importante de mi vida. Nunca imaginé llegar a la meta; quién diría que aquella niña que siempre soñó con sostener una muñeca en la mano terminaría sosteniendo una micropipeta durante cinco años. Se dice pronto, pero estos años han formado a una farmacéutica con un ferviente deseo de hacer ciencia y, sobre todo, de aprender sin límites. Sin embargo, no solo mi nombre debería estar reflejado en la portada de esta tesis, sino también los nombres de todas aquellas personas que, en diferentes grados, me brindaron asistencia, apoyo y orientación, y sin las cuales no habría tenido éxito. Por ello, me gustaría extender unas palabras a cada una de ellas.

En primer lugar, debo agradecer a la Universitat Politècnica de València por la ayuda para la formación de doctores dentro del subprograma 1 (PAID-1-2019) y al Ministerio de Ciencia, Innovación y Universidades por la ayuda para la formación del profesorado universitario (FPU19/00048). Ambas subvenciones resultaron fundamentales para la elaboración de mi tesis doctoral.

La decisión que tomé para embarcarme en el mundo de la investigación no fue premeditada ni particularmente clara. Fue en aquel agosto de 2019 cuando mi padre me acompañó hasta el Instituto de Tecnología Química, donde me recibió el profesor Miguel Ángel Miranda. Me sentí como si estuviera cambiando de un hogar a otro, consciente de que me aguardaban grandes experiencias. La elección de unirme al grupo de la Dra. Inmaculada Andreu me permitió acceder al Instituto de Investigación Sanitaria del Hospital La Fe; el resto de la historia se desarrolla por sí sola. Por ello les agradezco sinceramente haber depositado su confianza en mí y haberme permitido

demostrar mi valía. Hoy puedo afirmar que el pensamiento crítico y autocrítico que he desarrollado durante la tesis fue gracias al conocimiento que ambos me han transmitido. En efecto, mi interés en continuar en este campo se fundamenta en esas enriquecedoras conversaciones que solíamos mantener los tres durante extensas mañanas, tratando de ensamblar rompecabezas con el fin de entender los resultados experimentales. Por todo ello, les expreso mi más sincero agradecimiento.

Puedo decir que el hogar que he formado durante esta etapa predoctoral se compone de tres familias que me han acogido y respaldado desde el inicio hasta el final. En primer lugar, deseo expresar mi gratitud a los profesores del Departamento de Química, Ignacio Vaya y Raúl Pérez, así como a mis estimados colegas de laboratorio, Lorena, Jorge C, Dani y Jorge H, con los que solo compartí momentos muy agradables. En segundo lugar, agradezco a la Dra. Virginie Lhiaubet y a mis compañeros del grupo de fotoquímica del Instituto de Tecnología Química, Gemma, Luciana, Juanan y Alberto; sin su apoyo, todos mis conflictos con el láser habrían vencido contra mí en numerosas ocasiones.

Por último, pero no menos importante, quiero expresar mi profundo agradecimiento a la familia que más me ha visto crecer durante estos años y que me ha brindado apoyo para levantarme y recuperarme en los momentos más difíciles: mis queridos del IIS La Fe. A todos los miembros de Hepatología Experimental, así como al grupo más heterogéneo que conformamos en los últimos años, con mi química favorita, Tere, mi referencia italiana, Anna y el posdoc más inverosímil, Ernesto. También quiero expresar mi gratitud a los directores de estos grupos, especialmente a Laia Tolosa y Ramiro Jover, con quienes compartí sobre todo momentos de

celebración. En definitiva, el respaldo de todo este equipo ha sido fundamental especialmente en el desarrollo de la parte más biológica de esta tesis, y les estoy enormemente agradecida por ello. Además, el asesoramiento que he recibido de personas como Guillermo y la Dra. Pilar Marín ha sido de incalculable valor, especialmente por su contribución a mi pasión por la biología molecular y la microscopía celular.

Son numerosos los amigos que me llevo de la Torre A del hospital, pero me gustaría destacar especialmente la comunidad secreta que formamos, conocida como "la Llorería del 6.12". Pues, a pesar de no tener un título en psicología, el laboratorio 6.12 ha realizado más consultas que cualquier centro de terapia. Así, incumpliendo con los derechos de protección de datos hago mención a los siguientes "pacientes": Quique, quien ha sido mi guía en trámites administrativos y un amigo que ha escuchado mis preocupaciones más personales; Manu, a quien considero un amigo que me ha brindado apoyo tanto experimental como emocional; Polina, que siempre ha sabido darme consejos en el momento oportuno; y Nuri, cuya partida ha dejado claro que era el alma de la fiesta de la sexta planta.

Resulta intrigante que haya formado similares amistades durante mi estancia en Bélgica, de los cuales destaco a personas como Débora, Xiong, Laia, Leewon, Sudipta, Pranali, Charlotte, Aaron, Michiel, Pierre entre otros. Así, aprovecho para expresar mi más profundo agradecimiento al profesor Johan Hofkens por brindarme la oportunidad de integrarme en su grupo de investigación, así como por otorgarme todas las facilidades necesarias para llevar a cabo mis experimentos utilizando las técnicas más avanzadas.

Y ahora sí, mis personas favoritas, aquellas cuya ausencia en el último año generó un vacío inmenso que me hizo reflexionar sobre la importancia de

convertir mi lugar de trabajo en mi hogar: mi familia del 6.12. A Patri, con su actitud tan risueña que lograba hacerme olvidar las razones de mis frustraciones con su sentido del humor y sus chocolates internacionales. A la nueva incorporación, Maca y las ganas que tiene de comerse el mundo. Y sobre todo a mi querido Alejandro. ¿Qué puedo decir de él sin extenderme más que en esta tesis? Es sin duda la magia detrás de todo lo que me ha llevado hasta este punto sin rendirme, evitando que me sienta sola o aislada. Desde el primer día, he entendido el valor de contar con alguien que ilumine el camino en una carrera tan exigente como lo es la tesis doctoral. Nunca me he sentido perdida gracias a él, y planeo devolverle el favor más allá de ayudarle con figuras en PowerPoint, pues le entrego mi amistad para toda la vida.

Y cómo no, a Guillem, cuya personalidad única ha dejado una huella imborrable en la Fe. Él es, sin duda, la otra joya que me llevo para siempre. Dicho esto, dedico también mis agradecimientos a la más extravagante de las familias: Mari Carmen, Pepe, Elvira, Tuco, Josep, Ferrán, Rocío, María José, Rafa, Roger, Enric, Jan y todos los felinos de por medio.

Finalmente, a mi familia y amigos, a quienes, si comenzara a nombrar, esta tesis parecería un listado de asistencia, les agradezco por haberme criado y verme crecer. No pasa un solo día en el que no reflexione sobre todas las experiencias que han contribuido a mi formación y a lo que soy ahora, sin dejar de lado mis raíces, mi cultura y mi pasado. Espero que sientan orgullo por esa niña que dejó atrás las muñecas para atravesar el estrecho hacia un país que le brindó la educación y el conocimiento necesarios para cumplir su pequeño sueño de convertirse en investigadora.

A todos ellos, gracias.

شيء من الشك خير من كل اليقين

رسالة الغفرة ـ أبي العلاء المعري

Abstract

In recent decades, the emerge of tyrosine kinase inhibitors (TKIs) as a new class of targeted therapy has substantially enhanced the quality of life and survival rates for cancer patients. However, associated adverse effects, such as dermatological reactions, remain a challenge to sustained therapy. In light of our research group established insights into the photophysical and photobiological aspects of some TKIs, this thesis follows a similar multidisciplinary approach to investigate other photoactive drugs within the TKI family. In the initial stage, four TKIs, gefitinib, axitinib, dasatinib, and avapritinib, were selected based on their ability to absorb in the UVA region of the solar spectrum and their phototoxic potential. Consequently, photophysical and photobiological studies were conducted on these TKIs.

Gefitinib (GFT) is a TKI with a quinazoline moiety, in which modifications resulting from metabolism significantly alter the phototoxicity potential. Dealkylation of the propoxy-morpholine side chain (DMOR-GFT) exhibited the highest photoirritant value (PIF), reaching approximately 48, while the demethylated metabolite (DMT-GFT) displayed much lower phototoxicity (PIF ~7), nearly half the PIF value of the parent drug (*ca.* 13). In contrast, replacing the fluorine substituent with OH (DF-GFT) resulted in the absence of phototoxic activity. Surprisingly, only DMOR-GFT was confirmed to induce lipid photoperoxidation which occurred through a Type I oxidative mechanism, based on the weak singlet oxygen production and the efficient quenching of the triplet excited state by a lipid model. Furthermore, protein photooxidation was evident for GFT and, to a lesser extent, for DMOR-GFT, but negligible for DMT-GFT. However, unlike the parent drug, DNA photodamage induced by the demethylated metabolite exhibited limited repair even after several hours.

Axitinib (AXT), commercially available as *(E)*-AXT, showed a tendency for photoisomerization to *(Z)*-AXT, particularly within proteins. Thus, two phototoxicity mechanisms were unveiled. Firstly, the transformation of the initially non-cytotoxic *(E)*-AXT into the cytotoxic *(Z)*-AXT upon radiation. Secondly, the intrinsic phototoxicity exhibited by *(Z)*-AXT. Moreover, protein photooxidation was unequivocally attributed to the *(Z)*-isomer due to the similarity in carbonyl content between *E/Z*-isomers and the high protein affinity of the *(Z)*-isomer. Finally, the photogenotoxicity was only revealed through the detection of γ-H2AX histone foci.

Dasatinib (DAS) is a TKI suggested for topical treatment of dermatological diseases. Given this context and having determined a PIF value *ca.* 5, an evaluation of DAS phototoxicity in reconstructed human epidermis (RhE) was conducted. DAS formulated in an oil-in-water emulsion exhibited high phototoxicity, which was substantially reduced upon incorporating a broad-spectrum sunscreen. DAS, capable to generate both singlet oxygen and radicals, triggered photooxidation in both lipids and proteins. Similarly, DNA photodamage was evidenced by comet assay and γ-H2AX foci detection.

Avapritinib (AVP), a newly approved TKI, was proven to be a phototoxic drug with a PIF value *ca.* 11, which was highly photooxidative toward proteins and capable to induce DNA photodamage.

All in all, the study of skin toxicity of TKIs in combination with sunlight was achieved through a comprehensive evaluation of their photobehavior both in solution and within skin cells. The aim is to provide healthcare professionals with updated information on photo(geno)toxicity and encourage them to assess and implement photoprotection strategies for patients undergoing TKI-based therapy.

Resumen

En las últimas décadas, la aprobación de los inhibidores de la tirosina quinasa (del inglés TKI) como una nueva clase de terapia dirigida ha mejorado la calidad de vida y las tasas de supervivencia de los pacientes con cáncer. Sin embargo, los efectos adversos asociados a éstos, como son las reacciones cutáneas, siguen siendo un desafío para la terapia controlada. De acuerdo con anteriores estudios fotofísicos y fotobiológicos de TKI realizados por el grupo de investigación, esta tesis sigue un enfoque multidisciplinar para investigar nuevos fármacos fotoactivos dentro de esta familia. En la etapa inicial, se seleccionaron cuatro TKI, gefitinib, axitinib, dasatinib y avapritinib, por su capacidad para absorber luz UVA y por su potencial fototóxico. Los estudios, tanto fotofísicos como fotobiológicos, se llevaron a cabo en estos fármacos.

Gefitinib (GFT), un TKI con un cromóforo quinazolina, reveló cambios significativos en la fototoxicidad debido a modificaciones metabólicas en su estructura. Así, la desalquilación de la cadena lateral propoxi-morfolina (DMOR-GFT) presentó el valor más alto de factor de fotoirritación (PIF), aprox. 48, mientras que el metabolito desmetilado (DMT-GFT) mostró un valor de PIF mucho menor (~7), casi la mitad del valor de PIF del fármaco inalterado (~13). Por el contrario, el metabolito que presenta un grupo hidroxilo en lugar de flúor (DF-GFT) resultó no ser fototóxico. Notablemente, solo se confirmó que DMOR-GFT induce fotoperoxidación lipídica mediante un mecanismo oxidativo de Tipo I, basado en la escasa producción de oxígeno singlete y la eficiente desactivación del estado excitado triplete por un modelo lipídico. La fotooxidación de proteínas se evidenció en el caso de GFT y, en menor medida, en DMOR-GFT, pero resultó insignificante para DMT-GFT. Sin embargo, a diferencia de GFT, el daño al ADN inducido por el metabolito desmetilado no se reparó incluso después de varias horas.

Axitinib (AXT), comercialmente disponible como el isómero *(E)*-AXT, tiende a fotoisomerizar a *(Z)*-AXT, especialmente en presencia de proteínas. Así, se revelaron dos mecanismos de fototoxicidad. En primer lugar, la conversión del *(E)*-AXT (no citotóxico) en el *(Z)*-AXT (citotóxico) tras irradiación. En segundo lugar, la fototoxicidad intrínseca exhibida por *(Z)*-AXT. Además, la fotooxidación de proteínas se atribuyó al isómero *Z* debido a la similitud en el contenido de carbonilo entre ambos isómeros y la alta afinidad del isómero *Z* por las proteínas. Finalmente, la fotogenotoxicidad solo se reveló mediante la detección de histonas γ-H2AX.

Dasatinib (DAS) es un TKI propuesto para el uso tópico en enfermedades cutáneas. Tras establecer un PIF inicial de 5, se confirmó la fototoxicidad de DAS en una emulsión oleo-acuosa en epidermis humana reconstruida (RhE), la cual se redujo sustancialmente al incorporar un filtro solar de amplio espectro. DAS presenta capacidad de generar tanto oxígeno singlete como radicales, desencadenando fotooxidación tanto en lípidos como en proteínas. Asimismo, se evidenció daño fotoinducido al ADN mediante el ensayo cometa y la detección de histonas γ-H2AX.

Avapritinib (AVP), un TKI de nueva aprobación, demostró ser un fármaco fototóxico con un valor de PIF de aproximadamente 11. Además, fue capaz de inducir tanto fotooxidación a las proteínas como daño en el ADN.

En definitiva, el estudio de la toxicidad cutánea de los TKI en combinación con la luz solar se llevó a cabo mediante una exhaustiva evaluación de su fotocomportamiento tanto en disolución como en células de piel. El objetivo es proporcionar a los profesionales de la salud información actualizada sobre la foto(geno)toxicidad y alentarlos a evaluar e implementar estrategias de fotoprotección para los pacientes sometidos a la terapia basada en TKI.

Resum

En les últimes dècades, l'aparició d'inhibidors de la tirosina cinasa (de l'anglès TKI) com una nova classe de teràpia dirigida ha millorat la qualitat de vida i les taxes de supervivència dels pacients amb càncer. No obstant això, els efectes adversos associats a aquests, com les reaccions cutànies, continuen sent un desafiament per a la teràpia controlada. D'acord amb estudis fotofísics i fotobiològics prèvis de TKI realitzats pel grup de recerca, esta tesi segueix un enfocament multidisciplinari per a investigar nous fàrmacs fotoactius dins d´aquesta familia. En l'etapa inicial, es van seleccionar quatre TKI, gefitinib, axitinib, dasatinib i avapritinib, per la seua capacitat per absorbir llum en la regió UVA i el seu potencial fototòxic.

Gefitinib (GFT), un TKI amb un cromòfor quinazolina, va experimentar canvis significatius en la fototoxicitat a causa de modificacions metabòliques en la seua estructura. La desalquilació de la cadena lateral propoxi-morfolina (DMOR-GFT) va presentar el valor més alt de factor de fotoirritació (PIF), aprox. 48, mentre que el metabòlit desmetilat (DMT-GFT) va mostrar un valor de PIF molt menor (~7), quasi la meitat del valor de PIF del fàrmac inalterat (aprox. 13). Al contrari, el metabòlit que presenta un grup hidroxil en lloc de fluor (DF-GFT) va resultar no ser fototòxic. Notablement, només es va confirmar que DMOR-GFT induïx fotoperoxidació lipídica mitjançant un mecanisme oxidatiu de Tipus I, basat en l'escassa producció d'oxigen singlet i l'eficient desactivació de l'estat excitat triplet per un model lipídic. La fotooxidació de proteïnes va ser evident per a GFT i, en menor mesura, per a DMOR-GFT, però va resultar insignificant per a DMT-GFT. No obstant això, a diferència de GFT, el dany a l'ADN induït pel metabòlit desmetilat no es va reparar fins i tot després de diverses hores.

Axitinib (AXT), comercialment disponible com a *(E)*-AXT, tendeix a fotoisomeritzar a *(Z)*-AXT, especialment en presència de proteïnes. Així, es van revelar dos mecanismes de fototoxicitat. En primer lloc, la conversió de l'*(E)*-AXT (no citotòxic) en el *(Z)*-AXT (citotòxic) després d'irradiació. En segon lloc, la fototoxicitat intrínseca exhibida per *(Z)*-AXT. A més, la fotooxidació de proteïnes es va atribuir a l'isòmer *Z* a causa de la similitud en el contingut de carbonil entre ambdós isòmers i l'alta afinitat de l'isòmer *Z* per les proteïnes. Finalment, la fotogenotoxicitat només es va revelar mitjançant la detecció de histones γ-H2AX.

Dasatinib (DAS) és un TKI proposat per a l'ús tòpic en malalties cutànies. Després d'establir un PIF inicial de 5, es va confirmar la fototoxicitat de DAS en una emulsió oli-aquosa en epidermis humana reconstituïda (RhE), la qual es va reduir substancialment en incorporar un filtre solar d'ample espectre. DAS presenta capacitat de generar tant oxigen singlet com radicals, desencadenant la fotooxidació tant en lípids com en proteïnes. Així mateix, es va evidenciar mitjançant l'assaig cometa i la detecció de histones γ-H2AX dany fotoinduït a l'ADN.

Avapritinib (AVP), un TKI de segona generació, va demostrar ser un fàrmac fototòxic amb un valor PIF d'aproximadament 11. A més, va ser capaç d'induir tant la fotooxidació a les proteïnes com dany en l'ADN.

En definitiva, l'estudi de la toxicitat cutània dels TKI en combinació amb la radiació solar es va dur a terme mitjançant una exhaustiva avaluació del seu fotocomportament tant en dissolució como en cèl·lules de pell. L'objectiu és proporcionar als professionals de la salut informació actualitzada sobre foto(geno)toxicitat i fomentar l'avaluació e implementació d'estratègies de fotoprotecció per als pacients sotmesos a la teràpia basada en TKI.

Abbreviatures and acronyms

$^1\Delta g$	Singlet Oxygen
$^1O_2$	Singlet Oxygen
5',8-cPu	5',8-cyclo-2'-deoxynucleoside
8-oxoG	8-hydroxyguanine
A	Absorbance
Abs	Antibodies
AcX	Acryloyl-X
ADME	Absorption, distribution, metabolism, and excretion
ADP	Adenosine diphosphate
AdvSM	Advanced systemic mastocytosis
AFT	Afatinib
AK	Actinic keratosis
ALK	Anaplastic lymphoma kinase
ALS	Alkaline-labile sites
ANT	Anthracene
APS	Ammonium persulfate
ATM	Ataxia-telangiectasia mutated
ATP	Adenosine triphosphate
ATR	Ataxia telangiectasia and Rad3 related
AVP	Avapritinib
AXT	Axitinib
BCL-2	B-cell lymphoma 2 protein
BCR	Breakpoint cluster region protein
BHT	Butylated hydroxytoluene
BRG	Brigatinib

Cl	Class
CML	Chronic myelogenous leukemia
COVID-19	Coronavirus disease 2019
CPDs	Cyclobutane pyrimidine dimers
CPZ	Chlorpromazine
ctDNA	Calf thymus DNA
CYP	Cytochrome P450
DAS	Dasatinib
DCM	Dichloromethane
DF-GFT	4-defluoro-4-hydroxy Gefitinib
DHR	Delayed hypersensitivity
DMBA	1,4-dihydro-1,2-dimethylbenzoic
DMEM	Dulbecco's Modified Eagle Medium
DMOR-GFT	O-demorpholinopropyl Gefitinib
DMT-GFT	O-demethyl Gefitinib
DNA	Deoxyribonucleic acid
DNA-PK	DNA-dependent protein kinase
DNPH	2,4-dinitrophenylhydrazine
DPBS	Dulbecco's phosphate buffered saline
DSB	Double strand break
DX	1,4-dioxane
EDTA	Ethylenediaminetetraacetic acid
EGF	Epidermal growth factor
EGFR	Epidermal growth factor receptor
EMUL	Emulsion
EtOH	Ethanol
ExM	Expansion microscopy

E_{Δ}	Singlet oxygen energy
E_T	Triplet excited state energy
F	Fluorescence
FapyG	2,6-diamino-4-oxo-5-formamidopyrimidine
FDA	Food and Drug Administration
FGF	Fibroblast growth factor
FGFR	Fibroblast growth factor receptor
FIR	Fluorescence intensity ratio
GFT	Gefitinib
GIST	Gastrointestinal stromal tumor
Guo	Guanosine
GLOBOCAN	Global Cancer Observatory
H&E	Hematoxylin and eosin
HCl	Hydrochloric acid
HSA	Human serum albumin
h	Planck constant
HR	Homologous recombination
I	Fluorescence intensity
IC	Internal conversion
IC50	Half maximal inhibitory concentration
IFF	Inner filter fluorescence
INN	International nonproprietary name
InsR	Insulin receptor gene
ISC	Intersystem crossing
KP	Ketoprofen
kq	Quenching rate constant
kq_{Δ}	Singlet oxygen decay rate constant

LA	Linoleic acid
LAP	Lapatinib
LDH	Lactate dehydrogenase
LDL	Low-density lipoprotein
LFP	Laser flash photolysis
LOOH	Lipid hydroperoxides
mAbs	Monoclonal antibodies
MDA	Malondialdehyde
MDR	Multi-drug resistance
MeCN	Acetonitrile
MEK	Mitogen-activated protein kinase
MeOH	Methanol
MiliQ	Ultrapure water by Millipore MilliQ system
MKIs	Multikinase inhibitors
ML	Methyl linoleate
MTT	3-(4,5-dimethylthiazol-2-yl)-2,5-diphenyltetrazolium
n	Refractive index
Na_2EDTA	Ethylenediaminetetraacetic disodium salt
NaCl	Sodium chloride
NaOH	Sodium hydroxide
NH_4Cl	Ammonium chloride
NHEJ	Non-homologous end joining
NIR	Near infrared
NLT	Nilotinib
NRTK	Non-receptor tyrosine kinase
NRU	Neutral red uptake
NSAIDs	Non-steroidal anti-inflammatory drugs

NSCLC	Non-small-cell lung cancer
N-LAP	N-dealkylated lapatinib
O/W	Oil-in-water emulsion
O-LAP	O-dealkylated lapatinib
P	Phosphorescence
PARP	Poly (ADP-ribose) polymerase
PBS	Phosphate buffered saline
PDGF	Platelet-derived growth factor
PDGFR	Platelet-derived growth factor receptor
PDI	Photodynamic inactivation
PDT	Photodynamic therapy
PFA	Paraformaldehyde
PI3K	Phosphoinositide 3-kinase
PIF	Photoirritant factor
PIKK	Phosphatidylinositol 3-kinase-related kinase
PKC	Protein kinase C
PLCγ	Phosphoinositide phospholipase C
PN	1H-phenalen-1-one
PS	Photosensitizer
PTK	Protein tyrosine kinase
RCC	Renal cell carcinoma
RhE	Reconstructed human epidermis
ROS	Reactive oxygen species
RTK	Receptor tyrosine kinase
S_0	Singlet ground state
S_1	First singlet excited state
SARS-CoV-2	Severe acute respiratory syndrome coronavirus 2

SCCIS	Cutaneous squamous cell carcinoma in situ
SD	Standard deviation
SDS	Sodium dodecyl sulfate
Ser139	Serine 139
Sn	Singlet excited state
SOR	Sorafenib
SSB	Single strand break
SUN	Sunitinib
T_1	First triplet excited state
TBA	Thiobarbituric acid
TBARS	Thiobarbituric acid reactive substances
TCA	Trichloroacetic acid
Temed	Tetramethyl ethylenediamine
TEMPO	2,2,6,6-tetramethylpiperidinyloxy
TEP	1,1,3,3-Tetraethoxypropane
TK	Tyrosine kinase
TKI	Tyrosine kinase inhibitor
Tn	Triplet excited state
Tox	Toxicity
TRAEs	Treatment-related adverse events
UGT	Uridine diphosphate glucuronosyltransferase
UV	Ultraviolet
υ	Frequency
VC	Vehicle control
VEGF	Vascular endothelial growth factor
VEGFR	Vascular endothelial growth factor receptor
VIR	Vibrational relaxation

Vis	Visible
ε	Molar absorption coefficient
λ	Wavelength
τ_F	Fluorescence lifetime
τ_T	Triplet excited state lifetime
τ_Δ	Singlet oxygen lifetime
ϕ_F	Fluorescence quantum yield
ϕ_Δ	Singlet oxygen quantum yield

INDEX

List of contents

List of figures

List of tables

List of equations

CHAPTER 1 Introduction

1.1 Insights into cancer disease

Cancer is a broad term comprising a diverse range of diseases that have the potential to impact any region of the body. It is a non-infectious disease, which is characterized by the emergence of cells undergoing extensive and unregulated proliferation. This, except in hematological cancers, leads to the formation of an anomalous tissue mass, known as a tumor or neoplasm, that can extend to distant organs, commonly referred to as metastasis. Overall, the main factor leading to fatality is the widespread metastases[1,2].

Cancer continues to represent a major public health problem. In 2020, cancer ranked as the leading cause of mortality worldwide, responsible for nearly 10 million fatalities. Published data on recent global cancer incidence and mortality trends are limited, partially due to the delays in the diagnosis and treatment caused by the coronavirus disease 2019 (COVID-19) pandemic. In fact, the emergence of SARS-CoV-2 has been directly associated with an increase in cancer-related deaths, potentially slowing or even reversing the declining trend in mortality observed over the last few years. According to the Global Cancer Observatory (GLOBOCAN), in 2020, there were an estimated 20 million newly diagnosed cancer cases worldwide. Among these, female breast cancer, currently, takes the lead as the most frequently diagnosed cancer, surpassing lung cancer. Notably, the estimated incidence of new cases stands at 2.3 million, representing 11.7% of the total, while lung cancer follows closely at 11.4%. Other prevalent cancers include colorectal at 10%, prostate at 7.3%, and stomach at 5.6% (Figure 1)[3].

The anticipated global cancer burden for the year 2040 is projected to reach 28.4 million cases, reflecting a substantial 47% increase compared to the

statistics recorded in 2020. This alarming surge underscores the persistent and escalating challenges posed by cancer on a global scale[4]. In this context, there is a critical need to emphasize the awareness, early detection methods, and advancements in medical interventions.

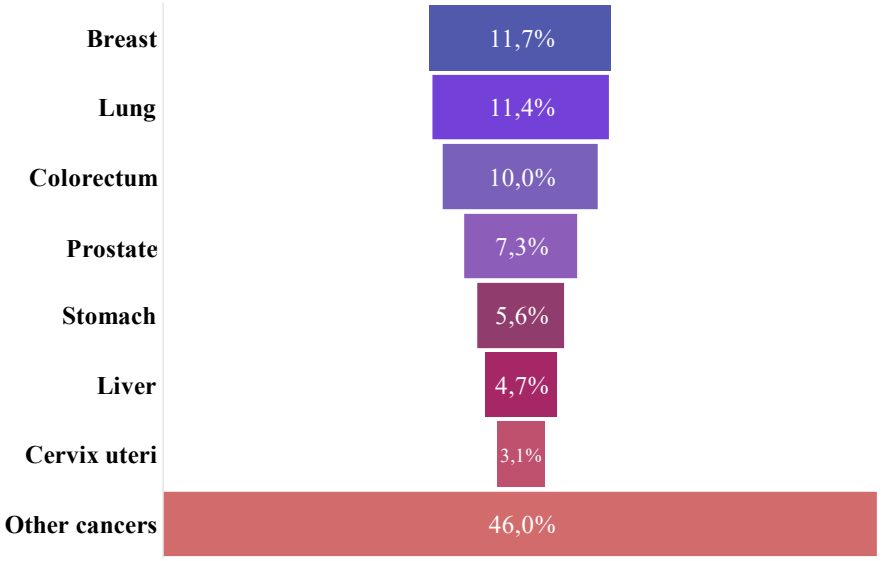

Figure 1 | Global cancer burden in 2020. Estimated incidence rates of new cancer cases in 2020 categorized by type of cancer. Figure adapted from GLOBOCAN[3].

In the conventional paradigm, treatment methods such as surgical procedures, chemotherapy, and radiation therapy have been employed. However, in recent years, several novel approaches have been achieved, for instance, targeted therapy, hormone therapy, stem cell therapy, immunotherapy, photodynamic therapy and various others (Figure 2)[5,6].

Although chemotherapy has indeed represented one of the major medical breakthroughs for cancer, the emergence of multi-drug resistance (MDR) and the undesirable reactions stand as prominent issues. In fact, chemotherapy

drugs display a narrow therapeutic index, and often, the responses produced are only palliative and unpredictable[7]. In contrast, targeted therapy, which has been introduced more recently, interferes with a specific molecular target, usually a protein with a critical role in tumor growth or progression, and therefore has a more limited profile of non-specific toxicity[8,9].

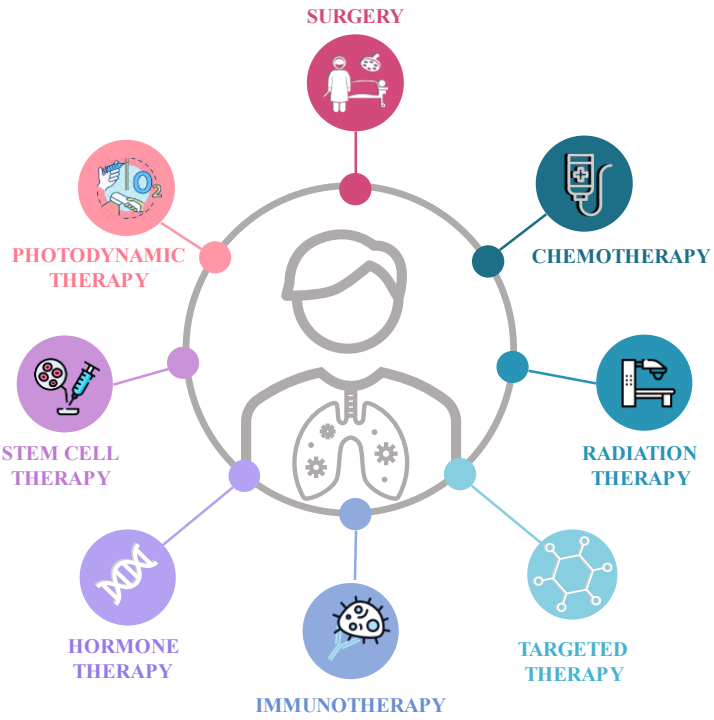

Figure 2 | Cancer therapy current approaches. Figure adapted from reference[10].

1.2 Protein tyrosine kinases

Protein tyrosine kinases (PTKs) represent a significant class of intracellular and membrane-associated enzymes, including approximately 90 different types, which have significant regulatory roles in various signaling cascades, including those associated with inflammatory responses. They catalyze the phosphorylation of specific tyrosine residues within target proteins through

ATP. This covalent modification is essential in normal cellular communication and the maintenance of the homeostasis. Thus, PTKs are implicated at various stages in the development and progression of cancer. Normally, these signaling pathways controlled by PTKs either prevent uncontrolled cell growth or enhance the cellular sensitivity to signals that trigger cell death (apoptosis). However, in cancer cells, these signaling pathways are frequently altered at the genetic or epigenetic level, providing a selective advantage to the tumoral cells. Consequently, it is not surprising that the abnormal and heightened signaling originating from PTKs elevates their status to that of dominant oncoproteins, ultimately leading to the disruption of the signaling network[11,12].

1.2.1 Classification of protein tyrosine kinases

The identification of the SRC proto-oncogene with non-receptor PTK activity, along with the discovery of EGFR as the pioneer receptor PTK, illuminated the understanding of the importance and function of these kinases in the context of cancer. In this setting, PTKs can be classified in 2 categories, the transmembrane receptor PTKs (RTKs) and the non-receptor PTKs (NRTKs)[13,14].

Receptor tyrosine kinases

More than 15 receptor tyrosine kinases (RTKs) have been identified which are involved in several key steps of tumor progression, such as cell proliferation, cell cycle, migration, metabolism, programmed cell death, survival, and differentiation[15].

The RTKs encompass various members, including the epidermal growth factor receptor (EGFR), platelet-derived growth factor receptor (PDGFR),

vascular endothelial growth factor receptor (VEGFR), insulin receptor (InsR) family, among others. Typically, these receptors feature an extracellular domain responsible for binding to specific ligands, a transmembrane region, and an intracellular kinase domain that specifically phosphorylates substrates (Figure 3). Moreover, RTKs have the capability to bind to ligands, phosphorylate tyrosine residues on target proteins, and transmit information through various signaling pathways like PI3K/AKT/mTOR, RAS/RAF/MEK/ERK, PLCγ/PKC, and others. This activation initiates a cascade of biochemical reactions or integrates different signals to trigger a specific cellular response, such as cell proliferation[15,16].

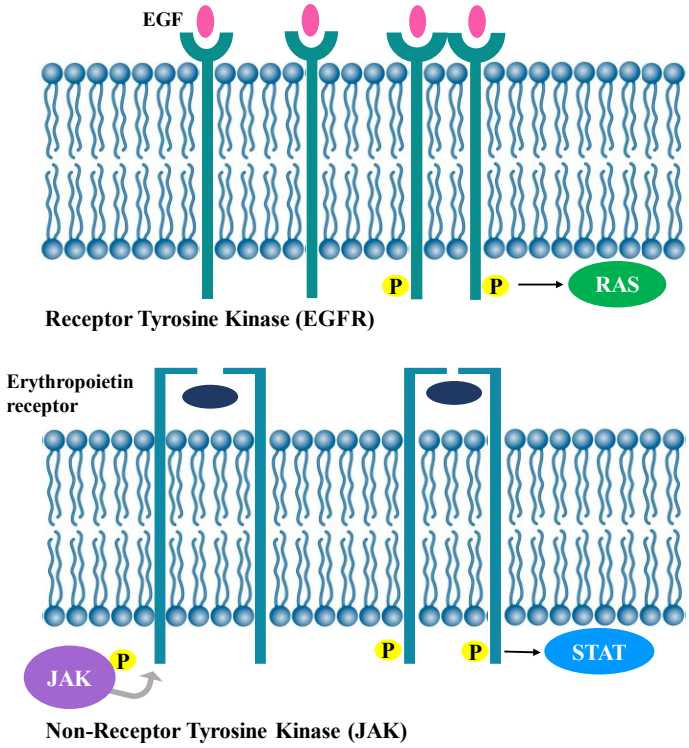

Figure 3 | Protein tyrosine kinases (PTKs). Signal transduction differences between receptor tyrosine kinase (RTK) and non-receptor tyrosine kinase (NRTK).

Non-receptor tyrosine kinases

Although non-receptor tyrosine kinases (NRTKs) represent a minority in the human kinome they display a wide-ranging role in cell signaling, providing an extra target for anticancer drugs. This group of proteins can be further subclassified in 9 families, Abl, FES, JAK, ACK, SYK, TEC, FAK, Src, and CSK kinases. The most frequent signaling pathway involves JAK-STAT proteins. While RTKs are activated by ligand binding, the activation of NRTKs follows a more intricate mechanism, involving specific protein-protein interactions that triggers transphosphorylation (Figure 3)[17].

1.2.2 Protein tyrosine kinases as targets in cancer therapy

Considering the significance of PTKs in the signaling pathways leading to cell growth, it is expected that a multitude of RTKs and NRTKs would be involved as potential targets for inhibitors capable of interfering with their catalytic activity[11]. For example, when agonists like EGF bind to their extracellular domains, it triggers dimerization and subsequent activation (Figure 4). Activated forms of these enzymes can enhance tumor cell proliferation, facilitate growth, prevent apoptosis, and promote processes such as angiogenesis and metastasis through signaling pathways like RAS or phosphoinositide 3-kinase (PI3-K)[11,18].

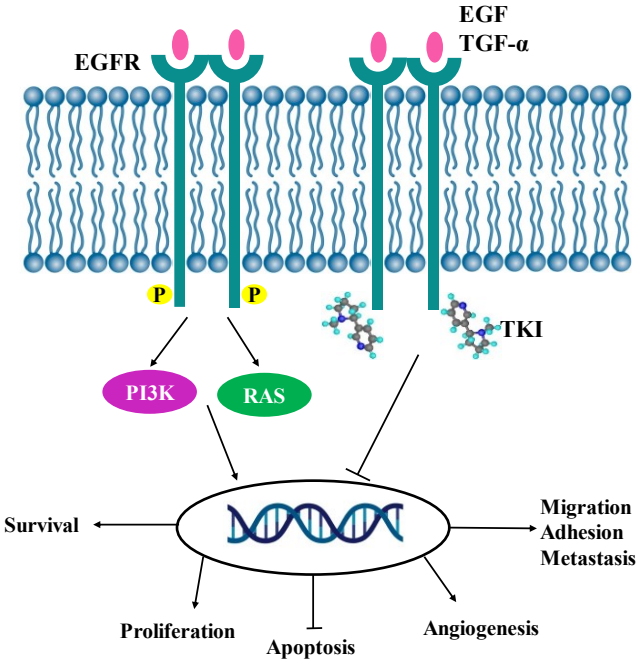

Figure 4 | Receptor tyrosine kinases (RTKs). The structure, function, and mechanism of activation of EGFR and its inhibition by tyrosine kinase inhibitor (TKI).

1.3 Tyrosine kinase inhibitors (TKIs)

Recent clinical outcomes revealed the crucial role played by growth factor receptors, consisting of transmembrane and cytoplasmic TK domains, in the key hallmarks of cancer progression[19]. Despite their activity is regulated in normal cells, overexpression can lead to malignancy. Thereby, using a specific TK inhibitor (TKI) can block the oncogenic activation in cancer cells, making it a potential and innovative strategy in cancer treatment[13].

A significant number of TKIs have the ability to inhibit multiple PTKs and they have demonstrated clinical success across a plethora of cancers since 2001. Typically, TKIs exert their effects by targeting the active site of the

kinase, thereby preventing the phosphorylation of intracellular targets often associated with cell proliferation and angiogenesis[15].

In the last two decades, there has been significant progress in the development of several effective and well-tolerated targeted TKIs. These inhibitors, designed to act on specific single or multiple targets such as EGFR, ALK, ROS1, HER2, NTRK, VEGFR, RET, MET, MEK, FGFR, PDGFR, and kit, have played a crucial role in advancing the clinical field of precision cancer medicine. By tailoring treatment based on the unique genetic alterations of individual patients and disease, TKIs have not only greatly enhanced survival rates and quality of life but also reshaped the approach to treating multiple solid tumors[20].

1.3.1 Classification of TKIs

The two main strategies in TKIs therapy are the monoclonal antibodies (mAbs) and the small-molecule inhibitors. Certainly, there is a significantly larger quantity of small-molecule TKIs compared to mAbs targeting PTKs[21]. According to the latest available data, the Food and Drug Administration (FDA) has approved approximately 43 TKIs for oncological applications (Table 1 and Figure 5). These are characterized by their small size (<900 Daltons), oral administration, high affinity for ATP binding pocket of the TKs, and well-established safety profiles, rendering them amenable to combination therapy with other chemotherapy or radiotherapy modalities[22]. Moreover, the nomenclature of this family of anticancer drugs commonly end with the suffix -nib[23].

Table 1 | Documentation on FDA-Approved tyrosine kinase inhibitors.

Class	Target	Indication	TKI (INN)	Brand name
Receptor Tyrosine Kinase	HER2/ EGFR	Breast cancer Lung cancer Lung cancer, pancreas cancer	Lapatinib Gefitinib Erlotinib	Tyverb Iressa Tarceva
	C-kit, PDGFR, VEGFR	Kidney cancer Medullary cancer Kidney cancer and hepatoma	Pazopanib Cabozantinib Sunitinib Sorafenib	Votrient Cometriq Sutent Nexavar
Non-Receptor Tyrosine Kinase	BCR/ ABL	CML	Imatinib Dasatinib Nilotinib	Glivec Sprycel Tasigna
	EML4-ALK	Kidney cancer Lung cancer	Brigatinib Crizotinib	Alunbrig Xalkori
	BRAF	Metastatic melanoma	Vemurafenib Dabrafenib	Zelboraf Tafinlar

Summary of the most frequently used and approved tyrosine kinase inhibitors (TKIs). Table adapted from reference[22].

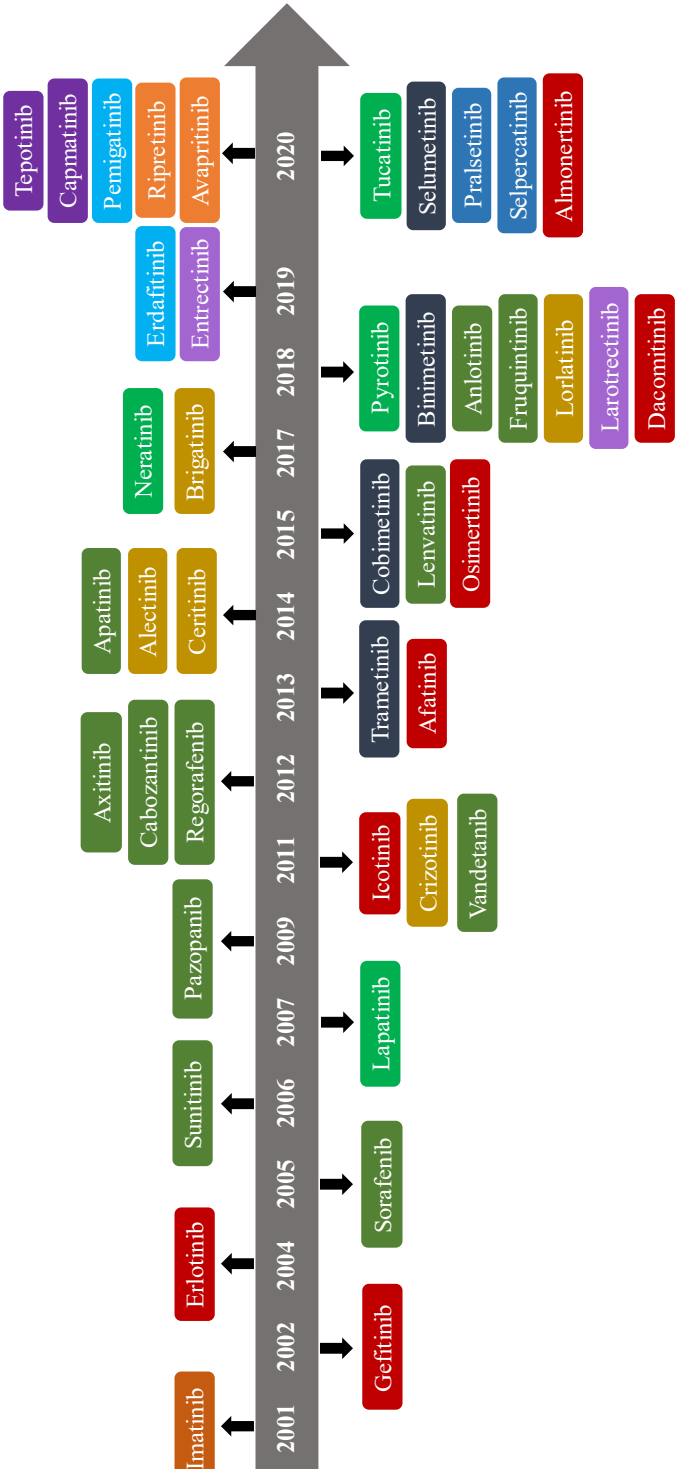

Figure 5 | Trends in tyrosine kinase inhibitors (TKIs) discovery. A schematic summary of the approved TKIs in 2001–2020. Figure adapted from reference[20].

1.3.2 Side effects of TKIs

Adverse effects are a significant concern during the drug development phase. Furthermore, they are of interest because, in certain cases, side effects can be linked to treatment responses[24]. In fact, targeted therapy has a unique toxicity profile that can be classified into 5 different categories:

I. Hypersensitivity and immunological reactions.
II. On-target events (mechanism-associated toxicity).
III. Off-target events (toxicity related to the type of agent, e.g., mAbs vs. TKIs).
IV. Toxic metabolite activation.
V. Idiosyncratic toxicities.

In this context, despite the specificity typical of targeted therapy, patients undergoing TKI treatment face several side effects. Skin rash manifestations are the most common events, expressed in the form of papulopustular eruption on the scalp, hands, neck, and face[25]. Nearly, all patients treated with EGFR or MEK TKI experienced skin toxicity. Diarrhea is considered the second most common event in patients treated with small TKIs. In the majority of cases, these adverse effects are related to the mechanism of action of the inhibitor drug (Table 2)[24–26].

Although the greater part of these adverse effects is almost never lethal, they represent the first cause of therapy discontinuation. In certain cases, serious adverse reactions demand the early termination of life-saving cancer treatment. For instance, cardiotoxicity associated with nilotinib in preclinical safety studies led the FDA to issue a black boxed warning, recognizing it as a possible life-threatening drug[26,27].

Table 2 | Classification of adverse effects of tyrosine kinase inhibitor (TKI) therapy.

Toxicity	Type of agent	Occurrence rate	Mechanism
Skin rash	EGFR TKIs	45-100%	EGFR inhibition
	MEK inhibitors	80%	MEK inhibition
	PI3K/AKT/mTOR inhibitors	26-51%	PI3K/AKT/mTOR inhibition
Diarrhea	EGFR TKIs	19-36%	-
	VEGFR TKIs	40-60%	-
	MEK inhibitors	42%	-
	PI3K inhibitors	21-48%	-
Hypertension	VEGFR TKIs	20-30%	VEGFR inhibition
Hypothyroidism	VEGFR TKIs	4-32%	VEGF inhibition
Proteinuria	VEGFR TKIs	21-63%	Inhibition of c-kit, PDGFR, RET
Hepatotoxicity	Various TKIs	11-50%	

Toxicological events associated with tyrosine kinase inhibitor (TKI) therapy. Table adapted from reference[24].

Toxicity	Type of agent	Occurrence rate	Mechanism
Skin or hair depigmentation	Pazopanib	38%	-
	Cabozantinib	34%	-
	Sunitinib	7-10%	-
	Sorafenib	Case reports	-
	Dasatinib	Case reports	-
	Imatinib	Case reports	-
Hemorrhage	VEGFR TKIs	16.7%	VEGFR inhibition
G1 perforation	VEGFR TKIs	1.3%	VEGFR inhibition
QT prolongation	Vandetanib	14%	-
	Nilotinib	1-10%	-
	Crizotinib	4.8%	-
Ocular toxicity	Various TKIs	1-38%	-
Dyslipidemia/hyperglycemia	PI3K/mTOR inhibitors	10-76%	Inhibition of PI3K/mTOR

Toxicological events associated with tyrosine kinase inhibitor (TKI) therapy. Table adapted from reference[24].

As stated above, skin-related adverse effects are frequently observed with targeted therapies, particularly with TKIs. Notably, a higher incidence rate of skin toxicity was reported immediately after initiating EGFR inhibitor therapy. In most cases, these skin-associated effects improved after dose reductions, demonstrating a significant correlation between the severity of the reactions and the dosage of EGFR-TKI[28]. It is worth noting that cutaneous toxicity appears to be mostly unlinked to the specific EGFR-TKI employed, and while these effects are typically moderate, they tend to be persistent and can negatively impact the quality of life of cancer patients[29].

The underlying mechanism of this side effect remains unclear. However, it is well known that EGFR plays a pivotal role in the normal functioning of the epidermis and is expressed mainly in undifferentiated, actively dividing keratinocytes located in the basal and suprabasal layers of the epidermis, sebocytes and the outer layers of hair[29–31]. Despite these adverse effects being typical after treatment with EGFR-TKI they were also manifested with BRAF, MEK and mTOR inhibitors[31].

1.3.3 Skin anatomy

Skin is the largest organ of the body, which functions as a highly metabolic and multifaceted organ characterized by intricate structural complexity. The main role is to serve as a protective barrier against external microorganisms and environmental factors. In adults, the average mass is about 4 kg and the surface area ranges from 1.5 to 2.0 square meters[32,33].

The main functions of the skin are[32,34,35]:

- Thermoregulation: The presence of hair and sweat glands contributes to the regulation of body temperature.

- Protection: The skin acts as a barrier preventing loss of vital body fluids, and infiltration of toxic agents.
- Photoprotection: Reduces the damage from the sunlight (especially from UVB light) and infection diseases.
- Clearence: Elimination of toxic substances through sweat.
- Immunological function: Innate and adaptive immune responses.
- Hormone synthesis: Serotonin, melatonin, etc.
- Mechanical support.
- Sensory organ.
- Storage of fat, water, and vitamin D.

From a structural standpoint, the skin is a dynamic, multifaceted entity with its biological and mechanical attributes changing across the various stages of life and in response to socio-environmental factors. At a larger scale, the skin is commonly categorized into three well-defined structures: the epidermis, dermis, and hypodermis[34,36].

The outermost layer of the skin, also known as the epidermis, is continuously renewing and lacks blood vessels. It primarily consists of squamous cells rich in filaggrin and keratin. This layer is further subdivided into four strata. The basement membrane, also called as the basal layer, is composed of rapidly proliferating cells, some of which differentiate to form the second layer, known as the stratum spinosum. The stratum granulosum is the last layer containing living cells, whereas the stratum corneum is the superficial layer containing only dead cells. Each of these layers has distinct functions and compositions that are closely tied to the cell cycle of keratinocytes, which make up the majority (90-95%) of the epidermal cells. In addition to

keratinocytes, smaller populations of other cell types exist, including melanocytes (3%), Langerhans cells (2%), and Merkel cells (0.5%)[33,34].

The dermis, situated in the middle layer of the skin, is primarily made up of a dense extracellular matrix. This matrix provides support to vascular tissue, sensory nerve cells, and various structures like sweat glands and hair follicles. The main contributors to this extracellular matrix are fibroblasts, responsible for producing primarily elastin and collagen. These elements give the skin its unique properties of resilience and elasticity[33–35].

The hypodermis, also known as subcutaneous tissue, is the innermost layer of the skin. It consists of a network of fat (adipocytes) and connective tissue that serves various functions, including insulation, energy storage, and protection of underlying structures. In addition to adipose tissue, the hypodermis contains blood vessels, nerves, and connective tissue fibers. These tissues are organized into lobes, which are further divided by partitions through which the microvascular network flows, supplying oxygen and nutrients[33–35].

Giving this background, the predominant cell types within skin tissue are keratinocytes and fibroblasts.

Keratinocytes

Keratinocytes are the predominant cells in the epidermis. They can be distinguished from melanocytes and Langerhans cells within the epidermis due to their larger size, intercellular connections, and abundant cytoplasm (Figure 6). They originate from the ectoderm and can be found in all four layers of the epidermis. In normal conditions, keratinocytes start to replicate from the basal layer and, over 30 to 50 days, migrate through the epidermis to the superficial layer, stratum corneum. Throughout this process, these cells

undergo significant functional and morphological transformations, accumulating keratin along the way. Ultimately, they shed or rub off [32,37].

Briefly, keratinocyte cells display the following characteristics[34]:

- They produce keratin, which is the most crucial structural protein that forms the basis of skin, hair, and nails.
- They release minimal extracellular matrix, which results in proximity between the cell membranes of adjacent keratinocytes, promoting the cohesion and integrity of the epidermis.
- Their rate of replication can change in response to an injury[38].
- They possess the highest skin biotransformation capability, thanks to their substantial reservoir of skin cytochrome P450 activity[39].

Keratinocytes also can release cytokines and are increasingly acknowledged as a significant component of the immune system. They secrete substances like interleukins, colony-stimulating factors, tumor necrosis factors, and growth factors. Various stimuli, including chemicals, ultraviolet (UV) light, and injury, can trigger the production of these cytokines by keratinocytes. This cytokine production potentially positions keratinocytes as intermediates in proinflammatory signaling, with a notable role in guiding and activating lymphocytes. It is important to highlight that keratinocytes contribute as barrier against UV radiation. They trigger melanocytes to produce melanin, a protective pigment that can absorb and dissipate harmful UV radiation as heat[35,40].

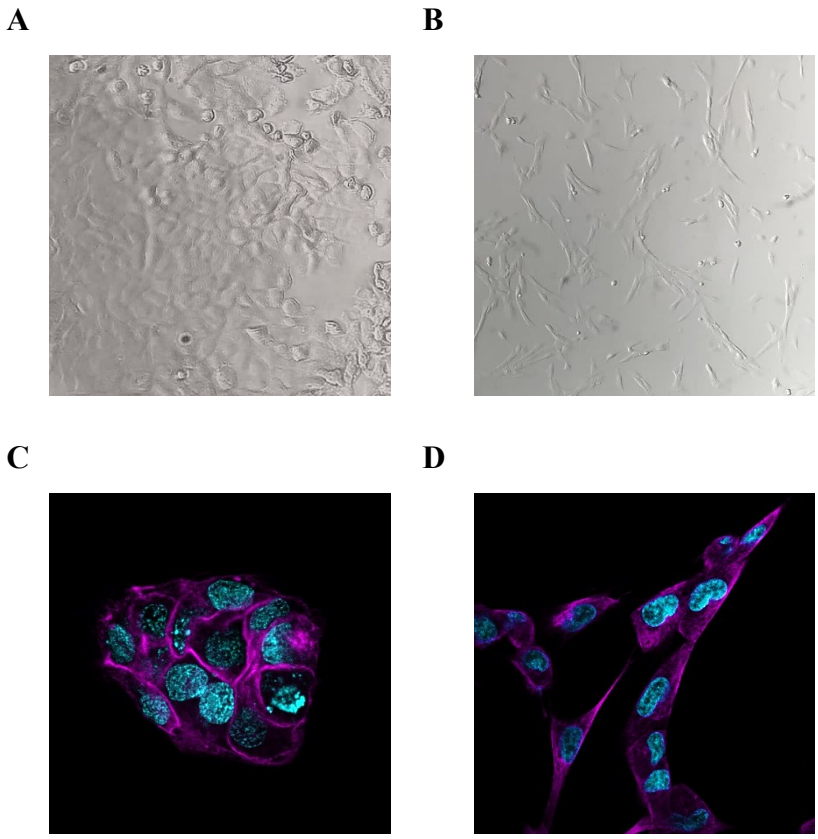

Figure 6 | Keratinocyte and fibroblast cells. Top: Bright field microscope images of human keratinocytes, HaCaT cells (A) and human fibroblasts, Bj-hTERT cells (B). Bottom: Confocal microscopy images of living HaCaT keratinocytes (C), and fixed Bj-hTERT fibroblasts (D). HaCaT cells were stained with CellMask™ Orange Plasma membrane and RedDot™ Far-Red nuclear stains. Bj-hTERT cells were immunostained with anti-α-tubulin and the nuclei was stained with Dapi.

Fibroblasts

Fibroblasts play an essential role in maintaining the structural integrity of tissues and organs. They are responsible for producing collagen (type I and/or type III collagen) and other components (elastin, glycoproteins, proteoglycans, etc.), giving them the role of arbiters in extracellular matrix remodeling (Figure 6). These cells originate from the mesoderm and are

distributed throughout the dermis. Fibroblasts have a spindle-shaped appearance with elongated, oval nuclei[46].

Within the dermis, fibroblasts are organized into three subpopulations: one in the papillary dermis, one in the reticular dermis, and one associated with hair follicles. These subpopulations exhibit subtle variations in collagen and extracellular matrix component production, which correspond to local structural differences[46]. Fibroblasts also play a significant role in wound healing. When an injury occurs, growth factors and cytokines, including platelet-derived growth factor, attract fibroblasts to the wound site. These fibroblasts have the ability to transform into myofibroblasts that aid in wound closure[41,42].

In summary, the primary cellular components of human skin are keratinocytes and fibroblasts. As the predominant cell types, their roles are pivotal in comprehending the intricate mechanisms that lead to skin reactions. Moreover, the interplay between keratinocytes and fibroblasts is essential in orchestrating skin responses to external factors, such as chemicals and/or UV radiation.

1.4 Drug-induced photosensitivity

The benefits from sunlight are widely acknowledged; from vitamin D production to the treatment of certain skin conditions, such as psoriasis, eczema, and vitiligo. However, the same light exposure can be potentially harmful leading to skin damage, cataracts, carcinoma and immune suppression[43]. Thus, different scenarios have been proposed in order to explain the molecular bases of photosensitivity, however, drug-induced photosensitized reactions are not completely determined.

The mechanisms behind drug-induced photosensitivity are intricate and can be detected at cellular, molecular, and biochemical levels. Usually, chemicals triggering photosensitized reaction are light-absorbing molecules. Therefore, photosensitivity is dependent on the ability of a drug to efficiently absorb light, typically in the UV or visible range. The electromagnetic spectrum of sunlight covers 3 components: UV light (180-400 nm), visible light (400-700 nm), and infrared (IR) rays (700 nm-3 μm)[43]. Approximately 10% of sunlight output is UV radiation and about 40% is visible light. In this context, UV spectrum can be further subdivided into 3 regions: UVC (100–280 nm), UVB (280–315 nm), and UVA (315–400 nm)[44]. The UV radiation that reaches the surface of the skin is composed of roughly 5% UVB and 95% UVA. In contrast, UVC, which is the highest-energy component of UV light, does not impact the skin since it is absorbed by the ozone layer (Figure 7). Interestingly, while UVB radiation is capable of directly reacting with biomolecules and causing direct damage, UVA radiation is the primary contributor to the development of photosensitivity reactions[44]. This is attributed to the fact that shorter UVB wavelengths only reaches the epidermis layer, while UVA radiation can penetrate into the papillary dermis, mediating damage to both the epidermis and dermis layers[45,46].

Furthermore, it is important to acknowledge that the photosensitivity potential of a drug is not exclusively contingent upon its capacity to absorb light. Additional determinants, including the concentration of the drug within the skin, the duration of light exposure, and individual variances in skin sensitivity, significantly contribute to the overall risk and appearance of photosensitivity reactions[47].

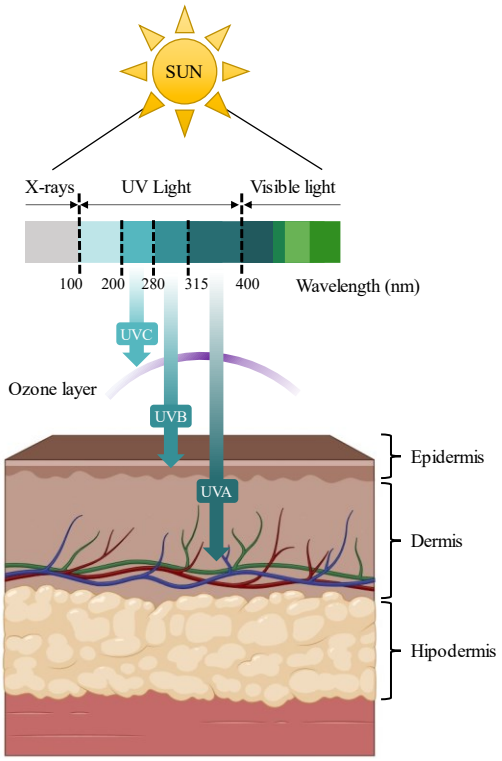

Figure 7 | Ultraviolet (UV) spectrum-dependent penetration into the skin layers.

Currently, there are more than 300 photosensitizing drugs belonging to 13 different pharmacological groups[45]. The FDA has not only provided a list of agents that may increase sensitivity to light exposure (Table 3) but also issued guidance for the evaluation of the photosafety of these pharmaceuticals toward the industry[48].

Table 3 | Photosensitizing FDA reported drugs.

Drug Family	Examples
Antibiotics	Azithromycin, erythromycin, ciprofloxacin, levofloxacin, sulfasalazine, doxycycline...
Antidepressants	Amoxapine, amitriptyline, nortriptyline, fluoxetine, paroxetine, sertraline, mirtazapine…
Antidiabetics	Sulfonylureas (chlorpropamide, glibenclamide, gliclazide, glimepiride, glipizide, tolbutamide...)
Antifungals	Griseofulvin, ketoconazole, voriconazole
Antihistamines	Azatadine, carbinoxamine, cetirizine, chlorphenamine, diphenhydramine, ebastine, loratadine...
Antihypertensives	Calcium channel blockers (amlodipine, felodipine...), ACE inhibitors (captopril, enalapril...) and Others (losartan, valsartan…)
Antipsychotics	Phenothiazines (chlorpromazine, thioridazine...) and others (clozapine, clotiapine, olanzapine...)
Anxiolytics	Barbiturates (pentobarbital, secobarbital...) and benzodiazepines (alprazolam, diazepam...)
Diuretics	Loop diuretics (furosemide, piretanide) and thiazides (hydrochlorothiazide, chlortalidone...)
Hypolipidemics	Statins (atorvastatin, lovastatin, pravastatin...) and fibrates (clofibrate, fenofibrate...)
Proton Pump Inhibitors	Omeprazole, pantoprazole…
Non-steroidal anti-inflammatory drugs (NSAIDs)	Topical anti-inflammatory agents: benzidamine, benoxaprofen, etofenamate, ibuprofen, ketoprofen, naproxen, piroxicam...

Main groups and list of prescribed photosensitizing drugs. Table adapted from reference[47].

Regarding TKIs, photosensitivity is the most reported reaction associated with BRAF inhibitors; between 22 to 67% of patients undergoing vemurafenib therapy expressed cutaneous eruption in sun-exposed areas within a few minutes of UV radiation. Previous case reports of photosensitivity reactions have been observed in multikinase inhibitors (MKIs) that have overlapping receptors, specifically pazopanib, sunitinib and vandetanib. Recently, a case of phototoxicity was reported in a patient who underwent sunlight exposure two years after enduring pazopanib treatment[49]. Moreover, retrospective studies and multiple clinical trials have documented phototoxicity events from sunitinib therapy[50]. Similarly, vandetanib has been conclusively linked to photosensitivity, with up to 37% of patients experiencing reactions characterized by skin eruptions ranging from heightened sunburn to severe, photodistributed erythematous eruption[51–54].

Interestingly, brigatinib photosensitive side effects were identified as phototoxic rather than a photoallergic reaction based on clinical manifestations resembling an intensified sunburn with the dermatosis localized to sun-exposed areas[55,56].

Finally, multiple case reports have been registered regarding photosensitive reactions induced by EGFRs inhibitors, such as gefitinib, erlotinib, imatinib, lapatinib and vandetanib[31].

1.4.1 Mechanisms of drug-induced photosensitivity

Photosensitivity represents a broad term, which describes various skin responses to light exposure, capturing both immune-mediated (photoallergy) and non-immune-mediated reactions (phototoxicity). This category also

includes idiopathic photodermatoses, such as porphyria, which contribute to the phototoxic reactions in specific pathologies.

Porphyrin-induced phototoxicity

Porphyrins constitute natural metabolites, serving as intermediates in the biosynthesis of haem within mammalian organisms. Haem, the final product of this pathway, is a tetrapyrrole in which ferrous iron is chelated with protoporphyrin IX. Due to its capability to bind and release oxygen, haem plays a crucial role in various metabolic pathways across living organisms. Disorders within the porphyric group arise from enzymatic abnormalities in haem synthesis, whether inherited or acquired. The interaction between excited porphyrins and oxygen results in the generation of ROS, ultimately causing tissue damage, as observed in patients affected by porphyria. Individuals diagnosed with erythropoietic protoporphyria experience skin burning, followed by erythema and edema, when exposed to sunlight. Protoporphyrin IX, with an intense UV absorption occurring between 400 and 410 nm, abnormally accumulates in this particular disorder, triggering photosensitized damage reactions that culminate in the well-known condition referred to as photodermatoses[57,58]. Interestingly, certain drugs are recognized for inducing pseudoporphyria; for instance, voriconazole has been linked to the onset of phototoxicity and the manifestation of bullous photodermatoses, which clinically and histologically mimics porphyria cutanea tarda[59]. Furthermore, numerous drugs, including phenobarbital, valproic acid, rifampicin, and others, are acknowledged for their potential to precipitate an acute porphyria attack (drug porphyrogenicity). Ergo, acute porphyrias are also regarded as pharmacogenetic or toxogenetic diseases[60].

Photoallergy

Drug-induced photoallergic reactions are less frequent compared to phototoxic reactions and typically require minimal exposure to photosensitizing drugs along with prior sensitization. It is an immunological process where a photosensitizing product acts as either a hapten or complete antigen, leading to a delayed hypersensitivity reaction (Type IV or DHR). Thus, a lower amount of energy is needed to trigger a photoallergic reaction compared to a phototoxic reaction[45]. Clinically, the onset of photoallergy occurs 24 h or more after the initial exposure and presents as an eczematous dermatitis that can extend beyond sun-exposed skin areas. Upon discontinuation of the photosensitizing drug, the photoallergic reaction typically resolves, although in rare instances, it may persist and progress into chronic dermatitis. Additionally, in some cases, prior exposure to the drug may not be necessary if the patient has previously been sensitized through contact with a similar molecule[61–64].

Phototoxicity

Phototoxic reactions, in addition to being more frequent, are dose-dependent reactions that take place upon the interaction with light and the absorption of a photon by the photosensitizer. Thus, producing a highly reactive excited intermediate capable of inducing oxidative damage to key cellular structures. In clinical context, these reactions can be identified by erythema and edema that begins several hours after the exposure and is subsequently followed by skin peeling and increased pigmentation[30,48]. The action spectra of drug photosensitizers typically involve, at the very least, UVA radiation, while in some molecules, the activating light include or is limited to visible wavelengths[52,53]. Unlike photoallergies, which may take time to develop,

phototoxic reactions often occur rapidly after exposure to light, sometimes within minutes to hours. Apart from the concentration of the photosensitizer, the severity of the reaction may vary depending on other factors such as the duration of light exposure and individual differences in skin sensitivity[61].

In summary, photosensitive adverse events are typically classified into either phototoxic or photoallergic reactions. The categorization is based on distinct pathophysiological mechanisms, and several features highlight the contrasts between them. Understanding these distinctions is crucial for accurate diagnosis and appropriate management of photosensitive reactions. For instance, photoallergic reactions, since they involve immune responses, require a specific treatment such as antihistamines or corticosteroids. In contrast, phototoxic reactions are not immune-mediated, and their management typically entails discontinuation of the photosensitizing agent or photoprotection guidelines, coupled with measures aimed at providing symptomatic relief.

Thus, while differentiating between photoallergic and phototoxic reactions can be challenging, certain guiding principles have been outlined in order to identify the specific type of photosensitivity reaction (Table 4)[61]. This contributes to a better understanding of drugs safety profile and is crucial for tailored treatment, effective prevention, and overall improved patient care.

Table 4 | Main differences between phototoxicity and photoallergy.

Characteristics	Phototoxicity	Photoallergy
Frequency	High	Low
Latency period/sensitization	No	yes
Doses of UV/photosensitizer	High	Low
Cross-reactions	No	Yes
Morphology of lesions	Sunburn polymorphic	Eczema, erythema multiforme
Sharp limits	Yes	No
Covered areas	Not involved	Possibly involved
Resolution	Quick	May recur, persistent reactors
Residual hyperpigmentation	Yes	No
Histology	Sunburn cells	Eczema
Pathomechanism	DNA/cell damage	Type IV hypersensitivity
	ROS/inflammation	Photoproduct

1.4.2 Sunlight-mediated damage to biomolecules

Photosensitized oxidation reactions involving key biomolecules such as unsaturated lipids, proteins, and nucleic acids, which initiate the referred to "photodynamic effects", have been demonstrated to be responsible for the harmful biological consequences of UVA radiation. In these photodynamic reactions, the photosensitizer drug interacts with molecular oxygen, either directly (Type II oxidative mechanism), or indirectly (Type I oxidative

mechanism)[67]. Frequently, Type I photoinduced reactions are radical-mediated reactions whereas Type II photooxidations are oxygen-mediated reactions (Scheme 1)[68]. In Type I oxidative reactions, the generation of reactive oxygen species (ROS) arises from the formation of free radicals through processes like electron transfer or hydrogen abstraction in the presence of oxygen. Contrary, in Type II reactions, there is a transfer of energy to molecular oxygen, resulting in the generation of another ROS species, singlet oxygen ($^1O_2$). Hence, ROS display a high potential to inflict damage to biomolecules such as lipids, proteins, and DNA, ultimately causing cell death (Table 5)[67,68].

All in all, photodynamic reactions are primarily responsible for most damage to biological structures, mainly by the generation of $^1O_2$ or free radicals through the absorption of light by a photosensitizer. Nevertheless, these types of reactions have broad utility, especially in photodynamic therapy (PDT) for cancer treatment[69]. For instance, porfimer sodium (Photofrin) exhibits well-demonstrated phototoxicity activated by red light and has received FDA approval for treating patients with certain types of esophagus and lung cancers[70]. Currently, Photofrin-mediated photodynamic therapy is under investigation for its potential in treating other cancer types. Furthermore, photosensitizers with the capability to induce photodynamic reactions against microorganisms are also being used in photodynamic inactivation (PDI)[69].

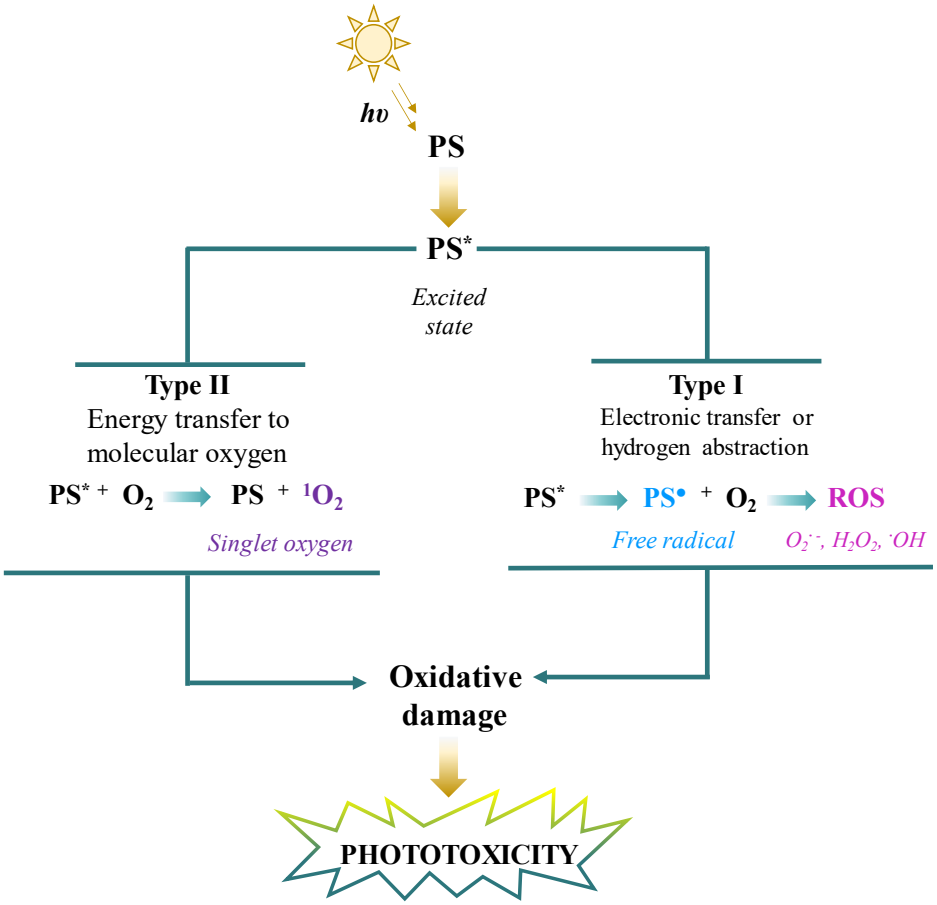

Scheme 1 | Photodynamic reactions. Type I and Type II photosensitized oxidative mechanisms. PS (photosensitizer). Figure adapted from reference[71].

Table 5 | Guideline for Type I/Type II oxidation mechanisms.

Characteristics of oxidative reactions	
Type I	Type II
Requirement of molecular oxygen as a reagent (photodynamic reactions)	
Photosensitized reactions initiate with one-electron oxidation and $^1O_2$ reactions that trigger biomolecule degradation	
Photochemical chain reaction that begins with electron or hydrogen atom abstraction as the initial oxidative step	Process of energy transfer to oxygen by the sensitizer
Formation of free radical	Sensitized production of $^1O_2$
Photosensitized oxidations are relevant to both molecules and living organisms	

Certainly, all biomolecules within the biological system, including lipids, proteins, and nucleic acids, are susceptible to oxidation. The specific chemical nature of the initiating agent, such as free radicals and $^1O_2$, determines the composition of primary and secondary oxidation products. Although cells generate ROS as a regulated physiological process, increasing levels of these species are capable of inducing cellular damage. This decompensation becomes evident during pathological events, such as infections or chemical attacks, which result in several alterations in macromolecules, including DNA mutations, alterations in transduction signals, and subsequently, cell death through apoptosis or necrosis[72–74].

In this context, xenobiotics, when exposed to UV-visible light, possess the ability to generate ROS, which can, subsequently, cause damage to lipids, proteins, and/or DNA within cells, ultimately leading to carcinogenesis or cell death[74].

Damage to biomolecules by ROS

Lipid peroxidation

Cell membranes are constituted by a diverse set of lipids, usually, by phospholipids, cholesterol, and glycolipids. The presence of polyunsaturated fatty acids makes the cell membranes vulnerable to oxidizing agents. Thus, one of the main consequences of ROS is lipid peroxidation (also called lipid peroxidation), leading to modifications in the membrane structure, which impact its flexibility and compromise its integrity (Scheme 2). This lipoperoxidation process is believed to be implicated in atherosclerosis because it results in the oxidation of LDL transporters that can no longer be recognized by scavenger receptors, consequently allowing these molecules to re-enter circulation[73–75].

Protein carbonylation

Another essential component within cellular structures is proteins, macromolecules constituted by amino acid residues connected by peptide bonds. In contrast to lipids, proteins are susceptible to oxidative stress through carbonylation reactions, which can compromise their structural integrity, leading to the loss of catalytic activity in various enzymes and disruption of the regulation of metabolic pathways.

Chemically, protein carbonylation involves the oxidation of the side chains to introduce ketones and aldehyde groups (Scheme 2). The amino acid residues typically affected are:

- Prolyl to pyrrolidone
- Glutamyl to glutamic semialdehyde
- Lysyl to aminoadipic acid semialdehyde

- Threonyl to amino ketobutyric acid

Usually, oxidative stress resulting in ROS attacking protein side chains leads to carbonylation events. Numerous diseases, including Alzheimer's disease, rheumatoid arthritis, and others, have been associated with the presence of oxidized proteins[73,74,76].

DNA damage

DNA consists of a double-stranded helical structure constituted by nucleotide units. It is the macromolecule responsible for carrying genetic information essential to the development and functioning of organisms. Various exogenous and endogenous stresses induce different forms of molecular modifications. Independently of the source of stress, DNA damage has been a significant breakthrough in carcinogenesis research over the past two decades.

Oxidative reactions toward DNA structures (nitrogenous bases and deoxyribose), such as guanine oxidation (8-oxoG) (Scheme 2), can result in mutations, carcinogenesis, apoptosis, necrosis, and hereditary diseases[58,59]. The major oxidative impact occurs upon DNA fragmentation, driven by the disruption of nucleosomes (fundamental structures involved in DNA organization within chromosomes), thus affecting DNA compaction and coiling within chromatin. Chromatin plays a crucial role in the regulation of gene transcription, and any alterations in its functional properties can lead to errors that contribute to mutagenesis[73,77,78].

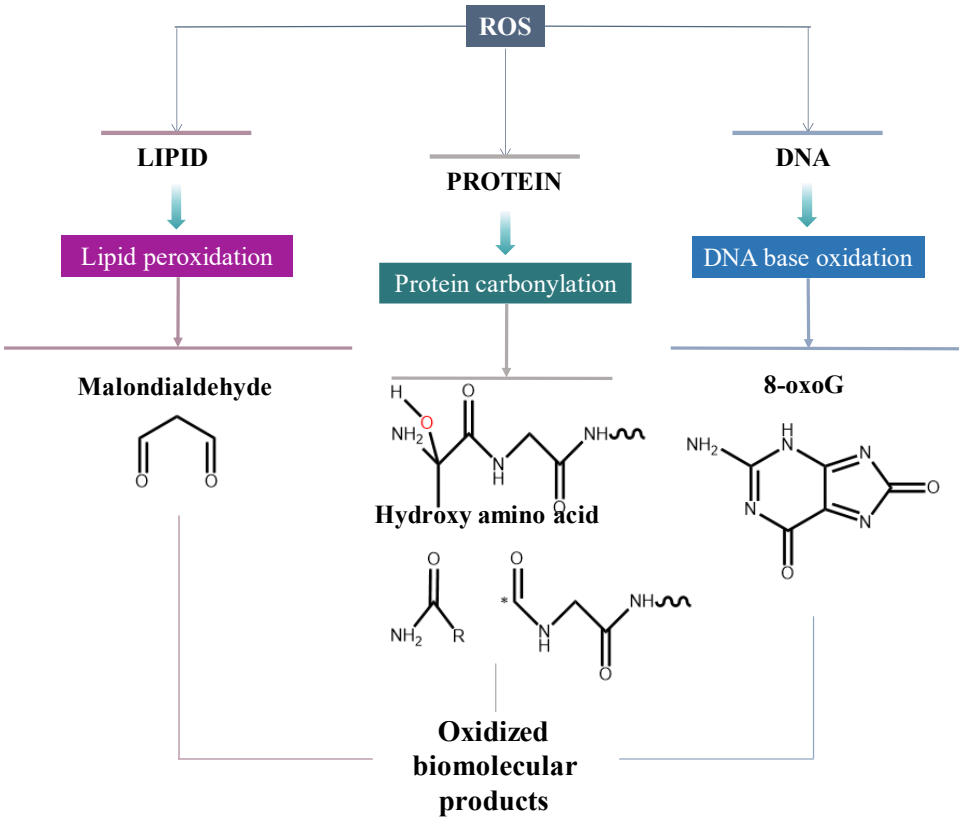

Scheme 2 | Oxidation products upon ROS action. Peroxidation of lipids, carbonylation of proteins, and oxidation of DNA bases. *Unpaired electron. Figure adapted from reference[74].

1.5 DNA damage repair

DNA damage represents a notable threat to the structural and functional integrity of an organism. While cells have developed intricate systems for identifying and rectifying these lesions, extensive or inadequately repaired DNA damage can result in mutations, carcinogenesis, and ultimately, cell death[79,80].

In light of the previous information, it is evident that DNA damage is primarily induced by UV light, particularly by longer-wavelength radiation

such as UVB and UVA. As stated previously, UVC radiation is regarded as benign since it is effectively absorbed by the ozone layer of the Earth. Notably, while UVA radiation is less energetic and therefore less injurious than UVC, it can initiate photosensitized reactions in response to various xenobiotics.

In this context, two primary processes can be discerned concerning UV light-induced DNA damage: direct damage, and photosensitized damage (Figure 8). Direct damage occurs as a result of the direct interaction of UV radiation with DNA molecules. DNA possesses the capability of absorbing light from the UVB region of the spectrum, thereby initiating various chemical reactions without requiring additional molecules or sensitizers. Contrary, photosensitized damage takes place when UV radiation is absorbed by a photosensitizer molecule, which triggers chemical reactions usually ROS-mediated. Thus, compounds capable of absorbing light in the UVA region and generate excited species are potential photosensitizers[81,82].

Generally, direct DNA damage is dominated by pyrimidine dimers such as cyclobutane pyrimidine dimers (CPDs) and thymine dimers (T-T), which constitute 75% of alterations. However, although less frequent, DNA photoproducts with (6-4) pyrimidine-pyrimidone adducts are more mutagenic than CPDs[83]. (Figure 8). However, the yield of these products is significantly lower when compared to the formation of CPDs[84].

In terms of indirect damage, 8-oxoG is the main photoproduct oxidatively generated by $^1O_2$, and is well-known to be mediated by drug photosensitization[85]. In contrast, 2,6-diamino-4-oxo-5-formamidopyrimidine (FapyG), another oxidatively damaged product of guanine, is mainly

triggered by the highly oxidative hydroxyl radical[86]. A similar mechanism has been described for the generation of 5',8-cyclo-2'-deoxynucleoside photoproducts (5',8-cPu)[87,88] (Figure 8). Interestingly, it was demonstrated that the generation of CPDs can also be triggered through photosensitized triplet-triplet energy transfer[89,90]. Overall, these photosensitized DNA damage products are directly linked to the cytotoxic, carcinogenic, and mutagenic effects of combining sunlight exposure, specifically UVA radiation, with photosensitizing drugs.

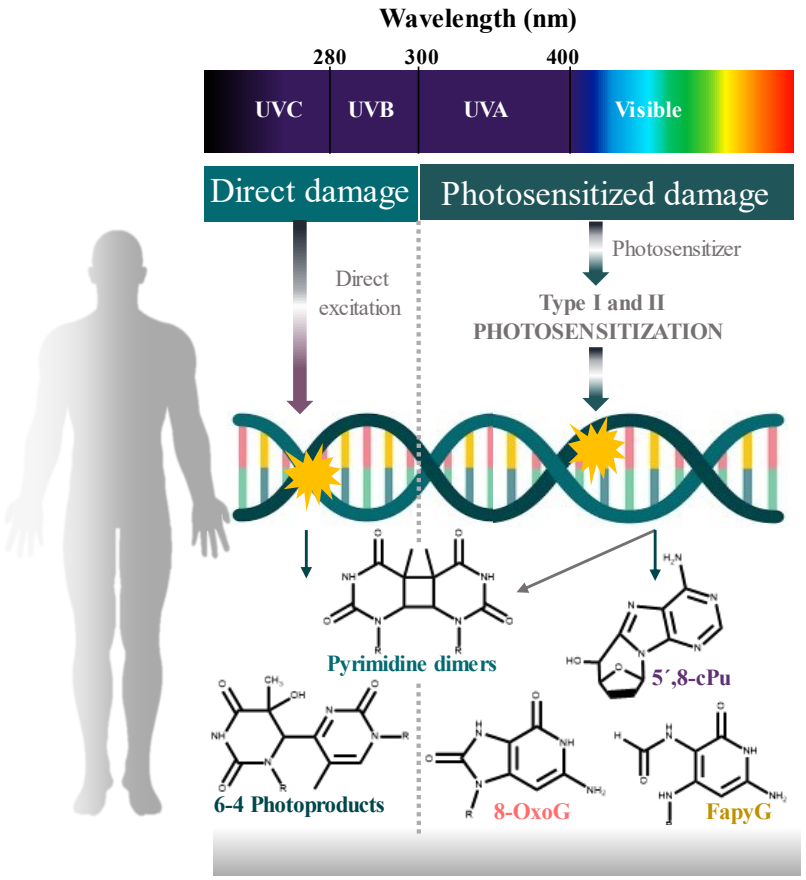

Figure 8 | Photoinduced DNA damage. Direct and photosensitized DNA damage induced by UV Light.

As for both damage mechanisms, double-strand breaks (DSBs) are regarded as one of the most destructive types of DNA damage, significantly compromising the stability of the genome. The DNA damage response involves decisions such as whether to engage in DNA repair, initiate terminal differentiation *via* senescence, or, in the case of severe damage, undergo apoptosis. The primary mediators of this pathway are proteins belonging to the phosphatidylinositol 3-kinase-like protein kinase (PIKKs) family, specifically ATM, ATR, and DNA-PK, along with members of the poly (ADP-ribose) polymerase (PARP) family. Ataxia Telangiectasia Mutated (ATM) and DNA-dependent protein kinase (DNA-PK) are activated in response to DSBs[91].

The recruitment of ATM is likely to contribute to the activation of γ-H2AX complexes and the stabilization of DNA damage response factors at DNA damage sites (Figure 9). The phosphorylated form of γ-H2AX establishes a positive feedback loop that spreads γ-H2AX over large genomic regions around the DSBs. These initial signaling events activate one of the two pathways for repairing DNA DSBs; nonhomologous end joining (NHEJ) is the primary pathway, whereas homologous recombination (HR) is limited to the S or G2 phases after DNA replication has concluded. Consistently, γ-H2AX phosphorylation event is recognized as one of the most firmly established chromatin modifications associated with DNA damage and repair processes[91–93].

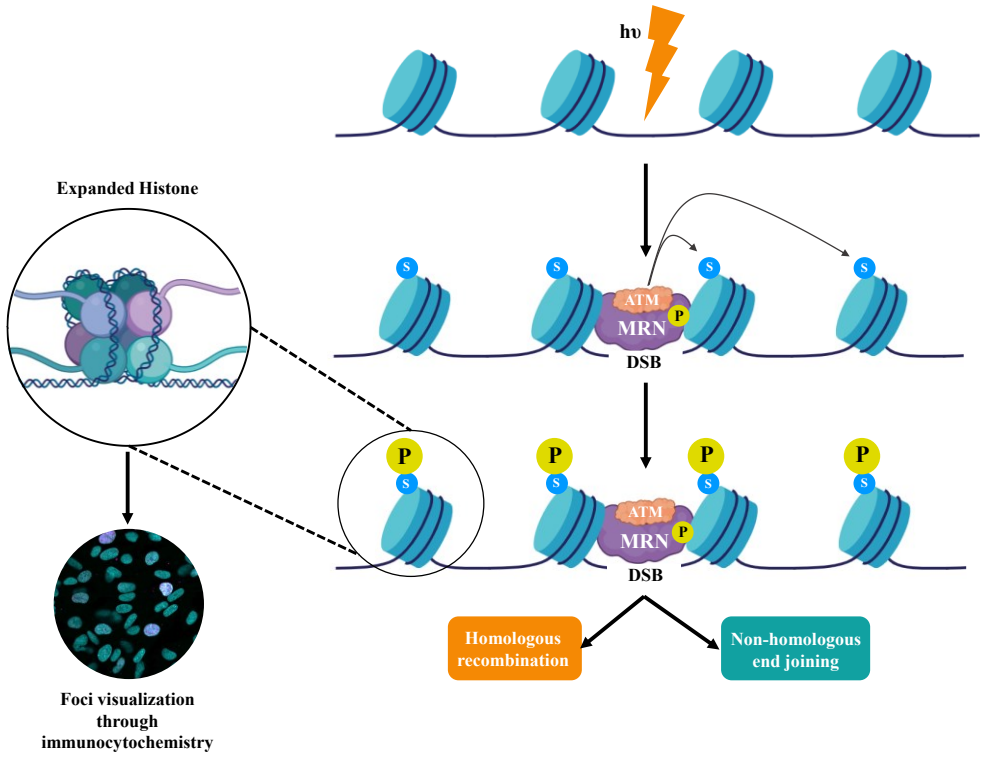

Figure 9 | Histone H2AX in DNA damage repair. Phosphorylation pathway of histone H2AX upon UV-induced DNA damage. Figure adapted from reference[94].

1.6 Cell death

Historically, cell death has been considered as the ultimate cellular decision achieved through complex signaling and communication, representing a critical process for maintaining the homeostasis of organisms. Typically, the hallmarks of cell death are categorized based on their reliance on specific signaling pathways in two different modes: programmed cell death (apoptosis) or non-programmed cell death (necrosis)[95,96].

Apoptosis, often referred to colloquially as "cellular suicide", is a meticulously regulated process in which cells cease their cycle of growth and

division, entering a process toward programmed cell death, guided by precisely controlled intracellular signaling pathways. Unlike non-programmed cell death, this process is characterized by the absence of cellular content leakage into the surrounding environment. The activation of the widely recognized caspase enzymes starts from their precursor forms, also known as zymogens. Upon detecting a signal of cellular damage, initiator caspases (caspases 8 and 9) are triggered from their inactive procaspase forms and proceed to activate the executioner caspases (caspases 3, 6, and 7). These activated caspases initiate a sequence of processes leading to DNA fragmentation, degradation of nuclear proteins and the cytoskeleton, protein crosslinking, the generation of ligands recognized by phagocytic cells, and the creation of apoptotic bodies. These apoptotic bodies are effectively engulfed by neighboring cells exhibiting phagocytic capabilities and subsequently degraded within lysosomes (Figure 10). Moreover, caspases 1 and 4 possess proinflammatory characteristics, and they have the capability to activate pyroptosis in reaction to various stimuli[97,98].

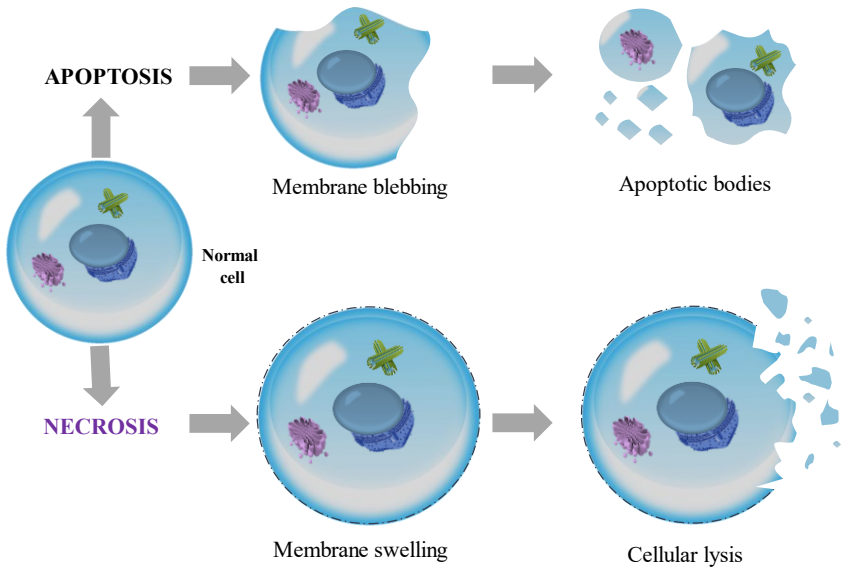

Figure 10 | Necrosis vs Apoptosis. Main differences between apoptosis and necrosis pathways. Figure adapted from reference[98].

Three signaling pathways can be triggered in apoptotic cells. The extrinsic pathway, also known as the death receptors pathway, is activated when cell-surface death receptors such as Fas are bound by their ligands. The mitochondrial pathway is initiated when pro-apoptotic proteins from the BCL-2 family induce the permeabilization of the outer mitochondrial membrane. Lastly, the perforin/granzyme pathway is employed by cytotoxic lymphocytes to eliminate virus-infected or transformed cells[99,100].

Necrosis, for an extended period, has been considered as an outcome of physical and chemical stress, typically seen as accidental and unregulated. Nowadays, there is a growing understanding that necrotic cell death is also meticulously regulated and programmed, similar to caspase-dependent apoptosis. Furthermore, the findings suggest that necrotic cell death may

serve as an alternative cell death pathway when caspases are inhibited or when the caspase-dependent pathways cannot be effectively engaged.

Necrosis is characterized by cytoplasmic expansion, irreparable damage to the cell membrane, and disintegration of organelles. Cellular components escape into the extracellular surroundings, potentially functioning as a "danger signal". Consequently, necrosis is typically linked with an inflammatory response (Figure 10). Thus, biochemical hallmarks of apoptosis, like the activation of specific proteases (caspases) and the fragmentation of DNA, are generally not present in necrotic cells[97,101,102].

The permeabilization of the plasma membrane is a common indicator of necrotic cells. Therefore, a widely used approach to monitor this phenomenon is by measuring the release of lactate dehydrogenase (LDH) enzyme. When combined with other techniques, the measurement of LDH release proves to be a valuable method for detecting necrosis[103].

1.7 Molecular photochemistry

Photochemistry is the field of chemistry that examines chemical reactions, isomerizations, and physical phenomena that occur when specific molecules are exposed to UV light and/or visible. The absorption of UV-visible radiation (200-800 nm) results from the interaction between a molecule and a photon, transferring the energy from this latter to the molecule, inducing a change in its electronic configuration. This energy is not randomly distributed within the molecule; instead, it is selectively absorbed by chromophore groups (unsaturated groups with electrons in n or π orbitals that can absorb energy and be excited at different wavelengths, such as dienes, carbonyl groups, aromatic rings, etc.)[104].

Based on Planck equation, $E = h\upsilon = hc / \lambda$, visible light with longer wavelengths (ranging from 400 to 800 nm) possesses lower energy levels (290 to 170 kJ/mol) compared to light in the shorter wavelength range (200 to 400 nm) found in the near-UV region (630 to 290 kJ/mol). Therefore, UV light is the primary radiation source for initiating photochemical transformations[104,105].

Drugs with photoreactive activity exhibit specific physicochemical properties, aside from their capability to absorb UV-visible light. Typically, these molecules are resonance structures with a cyclic or tricyclic configuration, featuring halogen substituents and heteroatoms[106].

The study and quantification of the absorbed energy distribution through molecular absorption and emission spectroscopy provide information about the structure, energy, and dynamics of excited electronic states, facilitating the understanding and interpretation of the photophysical properties and photochemical reactivity of compounds[105].

1.7.1 Photophysical processes

Photophysics is a branch of physical chemistry that focuses on the quantum changes in the excited molecules that result from the impact of photons without altering their chemical structure. These interactions lead to various phenomena and outcomes. For instance, the three major types of transitions are absorption, emission, and non-radiative processes. Typically, a graphical representation that illustrates the energy-level transitions that molecules undergo when they absorb and emit light is used in the field of photophysics, namely, Jablonski energy diagram (Figure 11). This visual framework showcases the energy transitions between the different electronic states of a

molecule, where the energy states are grouped vertically according to their energy and horizontally based on spin multiplicity. At the same time, radiative transitions are indicated by solid arrows, while non-radiative transitions are represented by dashed arrows. Moreover, when an electron within the molecule is raised to a higher energy level, it has the option to stay coupled with the electron in the ground state (with opposite spins), resulting in the creation of an excited singlet state (Sn). Alternatively, it may alter its multiplicity by uncoupling from the ground state electron, leading to the formation of an excited triplet state (Tn)[107,108].

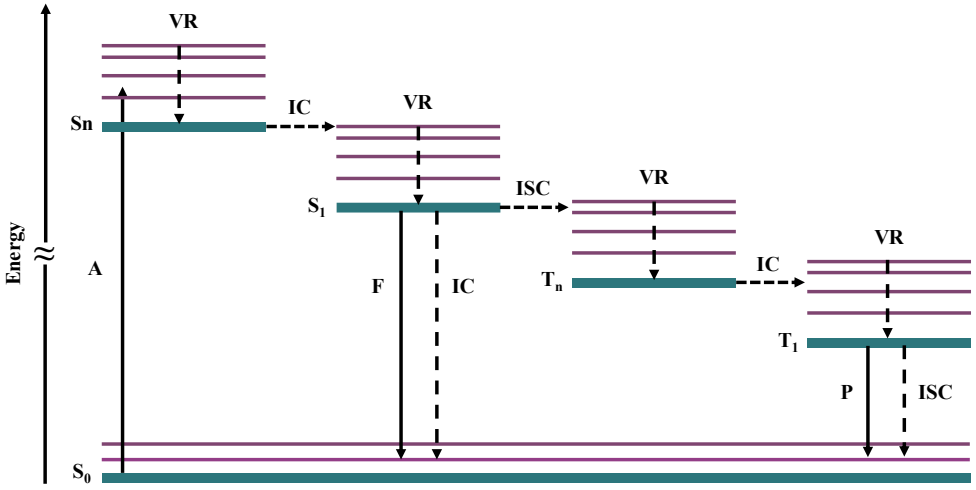

Figure 11 | Jablonski diagram. Illustration of different energy states and transitions in a molecule upon photon interaction. A: absorption, F: fluorescence, P: phosphorescence, IC: internal conversion, ISC: intersystem crossing and VR: vibrational relaxation. Figure adapted from reference[109].

Absorption (A)

Absorption is a photophysical property in which a molecule absorbs the energy of a photon and is promoted to a higher energy state than the initial one (excited state). Absorption is associated with electronic transitions between different energy levels within the molecule, which can be either permitted transitions, with high probability of occurring (singlet-singlet, $S_0 + h\upsilon \rightarrow Sn$) or forbidden transitions, having little to no chance of occurring (singlet-triplet, $S_0 + h\upsilon \rightarrow Tn$) according to the spin rule.

In order to absorb light, a compound must present a chromophore which contains both π electrons and n (non-bonding) electrons capable of capturing photons. Moreover, when a chromophore absorbs light, it selectively absorbs photons at particular wavelengths or energy levels. This distinctive absorption pattern at different wavelengths is referred to as an absorption spectrum. Interestingly, each molecule possesses a distinct absorption spectrum that can be used for identification or the examination of its characteristics.

In absorption spectroscopy, the Beer-Lambert law, also known as Beer's law or Beer-Lambert-Bouguer law, establishes a relationship between the absorption of light and the properties of the material through which the light travels (Equation 1). Beer's law asserts that the absorbance of a beam of focused monochromatic radiation in a uniform, isotropic medium is directly proportional to the absorption path length, l (cm), and the concentration, c (mol/L), of the substance or in the case of gas-phase analysis, to the pressure of the absorbing species.

$$A=\log_{10}\left(\frac{I_0}{I}\right)=\varepsilon\cdot l\cdot c$$

Equation 1 | Beer-Lamber law. A represents the absorbance, I_0 and I the intensities of incident and transmitted light, respectively, l is the absorption path length, c is the concentration and ε is referred to as the molar absorption coefficient.

This linear correlation between absorbance and concentration is only valid when absorbance values are low, because at higher values, this linearity tends to suffer from deviations, and absorbance exhibits asymptotic growth[110–112].

Fluorescence (F)

Fluorescence is another photophysical property resulting from the interaction between radiation and a molecule. In this process, a molecule, previously excited, emits a photon from the excited singlet state of lower energy (S_1) to the ground state (S_0) ($S_1 \rightarrow S_0 + h\upsilon$). This transition is permitted by the spin rule because it involves states with the same spin multiplicity.

Usually, the substance absorbs light higher in energy (shorter wavelengths), like in the UV or visible spectrum, and then re-emits light at a longer wavelength (lower energy), often in the visible spectrum. This occurs because some of the energy absorbed by the substance is often lost as heat or other non-radiative processes before the emission of light.

During fluorescence spectroscopy, an undesirable phenomenon can occur known as inner filter fluorescence (IFF). This occurs when both the excitation light and the emitted fluorescence light are absorbed by the same sample or medium, leading to distortion or quenching of the fluorescence signal. Typically, diluting the sample is an effective way to minimize this effect. Additionally, optical filters can be used to selectively remove either the excitation or emitted light, further mitigating this issue.

All substances capable to emit fluorescence when exposed to specific wavelengths of light are called fluorochromes. On the other hand, all fluorochromes have a fluorophore in their structure. It is the specific group within the molecule responsible for its fluorescence, which absorbs and then emits light at a different wavelength, giving rise to the fluorescence signal (in the nanosecond range).

The fluorescence exhibited by a compound is influenced by various factors, including the type of electronic transition (whether it is $n\pi^*$ or $\pi\pi^*$), the molecular structure, the properties of the solvent used, concentration, temperature, pH levels, the presence of dissolved oxygen, and more.

Fluorescence parameters encompass the following aspects: the fluorescence spectrum, which illustrates the emitted light wavelengths; the fluorescence quantum yield (Φ_F), quantifying emission efficiency; the fluorescence lifetime (τ_F), characterizing the duration of fluorescence after excitation; and fluorescence intensity, a measure of signal strength affected by factors like concentration and photobleaching[113–115].

Phosphorescence (P)

Phosphorescence is a luminescent process where an excited molecule emits light through a transition from the lowest energy triplet excited state (T_1) to the ground state (S_0) ($T_1 \rightarrow S_0 + h\upsilon$). Therefore, unlike fluorescence, which originates from the vibrational ground state of the lowest excited singlet level, S_1, phosphorescence will originate from the vibrational ground state of the lowest excited triplet level, T_1, regardless of the initial excited level of the molecule (Kasha's rule). Moreover, in contrast to fluorescence, phosphorescent emission persists over an extended period after the excitation

source is removed. This effect occurs since it involves a transition between states with different spin multiplicities, making the electrons relatively stable and resistant to rapid relaxation to the ground state. In other words, this transition has a low chance of occurring because it is prohibited by the spin rule. Therefore, the emission of light from this state is delayed, resulting in a persistent glow. Giving this fact, to detect this emission, measurements should be carried out under conditions of reduced temperature, within highly viscous surroundings, or by attaching the substance to solid surfaces[116].

Ultimately, the more common non-radiative processes include vibrational relaxation, internal conversion, and intersystem crossing.

Vibrational relaxation (VR)

Vibrational relaxation (VR) is a process in which an excited molecule transfers energy from an excited vibrational level to a lower-energy vibrational level within the same electronic state. This excess energy from the excited state is gradually dissipated or transferred through collisions with surrounding molecules, particularly solvent molecules, resulting in a nearly negligible rise in the medium temperature[116–118].

Internal conversion (IC)

Internal conversion (IC) is a process in which an excited molecule transitions from higher energy state to a lower electronic energy state without the emission of a photon. Thus, it involves permitted transitions between two electronic states of identical spin multiplicity. The efficiency of IC depends on the energy difference between the initial and final states. If this energy difference is small, internal conversion becomes a more probable pathway for the relaxation of the excited molecule[116,118,119].

Intersystem crossing (ISC)

Intersystem crossing is a process in which an electronically excited molecule transitions from one electronic spin state to another. Specifically, it involves the crossing between electronic states with different spin multiplicities. Therefore, ISC refers to prohibited transitions between two isoenergetic vibrational levels of different spin multiplicities. The probability of ISC depends on several factors, such as the strength of spin-orbit coupling and the extent of overlap between the wavefunctions of the initial and final electronic states. ISC is typically promoted by the presence of heavy atoms, including elements like P or Br[116,118,120].

1.7.2 Photochemical processes

Photochemistry is also referred as the branch of chemistry that focuses on the study of light-induced chemical processes. These reactions initiate by the absorption of light, typically in the UV or visible regions of the electromagnetic spectrum. As stated above, when a compound absorbs photons of specific energy, they can undergo changes in electronic configurations, leading to intramolecular or/and intermolecular interactions, and resulting in a variety of photochemical reactions. In this state, molecules tend to create a novel structure through different processes:

- Photodissociation: $AB + h\nu \rightarrow A^* + B^*$
- Photoinduced rearrangements, isomerization: $A + h\nu \rightarrow B$
- Photoaddition: $A + B + h\nu \rightarrow AB$
- Photosubstitution: $A + BC + h\nu \rightarrow AB + C$
- Photoredox reactions: $A + B + h\nu \rightarrow A^- + B^+$

In brief, photosensitization refers to a process in which a chemical transformation takes place in one compound, the substrate or target, due to the initial electronic absorption of UV-visible radiation by the photosensitizer in its ground state (Figure 12)[121].

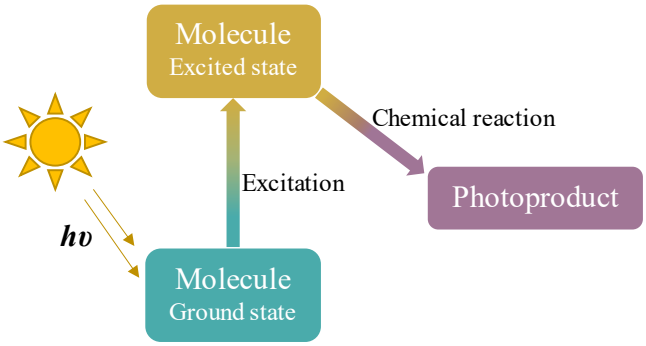

Figure 12 | Photochemical reactions. Schematic representation of photoinduced chemical reactions.

1.7.3 Singlet oxygen

As stated previously, the main photochemical product emerging from Type II photosensitized reactions is singlet oxygen ($^1\Delta g$, $^1O_2$). The photochemical excitation of a molecule upon UV-visible light absorption leads to the electronic transition from ground state to the excited singlet state (S_1). The singlet excited state undergoes the process of ISC, where the electron transitions from the excited singlet state to a lower-energy triplet state (T_1). The photosensitizer, now in the triplet state, can transfer its energy to ground state molecular oxygen ($^3O_2$) to generate $^1O_2$ (Figure 13).

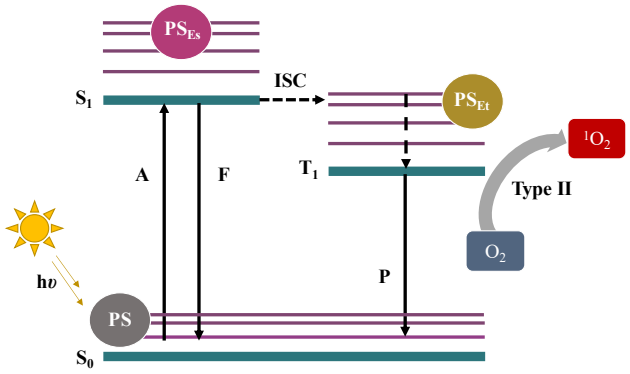

Figure 13 | Type II photodynamic reaction. Photogeneration of singlet oxygen induced by photosensitizer (PS). PS_{Es}; PS excited singlet state and PS_{Et}; PS excited triplet state. Figure adapted from literature[122].

Molecular oxygen is a diatomic homonuclear molecule that differs from other homonuclear compounds because, in its ground state ($^3O_2$), possesses an open-shell electronic configuration with two unpaired electrons in different molecular orbitals (Figure 14). Thus, molecular oxygen has a triplet multiplicity compared to the more common singlet multiplicity found in most natural compounds[123].

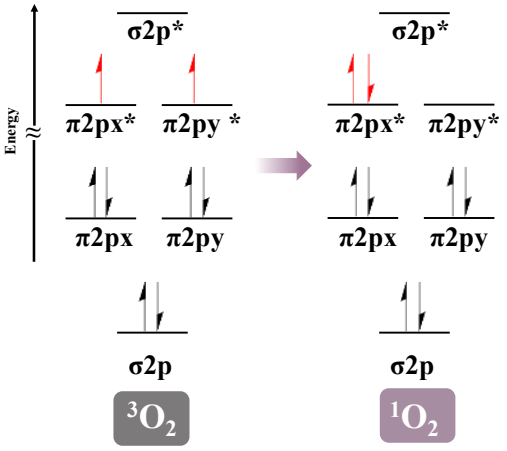

Figure 14 | Molecular orbital diagrams. Electron distribution in the molecular orbitals of triplet and singlet oxygen. Figure adapted from literature[124].

According to Wigner's spin selection rule, chemical reactions between $^3O_2$ and singlet organics to generate new singlet molecules are prohibited. Consequently, this triplet multiplicity is the primary reason why most reactions between oxygen and organic substances, while energetically favorable, do not occur at room temperature but require heating or the presence of catalysts. This kinetic inhibition of reactions between organic compounds and oxygen is a crucial factor that allows life to thrive in an oxygen-rich atmosphere.

Nevertheless, the interaction of molecular oxygen in the ground state with molecules electronically excited lead to the formation of $^1O_2$ through energy transfer from triplet excited state. Regarding its electronic structure, $^1O_2$ is distinguished by the arrangement of electrons within its two molecular orbitals, where all electrons possess opposite spins, resulting in a total spin value of zero (Figure 14).

Thermodynamically, the energy of the first excited state of molecular oxygen (E_Δ) is around 94 kJ/mol, higher than the energy displayed by oxygen in the ground state (63 kJ/mol). Thereby, luminescence decay originated from $^1O_2$ is detected at 1270 nm ($^1O_2 \rightarrow {}^3O_2 + h\upsilon$). Through this method, it is possible to definitively determine the decay rate constant (kq_Δ) of $^1O_2$ or its reciprocal value, the $^1O_2$ lifetime (τ_Δ), in different environments. This has unveiled the significant influence of the medium on the kinetics of $^1O_2$ decay[125,126].

1.8 Background on TKIs photobehavior

1.8.1 Phototoxicity prediction based on chemical structure

The development of new targeted therapies is frequently intricate and challenging. Indeed, the identification and approval of novel TKIs for the clinical management of cancer disease is a long process with numerous obstacles. Typically, the biggest burden pertains to the pharmacokinetics and the toxicological profile (ADME/Tox) of these drugs. Thus, it is crucial to predict, in preclinical studies, the biological availability and toxicity of new drug candidates based on their physicochemical properties[127].

Generally, the chemical structure of a compound dictates its physicochemical characteristics, therefore, both its pharmacological and ADME/Tox profile. In fact, drugs containing quinazoline, condensed benzene and pyrimidine ring, in their structure can trigger skin conditions such as photodermatoses (Figure 15)[31,128]. This was evident in the case of vandetanib, a multi-kinase inhibitor with a quinazoline chromophore, which has been reported as phototoxic in numerous studies, as indicated by clinical case reports[51,52]. Likewise, in prior studies, patients receiving lung cancer treatment with erlotinib (in 45-100% of cases) or afatinib (in 81-100% of cases), both belonging to the EGFR inhibitor quinazoline drug family, manifested photosensitive disorders[129,130].

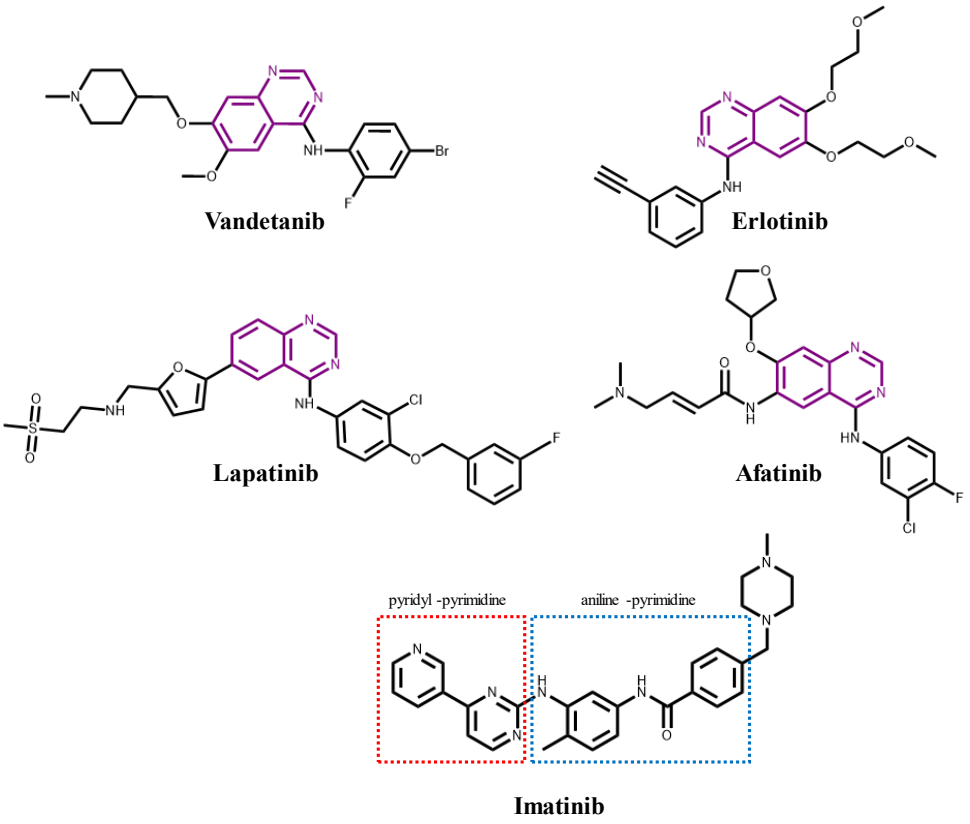

Figure 15 | Chemical structures of photoreactive tyrosine kinase inhibitors (TKIs). Quinazoline substructure is shown in violet.

With this background, several studies have been conducted with the underlying hypothesis of a correlation between the quinazoline moiety and photosensitizing characteristics of TKIs. Thus, our research group recently conducted an assessment study on the photo(geno)toxic potential of lapatinib (LAP), the first dual HER1 and HER2 inhibitor approved in 2007 for the treatment of breast and lung cancer. Subsequently, a comprehensive analysis of the photophysical properties using ultrafast spectroscopy and computational studies was carried out and the data outcome was sufficient to explain the photobehavior of LAP within human cells[131–133]. Moreover,

studies with LAP main metabolites, *N*-dealkylated (*N*-LAP) and *O*-dealkylated (*O*-LAP), have also been conducted. Surprisingly, the original drug LAP exhibited the highest activity in terms of membrane phototoxicity and protein oxidation, whereas *N*-LAP was associated with the highest photogenotoxicity through the oxidation of purine bases, as indicated by the detection of 8-oxoG. Accordingly, it has been inferred that reactive metabolites may be responsible for both direct and indirect toxicity targeting the cell membrane (lipids and proteins) or DNA[131]. Overall, this study has illustrated that small changes in the drug molecule structure during biotransformation can lead to modifications in the toxicity profile, influenced by factors such as chemical reactivity, biological activity, and interactions with cellular components.

Comparative structural correlations were also established in the case of imatinib, a BCR-Abl inhibitor prescribed for chronic myeloid leukemia. In this particular case, the anilino-pyrimidine substructure holds a close resemblance to pyrimethanil, a photosensitive fungicide that generates photoproducts upon irradiation, while the pyridyl-pyrimidine fragment is expected to display photoreactivity, similar to biphenyl and its derivatives, which are recognized for their well-defined singlet and triplet excited states (Figure 15). However, the phototoxic potential was primarily attributed to the pyridyl-pyrimidine segment and not to the drug itself[134].

In conclusion, the photobehavior of TKIs can be shared by different photosensitizers with similar chemical structures. Small changes made during the development of new TKIs for treating different tumor targets may result in either enhancement or reduction of their phototoxic properties. This

principle extends to chemicals arising from drug metabolism, which can also exhibit different photobehavior upon UVA exposure.

1.8.2 Photodynamic therapy

Photodynamic therapy (PDT), a therapeutic procedure for managing various malignant conditions, including skin cancer, involves the administration and uptake of photosensitizers by tumor cells. Subsequent illumination with light triggers photoactivation, generating ROS that induce oxidative damage to diverse cellular targets. This process ultimately leads to the death of cancerous cells through necrosis or apoptosis, resulting in the ablation of the tumor.

In this context, TKIs have been used in combination with PDT as coadjuvants. For instance, gefitinib and imatinib mesylate are recognized for their potent inhibition of ABCG2, an ATP-binding cassette (ABC) transporter, also known as breast cancer-resistant protein (BCRP). It has been reported that ABCG2 is overexpressed in numerous cancer cells and facilitates the transport of a diverse range of anti-cancer agents. By increasing intracellular photosensitizer levels in ABCG2-positive tumors, gefitinib and imatinib mesylate or other ABCG2 transport inhibitors can enhance efficacy and selectivity of clinical PDT[135,136]. Moreover, the VEGFR inhibitor axitinib has been proposed to modulate immunosuppression by fostering vascular normalization and improving the hypoxic microenvironment within tumors. Thus, axitinib is also believed to enhance the effectiveness of PDT immunotherapy[137].

Nevertheless, the direct use of TKIs as photosensitizers was only recently suggested, in 2021, specifically with sunitinib. Despite its established clinical

application as a TKI for renal cancer, sunitinib has also been revealed to possess photosensitizing properties, which could be valuable for PDT[138,139].

Additionally, with an understanding of the implication of TKIs in ABCG2-mediated drug resistance, a newly designed and synthesized chlorin e6-based conjugate of dasatinib and imatinib has been proven to be a potent photosensitizer. This conjugate exhibited significant phototoxicity in comparison to talaporfin, a well-known photosensitizer approved for PDT in clinical trials. It has demonstrated the ability to decrease the efflux of intracellular photosensitizer by inhibiting ABCG2 in HepG2 cells. Moreover, it localized in mitochondria, lysosomes, Golgi, and the endoplasmic reticulum, resulting in a higher rate of cell apoptosis and increased ROS production compared to talaporfin[140].

In summary, drugs selected for PDT undergo careful selection based on their capability to induce controlled photosensitizing reactions within targeted cells during therapy. However, in a broader context, TKIs have demonstrated to contribute to adverse photosensitivity reactions through similar mechanisms in non-target tissues. This duality highlights the importance of understanding the nuanced interactions of drugs with light, emphasizing the need for precise mechanistical studies in order to maximize the therapeutic benefits while minimizing unintended side effects of these drugs in clinical settings.

CHAPTER 2 Aims and Objectives

2.1 Significance of the study

The new class of targeted therapy introduced in recent decades, tyrosine kinase inhibitors (TKIs), has significantly improved the quality of life and survival rate of cancer patients. Moreover, the main dermatological adverse events of TKIs include skin rash, hyperpigmentation and papulopustular dermatitis. In this context, considering that lapatinib, showed significant phototoxic potential after exposure to UVA light, it makes sense to investigate the ability of the TKI family to induce photosensitivity reactions. To successfully achieve this overarching goal, a multidisciplinary approach is required, utilizing photophysical techniques combined with photobiological experiments in solution and within skin cells.

The photobiological properties of drugs have received significant attention in the last two decades, as a result of the growing awareness in the scientific community (and also among the general population) of the risks associated with exposure to solar radiation as a serious public health issue. Currently, very little is known about photosensitization mediated by widely used TKIs in cancer therapy, as well as the nature of the chemical processes involved. Interestingly, the chemistry of photoinduced processes (energy and/or electron transfer, hydrogen abstraction, ROS formation, etc.) occurring within cells is largely unknown, despite its importance in understanding and predicting photosensitivity reactions. Likewise, conclusive correlations between the molecular aspects of these phenomena and their clinical manifestations are still lacking. Therefore, from a clinical perspective, it is important to identify photoinduced events associated with these targeted therapies to reduce their incidence and to prevent treatment discontinuation in cancer patients. Moreover, in numerous cases of photosensitivity reactions,

discontinuing or replacing the photosensitizing drug may not be a feasible therapeutic option. Therefore, the main approach considered a preventive measure against adverse reactions, is protection from direct sunlight exposure using photoprotection or sunscreens along with anticancer therapy.

2.2 Objectives

The general objective of this thesis is to investigate the photobehavior of selected TKIs from two main standpoints. Firstly, the research will focus on the photophysical characterization to discern the possible generation of transient species with photosensitizing properties. This aspect aims to shed light on the interactions and chemical processes that occur when these inhibitors are exposed to UVA light. Secondly, the research will entail an in-depth *in vitro* evaluation of the photo(geno)toxicity potential within cellular milieu, with a specific emphasis on their impact on biomolecular components as targets for free radicals and/or ROS.

The initial stage of the thesis will encompass a screening investigation into the *in vitro* phototoxic profile displayed by a broad selection of TKIs chosen for their capability to absorb light within the UVA region of the spectrum. This study, assessed through the neutral red uptake (NRU) assay in keratinocytes cells (HaCaT), is aimed at identifying and narrowing down the list of drugs with the potential to induce *in vitro* phototoxic reactions.

Subsequently, the investigation will focus on the TKIs that have demonstrated phototoxicity, with the aim of conducting a comprehensive assessment of both their photophysical properties and photo(geno)toxic potential. The approach taken in the study will be tailored to the specific clinical applications

and unique characteristics of each selected drug, ensuring a multifaceted analysis from distinct perspectives.

All in all, this comprehensive analysis seeks to unravel the potential effects of these inhibitors when they encounter light in a biological context, providing critical insights into their safety and efficacy in cancer therapy.

Precisely, the specific objectives established for each of the TKIs under investigation are as follows:

1 To characterize the transient species generated upon UVA irradiation.
2 To examine the photostability of the compounds in steady state following UVA irradiation and to investigate photoproducts formation.
3 To evaluate the photo(geno)toxic potential of the compounds through neutral red uptake (NRU) and alkaline comet assay.
4 To assess the phototoxicity of topical TKIs in 3D reconstructed human epidermis.
5 To study *in vitro* photooxidative damage induced in the main cellular targets such as lipids, proteins, and DNA.
6 To detect double strand DNA breaks (DSBs) through γ-H2AX histone phosphorylation.
7 To visualize DNA damage biomarkers by High-Resolution Expansion Microscopy.
8 To establish the mechanism of cell death induced by oxidative stress through *in vitro* enzymatic assays.

CHAPTER 3 Materials and Methods

3.1 Chemicals and reagents

All solvents and chemicals, commercially available at HPLC grade, were used without extra purification. Chlorpromazine hydrochloride (CPZ; CAS 69-09-0), sodium dodecyl sulfate (SDS; CAS 151-21-3), brigatinib (BRG; CAS 1197953-54-0), sunitinib (SUN; CAS 557795-19-4), anthracene (ANT; CAS 120-112-7), (S)-(+)-ketoprofen (KP; CAS 22161-81-5), guanidine hydrochloride (CAS 50-01-1), 2-amino-2-hydroxymethyl-propane-1,3-diol (Tris; CAS 77-86-1), Triton™ X-100 (CAS 9036-19-5), calf thymus DNA (ctDNA; CAS 91080-16-9), guanosine (Guo; CAS 118-00-3), 3-methylindole (CAS; 83-34-1), linoleic acid (LA; CAS 60-33-3), 1H-phenalen-1-one (PN; CAS 548-39-0), (3-(4,5-dimethyl-2-thiazolyl)-2,5-diphenyl-2-H-tetrazolium bromide) (MTT) and trypan blue (CAS 72-57-1) were retrieved from Sigma-Aldrich (Madrid, Spain). Gefitinib hydrochloride (GFT; CAS 184475-55-6) was purchased from MedChemExpress (New Jersey, U.S.). 4-Defluoro-4-hydroxy gefitinib (DF-GFT; CAS 847949-50-2) and *O*-demorpholinopropyl gefitinib (DMOR-GFT; CAS 184475-71-6) were acquired from Santa Cruz Biotechnology (Dallas, U.S.). *O*-demethyl gefitinib (DMT-GFT; CAS 847949-49-9) was obtained from Toronto Research Chemicals (North York, Canada). Dasatinib (DAS; 302962-49-8), sorafenib (SOR; CAS 284461-73-0), afatinib (AFT; CAS 439081-18-2), nilotinib (NLT; CAS 641571-10-0) and axitinib (AXT; CAS 319460-85-0) were provided by TargetMol (Boston, U.S.). (*Z*)-axitinib isomer was purchased from Alsachim (Graffenstaden, France). 1,4-Dihydro-1,2-dimethylbenzoic acid (DMBA) was produced from a Birch reduction synthesis[141].

Dulbecco's Modified Eagle Medium (DMEM, low glucose with pyruvate and glutamine), Dulbecco's Modified Eagle Medium (DMEM, low glucose with

pyruvate and without glutamine and phenol red), penicillin-streptomycin ($1.0 \cdot 10^5$ U/mL, $1.0 \cdot 10^5$ µg/mL) and ethylenediaminetetraacetic acid (EDTA) were supplied by Honeywell Fluka (North Carolina, U.S.). GlutaMAX™ and gentamicin were obtained from Gibco (New York, U.S.). Fetal bovine serum (FBS) and Trypsin–EDTA (0.25–0.02%) were provided by Cultek (Madrid, Spain). Phosphate buffered saline solution (PBS, pH 7.4), human serum albumin fatty acid free (HSA), polyoxyethylenesorbitan monolaurate (TWEEN 20) were purchased from Sigma-Aldrich (Madrid, Spain).

3.2 Experimental procedures

3.2.1 Spectrophotometric techniques

Absorption spectroscopy

Absorption spectra were recorded in a JASCO V-760 (Tokyo, Japan) spectrophotometer. It consists of a white light source, a combination of a deuterium arc lamp for the UV range and a tungsten halogen lamp for the visible range, or a single xenon arc lamp covering the entire spectrum. Next, an excitation monochromator selects the light wavelength directed at the sample. The light is transmitted through the sample and the intensity of the transmitted or reflected light is measured using a detector (Figure 16)[142–144].

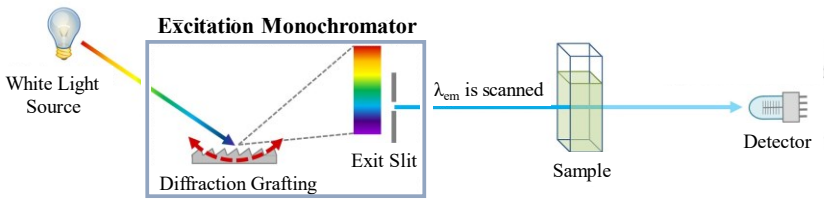

Figure 16 | Absorption spectrophotometry. Schematic representation of the light pathway and the main spectrophotometer components. Figure adapted from reference[142].

All the measurements were conducted at room temperature, employing 1 cm Suprasil quartz cells (Hellma Analytics, Müllheim, Germany) with a volume capacity of 3.5 mL.

Fluorescence spectroscopy

The acquisition of fluorescence spectra was achieved using a JASCO FP-8500 spectrofluorometer (Tokyo, Japan), an optical system consisting of two concave grafting monochromators for excitation and emission, featuring a 150W Xenon lamp as the light source. The excitation monochromator is adjusted to a known absorption wavelength of the sample, while the emission monochromator scans through the desired emission range. The measurement range, conducted at room temperature, spans from 200 to 750 nm. Thus, the fluorescence intensity is then recorded on the detector as a function of emission wavelength (Figure 17)[142].

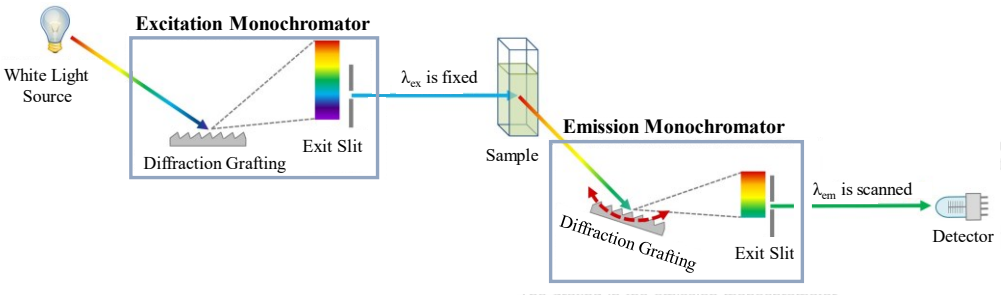

Figure 17 | Fluorescence spectrophotometry. Schematic representation of the light pathway and the main spectrofluorometer components. Figure adapted from reference[142].

The calculation of singlet state energy (E_s) is carried out through the Planck equation (Equation 2), which incorporates Avogadro's number (N_A). Here, λ represents the wavelength of emission-excitation (expressed in meters). This

wavelength is calculated based on the intersection between the normalized fluorescence emission and excitation spectra.

$$E_s = \frac{h \cdot c}{\lambda} \cdot N_A$$

Equation 2 | Planck equation. h is the Planck constant ($6.626 \cdot 10^{-34}$ J/s), c is the speed of light ($3 \cdot 10^8$ m/s), N_A is Avogadro's number, and λ is the intersection wavelength of emission-excitation spectra (expressed in meters).

To determine the fluorescence emission quantum yield (Φ_F) in steady state, the analysis was performed comparing the area under the emission curve between the drug and anthracene (λ_{exc}: 320 nm) (Equation 3). Anthracene was selected as the fluorescence standard, which possesses a quantum yield (Φ_F) *ca.* 0.27 in EtOH[145]. For all measurements, isoabsorptive samples with an absorbance at 320 nm approximately equal to 0.2 were utilized.

$$\Phi_F = \Phi_r \cdot \frac{A_r}{A_i} \cdot \frac{I_i}{I_r} \cdot \left(\frac{n_i}{n_r}\right)^2$$

Equation 3 | Fluorescence quantum yield. Φ_r represents the quantum yield of the reference. A_r and A_i denote the absorbance values of the reference and the sample, respectively. I_i and I_r correspond to the area under the fluorescence spectrum curve for the sample and the reference, respectively. n_i and n_r represent the refractive index values of the sample and reference solvents, respectively.

To determine the fluorescence lifetime (τ_F), emission decays were recorded using a time-resolved fluorescence system. The EasyLife™ X system, from Horiba Scientific (Kyoto, Japan), is a lifetime fluorescence spectrometer with pulsed nanosecond LEDs capable to register emission wavelengths from UV to NIR (200-670 nm). The excitation range is available from 280 to 670 nm, and the optical pulse width is typically around 1.5 ns.

Phosphorescence spectroscopy

The phosphorescence emission spectrum was acquired utilizing an Edinburgh Instruments spectrofluorometer FS5, which was furnished with a 150 W continuous-wave ozone-free xenon arc lamp and an SC-70 module featuring a liquid nitrogen EPR Dewar. The sample was introduced into a quartz tube with a diameter of 5 mm and subjected to cooling with liquid nitrogen (77 K) for precise temperature control during the experiment. From the phosphorescence emission spectrum, the calculation of the excited triplet state energy (E_T) is analogous to that of the singlet state, i.e., using the Planck equation (Equation 2), with the exception that in this case, the wavelength to be substituted corresponds to the point where the spectrum reaches 15% intensity.

Laser flash photolysis

Laser flash photolysis (LFP) experiments were conducted employing a pulsed Nd:YAG L52137 V LOTIS TII laser operating at 355 nm for excitation (Sp Lotis Tii, Minsk, Belarus). The LFP setup comprised a pulsed laser with a duration of approximately 10 ns each pulse, and an energy output of roughly 12 mJ per pulse. The detecting light source used was a pulsed Lo255 Oriel Xenon lamp (Newport, Irvine, CA, US.). The LFP system also incorporated a 77,200 Oriel monochromator, a photomultiplier (Oriel, model 70705PMT) system, and a TDS-640A Tektronix oscilloscope (Betashire, UK). Additionally, a customized Luzchem Research LFP-111 system was used to collect and transfer the output signal from the oscilloscope to a personal computer for data processing (Figure 18).

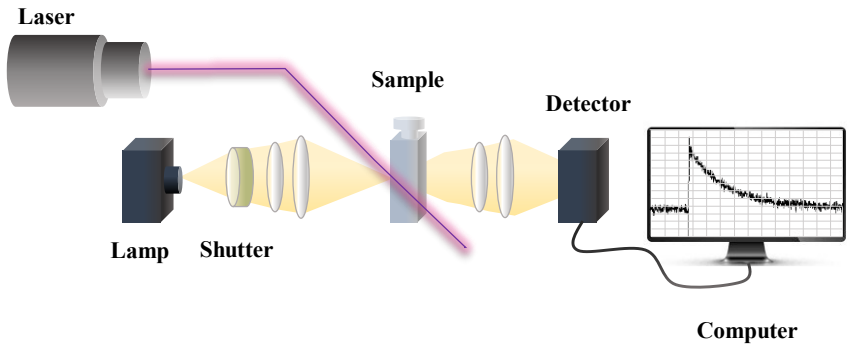

Figure 18 | Laser flash photolysis (LFP). Schematic representation of LFP components and laser/light pathways.

The measurements were carried out in deareated atmosphere, which was achieved by nitrogen bubbling for 15 min. The sample absorbance was adjusted to around 0.30 at 355 nm, and the rate constant for triplet excited state quenching (kq) was determined using the Stern–Volmer equation (Equation 4).

$$\frac{1}{\tau} = \frac{1}{\tau_0} + k_q\,[\text{quencher}]$$

Equation 4 | Stern-Volmer relationship. τ and τ_0 are the lifetime of transient species with and without quencher, respectively.

The detection of singlet oxygen ($^1O_2$, $^1\Delta g$) species was achieved by measuring near-infrared emissions using the previously mentioned LFP equipment. Each pulse had a single energy of 15 mJ, and the laser was set at 355 nm. The emission of the produced $^1O_2$ was registered at 1275 nm using a Hamamatsu NIR emission detector, which was cooled to -62.8 ºC and run at 800 V. This detector was paired with a grafting monochromator. The absorbance of the samples was adjusted to roughly 0.55 at 355 nm, and decay traces were recorded in an aerated atmosphere. The singlet oxygen quantum yield (Φ_Δ)

was determined using Equation 5. As a standard, ketoprofen (KP) was employed, which has a Φ_Δ of about 0.39 in MeCN[146]. All transient absorption experiments were performed at room temperature in 1 cm quartz cells.

$$\Phi_{\Delta}^{i} = \Phi_{\Delta}^{KP} \times \frac{\alpha_{KP}}{\alpha_i} \times \frac{I_i}{I_{KP}} \times \frac{n_{MeCN}}{n_i}$$

Equation 5 | Singlet oxygen quantum yield. Φ_Δ^{KP} is the quantum yield of the reference (KP). α_i and α_{KP} are the corrected absorbance factors ($\alpha = 1-10^{A}$, A: absorbance at λ: 355 nm) of the sample and KP, respectively. I_i and I_{KP} represent the maximum emission intensity of the drug and KP, respectively. n_{MeCN} and n_i the refractive index of acetonitrile and the sample solvent, respectively.

3.2.2 Irradiation equipment

A Luzchem multi-lamp LCZ-4 photoreactor, equipped with six top and eight side Hitachi lamps (with a maximum wavelength at 350 nm and a Gaussian distribution; Luzchem, Canada, U.S.), served as the irradiation source for all experiments. These lamps primarily emit 94% UVA radiation and 2% UVB radiation. In photostability studies of drugs in solution, the irradiation was carried out in 1 cm quartz cells with 3.5 mL capacity. In cellular experiments, irradiation occurred through the transparent plate lids, which exhibit minimal absorption beyond 310 nm, thereby reducing the potential direct influence of UVB radiation on the cell cultures. To prevent overheating, the plates were placed on ice during the irradiation period. The irradiation dose was calculated following the Equation 6.

$$\text{Dose}\left(\text{J/cm}^2\right) = \frac{\text{Time (min)} \cdot \text{ Irradiance (mW/cm}^2) \cdot 60}{1000}$$

Equation 6 | UVA irradiation dose. Irradiance is calculated by multiplying Luzchem UVA sensor reading (Lux) by the calibration factor provided by the supplier.

3.2.3 Cell culture conditions

Human keratinocyte cells (HaCaT) and human skin fibroblast cell lines (FSK), both from CLS (Eppelheim, Germany), were cultured using DMEM medium supplemented with 10% (v/v) FBS, 4 mM L-glutamine, and penicillin/streptomycin (100 U/mL and 100 µg/mL). Bj-hTERT fibroblasts, provided by Rocha Lab (KU Leuven, Belgium), were cultured in phenol red-free DMEM supplemented with 10% (v/v) FBS, 50 µg/mL gentamicin and 1% glutamax. The cells were cultured in 75 cm^2 plastic flasks at 37ºC in CO_2 incubator (100% relative humidity, 5% CO_2) and routinely split at 90% confluence. Finally cell viability was ensured through trypan blue exclusion assay[147].

3.2.4 Microscopic techniques

Drug colocalization by confocal microscopy

Keratinocytes (HaCaT) were cultured on sterile circular glass coverslips in 24-well plates at a density of $2.5 \cdot 10^4$ cells per well. Following 24 h of incubation, DMEM medium was replaced with 1 mL of fresh medium containing drugs. Subsequently, the cells were stained with CellMask™ Orange Plasma membrane (Invitrogen, Madrid, Spain) and RedDot™ Far-Red nuclear (Biotium, California, U.S.) stains, each at dilutions of 1:10,000 and 1:200, respectively. Cells treated with the compounds were further incubated for 1 h, while CellMask™ Orange Plasma membrane and RedDot™ Far-Red nuclear stains were incubated at 37ºC for 30 and 10 min, respectively. Following incubation, the coverslips were washed three times for 5 min with PBS and then mounted onto glass slides using a mowiol solution. Cell imaging was performed using a Leica SP5 (Leica Mycrosystems, Wetzlar, Germany) confocal microscope in sequential mode.

The excitation wavelengths were set at 543 and 662 nm for CellMask™ Orange Plasma membrane and RedDot™ Far-Red nuclear stains, respectively. The maximum emission wavelengths were 567, and 694 nm for the plasma membrane, and nuclear stains, respectively.

The Leica SP5 confocal microscope is provided with a laser system containing a blue 405 nm laser diode, argon laser (458, 476, 488, 496, 514 nm), DPSS 561 nm laser, and helium-neon laser (594, 633 nm). It features four internal detection channels with adjustable bandwidth and wavelength, as well as an external transmitted light detector for brightfield imaging.

Expansion microscopy

Optical microscopy has always confronted certain limitations when it comes to resolution. Until recently Boyden and colleagues[148] presented a super-resolution imaging method, called expansion microscopy (ExM) (Figure 19). This approach involves physically expanding fixed specimens, enabling the visualization of features closer than the diffraction limit of light (~250 nm) in the expanded sample. In contrast to other super-resolution techniques that require specialized instrumentation, ExM can be seamlessly employed with standard microscopes, such as widefield and confocal microscopes. Chemically, this process can isotropically magnify biomolecules through the synthesis of a compact cross-linked structure of expandable polyelectrolyte hydrogel within the specimen[149–151].

For this purpose, Bj-hTERT fibroblast cells were cultured on coverslips in two 6-well plates with $3.0 \cdot 10^5$ cells per well and incubated overnight at 37ºC. On the following day, the cells were treated with the compounds. One of the plates was exposed to UVA light (5 J/cm^2), while the other plate was kept in

dark conditions. Next day, samples were fixed for 10 min in 4% paraformaldehyde (PFA) in PBS solution. Then, PFA activity was quenched by incubating the specimen in 100 mM NH_4Cl in PBS for 10 min. After cells were washed three times with PBS, immunostaining was performed in order to detect γ-H2AX histone accumulation in the cellular nucleus (see section 3.2.8).

After completing the immunostaining, the samples were visualized before expansion using a confocal microscope. A slide with a central hole was used for this purpose. To prepare the slide, 50 µL of PBS was added directly to the hole, and the coverslips containing the specimens were inverted over the hole. Subsequently, the coverslips were sealed with photoglue and left drying for 10 min.

Following the imaging step, the samples were returned to the plates, and Acryloyl-X SE (AcX), provided by Invitrogen (Merelbeke, Belgium) was incorporated to facilitate the covalent anchoring of proteins to the swellable gel. Thus, 0.1 mg/mL solution of AcX was added to each sample and incubated overnight at room temperature.

Next day, coverslips were washed twice for 15 min with PBS. Then, the active monomer solution containing 188 µL bisacrylamide gelation stock, 4 µL Temed 10%, 4 µL APS 10%, 2 µL 4-Hydroxy-TEMPO 0.5% and 2 µL Milli-Q water was prepared on ice. Bisacrylamide gelation stock was previously prepared following the next formulation:

- Sodium acrylate 8.6 g/100 mL
- Acrylamide 2.5 g/mL
- N,N'-methylenebisacrylamide 0.15 g/mL

- NaCl 2 M
- PBS 1x
- Milli-Q water (q.s. to 100 mL)

Subsequently, coverslips, previously treated with SigmaCote, were coated with 80 µL of the activated monomer solution, and the specimens were carefully positioned upside down in the center of the coverslip, securing the sample with two spacer slides and binder clips. Since the gelation process involves free-radical polymerization, the chambers were placed inside a container and purged for 2 min with nitrogen gas to remove oxygen. Lastly, the containers were incubated for 2 h at 37ºC.

After gelation, the spacer slides were removed, and the gel obtained was cut into an asymmetric shape. Then, coverslips containing the gel were transferred back to the wells. Next, samples were digested, overnight, with Proteinase K (8 U/mL) in digestion buffer. The digestion solution was prepared as follows:

- Tris buffer 0.05 M
- EDTA 1 mM
- Triton X-100 0.5%
- Guanidine HCl 0.8%
- Milli-Q water (q.s. to 50 mL)

On the subsequent day, the gels were washed twice with PBS for 15 min. Following this, the gels were expanded through five 10-min incubations with Milli-Q water. Subsequently, the expanded gels were transferred to glass bottom imaging plates that were previously treated with poly-L-lysine to stabilize the gels and prevent them from shrinking. Finally, the expanded gels

were examined using the confocal microscope, and the expansion factor was estimated as the ratio between the nucleus size before and after expansion.

All reagents mentioned in these methods (besides AcX) were provided by Sigma-Aldrich (Overijse, Belgium).

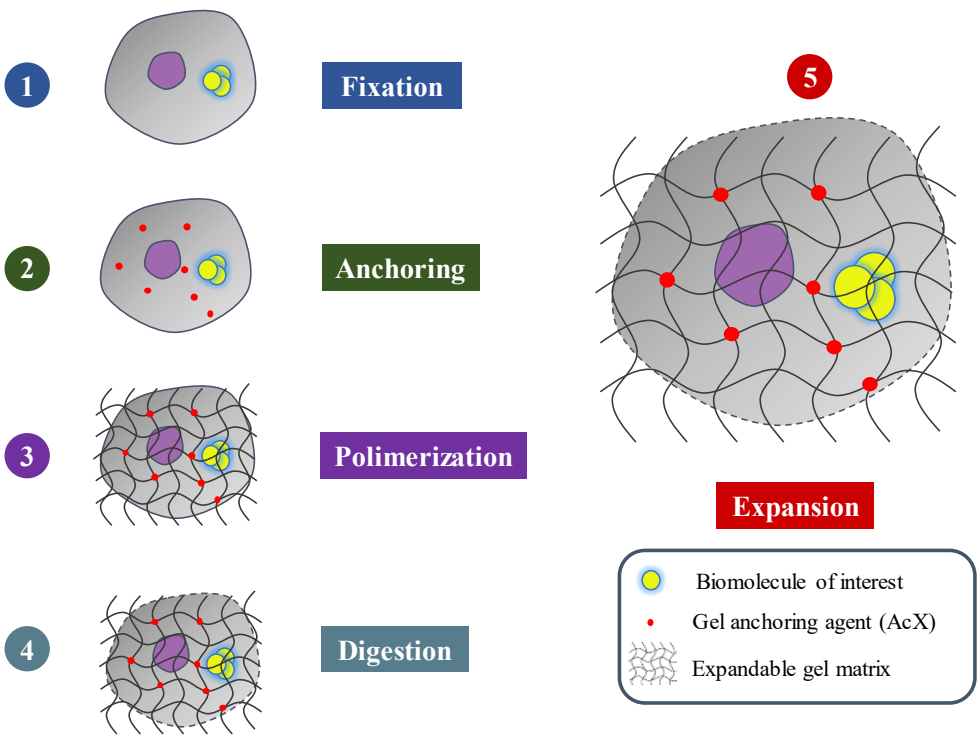

Figure 19 | Expansion microscopy. Key steps in high-resolution expansion microscopy technique.

3.2.5 Phototoxicity

Neutral red uptake (NRU) assay

The neutral red uptake (NRU) phototoxicity test was conducted to assess the viability of keratinocyte cells (HaCaT) when exposed to both TKIs and UVA light simultaneously. In a monolayer culturing method, NRU test was

conducted following OECD Guideline 432[152], with some minor adjustments[153]. Although the NRU assay was initially standardized in BALB/c 3T3 mouse fibroblasts according to these guidelines, it has been shown that HaCaT cells are a more suitable choice as they better represent the skin environment[154].

Moreover, chlorpromazine (CPZ) and sodium dodecyl sulfate (SDS) were used as the positive and negative phototoxic controls, respectively. CPZ is a well-known antipsychotic drug with established phototoxic properties[155], whereas SDS is a compound that lacks a chromophore in its structure and, as a result, does not absorb light.

In summary, for each compound, two 96-well plates were seeded with $2.0 \cdot 10^4$ cells per well. The following day, HaCaT cells, in fresh DMEM medium without phenol red, were exposed to the test compounds at eight increasing concentrations. Additional plates were treated with CPZ (ranging from 1.57 to 500 μM) and SDS (ranging from 3.13 to 1000 μM). All plates were incubated in the dark for 1 h at 37ºC. Subsequently, one plate for each sample was exposed to a non-cytotoxic dose of 5 J/cm² UVA while the other remained in a dark box. Afterward, the drug solutions were replaced with fresh DMEM medium, and the plates were further incubated overnight.

The next day, a solution of neutral red (50 μg/mL) was added to the wells and incubated for 2 h at 37ºC. The cells were then washed with PBS, and the neutral red was extracted from lysosomes using an extraction buffer composed of distilled water 50% (v/v), EtOH 49.5% (v/v), and acetic acid 0.5% (v/v). Finally, the absorbance of the plates was measured at 550 nm using a Synergy H1 microplate reader (BioTek, Vermont, U.S.). For each

compound, dose-response curves were obtained to determine the concentration at which neutral red uptake was reduced by 50% (IC50) under both dark and UVA light conditions. Subsequently, photoirritant factor (PIF) values were calculated using the Equation 7.

$$PIF = \frac{IC50\ (Dark)}{IC50\ (UVA\ Light)}$$

Equation 7 | Photoirritant factor (PIF). In accordance with OECD Guideline 432[152], a substance is classified as "nonphototoxic" if PIF is less than 2, "probably phototoxic" if PIF falls between 2 and 5, and "phototoxic" if PIF is greater than 5.

Reconstructed human epidermis (RhE) phototoxicity test

The assessment of topical drug phototoxicity requires the utilization of a biologically relevant model that better reflects the clinical context of treatment. Thus, evaluating phototoxicity in reconstructed human epidermis (RhE) introduces additional complexities with the aim to mimic the architecture and physiology of human skin, making it more relevant for assessing topical drug safety. An illustrative example is dasatinib (DAS), a promising TKI candidate for the topical treatment of skin carcinoma[156] and other skin inflammatory processes[157,158].

Topical dasatinib formulation

DAS 0.45% cream was selected as the test substance through the formulation of an oil-in-water (O/W) emulsion. DAS emulsion was meticulously prepared following the guidelines of the Spanish Pharmacopeia and the National Formulary[159]. O/W emulsion was prepared using decyl oleate, glycerol monostearate 40-55, propyleneglycol, all three from Guinama (Valencia, Spain), and Ceteareth-12 from PCC Group (Brzeg Dolny, Poland). This emulsion belongs to the class of non-ionic O/W emulsions, with the drug

being incorporated into the inner oil phase due to its lipophilic nature. Simultaneously, a formulation combining DAS with bemotrizinol (Tinosorb S) (TCI, Zwijndrecht, Belgium), known for its broad-spectrum UV-filter properties, was also prepared. Through a similar procedure, Tinosorb S was integrated into the oil phase of the O/W emulsion at a concentration of 3%. Both of these formulations were applied topically onto the tissue inserts, ensuring complete coverage of the surface. Furthermore, to prevent any interference with the UVA light due to the opacity of the cream samples, any residual material remaining on the emulsion surface was removed shortly before the irradiation process.

MTT assay on RhE

The EpiDerm System (MatTek Life Sciences, Bratislava, Slovakia) comprises human-derived epidermal keratinocytes that establish a sophisticated, multi-layered, and extensively differentiated representation of the human epidermis. This model consists of meticulously structured basal, spinous, and granular layers, alongside a multi-layered stratum corneum. Within the stratum corneum, intercellular lamellar lipid layers are arranged in a manner that closely mimics the patterns observed in living tissues. These elements are formed, through several cultivation steps, within a cell culture insert (Milicells, 10 mm), providing a faithful replication of the skin natural structure.

Upon receipt, the RhE tissue samples were placed in 6-well plates with assay medium and incubated for 1 h at 37ºC under conditions of 100% relative humidity and 5% CO_2. After this equilibration period, the assay medium was replaced with fresh medium, and the plates were left to incubate overnight,

following the guidelines provided by the supplier. Next day, the test materials were administered to the epidermal surface. Chlorpromazine (CPZ) was employed as the positive control for phototoxicity, while the vehicle (EtOH) served as the negative control.

Subsequently, CPZ, as a water-soluble substance, was incorporated in a volume of 50 µL, whereas DAS in both EtOH (10 mM) and O/W emulsion (0.45%) was added in a volume of 25 µL. Tissues were incubated for another 24 h (100% relative humidity, 5% CO_2) at 37ºC to allow the compounds to penetrate through the epidermis layers. Then, one set of tissues was exposed to 7 J/cm^2 UVA and the other set was kept in the dark for the same period. Culture inserts were then rinsed with DPBS buffered solution until the drugs were completely removed. Afterward, tissues were transferred to new 6-well plates with fresh medium and incubated overnight. Next day, assay medium was replaced by MTT solution (1 mg/mL), and inserts were incubated for 3 h in the same conditions. After the incubation is complete, the formazan was extracted with isopropanol for at least 2 h at room temperature, then small aliquots of the final solution were transferred to a 96-well plate. The optical density of the blue formazan was determined at 540/570 nm using isopropanol as a blank. The cell viability for each tissue was determined as the percentage of the corresponding vehicle control (EtOH). Mean values were obtained and then the results of irradiated or non-irradiated samples were compared. In accordance with the OECD guidelines[160], a substance is anticipated to exhibit phototoxicity if tissues treated with one or more test concentrations and subsequently subjected to irradiation display a reduction in relative viability of at least 30% when compared with the relative viability values of those same concentrations in the absence of irradiation.

Histological analysis of RhE

To confirm the phototoxic effects induced by DAS in response to UVA radiation, a histological examination of the RhE tissues was conducted. Thus, epidermal tissues were meticulously preserved by immersing them in a 10% formalin solution at room temperature for an overnight period. Subsequently, the tissues underwent a gradual dehydration process through an EtOH gradient before reaching the state of vitrification achieved by xylene. Following these preparatory steps, the tissue membranes were carefully encased in paraffin wax, and from this wax block, sections measuring 5 μm in thickness were precisely cut using a Leica rotary microtome (RM2235, Wetzlar, Germany). These sections were then subjected to staining with hematoxylin and eosin (H&E; Sigma-Aldrich, Madrid, Spain), after which they were securely mounted on glass slides and subjected to visualization under light microscopy, Leica DMD108 optical microscope (Wetzlar, Germany). This thorough histological process allowed for detailed inspection and analysis of the tissue samples aiming to determine the pathological impact of DAS induced photodamage.

3.2.6 Lipid photoperoxidation

Determination of thiobarbituric acid reactive substances (TBARS)

Various techniques have been established for assessing lipid photoperoxidation. The thiobarbituric acid reactive species (TBARS) method is the most common approach for monitoring lipid peroxidation regardless of the sample nature (solution, cell extract). This technique was conducted, using linoleic acid (LA) as a model, in accordance with previously established procedures[161] and, with minor adaptations as described in prior research[162].

In this assay, a solution of LA at a concentration of 1 mM in a 20 mM PBS solution (pH = 7.4) containing 0.05% Tween 20 was prepared. Subsequently, this solution was subjected to irradiation (15 J/cm^2) in the presence of the compound. Ketoprofen (KP) at a concentration of 200 µM was employed as a positive control, as previously outlined[161]. Both irradiated and non-irradiated samples were processed using the TBARS assay (Scheme 3). Therefore, 4 mM TBA (Sigma-Aldrich, Madrid, Spain) and a 10 µL BHT (Sigma-Aldrich, Madrid, Spain) solution in glacial acetic acid were added to each sample (500 µL). The samples were then heated at 95ºC for 60 min. After allowing them to cool for 10 min, the absorbance of the samples was measured at 532 nm to determine the TBARS levels. Additionally, a standard curve for 1,1,3,3-tetraethoxypropane (TEP) (Sigma-Aldrich, Madrid, Spain) was used to calculate the total amount of malondialdehyde (MDA) produced.

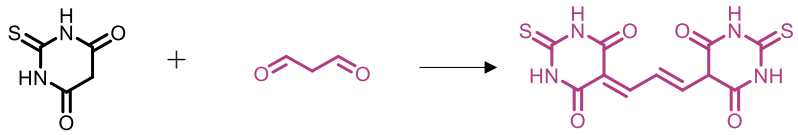

Scheme 3 | TBARS method. Formation of MDA-based chromogen during TBARS assay.

Assessment of lipid photoperoxidation using C11-Bodipy as a sensor

The extent of lipid peroxidation can also be determined using lipophilic fluorescent probes as an alternative to the detection of peroxidation products. In this case, the evaluation of lipid photoperoxidation was performed using Image-iT® Peroxidation kit (Invitrogen, Madrid, Spain). This kit contains a C11-Bodipy$^{581/591}$ sensor, 4,4-difluoro-5-(4-phenyl-1,3-butadienyl)-4-bora-3a,4a-diaza-s-indacene-3-undecanoic acid, which serves as a molecular probe

for evaluating lipid peroxidation within living cells. This probe undergoes a fluorescence shift from red to green when oxidized (Figure 20)[67,163].

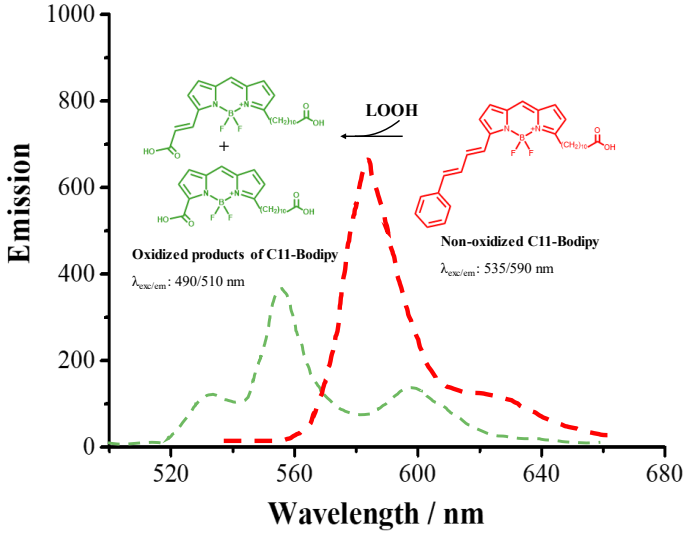

Figure 20 | Lipid peroxidation assay probe C11-Bodipy. Fluorescence emission shift of C11-Bodipy upon lipid peroxidation. Inset: conversion of C11-Bodipy to its oxidized products induced by lipid peroxidation. LOOH: lipid hydroperoxides.

To conduct this assessment, human skin fibroblast cells (FSK) were seeded in two 12-well plates at a density of $6.0 \cdot 10^4$ cells per well. The following day, the cells were treated with drug solutions and incubated for 30 min in darkness. Subsequently, one plate was irradiated (5 J/cm^2), while the other was maintained in the dark as a negative control. The cells were then labeled with the lipid peroxidation sensor C11 Bodipy$^{581/591}$ (10 µM) for 30 min at 37ºC. Finally, the cultures were observed using a Leica DMI 4000B fluorescence microscope (Wetzlar, Germany) in sequential mode to detect both the non-oxidized form (red fluorescence, λ_{exc}: 535 nm) and the oxidized form (green fluorescence, λ_{exc}: 490 nm) of the probe. To quantify the degree

of lipid peroxidation in each condition, the fluorescence intensity ratio (FIR) was calculated according to Equation 8, utilizing the Image-J software image analyzer (NIH).

$$FIR = \frac{\text{I red fluorescence}}{\text{I green fluorescence}}$$

Equation 8 | Quantification of lipid peroxidation. Fluorescence intensity ratio between red fluorescence (λ_{exc}: 535 nm) and green fluorescence (λ_{exc}: 490 nm).

3.2.7 Protein photooxidation

The evaluation of protein oxidation induced by TKIs upon photoirradiation was conducted using human serum albumin (HSA) as a model, employing a method similar to that previously described[164]. The DNPH (2,4-dinitrophenylhydrazine) carbonylation method consists of a derivatization of DNPH with carbonyl moieties generated upon the irradiation of proteins in the presence of photosensitizing agent. The interaction between DNPH and the carbonyl compound leads to the generation of hydrazone adducts (Scheme 4). These hydrazones are stable structures with an absorption spectrum characterized by a maximum within the range of 365 to 375 nm, which allows for their effective detection and quantification using spectrophotometry.

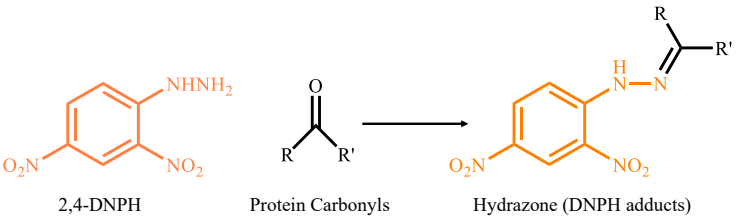

Scheme 4 | DNPH derivatization. Reaction of derivatization of protein carbonyl compounds with 2,4-dinitrophenylhydrazine (DNPH).

In brief, solutions of HSA at a concentration of 5 mg/mL in PBS were subjected to treatment with varying concentrations of the compounds at room temperature for 1 h. After this incubation, the samples were either exposed to UVA irradiation with doses ranging from 5 to 15 J/cm^2 or maintained in the dark for use as a control. Following irradiation, the degree of HSA oxidation was determined by means of spectrophotometry, measuring the absorbance at 375 nm, and the results were expressed in terms of nmol of carbonyl moiety per mg of protein according to Equation 9.

$$\text{Carbonyl content (nmol/mg protein)} = \frac{(A_{375}/\varepsilon^{mM})}{P} \times 100$$

Equation 9 | Quantification of carbonyl content. A_{375} represents the absorbance of the sample at 375 nm, ε^{mM} is the adjusted millimolar extinction coefficient (6.364), and P the amount of protein from standard well.

3.2.8 Photogenotoxicity

Alkaline comet assay

The single cell gel electrophoresis, commonly known as comet assay, was initially presented in 1984 by Ostling and Johanson[165] as a method to quantify DNA strand breaks leading to DNA supercoil relaxation. Typically, comet assay was used to detect double-stranded DNA breaks (DSBs) through electrophoresis under neutral conditions and is especially sensitive to large DNA fragments. Later, in 1988, a modified approach was introduced, incorporating alkaline conditions, which is more sensitive to detecting smaller amounts of DNA damage, including both single-stranded breaks (SSBs) and DSBs[166]. The fundamental idea behind this method was to integrate DNA gel electrophoresis with fluorescence microscopy, enabling the observation of DNA strand migration from individual cells embedded in agarose.

In this context, alkaline comet assay was conducted, as previously described[131,167], to detect both SSBs and DSBs, and alkaline-labile sites (ALS) in nuclear DNA. In brief, HaCaT cells were subjected to trypsinization, resuspended in cold PBS, and allowed to stand for 2 h at 4ºC to facilitate the repair of any damage generated during trypsin detachment. Subsequently, two 24-well plates were seeded with cells at a density of $5.0 \cdot 10^4$ cells per well and treated with the compound solution for 30 min at 4ºC in the absence of light. In this assay, CPZ (5 µM) was employed as the photogenotoxic reference compound. After the incubation, one plate was exposed to irradiation in the photoreactor (2-5 J/cm^2), while the other plate was maintained in the dark to serve as a negative control. Following irradiation, cells from both the irradiated and non-irradiated plates were collected. Subsequently, 100 µL of each sample was mixed with 100 µL of a 1% low melting point agarose solution, and the mixtures were deposited as single drops ($1.0 \cdot 10^4$ cells/gel) onto slides pretreated with Trevigen® (R&D Systems, Minnesota, U.S.) to allow gelation. The slides were immediately placed in a container filled with a lysis buffer (containing 2.5 M NaCl, 0.1 M Na_2EDTA, 0.01 M Tris, and 1% Triton X-100) and incubated at 4ºC overnight.

Additionally, DNA damage repair experiments were performed aiming to promote intrinsic cellular DNA repair mechanisms. Hence, slides were kept in DMEM medium at 37ºC for 6 or 18 h and subsequently lysed as described earlier. The following day, all slides were transferred to a Trevigen® comet assay electrophoresis tank and submerged in cold alkaline buffer (0.2 M NaOH, 1 mM EDTA, pH ≥ 13), and afterward, electrophoresis, 21 V (1 V/cm), was carried out for 30 min at 4ºC. After completing the

electrophoresis, the slides were washed twice with PBS for 5 min. Then, DNA was fixed through two consecutive incubations in 70 and 100% EtOH solutions. Following this, DNA was stained with SYBR Gold® (Invitrogen, Madrid, Spain), previously diluted 1:10,000 in TE buffer (Tris-HCl 10 mM pH 7.5, EDTA 1 mM), for 30 min at 4ºC in the absence of light. Lastly, washed slides were air-dried and stored in darkness. Comet nucleoids and tails were visualized using a Leica DMI 4000B fluorescence microscope (λ_{exc}: 490 nm). A minimum of 100 cells per sample were analyzed to determine DNA damage. The percentage of DNA damage in each sample was calculated by visually scoring at least 100 DNA comets, following the Equation 10:

$$\text{DNA damage (\%)} = \frac{\sum_{n=0}^{6} n^{o} \text{ comet class}_n \cdot n}{6}$$

Equation 10 | Quantification of DNA damage by comet assay. Class 0 (Cl_0) comets indicate comets with no DNA damage and class 6 comets indicate comets with maximum DNA damage.

γ-H2AX photoinduced phosphorylation assay

As an alternative to the comet assay, photosensitized DNA damage can also be assessed using a highly specific and sensitive molecular marker known as γ-H2AX histone. This marker becomes phosphorylated in response to the induction of DNA double-strand breaks as an early cellular response[168,169]. Therefore, the monitorization of this biomarker will improve the identification of TKIs with potential to induce DNA photodamage. For this purpose, immunostaining was conducted using Bj-hTERT fibroblasts.

In brief, fibroblasts subjected to drug treatment and irradiation were permeabilized with a 0.2% Triton X-100 solution in PBS for 15 min, followed

by three consecutive 5-min PBS washes. Subsequently, the samples were blocked for 15 min using a 10% goat serum solution, containing 0.1% Tween-20, as a blocking buffer.

Following the blocking step, coverslips were incubated overnight at 4ºC with the primary antibody, rabbit anti-H2AX-ser139 (1 µg/mL, Abcam, Amsterdam, Netherlands). The next day, the samples were rinsed with PBS and incubated for 1 h at room temperature with the secondary antibody, goat anti-rabbit IgG-Alexa Fluor 488 1:500 (Invitrogen, Merelbeke, Belgium). After a thorough PBS wash, the primary antibody mouse anti-α-tubulin (2 µg/mL) was added and incubated for 1 h at room temperature. Afterwards, samples, which were previously washed with PBS, were incubated for 1 h at room temperature with the secondary antibody, goat anti-mouse IgG 1:50 modified and labelled with Rhodamine red (a kind gift from the Hofkens Lab, KU Leuven, Belgium). Additionally, washed samples were stained with DNA marker, DAPI 1µg/mL (Sigma-Aldrich, Overijse, Belgium), and incubated for 5 min. Finally, the immunostained specimens were observed using the confocal microscope in sequential mode, with excitation lasers at 405, 488 and 638 nm for nucleus, γ-H2AX, and α-tubulin, respectively.

3.2.9 Cell death

In order to elucidate the mechanisms of cell death in keratinocyte cells, two main approaches were employed, depending on whether the process involves apoptosis or necrosis.

Caspase 3/7 activity assay

The primary effector caspases in mammals consist of caspase-3, -6, and -7, with caspase-3 being the most frequently associated with apoptosis[170].Given

this fact, the potential of selected TKIs to induce apoptosis in HaCaT cells upon exposure to UVA light was studied. This was accomplished using the Apo-ONE homogeneous caspase-3/7 assay (Promega, Madison, U.S.). The assay kit contains a profluorescent Rhodamine 110 substrate (Z-DEVD-R110) that is targeted by both caspase-3 and 7. Upon cleavage and removal of the DEVD peptide by caspase-3/7, Rhodamine 110 (the leaving group) becomes highly fluorescent. Thus, the activity of caspase-3/7 was tracked by fluorescence and represented as a relative change, indicating the level of apoptosis activation within the cells.

Thus, to conduct this experiment, HaCaT cells were initially seeded in 96-well plates at of $2 \cdot 10^4$ cells/well. The following day, the cells, in fresh phenol red-free DMEM medium, were exposed to the compounds at two different concentrations representing 100 and 50% of cell viability as determined by NRU dose-response curves. After a 1 h of incubation at 37ºC, one plate was subjected to UVA light irradiation (5 J/cm^2), while the other was kept in darkness. Subsequently, the plates were incubated for an additional 24 h at 37ºC with fresh DMEM medium. Samples were then analyzed using the Apo-ONE Homogeneous Caspase-3/7 assay according to the manufacturer instructions. Following this, fluorescence was measured 4 h after the addition of the substrate with an excitation at 499 nm and emission at 521 nm.

Lactate Dehydrogenase release assay

L-Lactate dehydrogenase (LDH) is an enzyme responsible for catalyzing the conversion of lactate to pyruvate, while converting NAD+ to NADH, as a crucial step in the process of glycolysis[171]. The LDH-release assay is employed to evaluate the extent of damage to the plasma membrane, as this

damage leads to the release of LDH enzyme from the cells[103]. Given that the primary factor contributing to necrosis is the permeabilization of the plasma membrane, measuring LDH-release can be considered an indicator of necrosis. However, it is worth noting that the release of LDH may also play a role in late-stage apoptotic events where the loss of membrane integrity is also detectable[172].

With this background, LDH activity assay was carried out in accordance with the manufacturer instructions. In brief, HaCaT cells were cultured in 96-well plates at a concentration of $2 \cdot 10^4$ cells/well and incubated for 24 h. Subsequently, the culture medium was replaced with fresh phenol red-free DMEM, and the cells were treated with the compounds for 1 h at two different concentrations, corresponding to 100% and 50% cell viability based on the NRU dose-response curves. One plate was then exposed to UVA light (5 J/cm^2), while the other plate was kept in a dark environment. The following day, samples were analyzed using the CytoTox-ONE™ Homogeneous Membrane Integrity Assay (Promega, Madison, U.S.), and a lysis solution (composed of a 9% weight/volume Triton X-100 solution in water) was employed to determine the maximum LDH content. Fluorescence measurements were taken 10 min after adding the substrate with an excitation at 560 nm and emission at 590 nm. The percentage of LDH release was calculated using Equation 11.

$$\% \text{ LDH release} = \frac{\text{Experimental LDH release}}{\text{Maximum LDH release}} \times 100$$

Equation 11 | Quantification of LDH activity. The percentage of lactate dehydrogenase (LDH) release was calculated as the ratio between the experimentally released LDH and the maximum LDH release, corresponding to the positive control (lysis solution).

CHAPTER 4 Screening of TKIs

4.1 Tyrosine kinase inhibitors (TKIs) selection criteria

The overarching aim of this thesis was to explore the photoreactivity of TKIs that have the potential to trigger photosensitivity disorders, such as photo(geno)toxicity. This investigation also assessed photoinduced damage to both biochemical targets and living cells. To achieve this, in-depth studies of the photophysical properties were carried out, in conjunction with photobiological experiments, on selected TKIs in diverse settings.

Currently, the FDA has approved over 50 TKIs for the treatment of diverse tumors. Many of these drugs have reported dermatological disorders associated with sun exposure[43,51,56,134,173,174]. However, specific criteria ought to be met to classify a TKI as a potential phototoxic drug.

4.1.1 Absorption of UVA light

Although there are a number of mechanisms that contribute to the eventual manifestation of phototoxic skin responses, it is widely acknowledged that the absorption of UVA light (315-400 nm) typically serves as the primary trigger for photosensitizing drug reactions. Considering that photosensitizing drugs generate excited species capable of inducing damage to cellular components upon UVA light absorption. Consequently, the photophysical study, as an initial step, is necessary to analyze the absorption characteristics of TKIs in the UVA range. Hence, in the context of this study, the selection process based on the absorption capability within the UVA region of the spectrum led to the inclusion of a total of 9 different TKIs (Figure 21): afatinib (AFT), avapritinib (AVP), axitinib (AXT), brigatinib (BRG), dasatinib (DAS), gefitinib (GFT), nilotinib (NLT), sorafenib (SOR) and sunitinib (SUN). All these TKIs displayed, in PBS solution, an intense absorption band within the range of 300-400 nm. Interestingly, both SUN and SOR, in

addition to their absorption within this UV range, exhibited a notable capability to absorb light across the visible wavelengths of the spectrum.

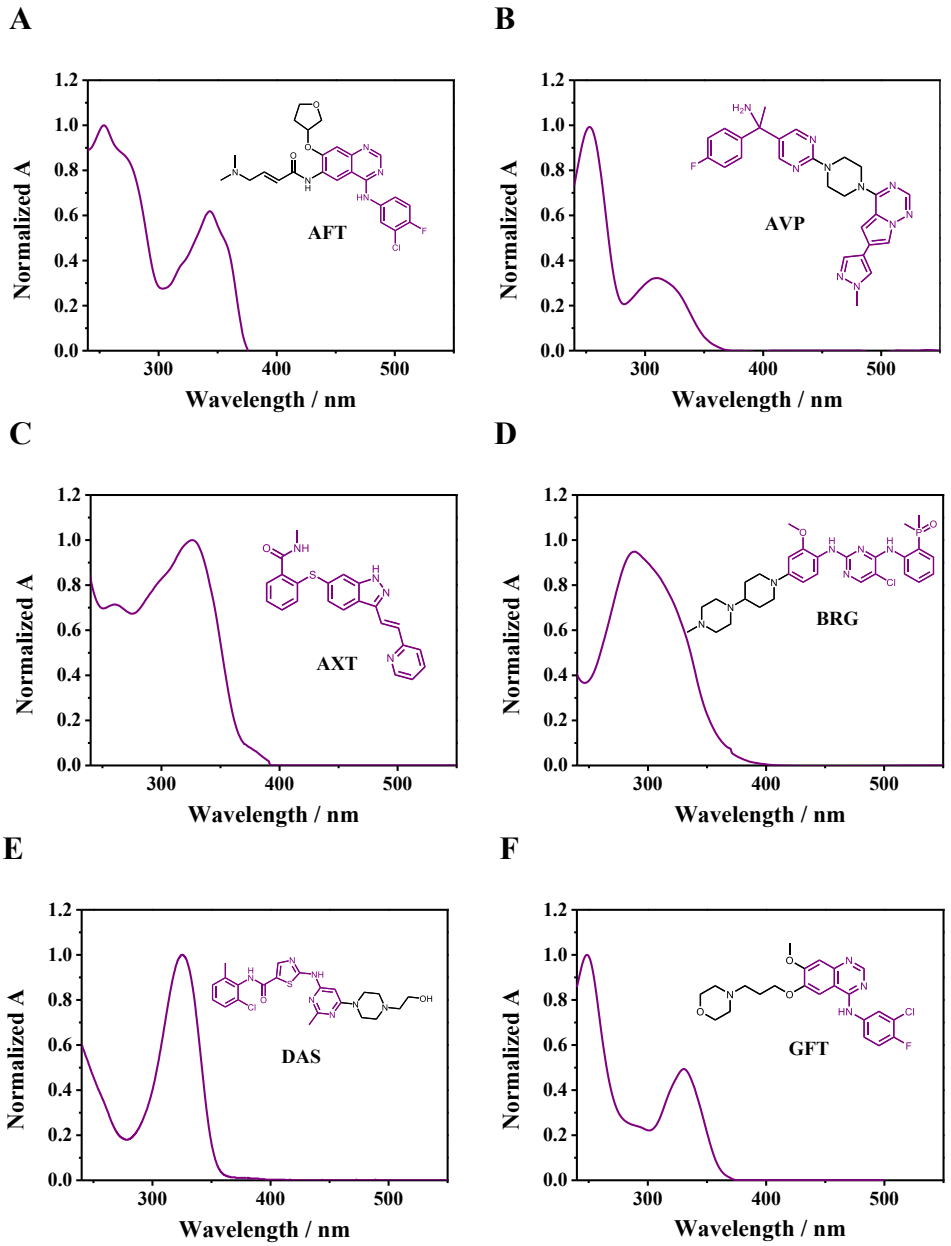

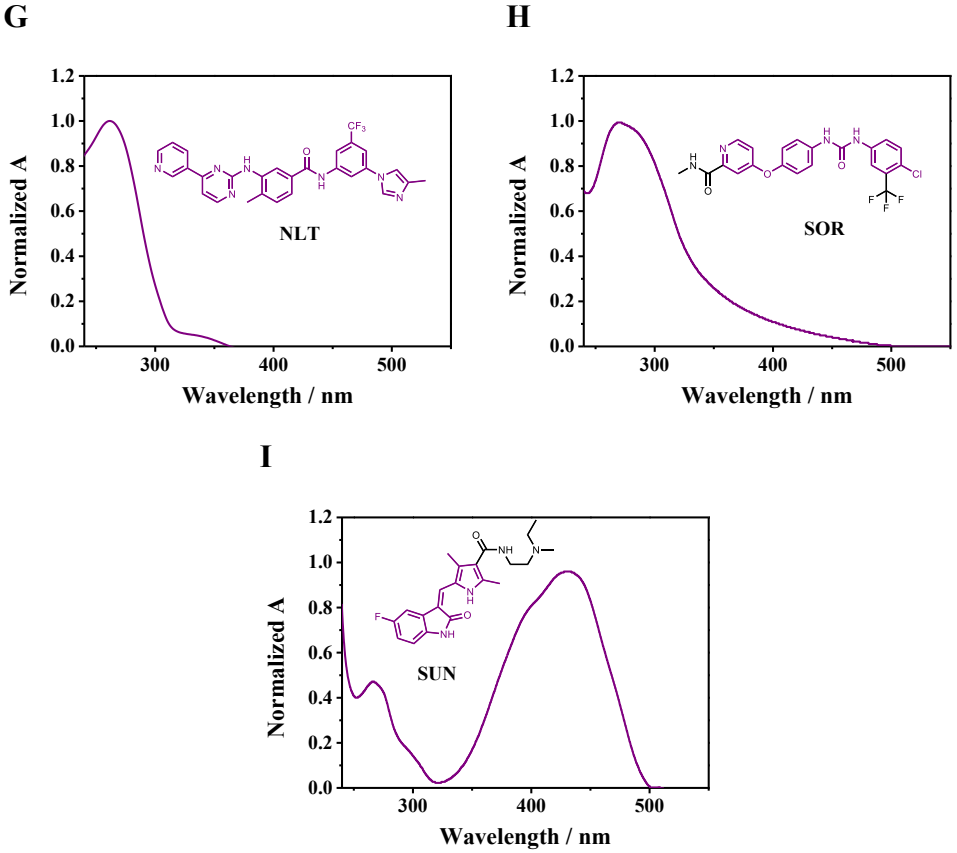

Figure 21 | Normalized absorption spectra of (A) afatinib, AFT; (B) avapritinib, AVP; (C) axitinib, AXT; (D) brigatinib, BRG; (E) dasatinib, DAS; (F) gefitinib, GFT; (G) nilotinib, NLT; (H) sorafenib, SOR and (I) sunitinib, SUN. Inset: Molecular structure of TKIs. Chromophore groups are colored in violet.

4.1.2 Neutral red uptake (NRU) phototoxicity test

According to OECD guidelines 432[152], once it is established that the selected TKIs indeed absorb UVA light, the absorbed energy has the potential to trigger molecular alterations within the drug. These changes may render the TKIs capable of acting as photosensitizers. Thus, they are suitable candidates for testing their phototoxicity potential. The *in vitro* neutral red uptake (NRU) assay is the standard method for the phototoxicity evaluation of chemicals activated by exposure to light.

Giving this background, TKIs exhibiting UVA absorption were subjected to the NRU phototoxicity test. This step aimed to narrow the focus of this study to those drugs with phototoxic potential. Thus, following the OECD guidelines[152] with minor modifications[153], the NRU assay was conducted. However, instead of BALB/c 3T3 mouse fibroblasts, human keratinocytes (HaCaT cells) were selected based on their demonstrated suitability and representation of the human skin[154].

The assessment of NRU assay was carried out by exposing HaCaT cells to the compounds, using neutral red as a vital dye. Dose-response curves were generated using non-linear regression, and IC50 values were obtained (Figure 22 and Table 6). Subsequently, the PIF factor was calculated as the ratio of IC50 values with and without UVA irradiation (Table 6). Accordingly, the results provide evidence that, among the TKIs studied through the NRU test, AVP, AXT, DAS, and GFT can be classified as phototoxic drugs. Notably, AXT exhibited the highest level of phototoxicity, displaying a PIF value of approximately 37. In comparison, AVP and GFT showed comparable phototoxicity, with PIF values around 11 and 13, respectively. Conversely, DAS manifested the lowest phototoxicity, registering a PIF value *ca.* 5. In contrast, AFT, BRG, NLT, SOR, and SUN did not exhibit significant phototoxic potential. Based on these results, these compounds were discarded from further studies.

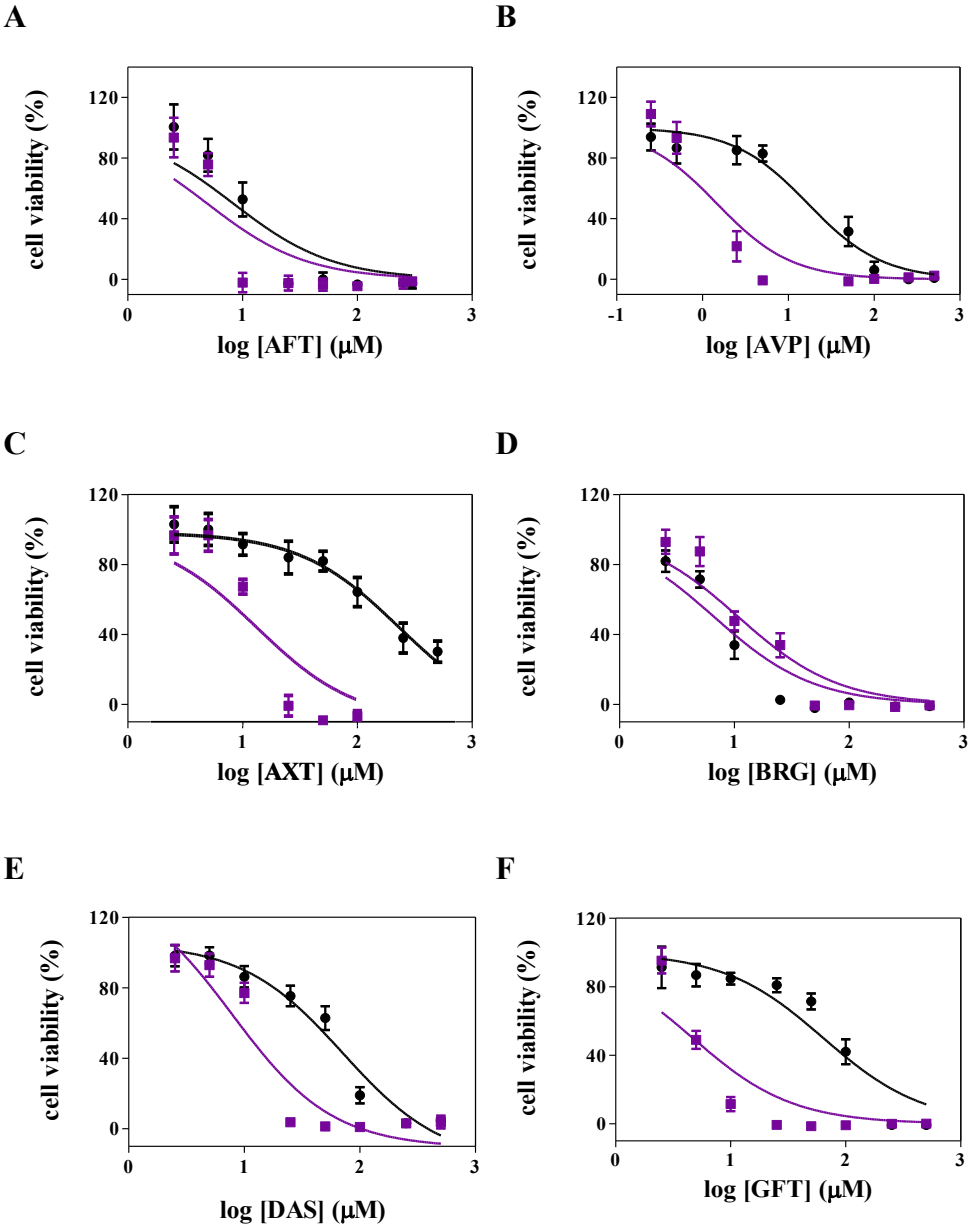
A
cell viability (%)
log [AFT] (μM)
B
cell viability (%)
log [AVP] (μM)
C
cell viability (%)
log [AXT] (μM)
D
cell viability (%)
log [BRG] (μM)
E
cell viability (%)
log [DAS] (μM)
F
cell viability (%)
log [GFT] (μM)

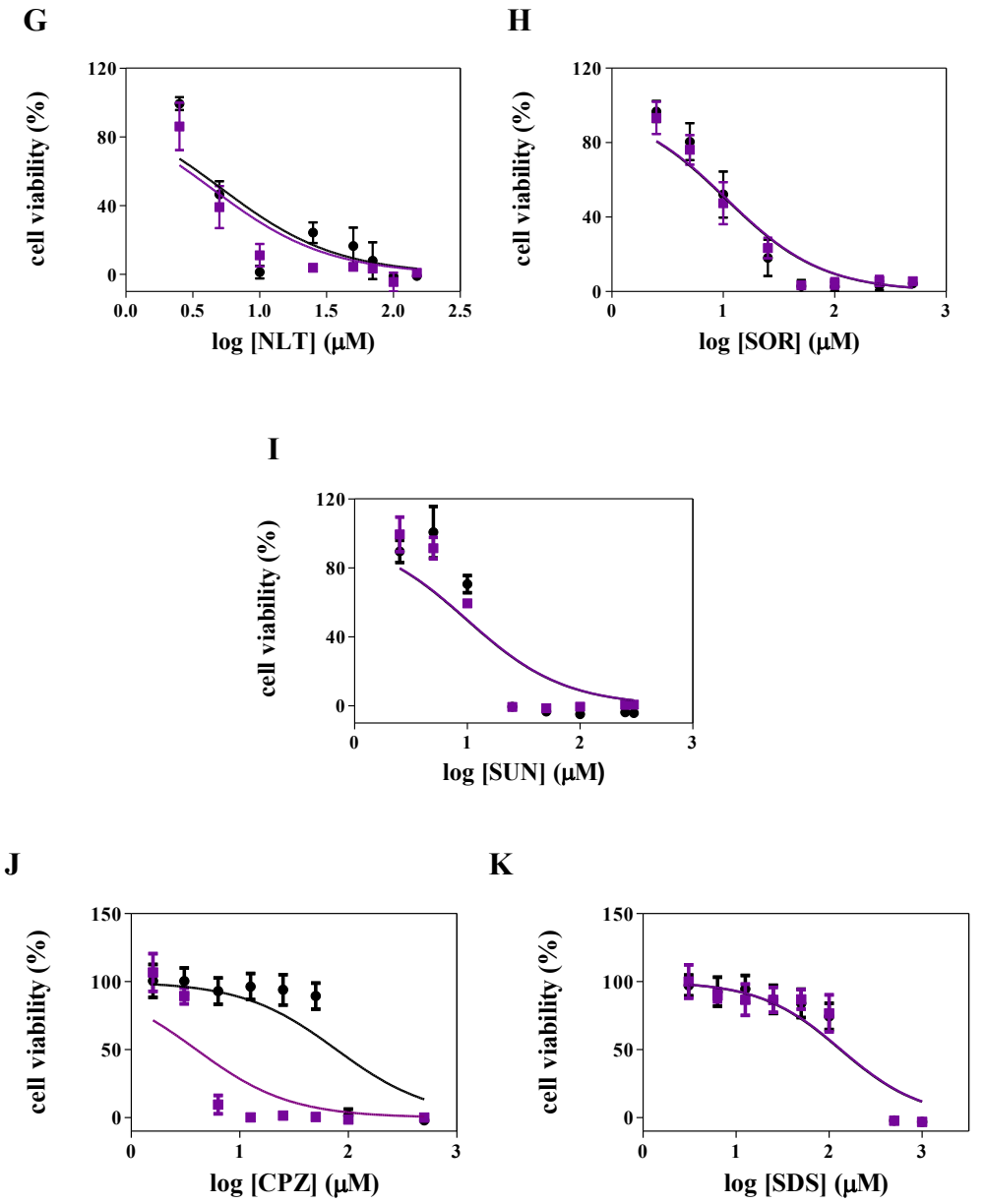

Figure 22 | Neutral red uptake (NRU) assay. Dose-response curves for cell viability of HaCaT cells treated with (A) afatinib, AFT; (B) avapritinib, AVP; (C) axitinib, AXT; (D) brigatinib, BRG; (E) dasatinib, DAS; (F) gefitinib, GFT; (G) nilotinib (NLT); (H) sorafenib, SOR or (I) sunitinib, SUN. Cells were either kept under dark conditions (-●-) or UVA light exposed (5 J/cm^2, -■-). Chlorpromazine, CPZ (J) and sodium dodecyl sulfate, SDS (K) were used as the positive phototoxic and negative non-phototoxic controls, respectively. Data are the mean ± SD from four independent experiments.

Table 6 | Summarizing the values of phototoxic potential (PIF) by NRU assay[a].

Compound	IC_{50} Dark (µM)	IC_{50} UVA Light (µM)	Photoirritant factor (PIF)[b]
AFT	9.4 ± 0.8	4.9 ± 0.6	2
AVP	17 ± 2.7	1.6 ± 0.4	11
AXT	>500	13.4 ± 2	37
BRG	6.7 ± 0.9	10.8 ± 1	1
DAS	55 ± 8	12 ± 3	5
GFT	64 ± 3	5 ± 1.7	13
NLT	4.8 ± 0.5	4.7 ± 0.8	1
SOR	10.4 ± 1	10.6 ± 1	1
SUN	10.8 ± 1	10.5 ± 0.9	1

[a] Data represent the mean ± SD from 4 independent dose-response curves. CPZ and SDS were selected as positive and negative controls of phototoxicity, respectively.
[b] According to the OECD 432 Guide[152], PIF < 2 means "no phototoxicity", 2 < PIF < 5 means "probable phototoxicity" and PIF > 5 means "phototoxicity".

4.2 Photostability of TKIs

In light of the previous outcomes, AVP, AXT, DAS, and GFT emerge as potential candidates for the investigation of their photophysical and photobiological properties. However, the observed phototoxicity revealed by the NRU assay could be attributed to either the photoexcitation of the unaltered drug or the generation of new photoproducts exhibiting heightened toxicity compared to the parent compound[175]. Consequently, photostability assessments were conducted using the same UVA light source employed in the previous NRU assay. To this end, the compounds were irradiated in a PBS solution at incremental UVA doses ranging from 1 to 20 J/cm², and absorption spectra were recorded. As illustrated in Figure 23, AVP, AXT, and DAS underwent minimal photodegradation, evidenced by a decrease in the absorption maxima, with AXT exhibiting a notably accelerated photodegradation rate. Conversely, the absorption spectra of GFT remained unchanged throughout the irradiation process. Overall, no new spectral

features were observed for the TKIs, indicating that UVA radiation did not induce the formation of photoproducts.

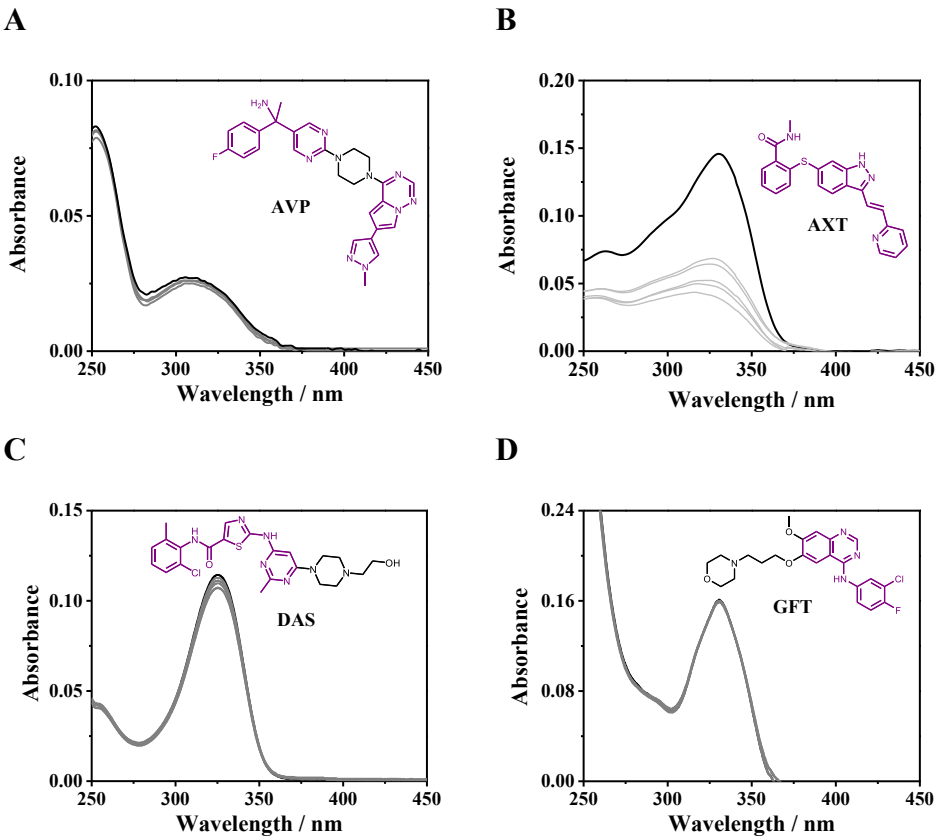

Figure 23 | Photostability of tyrosine kinase inhibitors (TKIs). Absorption spectra of avapritinib, AVP (A); axitinib, AXT (B); dasatinib, DAS (C) and gefitinib, GFT (D) upon irradiation with UVA light (1-20 J/cm^2).

Considering all these findings, the main objective of this study is to investigate the photophysical properties which can be responsible for the observed phototoxic behavior in keratinocyte cells. Additionally, the study also aimed at elucidating the underlying mechanisms of this phototoxicity. Therefore, AVP, AXT, DAS, and GFT were selected as the focus of this thesis, based on the previously established criteria.

CHAPTER 5 Gefitinib

5.1 Introduction

Gefitinib, GFT (Iressa®; AstraZeneca UK Limited), is a tyrosine kinase inhibitor that gained an early approval in 2003 by the FDA for the treatment of locally advanced or metastatic non-small cell lung cancer (NSCLC), particularly in patients with specific mutations in the epidermal growth factor receptor (EGFR) gene[176,177]. These mutations, specifically EGFR exon 19 deletions or exon 21 (L858R) substitution mutations, were the primary factors contributing to relapse in the majority of patients treated with conventional EGFR inhibitors[178,179].

Interestingly, activating EGFR mutations, pivotal in the growth and proliferation of around 20% of lung adenocarcinomas, significantly enhance responsiveness to EGFR TKIs like GFT or erlotinib (Tarceva)[180]. GFT is often regarded as the representative drug in this family. In fact, studies have demonstrated that GFT can elevate the disease control rate to 77% and efficacy to 35% in patients with advanced EGFR-mutated positive (EGFRm+) tumors. Moreover, the one-year survival rate can reach nearly 60%, showcasing a particularly pronounced therapeutic effect[181].

The antineoplastic effect of this drug is manifested through the activation of ErbB-1 (EGFR), a subtype within the ErbB family, which comprises four transmembrane receptor subtypes: EGFR (ErbB-1), HER2 (ErbB-2), ErbB3, and ErbB-4. The ErbB family receptors primarily consist of an extracellular ligand binding domain, a hydrophobic transmembrane domain, and an intracellular tyrosine kinase domain that can bind with adenosine triphosphate (ATP), excluding ErbB-3. In an inactive state, ErbB transmembrane receptors exist as monomers, which hardly can be phosphorylated. When proliferative factors like EGF bind to the extracellular ligand binding site, the

conformation of the ErbB protein alters to create a heterodimer or homodimer. In the dimeric state, the tyrosine kinase domain of ErbB can readily undergo autophosphorylation in the presence of ATP, activating downstream RAS/MAPK/Erk and PI3K/Akt pathways, thereby promoting cell proliferation and suppressing apoptosis. In cancer cells, ErbB receptors are primarily activated by an increase in the copy number of the ErbB gene, overexpression of ligands or receptors, genetic variations, or the production of autocrine ligands. The overexpression or inadequate regulation of EGFR or its ligands is recognized as characteristic for many types of solid tumors, including lung cancer, with reports indicating that 40-90% of NSCLCs exhibit EGFR overexpression[182,183].

Structurally, GFT is an anilinoquinazoline (4-quinazolinamine,*N*-(3-chloro-4-fluorophenyl)-7-methoxy-6-[3-(4-morpholinyl) propoxy] with a molecular weight of 446.90. Currently, there are five first-generation (gefitinib, erlotinib, lapatinib, vandetanib, and icotinib) and two second-generation (afatinib and dacomitinib) quinazoline-based EGFR inhibitors.

Oraly administered GFT is slowly absorbed (60% bioavailability) reaching its peak level at 3-5 h, while the elimination half-life is around 48 h. Approximately 90% of GFT binds to human serum albumin (HSA)[184]. Absorbed GFT is mainly metabolized in the liver and ~85% is excreted through feces, with less than 5% excreted in the urine[182,185]. In humans, GFT undergoes metabolic bioactivation primarily through Phase I hepatic metabolism, involving cytochromes CYP3A4 and CYP2D6. This process results in the formation of chemically reactive metabolites, including *O*-demethyl gefitinib (DMT-GFT), 4-defluoro-4-hydroxy gefitinib (DF-GFT), and *O*-demorpholinopropyl gefitinib (DMOR-GFT) (Figure 24A)[186–188].

A

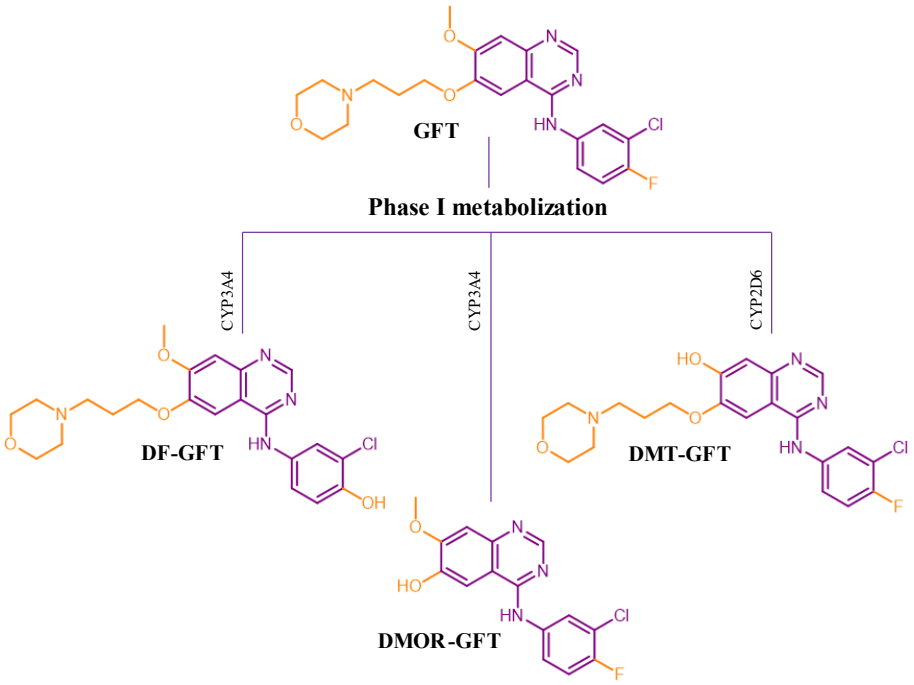

B

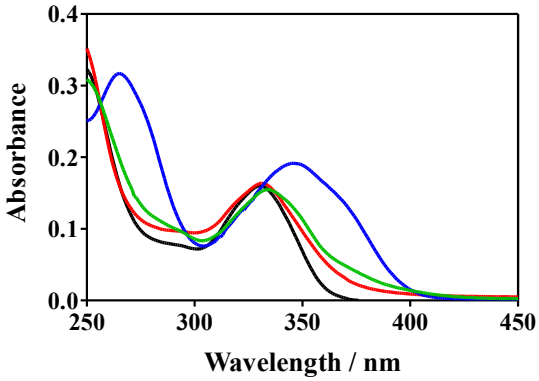

Figure 24 | Gefitinib and its metabolites. (A) Chemical structure of gefitinib (GFT), 4-defluoro-4-hydroxy gefitinib (DF-GFT), *O*-demethyl gefitinib (DMT-GFT) and *O*-demorpholinopropyl gefitinib (DMOR-GFT). Chromophore group is colored in violet. (B) Absorption spectra of GFT (black), DF-GFT (green), DMT-GFT (blue) and DMOR-GFT (red) in PBS solution (10 μM).

Although GFT is a well-tolerated drug, several adverse reactions were reported in NSCLC patients, such as mild or moderate skin reactions (including rash, acne and pruritus), gastrointestinal disorders, alteration in liver enzymes levels, diarrhea, nausea and vomiting[189,190]. Clinically, skin adverse reactions are managed by providing a brief (up to 14 days) therapy interruption. In cases where patients are unable to tolerate the treatment, discontinuation or the consideration of alternative therapies is often warranted. Interestingly, results from *in vitro* study on phototoxicity suggested that GFT could exhibit phototoxic potential[191]. In this context, we have previously demonstrated that these skin disorders can be linked to damage to biomolecules caused by radicals or reactive oxygen species arising from lapatinib excited state[131,132]. Thus, a good correlation between the photophysical properties and the photobiological behavior could serve as a valuable starting point for understanding the origin of these side effects induced by GFT. In line with this, we have previously documented the photo(geno)toxicity caused by one of the photoactive metabolites of lapatinib which maintained the quinazoline chromophore unaltered after biotransformation. In terms of chemical structure, GFT biotransformation induces significant alterations in the quinazoline chromophore, enhancing UV-light absorption efficiency (Figure 24B). Moreover, although drug metabolism is usually associated with reduced toxicity, certain metabolites may, in some cases, exhibit higher phototoxicity and photoreactivity than the original drug[153,155,192]. Consequently, investigating the photo(geno)toxicity of GFT and its metabolites becomes crucial for evaluating drug safety and understanding the risks associated with sunlight exposure during treatment.

5.2 Experimental procedures

Cell culture conditions and spectroscopic measurements were carried out in accordance with the procedures outlined in Chapter 3.

5.2.1 Neutral Red Uptake (NRU) phototoxicity test

Following the protocol described in Chapter 3, NRU phototoxicity assay was performed in HaCaT cells treated with GFT or its metabolites (DF-GFT, DMT-GFT or DMOR-GFT) at a concentration ranging from 2.5 to 500 μM, except for DMOR-GFT which was added in a concentration ranging from 125 to 0.625 μM.

5.2.2 Drug and metabolites cellular colocalization

The intracellular localization of GFT and its metabolites (DMT-GFT and DMOR-GFT) was performed according to the protocol described in Chapter 3, where HaCaT cells were treated with the compounds at a concentration of 15 μM, except for DMT-GFT, which was incorporated at a concentration of 25 μM. The excitation and emission wavelengths were 405 and 450 nm, respectively.

5.2.3 Photosensitized lipid peroxidation

The thiobarbituric acid reactive substances (TBARS) method was used to assess the lipid photoperoxidation potential of GFT and its metabolites (see Chapter 3). To this aim, a solution of linoleic acid (LA) was prepared and subjected to irradiation in the presence of GFT or its metabolites (DMT-GFT or DMOR-GFT) at a concentration of 100 μM and a UVA dose of 15 J/cm^2.

5.2.4 Photoinduced protein oxidation assay

The ability of GFT and its metabolites to induce the photooxidation of proteins was assessed using the 2,4-dinitrophenylhydrazine (DNPH) derivatization method using HSA as a model (see Chapter 3). In this regard, protein samples containing the chemicals at a concentration of 100 μM were irradiated with a UVA light dose ranging from 5 to 15 J/cm^2.

5.2.5 Single cell gel electrophoresis comet assay

The comet assay (alkaline single-cell gel electrophoresis) was performed according to the procedures detailed in Chapter 3. Thus, HaCaT cells were treated with 100 μM of GFT or its metabolites (DMT-GFT or DMOR-GFT). Then, both GFT and DMT-GFT were irradiated under 2 J/cm^2 UVA light dose, whereas DMOR-GFT was exposed to 4 J/cm^2 UVA radiation.

5.2.6 Cell death assays

The main mechanisms for cell death, apoptosis and necrosis, were studied through monitorization of biomarkers, caspase-3/7 and lactate dehydrogenase (LDH). Thus, both caspase-3/7 activity and LDH release were evaluated in HaCaT cells treated with the compounds (GFT, DMT-GFT or DMOR-GFT) at two different concentrations representing 100 and 50% of cell viability according to NRU dose-response curves (Table 7).

Table 7 | GFT and metabolites concentration for cell death assays.

Compound	**Concentration (μM)**	
	100% Viability[a]	50% Viability[b]
GFT	2.5	5
DMT-GFT	2.5	5
DMOR-GFT	1	3

[a] Concentration representing 100% of viability outcome from the NRU dose-response curves in UVA irradiated HaCaT cells.
[b] Concentration representing 50% of viability outcome from the NRU dose-response curves in UVA irradiated HaCaT cells.

5.3 Results and discussion

5.3.1 Phototoxicity of gefitinib metabolites

The early identification and screening of TKIs with potential phototoxic properties, as detailed in Chapter 4, revealed that GFT is a phototoxic drug with a PIF value of approximately 13. Consequently, it is anticipated that the phototoxicity profile of GFT will undergo alterations upon biotransformation. Thus, *in vitro* neutral red uptake (NRU) phototoxicity studies were conducted using keratinocyte cells (HaCaT) to assess the phototoxic potential of GFT and its metabolites, simultaneously, when exposed to UVA light.

Viability of HaCaT cells was assessed by treating with the compounds and using neutral red as a vital dye, both in the absence and presence of UVA light (5 J/cm^2). Nonlinear regression dose-response curves were obtained, and IC50 values were determined (Figure 25). Subsequently, PIF values were calculated as the ratio between the IC50 with and without UVA irradiation for GFT and its metabolites, and the resulting values are shown in Table 8.

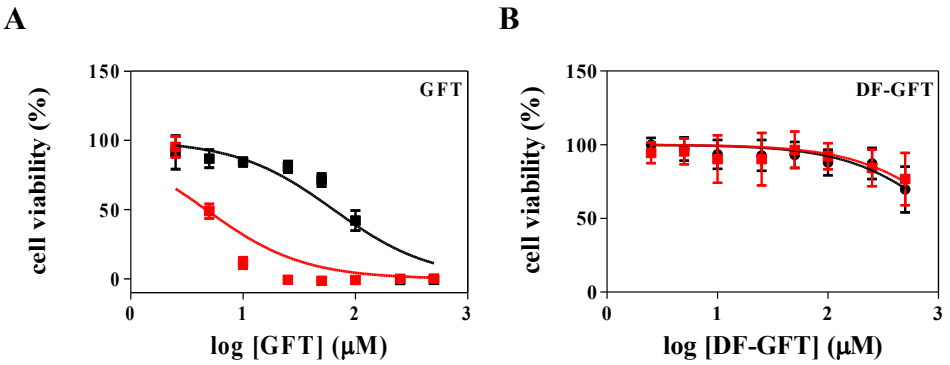

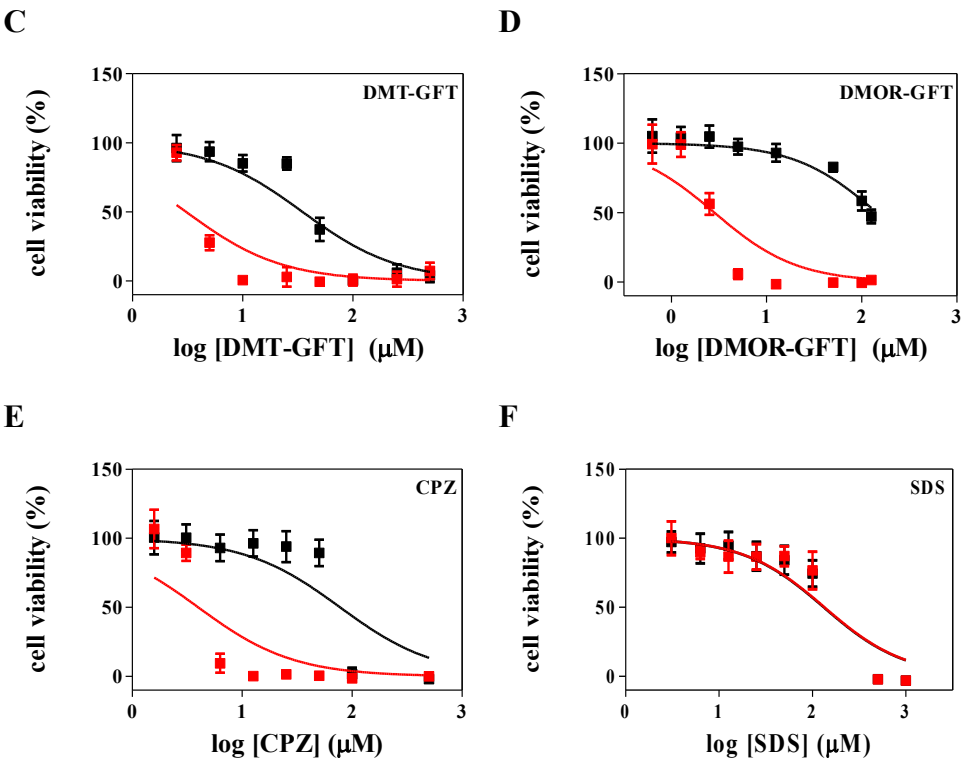

Figure 25 | Cell viability NRU dose-response curves. HaCaT cells were treated with GFT (A), GFT metabolites (B-D), CPZ (E) and SDS (F) in the presence (-■-) or absence (-■-) of UVA light (5 J/cm^2). Both CPZ and SDS were used as positive and negative phototoxicity controls, respectively. Data represent the mean ± SD from 4 independent experiments.

Table 8 | HaCaT NRU phototoxicity assay of GFT and its metabolites[a].

Compound	IC_{50} Dark (µM)	IC_{50} UVA Light (µM)	Photoirritant factor (PIF)[b]
CPZ	80 ± 17	4 ± 0.9	20
GFT	64 ± 3	5 ± 1.7	13
DF-GFT	1015 ± 222	1099 ± 406	1
DMT-GFT	34 ± 3	5 ± 0.1	7
DMOR-GFT	144 ± 6	3 ± 0.6	48
SDS	133 ± 31	136 ± 23	1

[a] Data represent the mean ± SD from 4 independent dose-response curves. CPZ and SDS were selected as positive and negative controls of phototoxicity, respectively.
[b] According to the OECD 432 Guide[152], PIF < 2 means "no phototoxicity", 2 < PIF < 5 means "probable phototoxicity" and PIF > 5 means "phototoxicity".

As already stated, GFT demonstrated clear phototoxicity with a PIF value of 13. Interestingly, the demethylated metabolite exhibited a reduction in phototoxic potential (PIF *ca.* 7), yet, following the OECD 432 Guideline[152], DMT-GFT is still considered phototoxic. In contrast, replacement of the fluorine substituent with OH group (DF-GFT) resulted in absence of phototoxic activity. Unexpectedly, the dealkylation of the propoxy-morpholine side chain (DMOR-GFT) led to a significant increase in phototoxic potential, with a notably high PIF value of 48.

5.3.2 Fluorescence

After establishing the phototoxic potential of GFT, DMT-GFT, and DMOR-GFT, an analysis of the fluorescence spectral characteristics of these compounds was conducted. This study aimed to investigate the differences in the photophysical behavior between GFT and its metabolites within different biological media. Consequently, the emission spectra (λ_{exc}: 320 nm) were recorded in PBS solution and in the presence of different biomolecules (lipids, proteins, and DNA), as well as within keratinocyte cells.

As depicted in Figure 26 and summarized in Table 9, a noticeable red shift in the emission maximum was observed for the metabolites in all models, likely attributable to emission from the phenolate form. As anticipated, the protein environment significantly increased fluorescence emission in all cases, especially for the DMOR-GFT metabolite, where the enhancement was particularly pronounced. This suggests that a similar effect is likely to be observed when the compounds are present within keratinocyte cells.

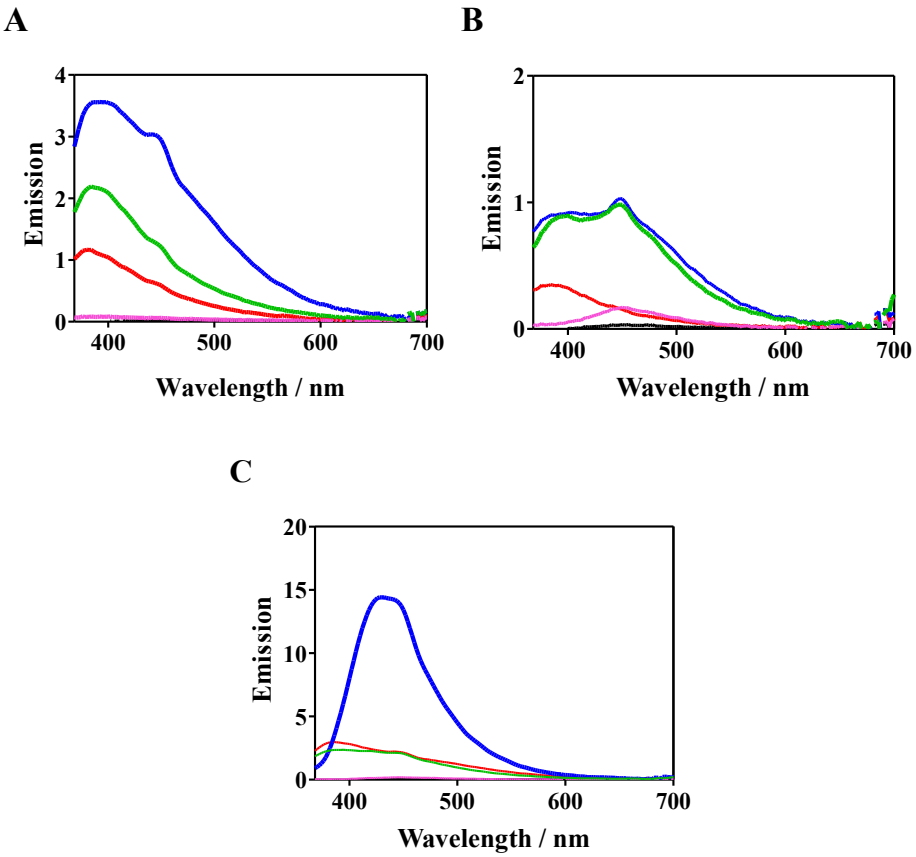

Figure 26 | Emission spectra (λ_{exc}: 320 nm) of GFT (A), DMT-GFT (B) and DMOR-GFT (C) alone (black) or in the presence of methyl linoleate (red), HSA (blue), ctDNA (magenta), or within keratinocyte cells (green). Fluorescence emission units are arbitrary.

Table 9 | Emission maximum wavelength of GFT and metabolites in different media[a].

Media	Emission (λ_{max})		
	GFT	DMT-GFT	DMOR-GFT
ML[b]	380	384	384
HSA	386	394, 448	432
ctDNA[c]	390	450	448
HaCaT cells	388	392, 448	392, 448

[a] Excitation wavelength = 320 nm.
[b] Methyl linoleate (ML).
[c] Calf thymus DNA (ctDNA).

Simultaneously, the fluorescence quantum yield (Φ_F) of the internalized compounds was determined, comparing them with anthracene as a standard (Φ_F = 0.27 in EtOH)[145]. Both GFT and DMT-GFT exhibited similar values, Φ_F = 0.07 and Φ_F = 0.04, respectively. In contrast, DMOR-GFT fluorescence within keratinocyte cells demonstrated a noticeable enhancement of the quantum yield (Φ_F = 0.1) (Figure 27).

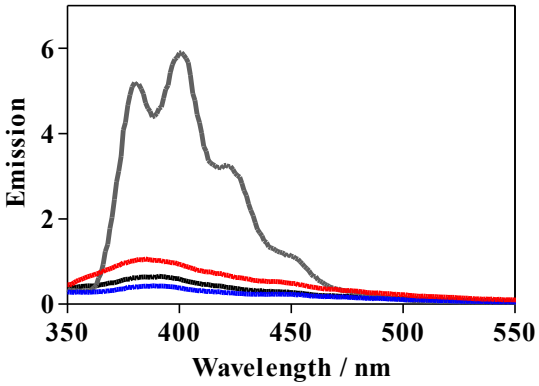

Figure 27 | Relative fluorescence emission of GFT (black), DMT-GFT (blue) and DMOR-GFT (red) within HaCaT cells (λ_{exc}: 320 nm). Anthracene (gray) was used as the reference for fluorescence quantum yield (Φ_F) measurements[145]. Fluorescence emission units are arbitrary.

Considering the intrinsic fluorescence properties mentioned above, confocal microscopy was employed to determine the intracellular colocalization of the compounds. Keratinocytes were seeded on coverslips and treated with GFT (15 µM), DMT-GFT (25 µM), and DMOR-GFT (15 µM), and subsequently labeled with both RedDot™ Far-Red Nuclear (far red fluorescence) and CellMask™ Orange Plasma membrane stains (red fluorescence). After a 1 h incubation, efficient uptake was observed in all compounds. A cytoplasmic distribution was evident in all cases, without a predominant specific localization in any organelle (Figure 28).

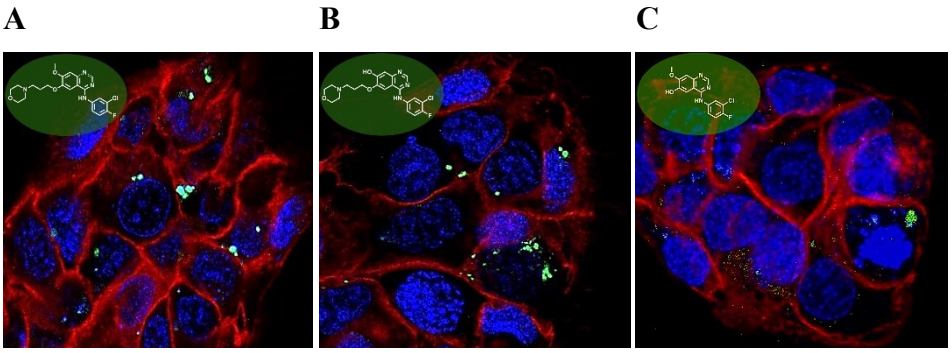

Figure 28 | Intracellular keratinocyte cells (HaCaT) colocalization of (A) GFT; (B) DMT-GFT and (C) DMOR-GFT by confocal microscopy. Cells were labeled with both RedDot™ Far-Red Nuclear and CellMask™ Orange Plasma membrane stains.

5.3.3 Lipid photoperoxidation

In the context of drug-induced phototoxicity, lipid photoperoxidation plays an important role. It is a process where ROS or free radicals induce the formation of hydroperoxides, leading to damage of cellular lipid membranes. A previous study has affirmed that several phototoxic drugs induce linoleic acid (LA) peroxidation, resulting in elevated levels of thiobarbituric acid reactive substances (TBARS)[161,162,193]. Therefore, the photosensitized lipid peroxidation properties of GFT and its metabolites were examined under UVA light radiation and in the presence of LA (1 mM). The results are presented in Figure 29. As anticipated, KP (200 μM), generated a substantial amount of TBARS, confirming its suitability as a reference for the photoinduced peroxidation of LA[161]. Conversely, neither GFT nor DMT-GFT exhibited detectable changes in TBARS levels, while irradiation with DMOR-GFT led to a significant enhancement in photosensitized lipid peroxidation comparable to the reference.

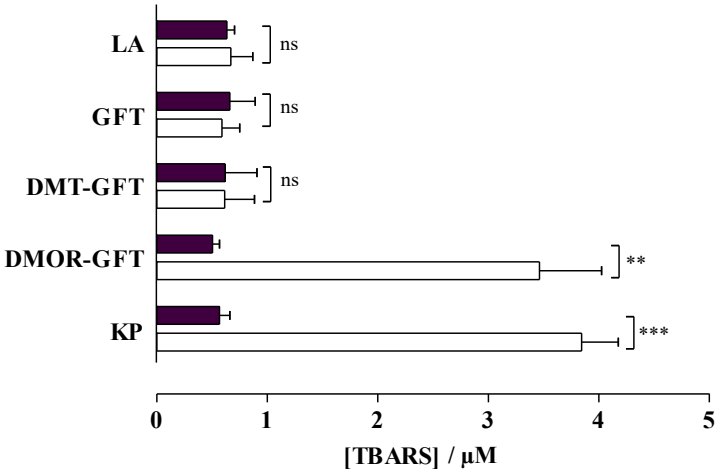

Figure 29 | Photosensitized lipid peroxidation. Linoleic acid (LA) solutions in PBS alone or with GFT/metabolites (100 µM) were kept in dark conditions (■) or exposed to a UVA dose of 15 J/cm^2 (□), and thiobarbituric acid reactive substances (TBARS) extent was monitored by TBARS assay. Ketoprofen (KP) 200 µM was selected as the standard[161]. Data represent mean ± SD of at least 4 independent experiments. Asterisks indicate significant changes in comparison with TBARS formation under darkness by the Student´s t-test (**p < 0.01, ***p < 0.001 and ns: non-significant).

As stated above, photodynamic lipid peroxidation can occur via Type I (radical-mediated) or Type II (through singlet oxygen, $^1O_2$) mechanism, where a common intermediate is the triplet excited state of the photosensitizer. For GFT and DMOR-GFT, the triplet excited states (^{3}GFT* and ^{3}DMOR−GFT*) were previously identified and characterized by their transient absorption at approximately 600 nm[194]. The ability of these species to produce $^1O_2$ was studied through time-resolved NIR emission at 1270 nm, revealing very low quantum yields ($\Phi_\Delta \leq 0.1$)[194]. This indicates minimal participation in the Type II process, suggesting the possible involvement of the Type I oxidative mechanism in DMOR-GFT-sensitized lipid peroxidation. To investigate this, ^{3}DMOR-GFT* quenching experiments were conducted using 1,4-dihydro-1,2-dimethylbenzoic (DMBA; obtained through Birch reduction synthesis) as a lipid model, which contains double allylic

hydrogens and serves as a suitable probe for studying lipid reactivity with photosensitizing drugs[141]. Employing the laser flash photolysis (LFP) technique, triplet decay traces were obtained in deareated MeCN solutions of DMOR-GFT after adding increasing quencher concentrations. As illustrated in Figure 30, DMOR-GFT triplet species was efficiently quenched by DMBA with a rate constant (kq) of approximately $1.96 \cdot 10^9$ $M^{-1}s^{-1}$. This aligns with the photoreaction between DMOR-GFT metabolite and DMBA model system proceeding through a Type I mechanism.

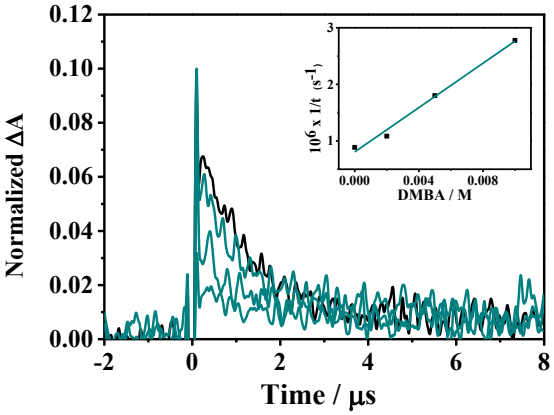

Figure 30 | Lipid peroxidation quenching experiment. Decay traces of ^{3}DMOR-GFT* alone (black) or in the presence of increasing amount of DMBA (0.1-10 mM) (cyan) in PBS solution (λ_{exc}: 355 nm). Inset: Stern-Volmer plot obtained from triplet excited state lifetime (τ_T) measurements for DMOR-GFT upon quenching with DMBA.

5.3.4 Protein photooxidation

As stated previously, the distribution of orally absorbed GFT is mainly mediated by ABCG2 and ABCB1 transporters[195]. Moreover, it is established that GFT has a high affinity for binding to proteins in human plasma, particularly human serum albumin (HSA)[184,196]. Consequently, the protein oxidation photoinduced by GFT, DMT-GFT, and DMOR-GFT was

investigated using HSA as a model. For this purpose, PBS solutions containing HSA and 100 µM of GFT, DMT-GFT, or DMOR-GFT were irradiated (5-15 J/cm^2), and the carbonyl content, serving as an early biomarker of oxidative damage, was determined through the 2,4-dinitrophenylhydrazine (DNPH) derivatization method.

As depicted in Figure 31, no significant differences were observed between irradiated and non-irradiated HSA, confirming the suitability of the selected UVA dose for this assay. In alignment with the NRU phototoxicity results, both GFT and DMOR-GFT exhibited a notable oxidative effect on HSA, with GFT demonstrating higher activity than the metabolite. It is noteworthy that DMOR-GFT, which showed the highest PIF value among the evaluated compounds, suggests a stronger correlation between phototoxic potential and lipid peroxidation rather than protein oxidation. Lastly, DMT-GFT did not induce any lipid or protein oxidative damage, aligning with the outcomes of the NRU phototoxicity assay.

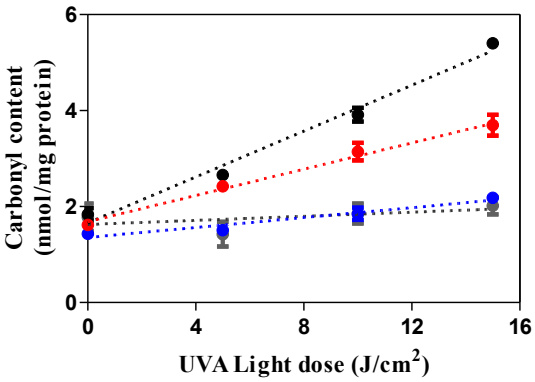

Figure 31 | Protein photooxidation. HSA solutions in PBS (5 mg/mL), alone (gray) or in the presence of 100 µM of GFT (black), DMT-GFT (blue) and DMOR-GFT (red) were irradiated with UVA dose from 5 to 15 J/cm^2. Protein oxidation was spectrophotometrically monitored by the determination of carbonyl content using 2,4-dinitrophenylhydrazine (DNPH) derivatization assay (λ: 375 nm). Data are the mean ± SD of 4 independent determinations.

5.3.5 Photogenotoxicity

The comet assay, conducted under alkaline conditions, was employed to evaluate DNA damage, photoinduced by GFT/metabolites, including single-strand (SSBs) and double-strand breaks (DSBs), as well as alkali-labile sites (ALS) in human keratinocytes. In this process, low melting point agarose embedded HaCaT cells, previously exposed to the compounds and irradiated with UVA light, were subjected to lysis followed by alkaline electrophoresis. During this process, damaged DNA migrates from the nucleus, leading to the formation of comet nucleoids and tails, which were visualized by fluorescence after staining with SYBR Gold. The percentage of DNA damage was calculated based on the classification of the images into six different classes[197].

As illustrated in Figure 32, GFT exhibited significant damage, approximately 72%, after 2 J/cm^2 of UVA light irradiation. Similarly, DMT-GFT resulted in a significant percentage of DNA damage, around 54%. In contrast, the irradiation of DMOR-GFT for 5 min did not induce DNA damage, as evidenced by the intact nucleoids compared to control cells. However, extended irradiation of DMOR-GFT up to 4 J/cm^2 led to a significant degree of DNA damage, approximately 45%.

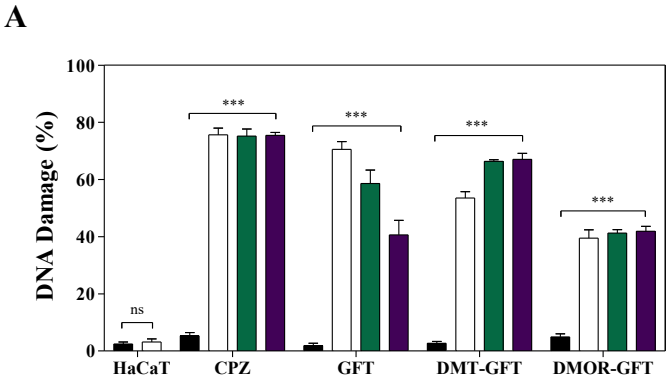

B

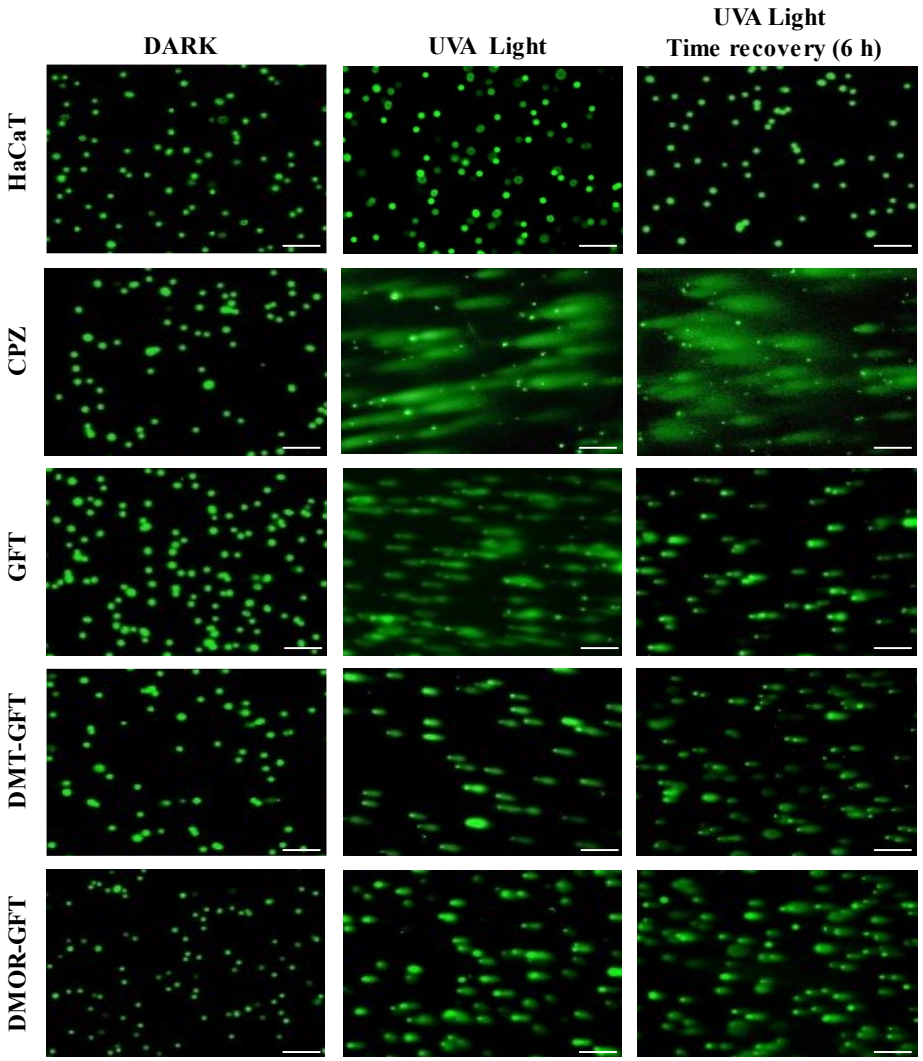

Figure 32 | (A) Photogenotoxicity and DNA damage repair. HaCaT cells were treated with 100 µM of GFT or metabolites and irradiated with UVA light at 2 J/cm^2 dose, 4 J/cm^2 for DMOR-GFT, (□) followed by 6 h (■) or 18 h (■) of cell recovery or kept in the dark (■). Data are displayed as the percentage of DNA damage calculated following the six visual scoring categories. Data represent the mean ± SD of 3 independent experiments. Asterisks indicate significant differences by the Student´s t-test (***$p < 0.001$, ns: non-significant). (B) Representative microscopy images of irradiated (UVA Light) or non-irradiated (Dark) cells non-treated or treated with GFT, DMT-GFT or DMOR-GFT and followed by 6 h of cell recovery (UVA Light + Time recovery 6 h). Chlorpromazine (CPZ) at 10 µM served as the positive control for photogenotoxicity. Scale bar: 250 µm.

In general, cells have developed various repair mechanisms to mitigate DNA damage. However, if these repair processes are flawed, DNA lesions may persist, leading to mutations that can potentially lead to carcinogenesis. To investigate the ability of keratinocyte cells to repair nuclear DNA photodamage induced by GFT and its metabolites following UVA light exposure, a complementary experiment was conducted. In summary, HaCaT cells containing GFT, DMT-GFT, or DMOR-GFT were subjected to irradiation and then underwent comet assay with two different incubation times (6 and 18 h) before cell lysis. Subsequently, the extent of DNA damage was assessed, as mentioned earlier. Notably, cells treated with GFT exhibited significant recovery from the initial DNA damage, although some residual damage persisted even after an 18 h recovery period (41%) (refer to Figure 32A). In contrast, this pattern was not observed in cells treated with DMT-GFT or DMOR-GFT, as they maintained the initial DNA damage without significant recovery.

5.3.6 Cell death

Apoptosis, commonly known as programmed cell death, plays a pivotal role in regulating the cellular lifecycle. Nevertheless, excessive activation of this process can lead to critical diseases. The apoptosis event typically involves the activation of zymogens, which are recognized as the precursors of the well-known caspase enzymes[170]. Upon receiving apoptotic signals, caspases are activated and, through their proteolytic activity, initiate protein digestion, inducing cell death[198]. Among the key effector caspases in mammals, caspase-3, -6, and -7 hold prominence, with caspase-3 being most frequently involved in apoptosis[170].

In light of these considerations, the impact of GFT and its metabolites on apoptosis upon UVA light exposure was investigated in HaCaT cells using the Apo-ONE homogeneous caspase-3/7 assay. This kit contains a profluorescent Rhodamine 110 (Z-DEVD-R110) substrate for both caspase-3 and caspase-7. Thus, following the cleavage and release of the DEVD peptide by caspase-3/7, Rhodamine 110 becomes intensely fluorescent. Caspase-3/7 activity was monitored by fluorescence, representing a relative change indicative of the level of apoptosis activation within the cells. As demonstrated in Figure 33A and Figure 33C, both GFT and DMOR-GFT induced a concentration-dependent activation of caspase-3/7 after UVA light exposure, particularly at concentrations close to the IC50 values (5 and 3 μM, respectively). In the case of DMT-GFT (Figure 33B), caspase-3/7 activity was similar between the concentration of 2.5 μM and the concentration corresponding to IC50 (5 μM).

L-Lactate dehydrogenase (LDH) is a stable cytoplasmic enzyme catalyzing the conversion of lactate to pyruvate during glycolysis, involving the conversion of NAD+ to NADH[171]. The LDH-release assay is employed to assess plasma membrane damage, as the permeabilization of the membrane causes the leakage of this enzyme out of the cells[103]. While the measurement of LDH release is commonly considered an indicator for necrosis, it is noteworthy that the leakage of LDH may also be involved in apoptotic events in late stages[172]. As depicted in Figure 33D and Figure 33F, a significant percentage of LDH release was observed for both GFT and DMOR-GFT metabolite at concentrations near the IC50, respectively. However, compared to caspase activity, the increase in LDH release upon UVA exposure was less notable. Surprisingly, DMT-GFT (Figure 33E) did not exhibit any effect on LDH release, maintaining levels comparable to unexposed keratinocytes.

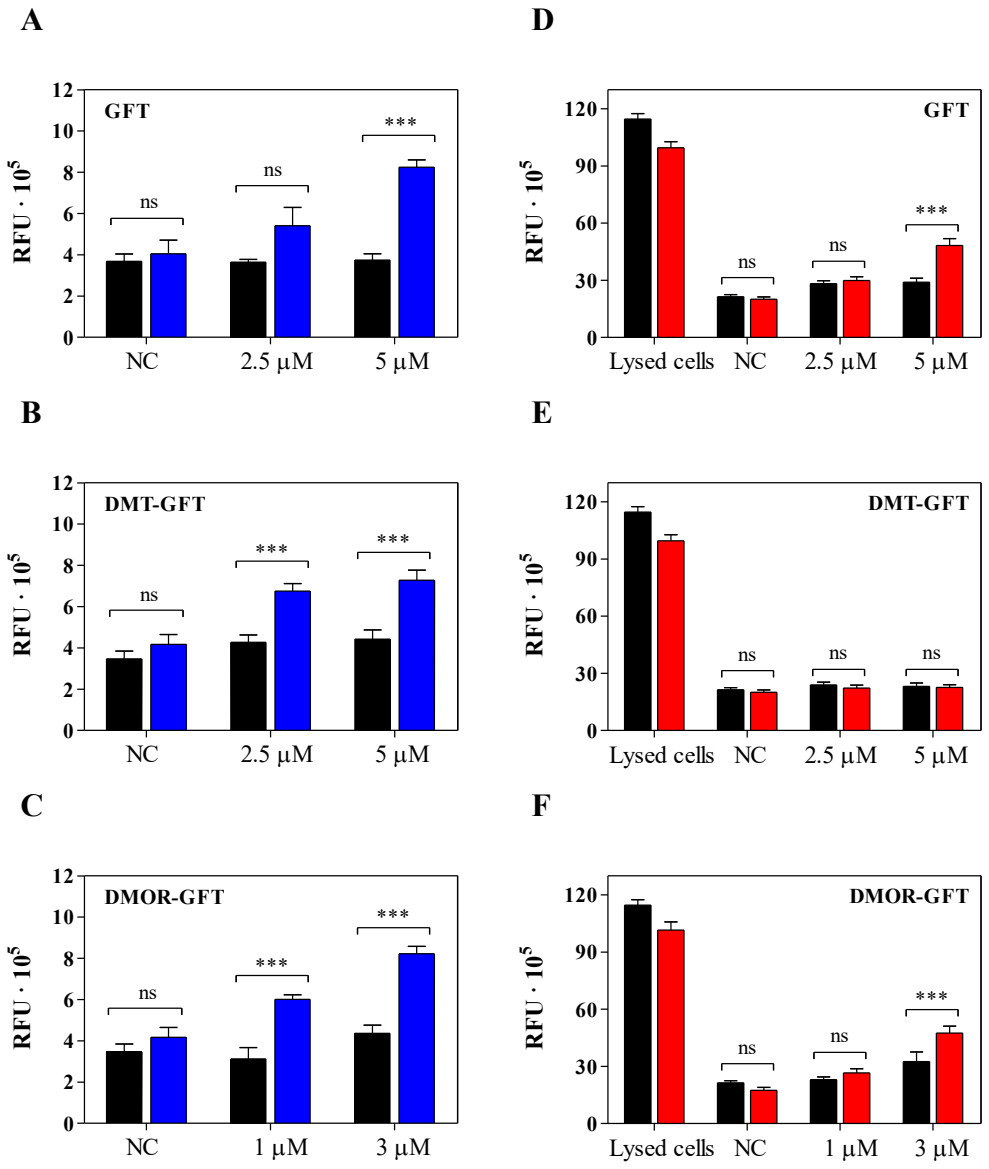

Figure 33 | (A-C) The effect of GFT and its metabolites on caspase-3/7 activity in HaCaT cells before (■) and after UVA light exposure at 5 J/cm^2 dose (■). Values are represented as relative fluorescence units (RFU). (D-F) Lactate dehydrogenase (LDH) release in HaCaT cells treated with GFT and metabolites before (■) and after UVA light exposure at 5 J/cm^2 dose (■). Data represent the mean ± SD of 3 independent experiments. Asterisks indicate significant differences by the Student´s t-test (***$p < 0.001$, ns: non-significant).

5.4 Conclusions

The Phase I biotransformation of GFT results in the formation of reactive metabolites, causing significant modifications in the quinazoline chromophore and altering its light-absorbing properties. In this study, the photobehavior of GFT and its reactive metabolites (DMT-GFT and DMOR-GFT) was investigated in both biomolecular targets (lipids, proteins, and DNA) and in cellular environment (human keratinocytes).

The metabolite DMOR-GFT exhibited markedly higher phototoxicity to cells than the parent drug in NRU *in vitro* studies, while DMT-GFT showed much lower phototoxicity. In the photosensitized lipid peroxidation assay, only DMOR-GFT demonstrated clear effectiveness in the TBARS assay, indicating the involvement of a Type I mechanism supported by the weak production of singlet oxygen and efficient quenching of the triplet excited state by a lipid model. Protein photooxidation, monitored by carbonyl content measurements, was primarily mediated by GFT and, to a lesser extent, by DMOR-GFT, with nearly undetectable protein oxidation associated with DMT-GFT. This reaction was previously explained by initial electron transfer from oxidizable amino acid residues to the quinazoline moiety. Damage to cellular DNA, as revealed by the comet assay, occurred upon irradiation in the presence of GFT and its two metabolites. Interestingly, following GFT, DMT-GFT was the most efficient photosensitizer in this case, and the induced DNA damage was hardly repaired by the cells after several hours.

Overall, the observed cellular phototoxicity can be correlated with the results from the mechanistic studies. DMOR-GFT, displaying the highest phototoxicity, showed the most remarkable lipid photoperoxidation and significant activity in protein oxidation and DNA damage studies.

Conversely, DMT-GFT, the weakest phototoxic, exhibited high photogenotoxicity in the comet assay. The parent drug GFT constituted an intermediate case. Cellular phototoxicity seems to be more related to the photooxidation of membrane components through a Type I (radical-mediated) mechanism. These findings underscore that the biotransformation of the anticancer drug GFT leads to a dual impact on cellular photo(gen)toxicity. In summary, GFT illustrated a scenario where the balance between the generation of phototoxic and non-phototoxic Phase I metabolites should be thoroughly investigated during drug development.

CHAPTER 6 Axitinib

6.1 Introduction

Axitinib, pharmacologically available as *(E)*-AXT isomer (Inylta®; Pfizer), is the latest agent approved by the FDA for the treatment of advanced renal cell carcinoma (RCC). Belongs to the second generation of TKIs with demonstrated activity against various solid tumors in addition to RCC, including metastatic melanoma, thyroid cancer, and advanced non-small cell lung cancer. AXT serves as a potent and highly selective inhibitor of VEGFR tyrosine kinase 1, 2 and 3. Additionally, at nanomolar concentrations, AXT also inhibits PDGFRα/β and c-Kit[199,200].

AXT has a short effective plasma half-life (range 2.5–6.1 h) and is highly bound (>99%) to human plasma proteins with preferential binding to albumin. Elimination of AXT involves hepatic metabolism, primarily mediated by cytochrome P450 CYP3A4, with the participation, to a lesser extent, from CYP1A2, CYP2C19, uridine diphosphate glucuronosyl-transferase (UGT) 1A1, and the drug transporter P-glycoprotein. Finally, AXT is eliminated mainly through hepatobiliary excretion, while the urinary excretion is negligible[201,202].

Although preclinical and clinical studies have established the important role of AXT in the management of RCC, aiming to improve efficacy and minimize toxicity, important dose-limiting toxicities such as hypertension, hemoptysis, and stomatitis have been described[203–205]. Despite the novelty of this TKI, there have been some unexpected clinical cases reporting skin eruptions after 5-months AXT therapy[206]. However, consistent with previously conducted *in vitro* and *in vivo* phototoxicity studies, AXT exhibited a non-significant potential for phototoxicity in the 3T3 fibroblast NRU assay (150 μg/mL)[207].

Structurally, AXT is an indazole derivative with photosensitive stilbene-like moiety that allows for *E/Z* isomerization (Figure 34). The isomerization of AXT in solution under light conditions has been briefly reported[208–210]. Surprisingly, only a few studies evaluated the pharmacological properties of *(Z)*-AXT isomer through VEGFR2 kinase activity profiling, aiming to develop a tunable pro-drug for therapeutic applications[211,212]. These studies showed that the photoswitching of AXT isomers could be controlled to administer AXT as the *Z*-isomer, which is less active compared to *(E)*-AXT. However, further studies on the photopharmacology of this TKI remain to be conducted in the future.

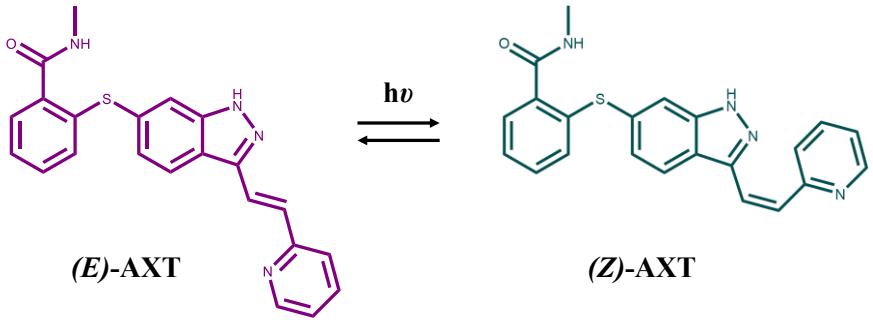

Figure 34 | Photoisomerization of axitinib (AXT).

Isomerism holds significant importance in clinical pharmacology and pharmacotherapeutics, especially concerning stereoisomers. Variations like enantiomers and diastereomers (cis/trans) display distinct pharmacokinetic and pharmacodynamic properties, influencing drug effectiveness and safety profiles. For example, *E*-isomers of benzhydro[f]quinoline *N*-alkyl derivatives demonstrated higher potency than their *Z*-isomers in inhibiting cardioaccelerator nerve stimulation responses[213]. A similar case involves acitretin, which has been experimentally proven to undergo *in vivo*

isomerization. Indeed, preliminary experiments in mice indicated that *(Z)*-acitretin is a product of "*in vivo* photoconversion" after exposure to UV light. However, in humans, enzymatic metabolism was likely responsible for this conversion, as the limited exposure to natural light would probably be insufficient to induce photoconversion in the bloodstream. The result is a compound with less pharmacological activity and reduced adverse events[214].

Similarly, photostability studies conducted by the European Medicines Agency, in accordance with the harmonized guidelines, have determined that AXT is a photolabile drug[207]. Notably, during the development phase, improvement was made to the drug coating system to provide better protection against light. Despite these efforts, the specialized literature lacks comprehensive coverage of free drug photodegradation, specifically in the understanding of the photokinetics of the bioactive drug, *(E)*-AXT. To address this gap, our study aimed to investigate the photophysical properties of *(E)*-AXT in various media and study the mechanisms underlying the phototoxicity associated with AXT therapy. In this context, considering that AXT has been demonstrated to be phototoxic (Chapter 4), it is noteworthy to assess the photobehavior of AXT in both its isomeric forms to identify which one is responsible for its phototoxicity. Additionally, a comprehensive analysis of the photophysical properties of this photoswitchable drug would provide more insights into the mechanisms underlying its phototoxic profile.

6.2 Experimental procedures

Cell culture conditions and spectroscopic measurements were carried out in accordance with the procedures outlined in Chapter 3.

6.2.1 Neutral red uptake (NRU) phototoxicity test

Following the protocol described in Chapter 3, NRU phototoxicity assay was performed in HaCaT cells treated with AXT *E/Z*-isomers at a concentration ranging from 2.5 to 500 μM.

6.2.2 Photoinduced protein oxidation assay

The potential of AXT isomers to induce protein photooxidation was assessed by monitoring the carbonylation using the 2,4-dinitrophenylhydrazine (DNPH) derivatization method (see Chapter 3). In this case, HSA samples containing AXT at two concentrations, 15 or 50 μM, were irradiated with a UVA light dose ranging from 5 to 15 J/cm^2.

6.2.3 Single cell gel electrophoresis comet assay

The comet assay (single-cell gel electrophoresis) was conducted according to the procedures detailed in Chapter 3. Thus, HaCaT cells were treated with 100 μM of *(E)*-AXT and, subsequently, irradiated under UVA light (5 J/cm^2).

6.2.4 Photoinduced phosphorylation of γ-H2AX

The detection of γ-H2AX foci in Bj-hTERT fibroblasts through immunostaining an expansion microscopy was assessed following the procedures detailed in Chapter 3. Therefore, fibroblasts were treated with *(E)*-AXT at a concentration of 50 μM and exposed to a UVA light dose of 5 J/cm^2. Subsequently, the cells underwent isotropic expansion, and immunostaining was conducted using anti-H2AX-ser139 antibody, along with anti-α-tubulin and DAPI.

6.3 Results and discussion

6.3.1 Photophysical properties

To date, several aspects of photodegradation remain inadequately addressed during drug development studies. Notably, the photokinetics of AXT have not been comprehensively investigated. In this context, this study aims to investigate specific photophysical properties, such as absorption spectroscopy, of this anti-cancer drug in different media. The anticipated outcomes may provide insights into the mechanisms underlying the evidenced photosensitivity associated with AXT therapy.

Photostability of *(E)*-AXT

Absorption spectra of *(E)*-AXT were recorded in various solvents, such as PBS, MeOH, EtOH and MeCN. Thus, *(E)*-AXT exhibits an absorption band in the wavelength range of 280 to 385 nm, with a maximum at approximately 332 nm (Figure 35). Interestingly, a less intense shoulder was detected within the wavelength range of 380 to 400 nm when AXT was dissolved in EtOH and, to a lesser extent, in MeCN.

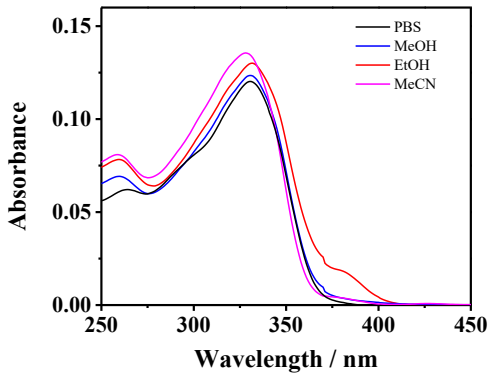

Figure 35 | Absorption spectra of axitinib (AXT). Solutions containing AXT 4 µM were prepared in PBS (black), MeOH (blue), EtOH (red) and MeCN (magenta).

Additionally, steady state photolysis of *(E)*-AXT was monitored in PBS solution, in the presence of calf thymus DNA 1:1 (ctDNA) or HSA 1:1 using UVA lamps (λ_{exc}: 355nm), with the samples being irradiated for a duration of up to 1 h. Moreover, MeCN was also employed in this experiment to mimic the lipophilic environment present in the cellular milieu. As depicted in the Figure 36A, upon irradiation in PBS, *(E)*-AXT underwent a photodegradation process without exhibiting changes in the maximum, indicating the absence of photoproduct formation. Contrarily, in MeCN, a clear isosbestic point emerges at 350 nm, guiding toward the formation of a single photoproduct with a UV spectrum characterized by multiple maxima. Specifically, the intensification of the shoulder at 380 nm, previously observed in the non-irradiated drug, was indeed pronounced (Figure 36B).

Similar to *(E)*-AXT in aqueous solution, the incorporation of ctDNA also led to drug photodegradation, with the absence of new maximum observed after UVA radiation (Figure 36C). Surprisingly, the *(E)*-AXT, when in the presence of a 1:1 HSA, demonstrated a photobehavior like that observed in MeCN solutions. Notably, this photoprocess occurred more rapidly, without the possibility for identification of an isosbestic point (Figure 36D).

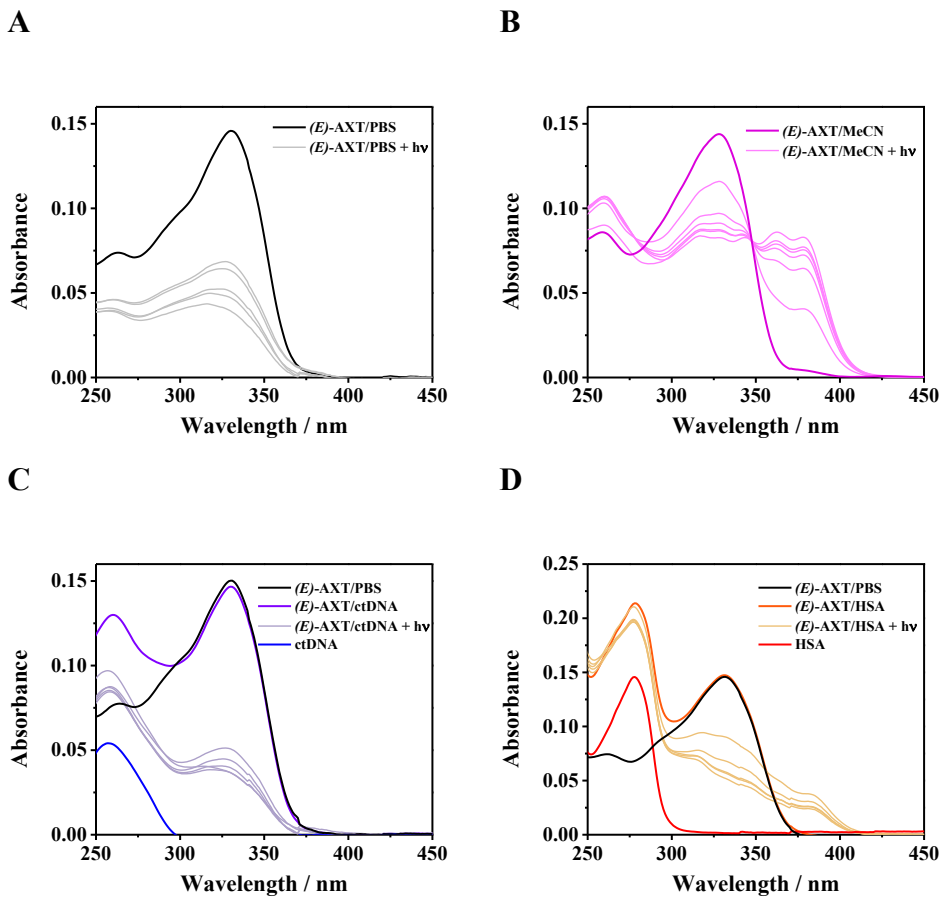

Figure 36 | Photostability of *(E)*-AXT upon UVA radiation. Absorption spectra of *(E)*-AXT in PBS (A), MeCN (B), or in the presence of 1:1 ctDNA (C) or 1:1 HSA (D), before and after irradiation with UVA lamp at 355 nm (hυ).

Photostability of *(Z)*-AXT

Taking into consideration that *(E)*-AXT photostability is dependent on the medium, the photobehavior of the *(Z)*-AXT isomer was also analyzed in various media. In Figure 37A, *(Z)*-AXT in PBS solution underwent spectrophotometric changes upon UVA exposure. A right shift in the maximum was observed, leading to a value of 332 nm, characteristic of the *E*-isomer of the drug. Similar results were obtained after the addition of

ctDNA 1:1 (Figure 37B). Surprisingly, *(Z)*-AXT demonstrated to be more photostable in the presence of a 1:1 HSA, with an absorption band that aligns with the one observed for the irradiated *(E)*-AXT/HSA complex (Figure 37C).

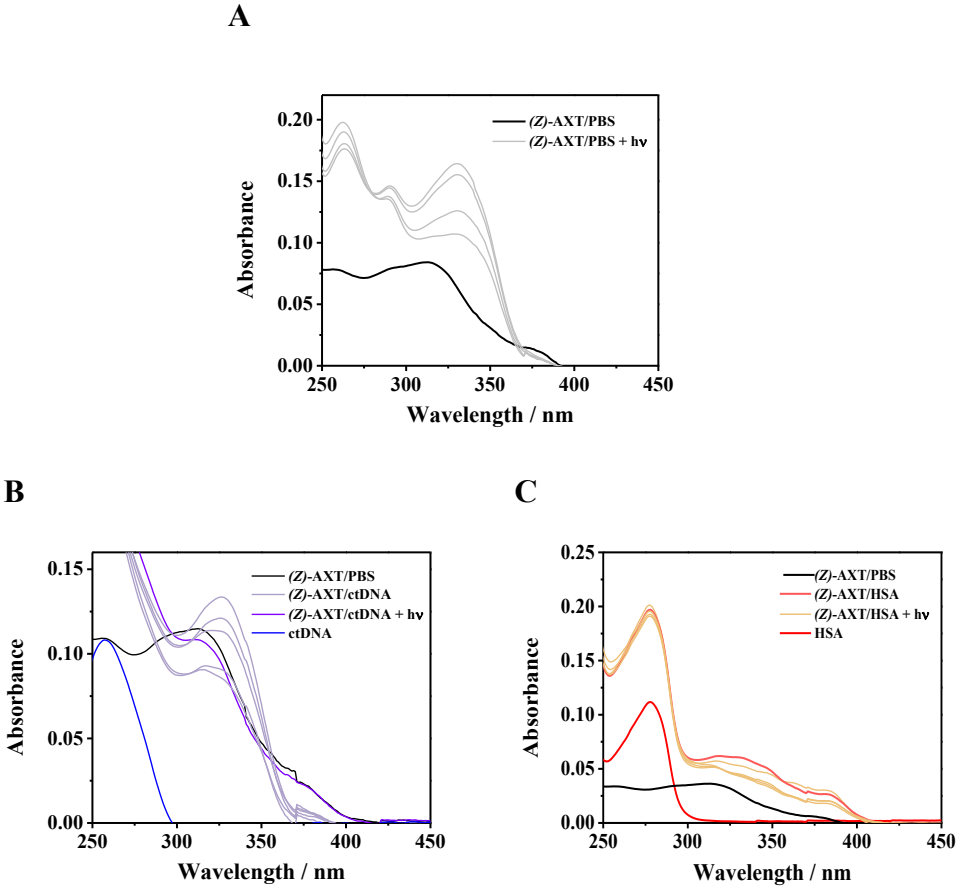

Figure 37 | Photostability of *(Z)*-AXT upon UVA radiation. Absorption spectra of *(Z)*-AXT in PBS (A) or in the presence of 1:1 ctDNA (B) or 1:1 HSA (C), before and after irradiation with UVA lamp at 355 nm (hυ).

In brief, *(E)*-AXT is a photolabile drug susceptible to isomerization in aprotic or lipophilic media such as EtOH, MeCN, and particularly within HSA solution. Surprisingly, *(Z)*-AXT exhibits an inverse photoisomerization in

aqueous media such as PBS. However, a hydrophobic environment, specifically HSA protein, provides a more appropriate environment that stabilizes the *Z*-isomer blocking the isomerization back to *(E)*-AXT, which is more stable in aqueous media. This phenomenon can be molecularly elucidated through the previously described tautomerism occurring in *(Z)*-AXT, where *(Z)*-2H-AXT is favored over *(Z)*-1H-AXT in the ground state due to the intramolecular hydrogen bond (Scheme 5)[215]. Therefore, in aprotic media, intramolecular hydrogen bonding takes place, while protic solvents form intermolecular hydrogen bonds with the drug, stabilizing the *(E)*-AXT over the *Z*-isomer.

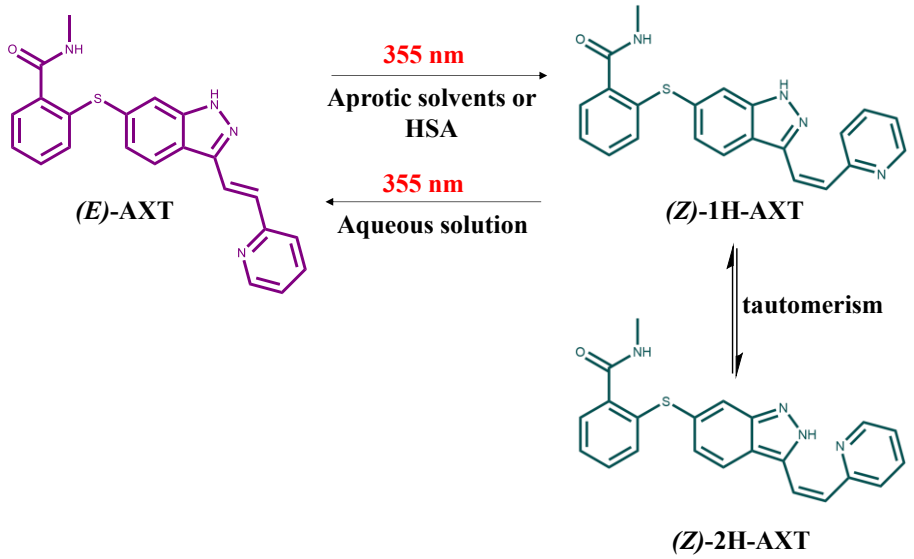

Scheme 5 | Photoinduced *E–Z* isomerization of AXT. Formation of *(Z)*-AXT and the tautomerism from 1H- to 2H-indazole annular AXT in aprotic solvents/HSA (λ_{exc}: 355 nm). In aqueous solution, irradiation of *(Z)*-AXT (λ_{exc}: 355 nm) leads to inverse *E–Z* isomerization.

6.3.2 Phototoxicity of axitinib isomers

Background studies have identified numerous distinctions in the binding properties of AXT isomers to the VEGFR2 pocket, leading to significant

pharmacological variations. Therefore, it is anticipated that different behavior in terms of phototoxic potential toward keratinocyte cells upon UVA exposure will be observed. Indeed, the previous data results suggested that the preferred isomer within a protein-rich environment, such as cellular components, is *(Z)*-AXT.

Neutral red uptake assay

The preliminary assessment of the potential phototoxic properties of the commercially available AXT (*E*-isomer) indicated that AXT is a phototoxic drug with a PIF value of approximately 37 (see Chapter 4). However, as depicted in Figure 38 and presented in Table 10, non-photoexposed HaCaT cells exhibited no reduction in cell viability, even at the highest concentration of 500 µM. Consequently, it was not feasible to precisely determine the IC50 in dark conditions. Therefore, the provided PIF value is an estimation, considering the highest test concentration (500 µM) as the IC50. Contrarily, *(Z)*-AXT did exhibit cytotoxic effects toward keratinocyte cells in the absence of UVA light, demonstrating an IC50 value of approximately 81 µM. Interestingly, following exposure to radiation, the IC50 decreased to a value of 13.9, close to that of *E*-isomer (IC50 = 13.4). Consequently, although the IC50 under light conditions is similar for both isomers, the cytotoxicity of the *Z*-isomer led to a PIF value lower than that of the *E*-isomer, which was *ca.* 6.

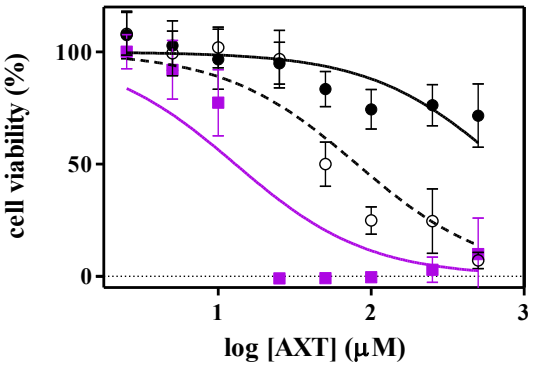

Figure 38 | Cell viability NRU dose-response curves. HaCaT cells were irradiated with UVA light (5 J/cm^2) (-■-) or maintained in dark conditions after treatment with *(E)*-AXT (-●-) or *(Z)*-AXT (-○-). Data represent the mean ± SD from 4 independent experiments.

Table 10 | HaCaT NRU phototoxicity of AXT isomers[a].

Compound	IC_{50} Dark (µM)	IC_{50} UVA Light (µM)	Photoirritant factor (PIF)[b]
CPZ	80 ± 17	4 ± 0.9	20
(E)-AXT	>500	13.4 ± 2	37
(Z)-AXT	81 ± 9	13.9 ± 1.7	6
SDS	133 ± 31	136 ± 23	1

[a] Data represent the mean ± SD from 4 independent dose-response curves. CPZ and SDS were selected as positive and negative controls of phototoxicity, respectively.
[b] According to the OECD 432 Guide[152], PIF < 2 means "no phototoxicity", 2 < PIF < 5 means "probable phototoxicity" and PIF > 5 means "phototoxicity".

Collectively, both photophysical and phototoxic properties of AXT suggest that the phototoxicity of this drug is induced through both direct and indirect mechanisms. On one hand, the direct mechanism is illustrated by the decrease in cell viability of HaCaT cells treated with *(Z)*-AXT upon UVA radiation. On the other hand, the indirect mechanism of phototoxicity is exhibited through the formation upon photoconversion of the *Z*-isomer, which itself

exhibits cytotoxicity toward keratinocyte cells. Thus, it confirms that the contributor to the phototoxicity of AXT is, indeed, the *Z*-isomer.

Protein photooxidation

The assessment of AXT phototoxicity raises the possibility that the *(Z)*-AXT might be the responsible isomer. Consequently, a carbonylation assay was conducted to clarify whether AXT has the potential to induce the oxidation of HSA protein and to discern differences between the isomers that could determine which one is involved in the photooxidation activity. As illustrated in Figure 39, comparable dose-dependent carbonyl content was detected for both isomers, reaching a value of approximately 3 nmol at a UVA dose of 15 J/cm^2. Therefore, given the photophysical behavior of AXT in the presence of HSA, where *(Z)*-AXT was identified as the preferred isomer, the outcome for this carbonylation assay was as expected. The similarity in the carbonyl content between both isomers indicates that both results correspond to the *Z*-isomer.

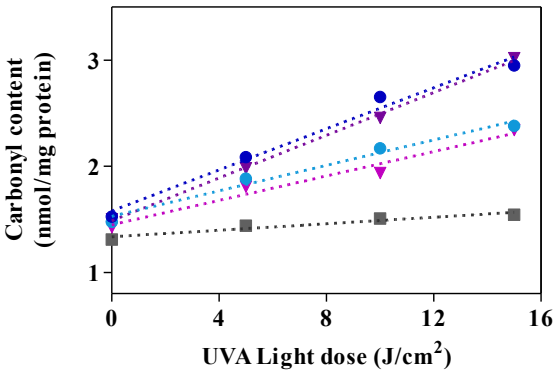

Figure 39 | Protein photooxidation. HSA solutions in PBS (5 mg/mL), alone (gray) or in the presence of 15 µM (light violet) and 50 µM (dark violet) of *(E)*-AXT, or *(Z)*-AXT 15 µM (light blue) and 50 µM (dark blue) and were irradiated with UVA dose from 5 to 15 J/cm^2. Protein oxidation was spectrophotometrically monitored by the determination of carbonyl content using 2,4-dinitrophenylhydrazine (DNPH) derivatization assay (λ: 375 nm). Data are the mean ± SD of 4 independent experiments.

6.3.3 Photogenotoxicity

Having confirmed the capability of *(E)*-AXT to induce photooxidation in proteins, the evaluation was extended to another cellular biomolecule, DNA, which could potentially be a target for *(E)*-AXT phototoxicity. Surprisingly, *(E)*-AXT did not cause photodamage to DNA, as evidenced by the alkaline comet assay, even at a concentration of 100 µM and a UVA dose of 5 J/cm² (Figure 40). Therefore, *(E)*-AXT was a suitable candidate for assessing nuclear DNA photodamage through the detection of phosphorylated γ-H2AX via immunostaining and expansion microscopy (ExM).

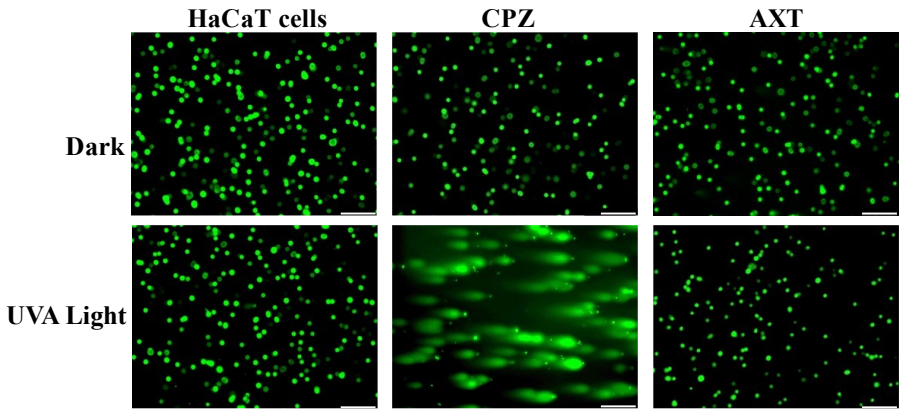

Figure 40 | Alkaline comet assay experiment. HaCaT cells were treated with *(E)*-AXT (100 µM) and were then either kept in the dark or exposed to UVA light at a dose of 5 J/cm². Chlorpromazine (CPZ) at 5 µM served as the positive control for photogenotoxicity. Scale bar: 250 µm. Images are representative of 3 independent experiments.

DNA damage assessed by γ-H2AX immunostaining

Recently, there has been a rise in the use of immunofluorescence-based assays for detecting DSBs, allowing the visualization of specific nuclear foci formed due to H2AX histone phosphorylation. These methods have proven to be highly sensitive and reliable. The preferred approach for DSB detection involves quantifying individual γ-H2AX foci through fluorescence microscopy, as each break corresponds to a γ-H2AX focus. This method,

based on γ-H2AX foci, is over 100 times more sensitive compared to other DSBs detection methods. Moreover, unlike the comet assay, the analysis of γ-H2AX foci does not require lysis or other potentially harmful procedures. Consequently, the discrete nuclear foci resulting from H2AX phosphorylation are now widely adopted as a quantitative indicator of individual DSBs[92,93,216].

In this context, Bj-hTERT fibroblasts were treated with *(E)*-AXT at a concentration of 50 μM and exposed to a UVA light dose of 5 J/cm^2. Subsequently, the samples underwent isotropic expansion, and immunostaining against γ-H2AX was conducted using anti-H2AX-ser139 antibody. Additionally, anti-α-tubulin and DAPI staining were also performed. As displayed in Figure 41, hydrogel-embedded control samples were successfully expanded reaching an estimated expansion factor (E.F) of approximately 4, calculated as a ratio between nuclei size after and before expansion (Table 11).

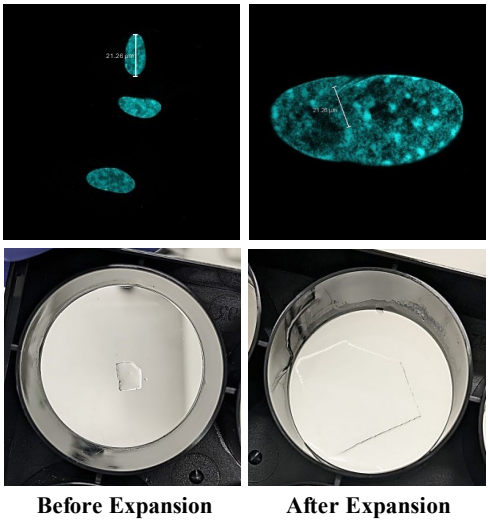

Figure 41 | Expansion microscopy. Top: Untreated Bj-hTERT fibroblast nuclei stained by DAPI and imaged under confocal microscopy before and after expansion. The scale bar is 21.26 μm, and the images are representative of 4 independent experiments. Bottom: Images of a gel cut in a 6-well plate before and after expansion.

Table 11| Expansion microscopy.

	Nuclei size (µm)	
	Before expansion	**After expansion**
1	23.36	105.24
2	21.72	75.27
3	20.74	83.48
4	23.12	90.37
5	20.38	93.14
6	21.14	89.50
7	20.72	79.97
8	22.68	93.58
9	23.36	90.13
10	21.85	88.33

Nuclei size data of Bj-hTERT fibroblasts before and after expansion.

Given that expansion microscopy (ExM) was successfully applied to enhance the optical resolution of Bj-hTERT cells nuclei, the sensitivity of γ-H2AX foci detection through immunolabeling was further optimized by this technique. In fact, as depicted in the Figure 42A, phosphorylated γ-H2AX foci were barley detected in non-expanded AXT-treated samples, making the quantification of individual foci challenging. Contrary, as shown in Figure 42B, ExM-processed samples exhibited individually quantifiable γ-H2AX foci. Therefore, the combination of ExM, indirect immunolabeling of phosphorylated γ-H2AX, and confocal microscopy proved effective in offering detailed information about the expression of DSB-associated histones in DNA photodamage.

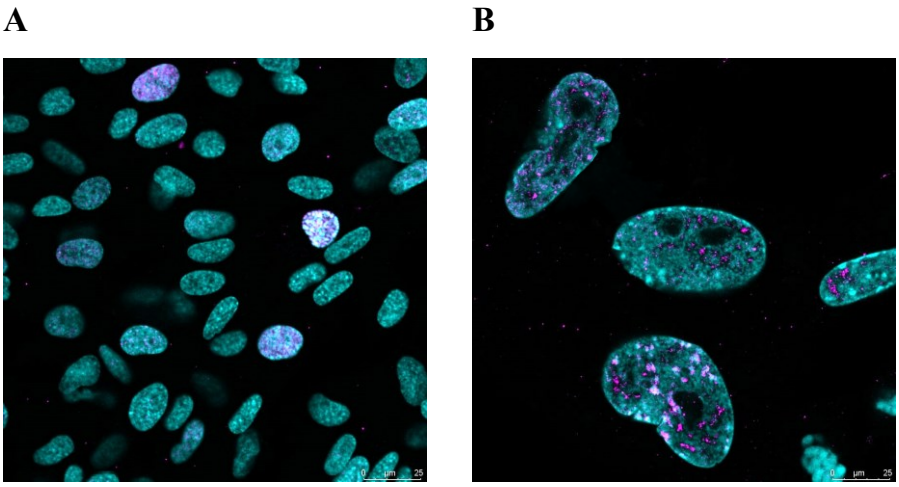

Figure 42 | Detection of phosphorylated H2AX histone after expansion microscopy. Fibroblast cells (Bj-hTERT) were treated with *(E)*-AXT 50 µM followed by 5 J/cm^2 UVA radiation. Then samples were fixed and subjected to immunolabelling using Rabbit anti-H2AX-ser139 (1 µg/mL) and secondary antibody Goat Anti-Rabbit Alexa Fluor 488, 1:500. Then cells were further stained with DAPI (cyan) and imaged by confocal microscopy either before (A) or after expansion (B). Images are representative of 4 independent experiments. Scale bar: 25 µm.

According to the previous results, *(E)*-AXT treated fibroblast cells were subjected to UVA light exposure of 5 J/cm^2 dose and immunostained before ExM and visualization under confocal microscope. As illustrated in Figure 43, numerous γ-H2AX foci were observed only within the nucleus of photoexposed Bj-hTERT cells. In contrast, non-irradiated cells exhibited only a minimal formation of γ-H2AX foci, highlighting the specificity of this DNA damage response to drug photosensitization. In summary, this outcome confirms that phosphorylated γ-H2AX immunostaining is a sensitive and reliable method in monitoring the formation of DSBs. Hence, this method is a valuable alternative to the traditional gel electrophoresis approach (comet assay), enhancing the accuracy and detail in studying drug photoinduced DNA damage.

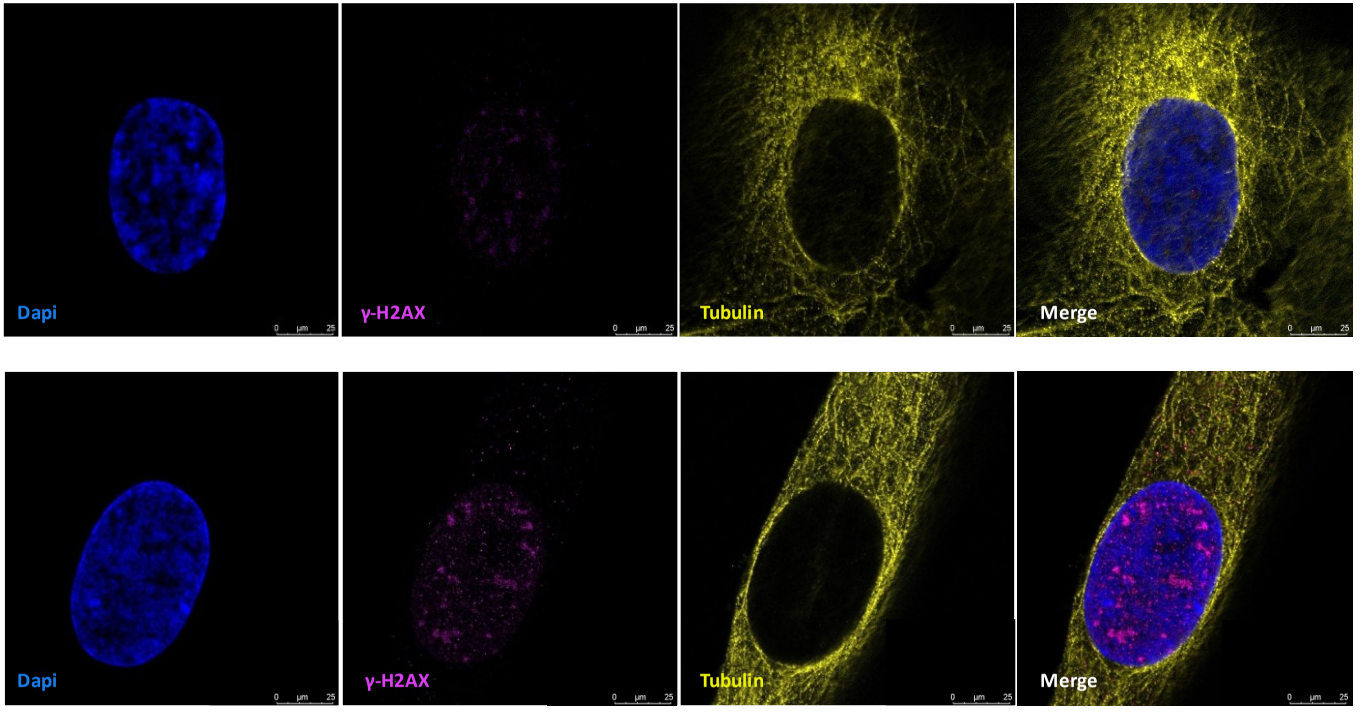

Figure 43 | Immunofluorescence staining of γ-H2AX. Bj-hTERT fibroblasts were exposed to *(E)*-AXT 50 µM and kept either in darkness of irradiated with UVA light (5 J/cm^2). Fixed cells were immunostained with Rabbit anti-H2AX-ser139 (1 µg/mL) and secondary antibody Goat Anti-Rabbit Alexa Fluor 488, 1:500 (magenta); Mouse Anti-α-tubulin (2 µg/mL) and secondary antibody Goat anti-Mouse Rhodamine (yellow). Then cells were further stained with DAPI (blue) and imaged by confocal microscopy. Images are representative of 4 independent experiments. Expansion factor was approximately 4. Scale bar: 25 µm

6.4 Conclusions

Photolysis experiments revealed that *(E)*-AXT undergoes photodegradation in aqueous media, with a tendency for isomerization to *(Z)*-AXT in a lipophilic environment. This isomerization process was notably accelerated in the presence of equimolar HSA protein. Additionally, the photostability of the commercially available *(Z)*-AXT isomer also highlighted its dependence on the medium. In the presence of HSA, *(Z)*-AXT exhibited enhanced photostability, while aqueous media favored the isomerization back to *(E)*-AXT. In summary, *(Z)*-AXT emerges as the preferred isomer in a lipophilic or aprotic environment, especially in the presence of proteins such as HSA, more likely attributed to the formation of an intramolecular hydrogen bond leading to the 2H-AXT tautomer.

Given this context, the NRU assay assessment revealed two primary mechanisms underlying AXT phototoxicity on keratinocyte cells. Firstly, the transformation of the initially non-cytotoxic *(E)*-AXT into the cytotoxic *(Z)*-AXT upon UVA exposure. Secondly, the inherent phototoxicity exhibited by *(Z)*-AXT after irradiation. The overall outcome suggests that AXT, initially perceived as a safe kinase inhibitor based on preclinical safety data regarding skin adverse reactions, can alter its toxicity profile upon photoconversion to the *Z*-isomer.

Certainly, carbonylation assays indicated comparable levels of protein photooxidation for both *(E)*-AXT and *(Z)*-AXT. Considering the enhanced stability of the latter in the presence of HSA, this assay confirms that the significant photooxidation activity observed against proteins is attributed to the *Z*-isomer. Nevertheless, AXT did not induce photodamage to DNA in the

alkaline comet assay. However, immunostaining and expansion microscopy revealed the formation of phosphorylated γ-H2AX foci, indicating DNA DSBs photoinduced by AXT.

In summary, while commercially available as *(E)*-AXT, AXT reveals an interesting photochromic system that undergoes a shift upon exposure to UVA light. The previously undisclosed biological behavior of the *Z*-isomer implies that, despite its reduced activity in the *in vitro* VEGFR2 kinase assay, it exhibits a novel profile of toxicities, as elucidated in this study. Indeed, the *Z*-isomer is more likely to be responsible for the observed phototoxic behavior within keratinocyte cells, owing to its heightened affinity for macromolecules, particularly proteins. Overall, these findings underscore the necessity for an in-depth understanding of AXT photobiological properties and offer valuable insights for improving its clinical applications, acknowledging the complexity introduced by its photochromic behavior and isomeric nature.

CHAPTER 7 Dasatinib

7.1 Introduction

Dasatinib, DAS (Sprycel®; Bristol-Myers Squibb) is a thiazole carboximide derivative (Figure 44) approved by the FDA in 2006 as the first and only second-generation tyrosine kinase inhibitor designed for the treatment of pediatric patients with Philadelphia chromosome-positive acute lymphoblastic leukemia. Additionally, DAS is indicated in the management of newly diagnosed chronic myeloid leukemia (CML) during the chronic, accelerated, or blastic phase, particularly in cases where there is resistance or intolerance to prior treatments, including imatinib[217,218].

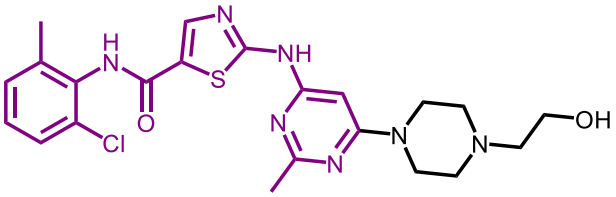

Figure 44 | Chemical structure of dasatinib (DAS). Chromophore group is colored in violet.

While DAS was initially identified as a promising treatment for chronic myelogenous leukemia with activated Bcr-Abl kinase, it also exhibited efficacy against epithelial tumor cells, including human prostate and breast cancer cells[219]. Interestingly, DAS was initially developed as a Src-family kinase inhibitor; however, it is currently known for its inhibitory activity against Bcr-Abl, ephrinA2, PDGFR, and c-kit[220].

DAS has proven effective in treating CML at various stages following imatinib failure. A prolonged follow-up of DAS therapy post-imatinib failure revealed a significant cytogenetic response in 59% of patients. Furthermore, the 7-year survival and overall survival rates reached 65% of cases[221].

DAS is orally administered and reaches peak concentrations within 0.5 to 6 h after oral dosing, with a half-life ranging from 3 to 5 h. *In vitro* studies indicate extensive binding to human plasma proteins, reaching approximately 96%. Metabolism of DAS occurs through the cytochrome P450 (CYP) 3A4 isozyme, leading to the formation of both active and inactive metabolites. The primary route of DAS elimination is through the feces[222,223].

Generally, DAS is well tolerated. The most frequent non-hematologic adverse events are the mucocutaneous events, especially skin pigmentation disorders[224]. Furthermore, DAS has been associated with a diverse range of skin reactions, including erythema multiforme, urticaria, photosensitivity, nail disorders, neutrophilic dermatosis, palmoplantar erythrodysesthesia syndrome, asteatosis, leukocytoclastic vasculitis and skin fibrosis[225]. Despite the structural similarity to imatinib, the comprehensive evaluation of photosensitization reactions related to DAS has not been conducted thus far. Hence, it appears intriguing to perform both photobiological and photophysical studies to elucidate the photosensitized reactions that may contribute to the manifestation of photoinduced skin lesions in CML patients undergoing DAS therapy.

Interestingly, a recent animal model study conducted at the Perelman School of Medicine at the University of Pennsylvania, suggested that the use of topical targeted therapies in the treatment of precancerous skin lesions may significantly diminish their size and inhibit the development of cutaneous squamous cell carcinoma, which is the second most prevalent form of cancer. Notably, one of the two treatments in focus, DAS, demonstrated better toxicity profile when compared to 5-fluorouracil, a first-line topical agent that eradicates both precancerous and cancer cells but is associated with known

adverse side effects[156]. Accordingly, DAS was proposed as a potential candidate molecule capable of penetrating the epidermal barrier due to its molecular weight of 488 Daltons and to exert significant inhibition on Src family kinases, thereby suppressing the growth of actinic keratosis/squamous cell carcinoma in situ (AK/SCCIS)[226,227].

Intriguingly, a study from 2013 has already demonstrated the effectiveness of topically applied DAS for the treatment of allergic contact dermatitis in mice, without the adverse side effect of skin atrophy, typically associated with steroidal agents[228]. Furthermore, recent data suggested that DAS-loaded topical nano-emulgel is a viable alternative for treating rheumatoid arthritis, aiming to reduce systemic side reactions[157]. In that same year, another study has shown that topical DAS could also emerge as a promising novel option to enhance the process of skin wound healing[158].

Considering all these background studies, the primary focus of this thesis is not only to assess the phototoxic behavior of DAS in the cellular milieu (keratinocyte cells) but also to mimic the proposed topical application by using a reconstructed human epidermis (RhE) as an *in vitro* 3D model for phototoxicity. Therefore, the findings of this study will offer additional insights into the mechanisms underlying photosensitivity adverse events linked to DAS therapy. This is particularly relevant as these mechanisms might exhibit variations when the drug is topically applied to the skin. The expanded understanding gained from this research could contribute to refining strategies for managing and mitigating potential skin adverse reactions in future clinical applications involving topical DAS.

7.2 Experimental procedures

7.2.1 Spectroscopic measurements

Spectroscopic measurements were carried out following the methods described in Chapter 3. The quenching rate constant of singlet oxygen emission (kq_{Δ}) upon the excitation of 1H-phenalen-1-one (PN) by the addition of increasing concentrations of DAS was calculated through the Stern-Volmer equation (Equation 12).

$$\frac{1}{\tau_{\Delta}} = \frac{1}{\tau_{\Delta_0}} + kq_{\Delta}\,[DAS]$$

Equation 12 | Stern Volmer equation for singlet oxygen ($^1O_2$) quenching by DAS. 1H-phenalen-1-one (PN) was excited using a laser at 355 nm after the addition of increasing amounts of DAS (0.2-4 mM). Where τ_{Δ} and τ_{Δ_0} are the lifetime of $^1O_2$ species with and without DAS, respectively.

7.2.2 Phototoxicity test in reconstructed epidermis (RhE)

Dasatinib pharmaceutical formulations, phototoxicity assay in reconstructed human epidermis (RhE) and histological experiments were carried out in accordance with the procedures outlined in Chapter 3.

7.2.3 Photosensitized lipid peroxidation

Lipid photoperoxidation was determined using C11-Bodipy$^{581/591}$ as a fluorescent sensor (see Chapter 3). Thus, human skin fibroblast cells (FSK) were treated with DAS solution at a concentration of 20 or 50 μM followed by UVA irradiation (dose: 5 J/cm^2) or maintained in darkness as a control.

7.2.4 Photoinduced protein oxidation assay

The potential of DAS to induce protein photooxidation was assessed by the carbonylation measurement using the 2,4-dinitrophenylhydrazine (DNPH)

derivatization method (see Chapter 3). In this case, HSA samples containing DAS at two concentrations, 20 or 50 μM, were irradiated with a UVA light dose ranging from 5 to 15 J/cm^2.

7.2.5 Single cell gel electrophoresis comet assay

The comet assay (single-cell gel electrophoresis) was carried out according to the procedures detailed in Chapter 3. Thus, HaCaT cells were treated with 50 μM of DAS and, subsequently, irradiated under UVA light (dose: 5 J/cm^2). In the DNA recovery experiments cells were maintained in DMEM medium at 37 ºC for 18 h.

7.2.6 Photoinduced phosphorylation of γ-H2AX

Bj-hTERT fibroblasts were treated with DAS at a concentration of 50 μM and exposed to a UVA light dose of 5 J/cm^2. Subsequently, the samples underwent isotropic expansion, and immunostaining was conducted using anti-H2AX-ser139 antibody, along with anti-α-tubulin and DAPI. Leica confocal microscope was used to visualize and detect phosphorylated γ-H2AX foci.

7.3 Results and discussion

7.3.1 Photophysical properties

Generally, drug photosensitized damage to biomolecules can be associated with the generation of ROS or radicals arising from excited states of the molecule[229,230]. Consequently, in order to anticipate the phototoxicity of DAS, prior studies on its photobehavior were carried out using various photophysical techniques including fluorescence, transient absorption, and near-infrared luminescence spectroscopy.

Emission spectra

The fluorescence spectra of DAS, both in PBS and within cells, exhibited a maximum centered at 374 nm (Figure 45A). Similar results were observed when using EtOH as a solvent, mimicking the lipophilic environment present in the cellular milieu (Figure 45A). Moreover, the fluorescence quantum yield (Φ_F) of DAS in HaCaT cells was determined by comparing the area under the emission curve to anthracene as a reference (Φ_F in EtOH = 0.27)[145], revealing a value of approximately 0.001 (Figure 45B). Additionally, the energy of the singlet excited state (E_s) was calculated through the intersection point between the normalized excitation and emission spectra, resulting in a value *ca.* 343 kJ/mol for both PBS (Figure 45C) and EtOH solution (Figure 45D). Finally, to determine the singlet excited state lifetime (τ_F), time-resolved fluorescence spectroscopy was conducted. However, the τ_F was found to be very short (less than 1 ns), and accurately determining this value proved to be challenging due to limitations of the equipment.

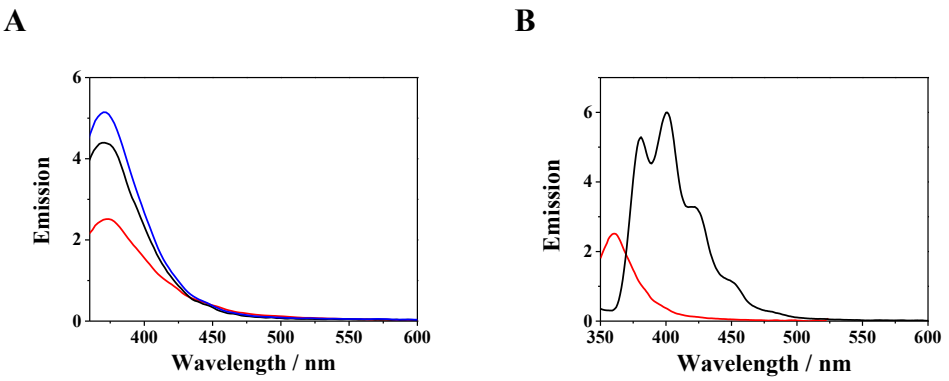

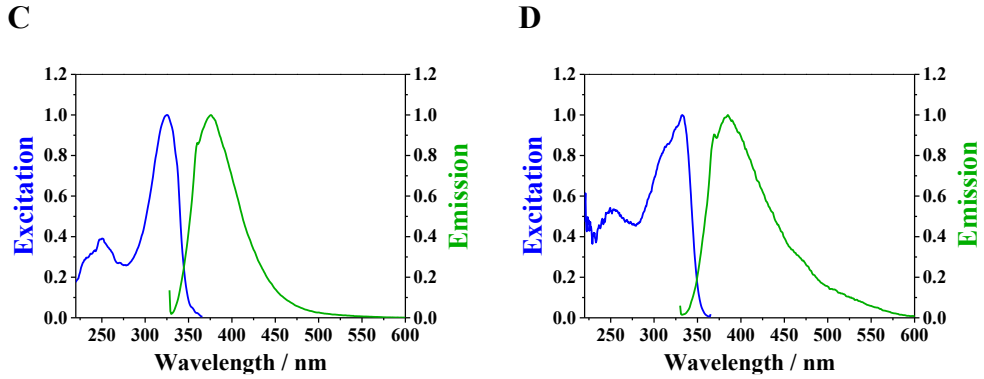

Figure 45 | Fluorescence properties of DAS. (A) Fluorescence emission spectra of DAS (λ_{exc}: 350 nm) recorded in PBS (black), in EtOH (blue) or within HaCaT cells (red). (B) Fluorescence emission spectra (λ_{exc}: 320 nm) of DAS in HaCaT (red). Anthracene (black) in EtOH was used as the standard for fluorescence quantum yield (Φ_F) measurement[145]. (C) Normalized fluorescence emission spectra registered at λ_{exc}: 325 nm (green) and normalized fluorescence excitation spectra recorded at λ_{max}: 374 nm (blue) in PBS (C) or EtOH solution (D). Fluorescence emission units are arbitrary.

Laser flash photolysis

Laser flash photolysis (LFP) was used as a technique to detect, in the microsecond timescale, the generation of transient species upon the excitation of DAS. In this approach, the excitation of DAS in deareated EtOH solution with a nanosecond laser pulse at 355 nm led to the formation of a transient with a maximum at 490 nm (Figure 46A). Similar results were obtained in aprotic solvents such as MeCN, dichloromethane (DCM) and 1,4-dioxane (DX) (see Table 12). Furthermore, this transient species exhibited a lifetime of approximately 2 µs in a deareated atmosphere, showing a slight increase in DCM and DX which was around 3 µs (Table 12 and Figure 46B). Additionally, as depicted in Figure 46C, the identified species demonstrated effective quenching by molecular oxygen, with a rate constant (kq) around $6.9 \cdot 10^{10}$ M^{-1} s^{-1}, determined through a mono-exponential decay function

(Figure 46D). Consequently, the results strongly suggest that the transient species corresponds to a triplet excited state of DAS (^{3}DAS*).

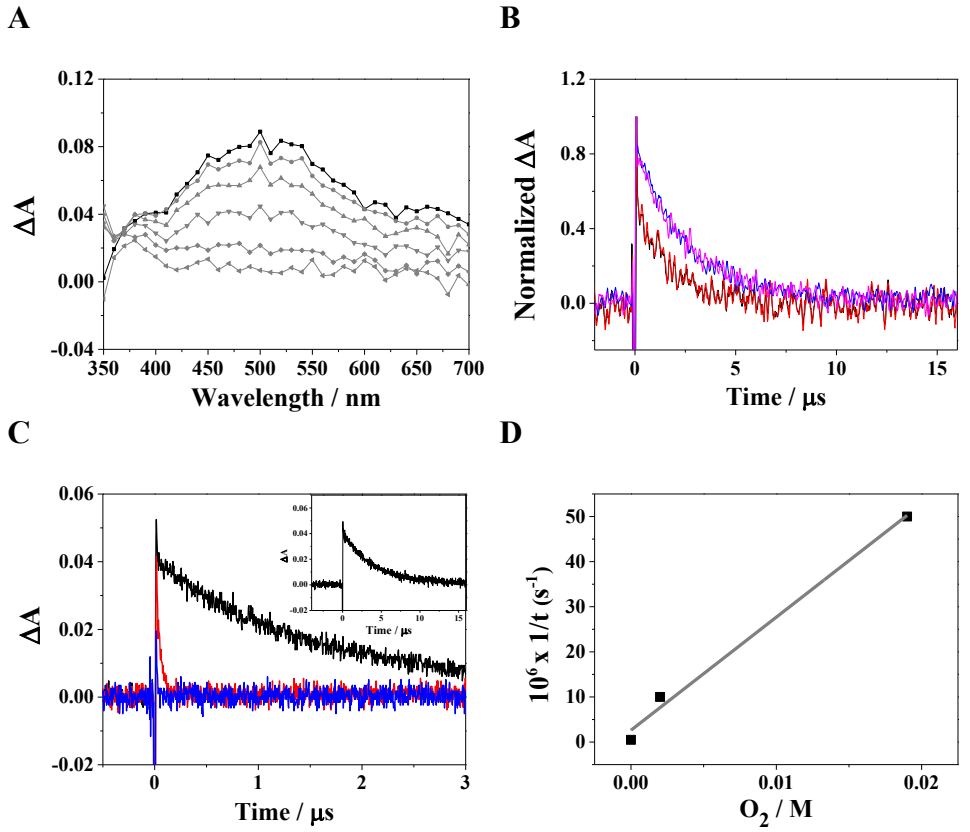

Figure 46 | Laser flash photolysis (λ_{exc}: 355 nm) measurements. (A) Transient absorption spectra (from 1 to 16 μs) for DAS in deareated EtOH solution (B) Normalized decay traces for ^{3}DAS* monitored at 490 nm in deareated EtOH (black), MeCN (red), dichloromethane (blue) and 1,4-dioxane (magenta) solutions. (C) Decay traces for ^{3}DAS* monitored at 490 nm in deareated (black), aerated (red) and oxygen saturated EtOH solutions (blue). Inset: Transient decay of DAS in deareated atmosphere on a longer timescale. (D) Stern-Volmer plot obtained for ^{3}DAS* in EtOH quenched by increasing amounts of molecular oxygen (O_2).

To accurately confirm the triplet nature of DAS excited species, photosensitization LFP experiments were performed with naproxen (NPX) as an acceptor. The energy level of ^{3}NPX* was found to be 259.4 kJ/mol,[231] whereas ^{3}DAS* energy level, determined through a 15% rise in its

phosphorescence emission within an EtOH solid matrix at 77 K (Figure 47A), was approximately 274.5 kJ/mol. Consequently, when DAS was selectively excited at 355 nm in the presence of NPX, a notable decrease in the signal at 490 nm was observed (kq *ca.* 1.02 × 10^{10} M^{-1} s^{-1}), concurrent with the formation of $^{3}NPX^{*}$ (λ_{max} ~430 nm) via a triplet–triplet energy transfer process from DAS to NPX (Figure 47B-D). Therefore, the transient band with a maximum at ~490 nm can unequivocally be assigned to the triplet excited state of the drug.

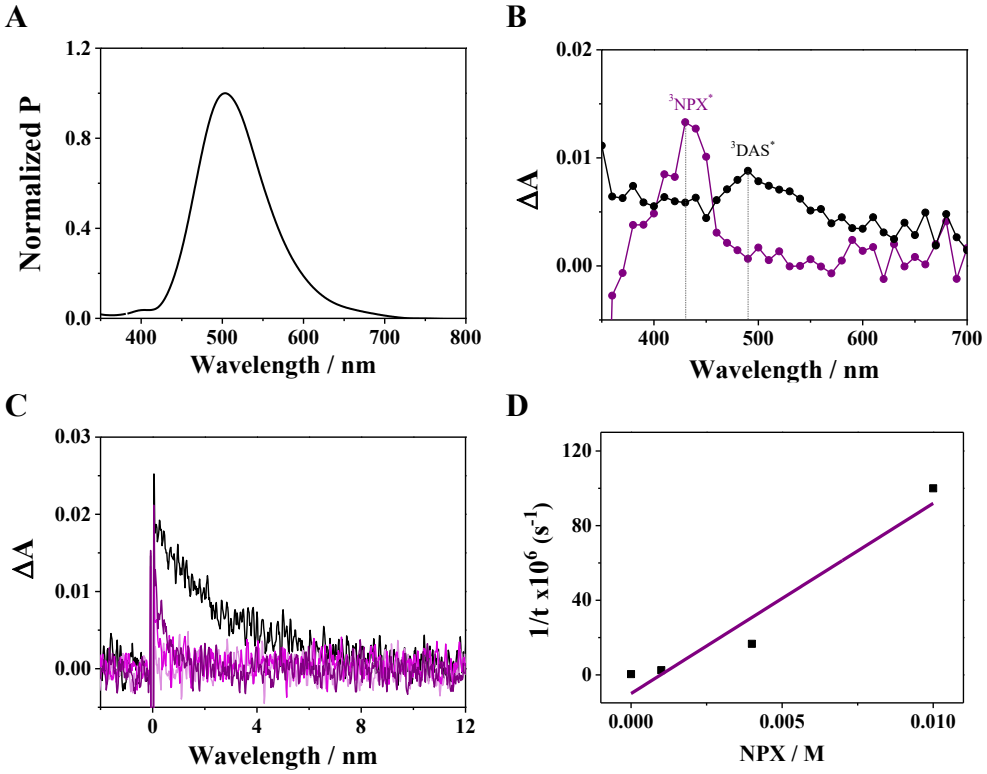

Figure 47 | (A) Normalized phosphorescence (P) spectrum (λ_{exc}: 300 nm) for DAS in a solid matrix of EtOH at 77 K. (B) Laser flash photolysis spectra for DAS (black) and for a mixture containing DAS and NPX 10 mM (violet). (C) Decay traces at 490 nm for DAS (black) and for a mixture containing DAS and increasing amounts of NPX (1-10 mM) (violet). (D) Stern-Volmer plot obtained for $^{3}DAS^{*}$ quenched by increasing amounts of NPX. All LFP measurements were performed in deareated EtOH after excitation at 355 nm.

It is well-established that the generation of singlet oxygen ($^1O_2$) occurs as a consequence of the interaction between triplet excited species and molecular oxygen (Type II oxidative reactions)[232]. Moreover, $^1O_2$ species possess the ability to induce significant oxidative damage to cellular targets. This includes the formation of lipid hydroperoxides through lipid peroxidation[163,233], oxidation of proteins[234], and DNA nucleoside oxidation[67]. Consequently, time-resolved NIR measurements of DAS in an aerated solution were recorded upon excitation at 355 nm. This resulted in the detection of a $^1O_2$ luminescence signal at 1270 nm with a lifetime (τ_Δ) of approximately 8 μs in EtOH solution (Figure 48A). As displayed in Table 12, the quantum yield, calculated considering ketoprofen (KP) in MeCN as the standard (Φ_Δ = 0.39)[146], were approximately estimated to be 0.1 for both EtOH and MeCN solutions and were enhanced in DCM and DX solutions (Φ_Δ *ca.* 0.2). Unexpectedly, the $^1O_2$ lifetimes (τ_Δ) for DAS were lower than those estimated for organic solvents (Table 12)[123,235,236]. This can be elucidated by the reaction of $^1O_2$ with tertiary aliphatic amines, which typically behave as $^1O_2$ quenching agents. In this case, DAS structure contains a piperazine, which displays a $^1O_2$ quenching rate around $1.0 \cdot 10^6$ M^{-1} s^{-1} [237]. Subsequently, to confirm this phenomenon, the quenching of the luminescence emission of 1H-phenalen-1-one, also known as perinaphtenone (PN), was conducted. PN is recognized as one of the most efficient $^1O_2$ sensitizers in both polar and non-polar media, yielding a Φ_Δ close to unity[238]. Thus, $^1O_2$ NIR-luminescence signal was recorded at 1270 nm in both MeCN and DCM upon increasing concentrations of DAS. As depicted in Figure 48B and Figure 48C, $^1O_2$ generated from PN was quenched by DAS (0.2-4 mM), displaying a rate constant (kq_Δ) of approximately 9.2×10^6 M^{-1} s^{-1} and 1.20×10^7 M^{-1} s^{-1} in aerated MeCN and DCM, respectively. Accordingly, it was demonstrated that

DAS exhibits a quenching effect on $^1O_2$ production, most likely due to the interaction between piperazine moiety and $^1O_2$. Such interaction is believed to constitute the primary mechanism behind the observed low τ_Δ values.

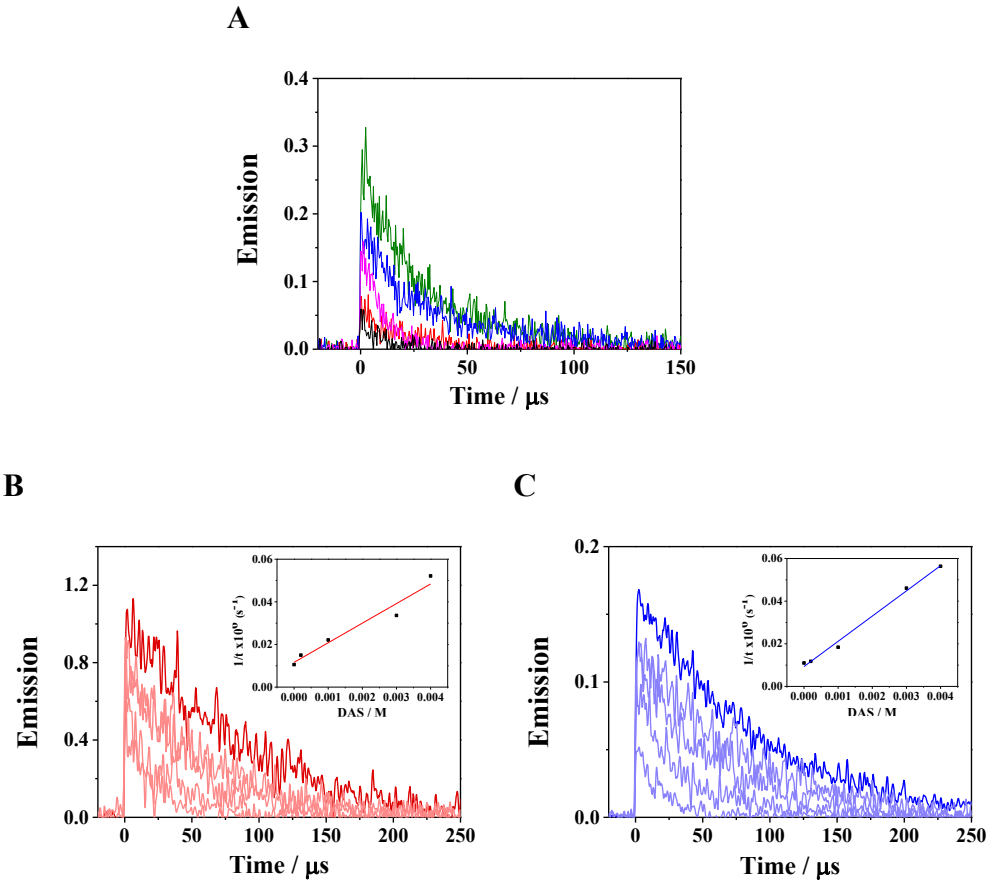

Figure 48 | Singlet oxygen measurements. A) NIR-emission decays at 1270 nm for DAS in aerated EtOH (black), MeCN (red), dichloromethane (blue) and 1,4-dioxane (magenta) solutions. Ketoprofen (KP) in MeCN was used as reference (green), which displays a Φ_Δ around 0.39[146]. B) Kinetic traces of $^1O_2$ emission quenching for PN in the presence of DAS (0.2-4 mM) in MeCN solution. C) Kinetic traces of $^1O_2$ emission quenching for PN in the presence of DAS (0.2-4 mM) in DCM solution. Insets: Stern-Volmer plots obtained for PN $^1O_2$ quenching by DAS.

Table 12 | Photophysical parameters of DAS in different media. Relative errors were lower than 5% of the stated values.

	EtOH	MeCN	DCM[a]	DX[a]
$\lambda_{max\ (transient\ absorption)}$ / nm	490	490	490	490
τ_T / μs[b]	1.76	1.11	2.62	2.58
τ_Δ / μs[c]	7.57	13.36	24.30	9.29
k_q / 10^{10} (M^{-1} s^{-1})[d]	6.90	-[*]	1.75	1.53
Φ_Δ[e]	0.07	0.10	0.24	0.19

[a] DCM and DX are dichloromethane and 1,4-dioxane, respectively.
[b] Triplet excited state lifetimes (τ_T) were obtained in deareated conditions.
[c] Singlet oxygen lifetimes (τ_Δ) were obtained in aerated conditions.
[d] kq values were calculated using increasing concentrations of molecular oxygen.
[e] Φ_Δ values were determined by comparison with ketoprofen (KP) in MeCN as standard[146].
[*] kq in MeCN was not feasible to calculate due to complete quenching of ^{3}DAS*.

In summary, DAS showcased its capability to generate $^1O_2$ species, which can subsequently trigger Type II photooxidative reactions toward biomolecules. Furthermore, the potential role of a Type I oxidative mechanism was examined using linoleic acid (LA), 3-methylindole (in lieu of tryptophan), and guanosine (Guo) as models for lipids, proteins, and DNA, respectively. Consequently, transient absorption decays for DAS were recorded at 490 nm in deareated EtOH solution with increasing concentrations of the quencher. As depicted in Figure 49A and Figure 49B, a significant quenching of ^{3}DAS* species by LA and 3-methylindole was observed, with a calculated kq of around 1.7×10^8 M^{-1} s^{-1} and 4.3×10^7 M^{-1} s^{-1}, respectively. This indicates the potential involvement of radical formation induced by DAS in the photodamage to lipids and proteins (Type I mechanism). Conversely, Guo did not demonstrate the ability to quench the ^{3}DAS* species (Figure 49C). Consequently, there was no evidence of Type I mechanism involvement in the photooxidation of guanine bases.

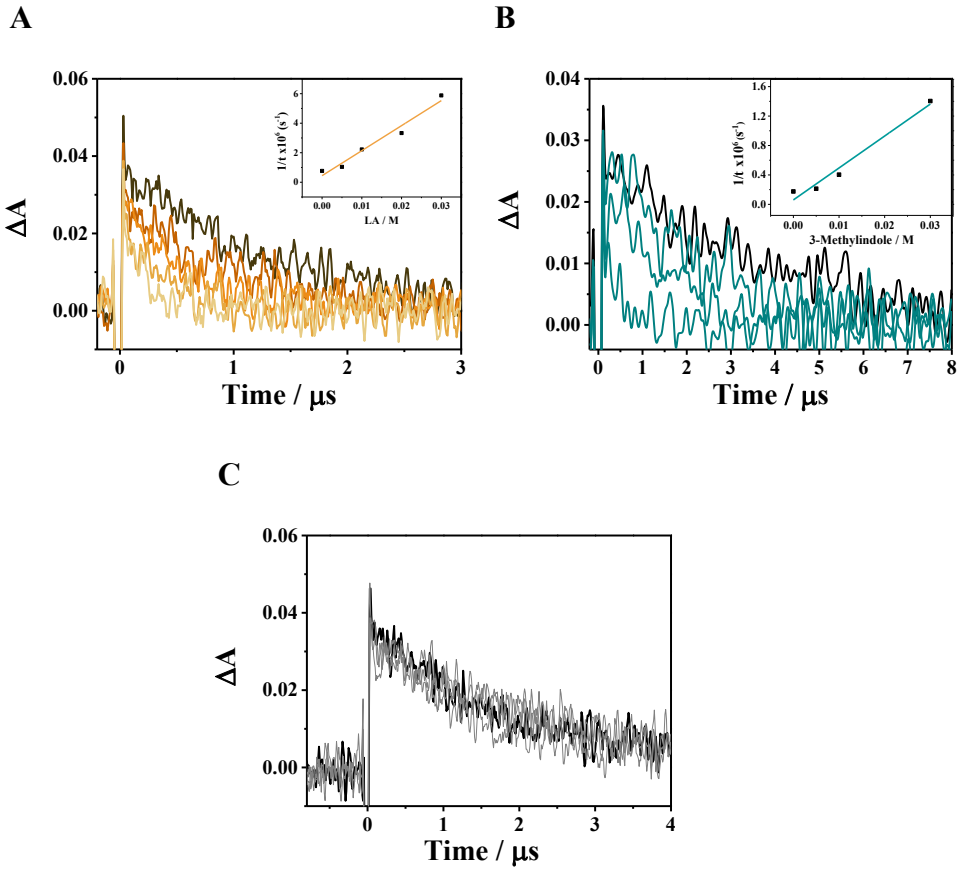

Figure 49 | Decays at 490 nm for DAS in deareated EtOH in the presence of increasing concentrations of (A) linoleic acid, LA, (B) 3-methylindole, or (C) guanosine, Guo (5-30 mM). Insert: Stern-Volmer plots.

7.3.2 Photosensitized damage to lipids and proteins

The phototoxicity potential of DAS in HaCaT cells was initially assessed using the *in vitro* neutral red uptake (NRU) phototoxicity test (refer to Chapter 4). The PIF factor was calculated through the ratio of the IC50 values under light and dark conditions, resulting to be approximately 5. Then, based on the OECD[152] classification, DAS was considered a phototoxic compound. Given DAS pronounced lipophilic properties, its potential phototoxicity may target

membrane components such as proteins and lipids. To validate this assumption, both lipid and protein photooxidation were examined.

Lipid photoperoxidation

In order to assess lipid peroxidation, a lipid-soluble fluorescent marker, C11-Bodipy$^{581/591}$, was employed. This marker, designed to penetrate the plasmatic membrane, exhibits a unique spectral range between the non-oxidized (595 nm) and oxidized forms (520 nm)[163,167,233]. Upon oxidation, the fluorescence emission shifts from red (λ_{exc}: 535 nm) to green (λ_{exc}: 490 nm). Accordingly, human skin fibroblast cells (FSK) exposed to DAS (20 or 50 μM) followed by UVA irradiation (dose: 5 J/cm^2) or kept in darkness as a control were labeled with C11-Bodipy$^{581/591}$.

Fluorescence microscope images (Figure 50A) revealed a notable increase in green fluorescence intensity, particularly at a concentration of 50 μM. However, green fluorescence emission was hardly detected in non-irradiated samples. Quantitative analysis supported these findings, where UVA exposed FSK cells showed a substantial reduction on the ratio between red and green fluorescence emission intensity (FIR reduction > 1-fold) (Figure 50B). All in all, the results suggest that the lipid membrane could be a plausible target for DAS phototoxicity.

A

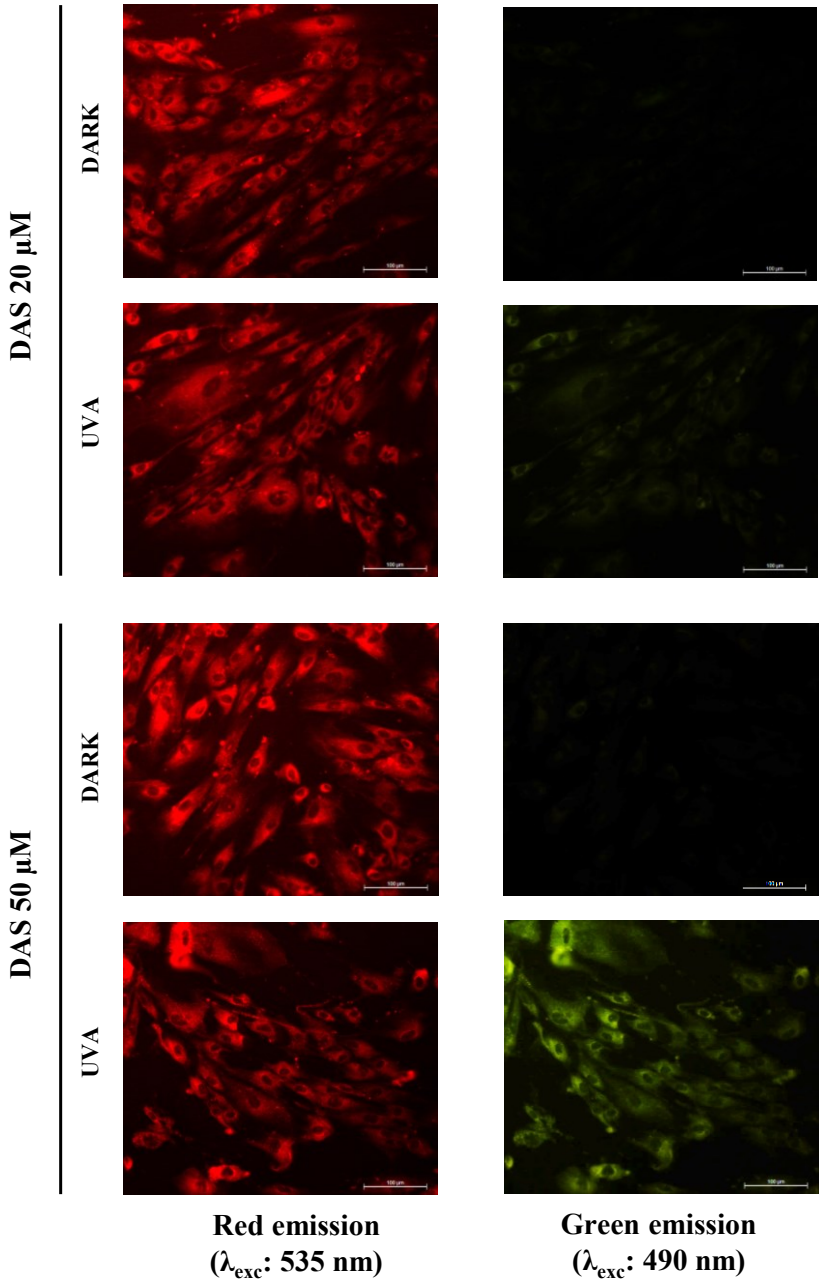
DAS 20 µM
DARK
UVA
DAS 50 µM
DARK
UVA
Red emission
(λexc: 535 nm)
Green emission
(λexc: 490 nm)

B

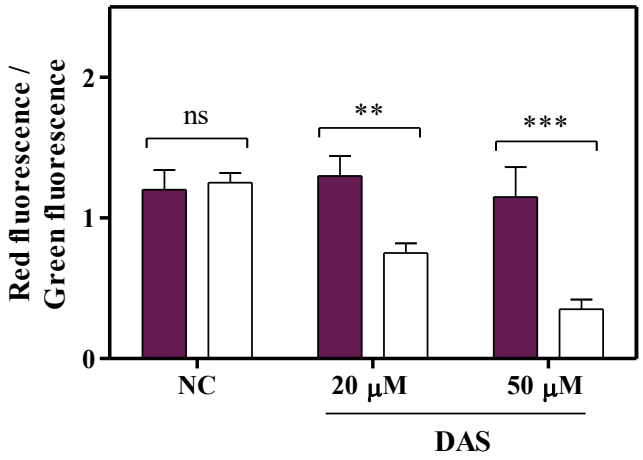

Figure 50 | Photosensitized lipid peroxidation. (A) Human fibroblast cells (FSK) were treated with DAS at 20 or 50 µM, and either kept under dark conditions or UVA radiation at a dose of 5 J/cm^2. Subsequently, cells were labelled with 10 µM C11-Bodipy$^{581/591}$, and the extent of lipid peroxidation was monitored based on the intensity of the oxidized Bodipy fluorescence (green emission). Scale bar: 100 µm. Images are representative of 3 independent experiments. (B) Fluorescence intensity ratio between non-oxidized C11-Bodipy (red fluorescence) and oxidized C11-Bodipy (green fluorescence) in either dark (■) or UVA light conditions (□). Data are the mean ± SD from 3 independent experiments. Asterisks indicate significant differences between groups by the Student´s t-test (***$p < 0.001$; **$p < 0.01$; ns: non-significant).

Protein photooxidation

The evaluation of photoinduced protein oxidation involved the quantification of carbonyl content using the 2,4-dinitrophenylhydrazine (DNPH) derivatization method. HSA protein served as the selected protein model. Consequently, HSA, incubated in the presence of DAS (20 or 50 µM), underwent exposure to 5-15 J/cm^2 UVA radiation and was labeled with DNPH. According to this method, DAS induced a dose-dependent carbonylation in the HSA protein, resulting in an approximately 3-fold increase at 50 µM (Figure 51). In contrast, the carbonyl content in the non-

treated HSA control remained unchanged after irradiation, confirming the suitability of the selected UVA dose for this experiment.

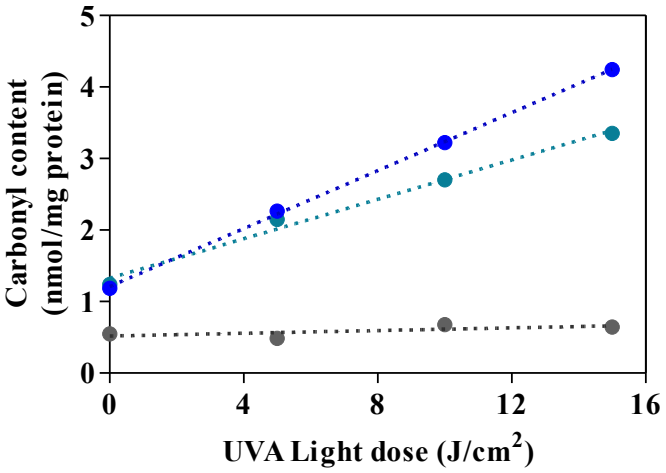

Figure 51 | Photooxidation of HSA protein. Samples were treated either with 20 µM (cyan) or 50 µM (blue) DAS in the presence of increasing UVA radiation dose (5-15 J/cm^2), and carbonyl content was monitored by 2,4-dinitrophenylhydrazine derivatization method (λ: 375 nm). Untreated HSA carbonyl content is displayed in gray plots. Data represent the mean ± SD of 3 independent experiments.

7.3.3 Photogenotoxicity

DNA damage assessed by comet assay

The alkaline comet assay, used to quantify various forms of DNA damage, including SSB, DSB, and ALS, was conducted[239]. In this experiment, keratinocyte cells underwent a 30 min incubation with DAS followed by exposure to UVA radiation (5 J/cm^2). Subsequently, agarose-embedded cells were lysed, and electrophoresis allowed the migration of damaged DNA fragments out of the cell nucleus, forming comet nucleoids and tails. Following staining with SYBR Gold, the comets were observed under a fluorescence microscope, and a visual scoring system with six different categories was employed to quantify the extent of nuclear DNA damage[197].

As depicted in Figure 52, the level of DNA damage induced by DAS was substantial (approximately 55%), and recovery experiments indicated persistent DNA damage even after an 18 h period. It is established that impaired DNA repair can lead to genomic instability, apoptosis, senescence, and ultimately, carcinogenesis.

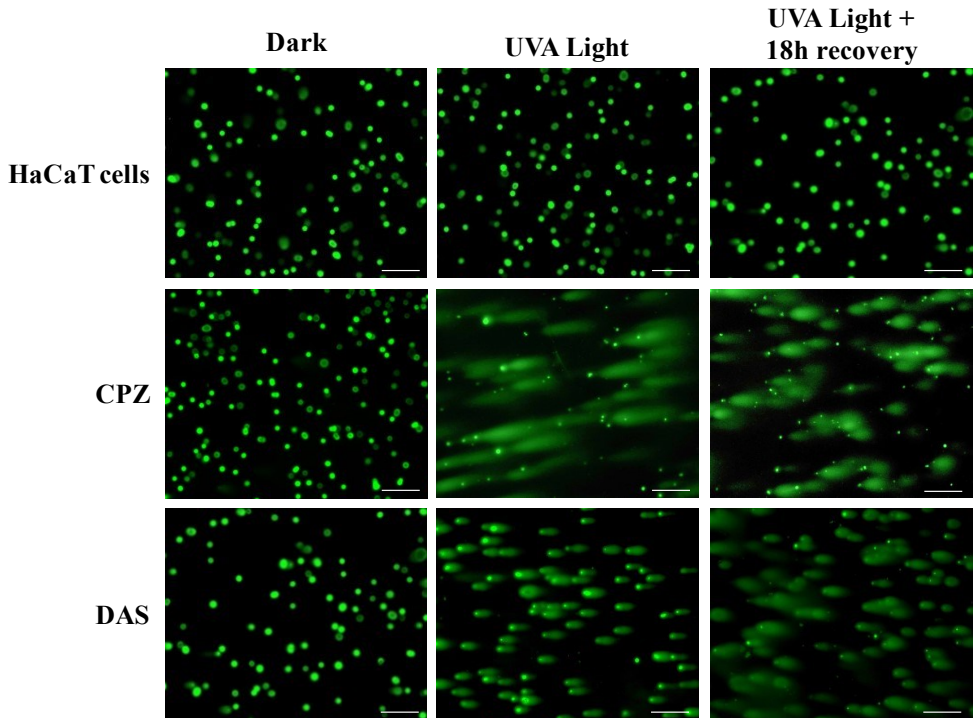

Figure 52 | Alkaline comet assay experiment. HaCaT cells were treated with DAS (50 µM) and were then either kept in the dark or exposed to UVA light at a dose of 5 J/cm^2. Furthermore, photoexposed keratinocyte cells were allowed to recover for 18 h. Chlorpromazine (CPZ) at 5 µM served as the positive control for photogenotoxicity. The scale bar is 250 µm, and the images are representative of 3 independent experiments.

DNA damage assessed by γ-H2AX immunostaining

In light of the observed DNA damage potential through comet assay, DAS photogenotoxicity was further confirmed through the detection of γ-H2AX foci. Thus, fibroblast cells treated with DAS underwent exposure to UVA light at a dose of 5 J/cm^2 and were immunostained before expansion microscopy (ExM) for subsequent visualization using a confocal microscope. As depicted in Figure 53, a considerable number of γ-H2AX foci were exclusively observed within the nuclei of DAS-treated Bj-hTERT cells subjected to photoexposure. In contrast, cells not exposed to irradiation exhibited minimal formation of γ-H2AX foci, confirming the ability of DAS to photoinduce DNA damage, specifically through DSBs.

Hence, these findings validate phosphorylated γ-H2AX immunostaining as a sensitive and reliable method for monitoring the formation of DSBs within the nuclear DNA. Indeed, this recently developed γ-H2AX assay may prove to be more sensitive to early DNA damage when compared to the comet assay. Consequently, it emerges as a valuable alternative to the conventional comet assay, contributing to both enhanced precision and specificity in the evaluation of drug-induced DNA damage.

In summary, the *in vitro* NRU assay successfully demonstrated the phototoxicity of DAS in skin cell culture. Moreover, the evaluation of biomolecular photosensitized damage revealed that DAS has the potential to initiate oxidative reactions targeting lipids, proteins, and genomic DNA. In this context, the following studies entail validating this phototoxicity behavior within a more realistic setting, considering the potential clinical use of DAS drug as a topical therapy for a wide range of dermatological conditions.

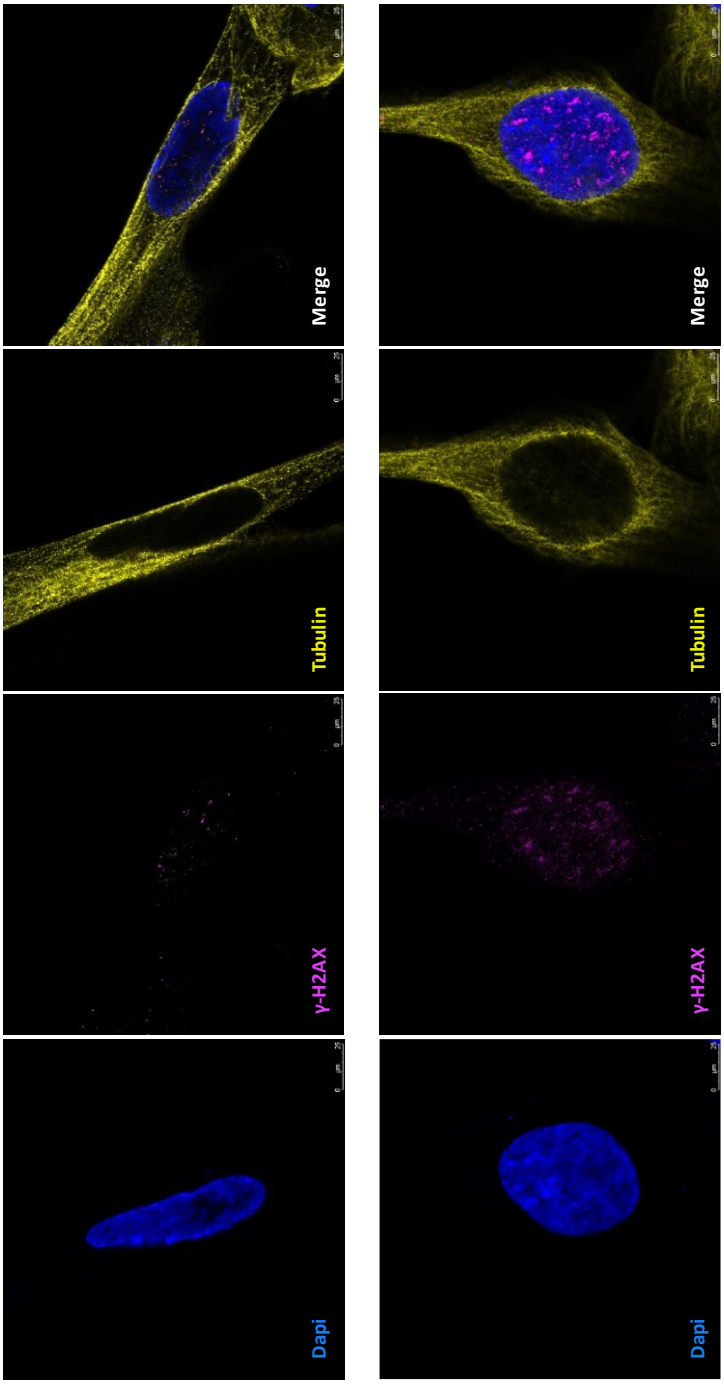

Figure 53 | Immunofluorescence staining of γ-H2AX. Bj-hTERT fibroblasts were exposed to DAS 50 µM and kept either in darkness of irradiated with UVA light (5 J/cm^2). Fixed cells were immunostained with Rabbit anti-H2AX-ser139 (1 µg/mL) and secondary antibody Goat Anti-Rabbit Alexa Fluor 488, 1:500 (magenta); Mouse Anti-α-tubulin (2 µg/mL) and secondary antibody Goat anti-Mouse Rhodamine (yellow). Then cells were further stained with DAPI (blue) and imaged by confocal microscopy. Images are representative of 4 independent experiments. Expansion factor was approximately 4. Scale bar: 25 µm.

7.3.4 Phototoxicity in reconstructed human epidermis (RhE)

The determination of DAS phototoxic potential in keratinocytes by NRU assay was effectively demonstrated. However, this method, based on a monolayer cell culture, may not be suitable for chemicals applied topically. Therefore, using a 3D human skin model, better reflecting the penetration and barrier function of the stratum corneum, becomes more appropriate for assessing the phototoxicity of topically applied drugs, such as DAS.

In this study, DAS was tested in both an EtOH solution (10 mM) and an oil-in-water (O/W) emulsion (0.45%) using the MTT assay[240] on reconstructed epidermis. The UVA light dose was 7 J/cm^2, and CPZ, previously used in the initial NRU experiments, served as the positive control. Figure 54A illustrates the impact of different DAS formulations on EpiDerm tissue model. Compared to non-photoexposed tissues, topically applied DAS as a solution (10 mM in EtOH) resulted in a 41% reduction in tissue viability. This finding aligns well with the earlier revealed phototoxic potential in the *in vitro* NRU experiments. Furthermore, DAS formulated in an O/W emulsion at a similar concentration (0.45%) displayed a comparable reduction in tissue viability (approximately 45%) upon UVA radiation. As expected, the DAS emulsion combined with 3% tinosorb S, a photostable UV broad-spectrum filter (Figure 54B), exhibited a lower reduction in tissue viability (20%) compared to the original emulsion, demonstrating the protective effect of tinosorb S against UVA radiation.

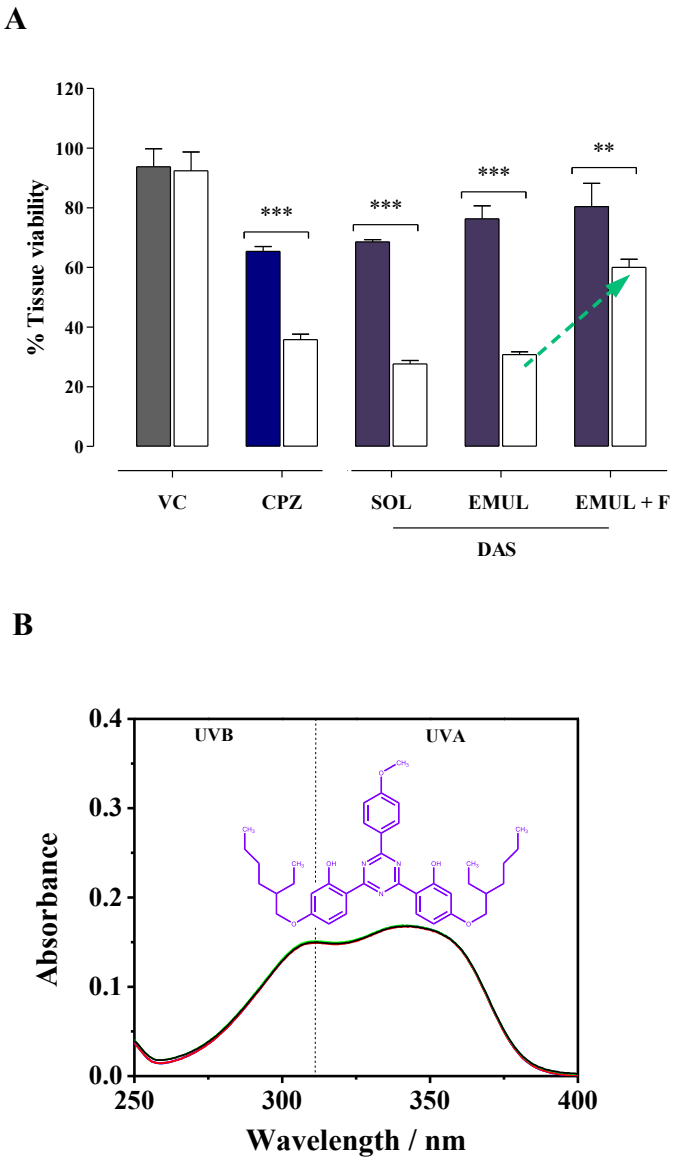

Figure 54 | Phototoxicity of DAS in the reconstructed human skin model. (A) Viability of treated tissues with DAS 10 mM in EtOH solution (SOL), 0.45% DAS O/W emulsion (EMUL), or 0.45% DAS O/W emulsion combined with 3% UV filter, tinosorb S (EMUL + F). Tissues where either kept in dark conditions (filled bar) or exposed to UVA dose of 7 J/cm^2 (empty bar). CPZ 300 µM was used as the positive control. EtOH was used as the vehicle control (VC). Data are the mean ± SD from 3 independent experiments. Asterisks indicate significant differences between groups by the Student´s t-test (***$p < 0.001$; **$p < 0.01$). (B) Absorption photostability spectra of tinosorb S in EtOH solution upon irradiation at λ: 355 nm (5-25 min). Inset: Molecular structure of tinosorb S.

To gain insight into the phototoxic effects of DAS, histological sections of the reconstructed epidermis were characterized through hematoxylin and eosin staining. As shown in Figure 55, no significant alterations in morphology were observed for the untreated skin tissues. Similarly, non-irradiated samples treated with DAS emulsion 0.45% showed no major modification of epidermal histology. Conversely, some disorders in the basal layers became visible after exposing the tissue to a UVA dose of 7 J/cm^2. Specifically, disorganization of the epidermal layer, vacuoles/spongiosis, and parakeratosis (retention of nuclei in the stratum corneum) were noted.

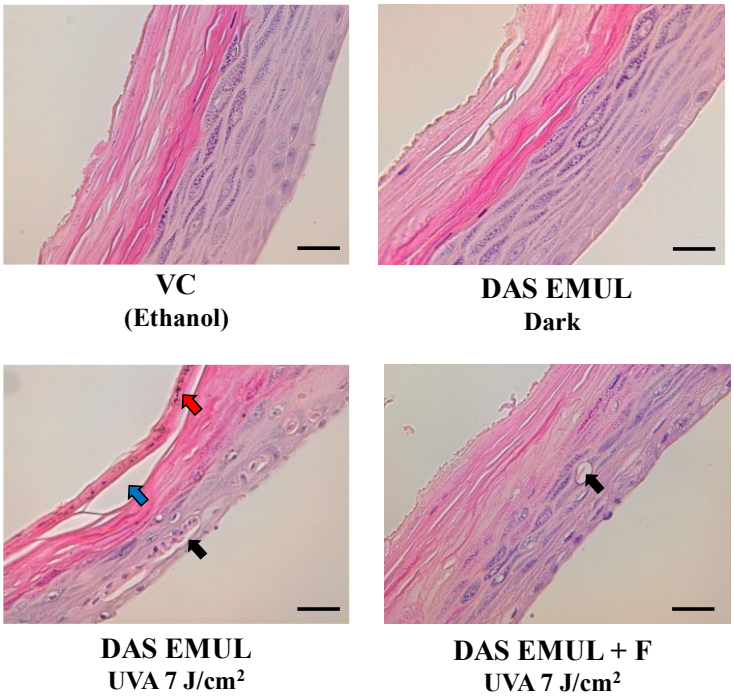

Figure 55 | Histological analysis. Examination of the reconstructed human epidermis using hematoxylin and eosin (H&E) staining technique. Tissues were treated with either the vehicle (EtOH), DAS 0.45% O/W emulsion alone (EMUL) or combined with a 3% UVA filter, tinosorb S (EMUL + F), in the presence or absence of UVA radiation at 7 J/cm^2. Paraffin-embedded sections were subsequently prepared for hematoxylin and eosin staining. Represented alterations: spongiosis (black arrow), parakeratosis (red arrow) and disorganization in the epidermal layers (blue arrow). Scale bar: 50 µm. Images are representative of 3 independent experiments.

Overall, these alterations collectively indicate morphological dysfunction compromising the skin barrier integrity and resistance. As anticipated, the incorporation of a UV filter was associated with a protective effect against the photosensitization reaction induced by DAS treatment.

7.4 Conclusions

DAS is an anticancer drug that has recently drawn attention for its potential application as a topical therapy for skin disorders. Preliminary investigations have demonstrated the phototoxic potential of DAS in monolayer keratinocyte cells (HaCaT). Furthermore, a topical O/W emulsion applied to reconstructed human epidermis resulted in significant phototoxicity. Notably, this effect was effectively mitigated by formulating DAS along with a broad-spectrum UV filter (tinosorb S).

Moreover, the transition from red to green fluorescence of the lipid-soluble fluorescent marker C11-Bodipy$^{581/591}$ in FSK cells demonstrated the lipid photoperoxidation potential of DAS. Likewise, the carbonylation assay effectively proved the ability of this drug to trigger photoinduced protein oxidation, using HSA as a model. Furthermore, DNA photodamage, evaluated through both comet assay (in HaCaT cells) and γH2AX immunostaining (in Bj-hTERT fibroblasts), was demonstrated to be photoinduced by DAS. Altogether, these outcomes strongly suggest that membrane components and genomic DNA are potential targets for DAS-induced phototoxicity.

DAS is a photoactive molecule that, upon excitation in the UVA region of the spectrum, generates a transient species that corresponds to the triplet excited state of the molecule (^{3}DAS*), characterized by an absorption band at 490 nm. The quenching of this transient species by molecular oxygen yields singlet

oxygen, which is proved to engage in Type II photooxidation to biomolecules. Additionally, radical-mediated photodamage to lipids and proteins was also conceivable via a Type I mechanism, as indicated by the quenching of $^{3}DAS^{*}$ in the presence of linoleic acid and 3-methylindole.

Overall, DAS presents promising therapeutic applications in the treatment of skin disorders due to its ability to interact with crucial targets implicated in cancer and other skin pathologies. However, the phototoxic effects of DAS should be approached with caution, especially when considering its potential application as a topical treatment. The mechanisms through which DAS induces phototoxicity, including the generation of singlet oxygen and radical species, highlight the need to explore strategies such as combining DAS with UV filters or incorporating the drug into a controlled-release formulation. Additionally, adjusting the dose and exposure parameters to minimize phototoxicity while maximizing therapeutic efficacy is essential.

CHAPTER 8 Avapritinib

8.1 Introduction

Avapritinib, AVP (Ayvakyt®; Blueprint Medicines) is the first and only drug approved by the FDA, in 2020, to treat advanced systemic mastocytosis (AdvSM) (Figure 56). It is considered a highly selective D816V-mutant KIT inhibitor, which is a gene mutation detected in 90 to 95% of patients with AdvSM. The efficacy analysis of AVP is around 71% overall response, including 19% with complete remission[241–243]. Moreover, AVP was also approved for first-line treatment of patients with PDGFR exon 18 (D842 V)-mutated gastrointestinal stromal tumor (GIST), which is resistant to imatinib, sunitinib, and regorafenib[244].

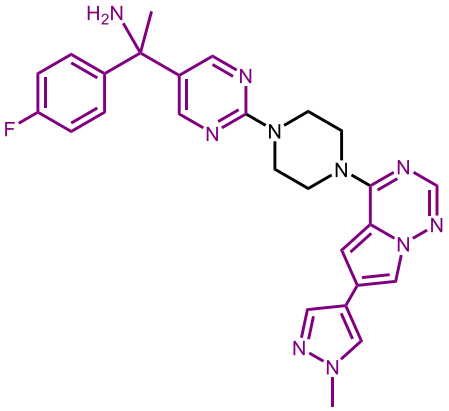

Figure 56 | Chemical structure of avapritinib (AVP). Chromophore groups are colored in violet.

Orally administered AVP presented a half-life ranging from 32 to 57 h following single doses of the drug. AVP is 98.8% protein bound in serum and the primary metabolic pathways involve CYP3A4 and CYP2C9. Approximately 49% of the drug remains unchanged, 35% is in the form of a hydroxy glucuronide metabolite, and 14% is an oxidatively deaminated metabolite. AVP undergoes 70% elimination through feces, with 11% being

excreted as the unchanged drug, and 18% is eliminated in the urine, with 0.23% as the unchanged drug[245].

The predominant treatment-related adverse events (TRAEs) of any grade, observed in at least 20% of patients, included peripheral edema, periorbital edema, and diarrhea. Notably, the most frequent grade 3 or higher TRAEs, occurring in 10% or more of patients, comprised neutropenia, thrombocytopenia, and anemia[242]. In terms of skin adverse disorders, a pharmacovigilance analysis revealed a statistically significant association between the use of AVP and photosensitivity[43]. In fact, nonclinical phototoxicity associated with the use of AVP was identified in both *in vitro* mouse fibroblasts and *in vivo* rat studies[246]. In clinical context, a 56-year-old patient undergoing AVP therapy manifested several skin reactions, including erythematous plaques, edema, and inflammatory infiltrates, which were indicative of photosensitivity associated with AVP[247]. Moreover, the European Medicines Agency issued a warning regarding photosensitivity with AVP, and clinical trials reported an incidence of photosensitivity at 1.1%[248]. Overall, despite the limited literature on the photosensitivity potential of this drug, the numerous case reports of photo-aggravated reactions secondary to AVP are sufficient to warrant consideration of photoprotection.

8.2 Experimental procedures

Cell culture conditions and spectroscopic measurements were carried out in accordance with the procedures outlined in Chapter 3.

8.2.1 Photoinduced protein oxidation assay

The potential of AVP to induce protein photooxidation was assessed by the carbonylation measurement using the 2,4-dinitrophenylhydrazine (DNPH) derivatization method (see Chapter 3). In this case, HSA samples containing AVP at 3 concentrations, 10, 25 or 50 μM, were irradiated with a UVA light dose ranging from 5 to 15 J/cm^2.

8.2.2 Single cell gel electrophoresis (comet) assay

The comet assay (single-cell gel electrophoresis) was carried out according to the procedures detailed in Chapter 3. Thus, HaCaT cells were treated with either 2 or 5 μM of AVP and, subsequently, irradiated under UVA light (dose: 5 J/cm^2).

8.3 Results and discussion

8.3.1 Fluorescence

Having established the phototoxic potential of AVP in HaCaT cells, with a PIF value of 11, as detailed in Chapter 4, an analysis of the fluorescence spectral characteristics of this compound was conducted. Thus, as revealed in Figure 57, AVP displayed similar emission spectrum in PBS and within HaCaT cells, revealing a fluorescence quantum yield (Φ_F) of approximately 0.06 in both cases.

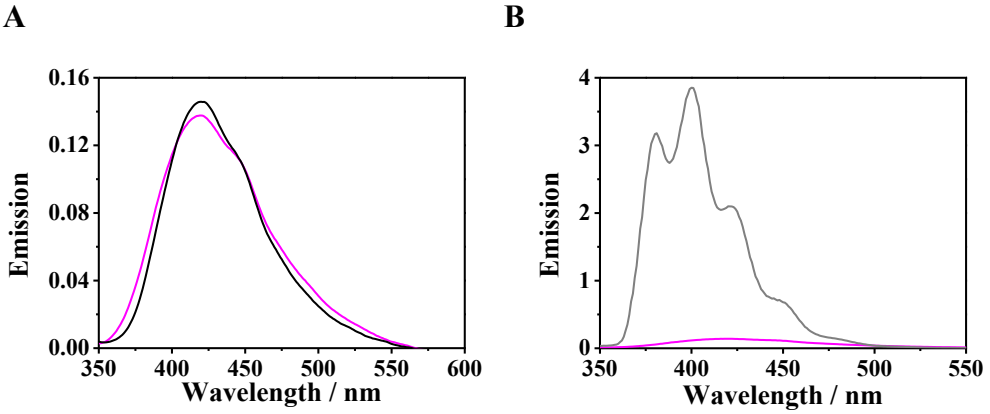

Figure 57 | Fluorescence emission properties of AVP. (A) Relative fluorescence emission of AVP in PBS (black) and within HaCaT cells (magenta) (λ_{exc}: 320 nm). (B) Relative fluorescence emission of AVP within HaCaT cells (magenta) (λ_{exc}: 320 nm) and anthracene in EtOH solution (gray), which was used as the reference for fluorescence quantum yield (Φ_F) measurements[145]. Fluorescence emission units are arbitrary.

8.3.2 Protein photooxidation

The evaluation of AVP photoinduced protein oxidation through the quantification of carbonyl content, using the 2,4-dinitrophenylhydrazine (DNPH) derivatization method, was performed. Consequently, HSA, incubated in the presence of AVP (10, 25 or 50 μM), underwent exposure to increasing UVA dose (from 5 to 15 J/cm^2) and was labeled with DNPH. Accordingly, AVP induced a dose-dependent carbonylation in the HSA protein, resulting in an approximately 4-fold increase at 50 μM and 15 J/cm^2 UVA dose (Figure 58).

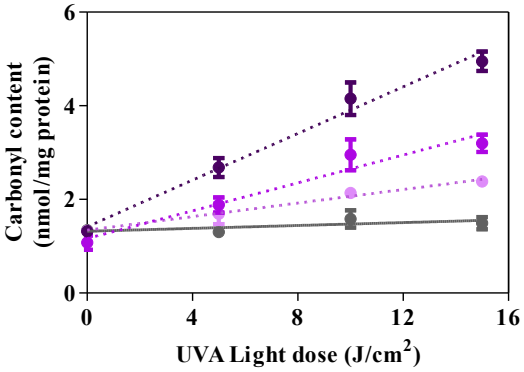

Figure 58 | Photooxidation of HSA protein. Samples were treated either with AVP at a concentration ranging from 10 to 50 µM (from light violet to dark violet) in the presence of increasing UVA radiation dose (5-15 J/cm^2), and carbonyl content was monitored by 2,4-dinitrophenylhydrazine derivatization method (λ: 375 nm). Untreated HSA carbonyl content is displayed in gray plots. Data represent the mean ± SD of 3 independent experiments.

8.3.3 Photogenotoxicity

The alkaline comet assay was performed to detect and quantify various forms of DNA damage, including SSB, DSB, and ALS. In this experiment, keratinocyte cells underwent a 30 min incubation with AVP followed by exposure to UVA radiation at a dose of 5 J/cm^2. Subsequently, agarose-embedded cells were lysed, and electrophoresis allowed the migration of damaged DNA fragments out of the cell nucleus, forming comet nucleoids and tails. Following staining with SYBR Gold, the comets were observed under a fluorescence microscope, and a visual scoring system with six different categories was employed to quantify the extent of nuclear DNA damage[197]. As displayed in Figure 59, the level of DNA damage induced by AVP was approximately 45% at a concentration of 2 µM, and it was even higher at 5 µM (approximately 55%). However, recovery experiments indicated persistent DNA damage even after an 18 h period.

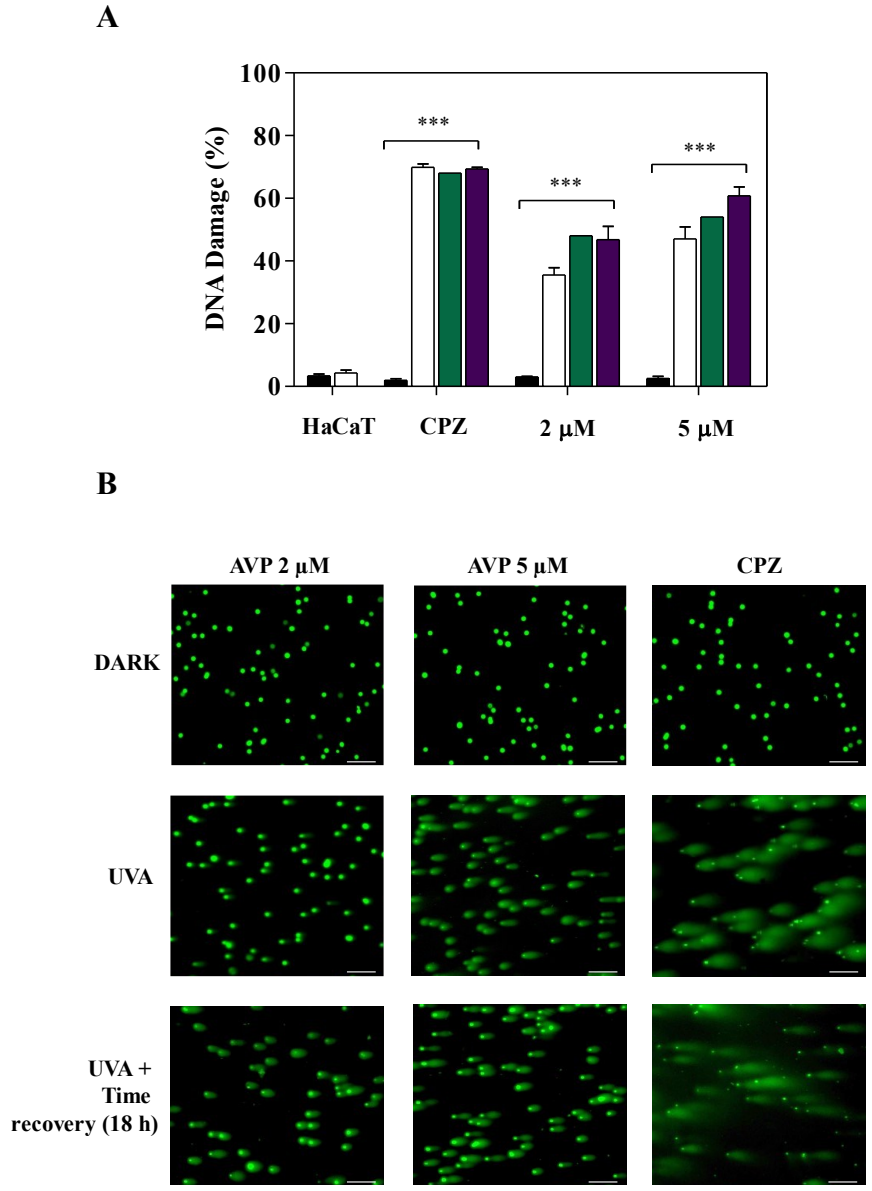

Figure 59 | (A) Photogenotoxicity of AVP. HaCaT cells were treated with 2 or 5 µM of AVP and irradiated with UVA light at 5 J/cm^2 dose (□), followed by 6 h (■) or 18 h (■) of cell recovery, or kept in the dark (■). Data are displayed as the percentage of DNA damage calculated following the six visual scoring categories. Data represent the mean ± SD of 3 independent experiments. Asterisks indicate significant differences by the Student´s t-test (***$p < 0.001$). (B) Representative microscopy images of irradiated (UVA Light) or non-irradiated (Dark) cells non-treated or treated with AVP and followed by 18 h of cell recovery (UVA Light + Time recovery 18 h). Chlorpromazine (CPZ) at 5 µM served as the positive control for photogenotoxicity. Scale bar: 250 µm.

8.4 Conclusions

The recent approval of AVP for the selective treatment of both GIST and AdvSM has significantly improved most symptoms and the overall quality of life for patients. However, a surprisingly high number of patients discontinued treatment due to adverse effects related to the therapy. Skin reactions, previously reported and confirmed to be associated with sunlight exposure, lead our study to further investigate the phototoxicity of AVP. Therefore, AVP, through the *in vitro* NRU assay, revealed a PIF value of approximately 11, indicating clear phototoxic potential. This aligns with FDA toxicity outcomes, which reported a slight potential for phototoxicity associated with AVP.

Given this context, we investigated protein photooxidation to understand the mechanisms underlying the observed phototoxicity. Thus, AVP demonstrated the ability to induce dose-dependent protein oxidation, leading to an approximately 4-fold increase in carbonyl content. Consequently, AVP exhibited significant photooxidative activity toward proteins. Moreover, DNA was also identified as potential target for AVP phototoxic properties. In fact, the drug induced approximately 45% DNA damage after exposure to UVA light, and recovery experiments indicated persistent damage even after an 18 h recovery period.

Despite the highlighted phototoxicity of AVP in keratinocyte cells, the photophysical studies failed to elucidate the mechanisms underlying this photobiological behavior. Nonetheless, as previously outlined, the oxidatively deaminated metabolite serves as the primary circulating Phase I radioactive component. Furthermore, research indicates that keratinocytes can express select isoforms of CYP450 enzymes, albeit at lower levels

compared to hepatocytes. These enzymes may participate in the metabolism of specific compounds, thereby contributing to the overall drug biotransformation process[249,250]. For instance, the oxidative metabolism of AVP is predominantly mediated by isoforms such as CYP3A4, which has been previously identified in monolayers of cultured keratinocytes[251]. Thus, one feasible explanation behind the inactivity of AVP upon UVA excitation could be its in vitro biotransformation to a more reactive metabolite. However, this does not exclude other mechanisms contributing to the low photophysical profile of this drug, which should be further studied.

All in all, the phototoxic behavior of AVP was successfully demonstrated in keratinocyte cells and the observed protein photooxidative potential and photogenotoxicity suggest potential mechanisms contributing to this phototoxicity. Thus, confirming the previously reported and warranted risk of photosensitivity associated with this anticancer drug.

CHAPTER 9 Conclusions

This doctoral thesis delves into a multidisciplinary study, evaluating the photophysical and photobiological properties of several tyrosine kinase inhibitors (TKIs), a family of anticancer drugs introduced in the last century for treating a multitude of cancer diseases. Thus, four TKIs were selected based on two criteria: UVA light absorption and phototoxicity potential in keratinocyte cells (HaCaT). Subsequently, a comprehensive study of the photo(geno)toxicity and photophysics was conducted for gefitinib, axitinib, dasatinib, and avapritinib. The following conclusions can be derived for each investigated drug:

1. Gefitinib (GFT):
    - GFT is a phototoxic drug with a photoirritant factor (PIF) of approximately 13 determined by the neutral red uptake assay (NRU) in keratinocyte cells (HaCaT).
    - Compared to GFT, *O*-demethyl gefitinib (DMT-GFT) metabolite was less phototoxic (PIF value of approximately 7).
    - *O*-Demorpholinopropyl gefitinib (DMOR-GFT) metabolite exhibited higher phototoxicity compared to the parent drug (PIF value of approximately 48).
    - 4-Defluoro-4-hydroxy gefitinib (DF-GFT) metabolite was not phototoxic.
    - Fluorescence emission of GFT and metabolites experienced enhancement in the presence of human serum albumin (HSA) and within HaCaT cells. The fluorescence emission quantum yield in HaCaT cells (Φ_F) was *ca.* 0.07, 0.04 and 0.1 for GFT, DMT-GFT and DMOR-GFT, respectively.

- Efficient uptake and cytoplasmic distribution within HaCaT cells for both the drug and metabolites were observed by confocal microscopy.
- Photosensitized lipid peroxidation was only detected for DMOR-GFT metabolite, generating a substantial amount of thiobarbituric acid reactive substances (TBARS) comparable to the reference (ketoprofen).
- Photodynamic lipid peroxidation was triggered by DMOR-GFT through a Type I mechanism based on the low generation of singlet oxygen ($^1O_2$) and the quenching of triplet species by the lipid model, 1,4-dihydro-1,2-dimethylbenzoic (DMBA).
- GFT and DMOR-GFT exhibited high photooxidative activity toward HSA through the 2,4-dinitrophenylhydrazine (DNPH) derivatization method. However, DMT-GFT did not display significant photooxidative activity toward HSA.
- GFT followed by DMT-GFT exhibited the highest photogenotoxicity potential (72 and 54%, respectively), whereas DMOR-GFT showed a 45% DNA photodamage. Only GFT-treated keratinocytes repaired *ca.* 30% of the initial DNA damage.
- GFT and DMOR-GFT induced a concentration-dependent activation of caspase-3/7, indicative of apoptosis, after UVA light exposure. In contrast, DMT-GFT caspase-3/7 activity was similar between the concentration representing the 100% cell viability and the concentration corresponding to IC50.
- GFT and DMOR-GFT showed a significant increase in lactate dehydrogenase (LDH), as a marker for necrosis. Contrary, DMT-GFT did not exhibit any increase in LDH release.

2. Axitinib (AXT)
   - *(E)*-AXT undergoes photolysis in PBS solution and in the presence of equimolar concentration of calf thymus DNA (ctDNA). A photoisomerization to *(Z)*-AXT was observed in both MeCN solution and in the presence of equimolar HSA.
   - *(Z)*-AXT experiences photoisomerization back to *(E)*-AXT both in PBS solution and in the presence of equimolar ctDNA. However, the *Z* isomer was photostable within HSA protein.
   - *(E)*-AXT is non-cytotoxic drug with an IC50 in dark conditions higher than 500 μM.
   - *(Z)*-AXT is a cytotoxic drug with an IC50 in dark conditions of approximately 81 μM and a phototoxic drug with a PIF value of about 6.
   - *(Z)*-AXT induced photooxidation toward HSA with a carbonyl content reaching a value of approximately 3 nmol at a UVA dose of 15 J/cm^2.
   - UVA-irradiated HaCaT cells did not express DNA damage through comet assay upon drug exposure. However, UVA-irradiated, and treated Bj-hTERT fibroblasts expressed γ-H2AX foci.

3. Dasatinib (DAS)
   - DAS is a phototoxic drug with a PIF value of approximately 5 determined by the NRU assay in HaCaT cells.
   - DAS formulated in an oil-in-water (O/W) emulsion (0.45%) resulted to be phototoxic (viability reduction of *ca.* 45%) as revealed by MTT assay performed on reconstructed human epidermis. However, the phototoxic effect was efficiently

mitigated following the incorporation of a broad-spectrum UV filter (tinosorb S) into the formulation.

- DAS induced significant lipid photoperoxidation in FSK fibroblast cells detected by C11-Bodipy$^{581/591}$ sensor. The reduction on the ratio between red and green fluorescence emission intensity at 50 μM was higher than 1-fold.
- DAS induced a dose-dependent carbonylation in the HSA protein, resulting in an approximately 3-fold increase at 50 μM.
- DAS-induced level of DNA damage was approximately 55%, and recovery experiments indicated persistent DNA damage even after an 18 h period.
- DAS stimulated considerable number of γ-H2AX foci within the nuclei of photoexposed-Bj-hTERT cells.
- Singlet excited state of DAS displayed low quantum yield in HaCaT cells (Φ_F around 0.001) and singlet energy of about 343 kJ/mol in both EtOH and PBS solution.
- Through transient absorption spectroscopy, a maximum of around 490 nm was detected in EtOH, acetonitrile (MeCN), dichloromethane (DCM) and 1,4-dioxane (DX). The lifetime of this transient species (τ_T) in deareated atmosphere ranged between 1 and 3 μs.
- The transient species was effectively quenched by molecular oxygen with a quenching rate constant (kq) *ca.* $6.9 \cdot 10^{10}$ M^{-1} s^{-1}.
- The transient species was substantially quenched in the presence of naproxen (NPX) through a triplet–triplet energy transfer process from DAS to NPX (kq *ca.* 1.02×10^{10} M^{-1} s^{-1}). A new

transient was formed at λ_{max} ~430 nm corresponding to NPX triplet excited state.

- The triplet excited energy level of DAS, determined through a 15% increase in its phosphorescence emission, was approximately 274.5 kJ/mol.
- A singlet oxygen ($^1O_2$) luminescence signal was detected at 1270 nm upon the excitation of DAS at 355 nm. The $^1O_2$ lifetimes (τ_Δ) were approximately 8, 13, 24 and 9 μs in EtOH, MeCN, DCM and DX, respectively. The $^1O_2$ quantum yields (Φ_Δ) were approximately 0.1 in EtOH and MeCN, and 0.2 in DCM and DX, respectively. $^1O_2$ generated upon the excitation of perinaphtenone was significantly quenched by DAS (kq_Δ *ca.* 1×10^7 M^{-1} s^{-1}).
- The triplet excited state of DAS was quenched by both linoleic acid (kq *ca.* 1.7×10^8 M^{-1} s^{-1}) and 3-methylindole (kq *ca.* 4.3×10^7 M^{-1} s^{-1}), but not by guanosine.

4. Avapritinib (AVP)
   - AVP is a phototoxic drug with a PIF value of approximately 11 determined by the NRU assay in HaCaT cells.
   - The singlet excited state of AVP has low quantum yield in both PBS and HaCaT cells (Φ_F around 0.06).
   - AVP induced a dose-dependent HSA carbonylation, resulting in an approximately 4-fold increase at 50 μM and 15 J/cm^2 UVA dose.
   - The level of DNA damage induced by AVP was approximately 45% at a concentration of 2 μM, and it was even higher at 5 μM (*ca.* 55%).

REFERENCES

1. Hanahan, D. “Hallmarks of Cancer: New Dimensions,” *Cancer Discovery*, V. 12, No. 1, 2022, pp. 31–46.

2. Hanahan, D., and Weinberg, R. A. “Hallmarks of Cancer: The Next Generation,” *Cell*, V. 144, No. 5, 2011, pp. 646–74.

3. International Agency for Research on Cancer. “Statistics on Cancer 2020,” *Global Cancer Observatory*, n.d.

4. Sung, H., Ferlay, J., Siegel, R. L., et al. “Global Cancer Statistics 2020: GLOBOCAN Estimates of Incidence and Mortality Worldwide for 36 Cancers in 185 Countries,” *CA: A Cancer Journal for Clinicians*, V. 71, No. 3, 2021, pp. 209–49.

5. Debela, D. T., Muzazu, S. G., Heraro, K. D., et al. “New approaches and procedures for cancer treatment: Current perspectives,” *SAGE Open Medicine*, V. 9, 2021, pp. 205031212110343.

6. Pucci, C., Martinelli, C., and Ciofani, G. “Innovative approaches for cancer treatment: current perspectives and new challenges,” *ecancermedicalscience*, V. 13, 2019.

7. Padma, V. V. “An overview of targeted cancer therapy,” *BioMedicine*, V. 5, No. 4, 2015, pp. 19.

8. Zhou, Z., and Li, M. “Targeted therapies for cancer,” *BMC Medicine*, V. 20, No. 1, 2022, pp. 90, s12916-022-02287–3.

9. Baudino, T. “Targeted Cancer Therapy: The Next Generation of Cancer Treatment,” *Current Drug Discovery Technologies*, V. 12, No. 1, 2015, pp. 3–20.

10. Houston Methodist “Cancer tratment options.”

11. Hubbard, S. R., and Till, J. H. “Protein Tyrosine Kinase Structure and Function,” *Annual Review of Biochemistry*, V. 69, No. 1, 2000, pp. 373–98.

12. Sudhesh Dev, S., Zainal Abidin, S. A., Farghadani, R., et al. “Receptor Tyrosine Kinases and Their Signaling Pathways as Therapeutic Targets of Curcumin in Cancer,” *Frontiers in Pharmacology*, V. 12, 2021, pp. 772510.

13. Paul, M. K., and Mukhopadhyay, A. K. “Tyrosine kinase – Role and significance in Cancer,” *International Journal of Medical Sciences*, 2004, pp. 101–15.

14. Gocek, E., Moulas, A. N., and Studzinski, G. P. “Non-receptor protein tyrosine kinases signaling pathways in normal and cancer cells,” *Critical Reviews in Clinical Laboratory Sciences*, V. 51, No. 3, 2014, pp. 125–37.

15. Yamaoka, T., Kusumoto, S., Ando, K., et al. “Receptor Tyrosine Kinase-Targeted Cancer Therapy,” *International Journal of Molecular Sciences*, V. 19, No. 11, 2018, pp. 3491.

16. Jiao, Q., Bi, L., Ren, Y., et al. “Advances in studies of tyrosine kinase inhibitors and their acquired resistance,” *Molecular Cancer*, V. 17, No. 1, 2018, pp. 36.

17. Siveen, K. S., Prabhu, K. S., Achkar, I. W., et al. “Role of Non Receptor Tyrosine Kinases in Hematological Malignances and its Targeting by Natural Products,” *Molecular Cancer*, V. 17, No. 1, 2018, pp. 31.

18. Mongre, R. K., Mishra, C. B., Shukla, A. K., et al. “Emerging Importance of Tyrosine Kinase Inhibitors against Cancer: Quo Vadis to Cure?,” *International Journal of Molecular Sciences*, V. 22, No. 21, 2021, pp. 11659.

19. Pottier, C., Fresnais, M., Gilon, M., et al. “Tyrosine Kinase Inhibitors in Cancer: Breakthrough and Challenges of Targeted Therapy,” *Cancers*, V. 12, No. 3, 2020, pp. 731.

20. Huang, L., Jiang, S., and Shi, Y. “Tyrosine kinase inhibitors for solid tumors in the past 20 years (2001–2020),” *Journal of Hematology & Oncology*, V. 13, No. 1, 2020, pp. 143.

21. Imai, K., and Takaoka, A. “Comparing antibody and small-molecule therapies for cancer,” *Nature Reviews Cancer*, V. 6, No. 9, 2006, pp. 714–27.

22. Roskoski, R. “Properties of FDA-approved small molecule protein kinase inhibitors,” *Pharmacological Research*, V. 144, 2019, pp. 19–50.

23. World Health Organization. “Suffixes used in the selection of INN,” *Medicines and Health Products*, 2021.

24. Liu, S., and Kurzrock, R. “Toxicity of targeted therapy: Implications for response and impact of genetic polymorphisms,” *Cancer Treatment Reviews*, V. 40, No. 7, 2014, pp. 883–91.

25. Obradovic, J., Todosijevic, J., and Jurisic, V. “Side effects of tyrosine kinase inhibitors therapy in patients with non-small cell lung cancer and associations with *EGFR* polymorphisms: A systematic review and meta-analysis,” *Oncology Letters*, V. 25, No. 2, 2022, pp. 62.

26. Shyam Sunder, S., Sharma, U. C., and Pokharel, S. “Adverse effects of tyrosine kinase inhibitors in cancer therapy: pathophysiology, mechanisms and clinical management,” *Signal Transduction and Targeted Therapy*, V. 8, No. 1, 2023, pp. 262.

27. Xu, Z., Cang, S., Yang, T., et al. “Cardiotoxicity of tyrosine kinase inhibitors in chronic myelogenous leukemia therapy,” *Hematology Reports*, V. 1, No. 1, 2009, pp. 4.

28. Tseng, L.-C., Chen, K.-H., Wang, C.-L., et al. “Effects of tyrosine kinase inhibitor therapy on skin toxicity and skin-related quality of life in patients with lung cancer: An observational study,” *Medicine*, V. 99, No. 23, 2020, pp. e20510.

29. Holcmann, M., and Sibilia, M. “Mechanisms underlying skin disorders induced by EGFR inhibitors,” *Molecular & Cellular Oncology*, V. 2, No. 4, 2015, pp. e1004969.

30. Liu, H., Wu, Y., Lv, T., et al. “Skin Rash could Predict the Response to EGFR Tyrosine Kinase Inhibitor and the Prognosis for Patients with Non-Small Cell Lung Cancer: A Systematic Review and Meta-Analysis,” *PLoS ONE*, V. 8, No. 1, 2013, pp. e55128.

31. Lembo, S., Raimondo, A., Conti, V., et al. “Photosensitivity and cancer immune-targeted therapies,” *Photodermatology, Photoimmunology & Photomedicine*, V. 36, No. 3, 2020, pp. 172–8.

32. Fenner, J., and Clark, R. A. F. “Anatomy, Physiology, Histology, and Immunohistochemistry of Human Skin.” Skin Tissue Engineering and Regenerative Medicine. Elsevier, 2016. pp. 1–17.

33. Greaves, M. W. “Physiology of Skin,” *Journal of Investigative Dermatology*, V. 67, No. 1, 1976, pp. 66–9.

35. Gilaberte, Y., Prieto-Torres, L., Pastushenko, I., et al. “Anatomy and Function of the Skin.” *Nanoscience in Dermatology*. Elsevier, 2016. pp. 1–14.

35. Slominski, A. T., Hardeland, R., Zmijewski, M. A., et al. “Melatonin: A Cutaneous Perspective on its Production, Metabolism, and Functions,” *Journal of Investigative Dermatology*, V. 138, No. 3, 2018, pp. 490–9.

36. Graham, H. K., McConnell, J. C., Limbert, G., et al. “How stiff is skin?,” *Experimental Dermatology*, V. 28, No. S1, 2019, pp. 4–9.

38. Barbieri, J. S., Wanat, K., and Seykora, J. “Skin: Basic Structure and Function.” *Pathobiology of Human Disease*, 2014. pp. 1134–44.

38. Bennett, M. F., Robinson, M. K., Baron, E. D., et al. “Skin Immune Systems and Inflammation: Protector of the Skin or Promoter of Aging?,” *Journal of Investigative Dermatology Symposium Proceedings*, V. 13, No. 1, 2008, pp. 15–9.

39. Baron, J. M., Höller, D., Schiffer, R., et al. “Expression of Multiple Cytochrome P450 Enzymes and Multidrug Resistance-Associated Transport Proteins in Human Skin Keratinocytes,” *Journal of Investigative Dermatology*, V. 116, No. 4, 2001, pp. 541–8.

40. Young, A. R., Potten, C. S., Nikaido, O., et al. “Human Melanocytes and Keratinocytes Exposed to UVB or UVA In Vivo Show Comparable Levels of Thymine Dimers,” *Journal of Investigative Dermatology*, V. 111, No. 6, 1998, pp. 936–40.

41. Plikus, M. V., Wang, X., Sinha, S., et al. “Fibroblasts: Origins, definitions, and functions in health and disease,” *Cell*, V. 184, No. 15, 2021, pp. 3852–72.

42. McAnulty, R. J. “Fibroblasts and myofibroblasts: Their source, function and role in disease,” *The International Journal of Biochemistry & Cell Biology*, V. 39, No. 4, 2007, pp. 666–71.

43. Venkatakrishnan, A., Chu, B., and Aggarwal, P. “Photosensitivity From Avapritinib: Pharamacovigilance Analysis,” *JMIR Dermatology*, V. 5, No. 3, 2022, pp. e39229.

44. Diffey, B. L. “Sources and measurement of ultraviolet radiation,” *Methods*, V. 28, No. 1, 2002, pp. 4–13.

45. Monteiro, A. F., Rato, M., and Martins, C. “Drug-induced photosensitivity: Photoallergic and phototoxic reactions,” *Clinics in Dermatology*, V. 34, No. 5, 2016, pp. 571–81.

46. Wang, P.-W., Hung, Y.-C., Lin, T.-Y., et al. “Comparison of the Biological Impact of UVA and UVB upon the Skin with Functional Proteomics and Immunohistochemistry,” *Antioxidants*, V. 8, No. 12, 2019, pp. 569.

47. Hofmann, G. A., and Weber, B. “Drug-induced photosensitivity: culprit drugs, potential mechanisms and clinical consequences,” *JDDG: Journal der Deutschen Dermatologischen Gesellschaft*, V. 19, No. 1, 2021, pp. 19–29.

48. Department of Health and Human Services Food and Drug Administration. “S10 Photosafety Evaluation of Pharmaceuticals,” 2015.

49. Udompanich, S., Chanprapaph, K., and Rajatanavin, N. “Phototoxic Reaction Induced by Pazopanib,” *Case Reports in Dermatology*, V. 10, No. 3, 2018, pp. 251–6.

50. Rosenbaum, S. E., Wu, S., Newman, M. A., et al. “Dermatological reactions to the multitargeted tyrosine kinase inhibitor sunitinib,” *Supportive Care in Cancer*, V. 16, No. 6, 2008, pp. 557–66.

51. Bostan, E., Gulseren, D., and Gokoz, O. “Phototoxic drug eruption induced by vandetanib used for the treatment of metastatic medullary thyroid cancer,” *Anais Brasileiros de Dermatologia*, V. 97, No. 5, 2022, pp. 695–6.

52. Korman, A. M., Reynolds, K. A., Nabhan, F. A., et al. “Vandetanib-induced Phototoxic Drug Eruption Treated with Polypodium Leucotomos Extract: A Case Report and Review of the Literature.,” *The Journal of clinical and aesthetic dermatology*, V. 12 10, 2019, pp. 35–8.

53. Salvador, A., Vedaldi, D., Brun, P., et al. “Vandetanib-induced phototoxicity in human keratinocytes NCTC-2544,” *Toxicology in Vitro*, V. 28, No. 5, 2014, pp. 803–11.

54. Goldstein, J., Patel, A. B., Curry, J. L., et al. “Photoallergic reaction in a patient receiving vandetanib for metastatic follicular thyroid carcinoma: a case report,” *BMC Dermatology*, V. 15, No. 1, 2015, pp. 2.

55. Morgado, F., Calvão, J., Barata, F., et al. “Phototoxic reaction to brigatinib – a new photosensitizing drug,” *Journal of the European Academy of Dermatology and Venereology*, V. 33, No. 12, 2019.

59. Yie, C., Rosenblum, J., Banta, E., et al. “Brigatinib induced photosensitivity,” *Annals of Allergy, Asthma & Immunology*, V. 129, No. 5, 2022, pp. S104.

57. Böhm, F., Edge, R., Foley, S., et al. “Antioxidant inhibition of porphyrin-induced cellular phototoxicity,” *Journal of Photochemistry and Photobiology B: Biology*, V. 65, Nos. 2–3, 2001, pp. 177–83.

58. Hussain, Z., Qi, Q., Zhu, J., et al. “Protoporphyrin IX-induced phototoxicity: Mechanisms and therapeutics,” *Pharmacology & Therapeutics*, V. 248, 2023, pp. 108487.

59. Willis, Z. I., Boyd, A. S., and Cecilia Di Pentima, M. “Phototoxicity, Pseudoporphyria, and Photo-onycholysis Due to Voriconazole in a Pediatric Patient With Leukemia and Invasive Aspergillosis,” *Journal of the Pediatric Infectious Diseases Society*, V. 4, No. 2, 2015, pp. e22–4.

60. Roveri, G., Nascimbeni, F., Rocchi, E., et al. “Drugs and Acute Porphyrias: Reasons for a Hazardous Relationship,” *Postgraduate Medicine*, V. 126, No. 7, 2014, pp. 108–20.

61. Epstein, J. H. “Phototoxicity and photoallergy,” *Seminars in Cutaneous Medicine and Surgery*, V. 18, No. 4, 1999, pp. 274–84.

62. Gad, S. C. “Photoallergens.” Reference Module in Biomedical Sciences. Elsevier, 2023. pp. B9780128243152005212.

66. Ibbotson, S. H. “Photoallergic Contact Dermatitis.” *Applied Dermatotoxicology*, 2014. pp. 85–114.

67. Hughes, M. F. “Dermal toxicity.” *An Introduction to Interdisciplinary Toxicology*, 2020. pp. 141–51.

65. Stein, K. R., and Scheinfeld, N. S. “Drug-induced photoallergic and phototoxic reactions,” *Expert Opinion on Drug Safety*, V. 6, No. 4, 2007, pp. 431–43.

66. Hinton, A. N., and Goldminz, A. M. “Feeling the Burn,” *Dermatologic Clinics*, V. 38, No. 1, 2020, pp. 165–75.

67. Baptista, M. S., Cadet, J., Di Mascio, P., et al. “Type I and Type II Photosensitized Oxidation Reactions: Guidelines and Mechanistic Pathways,” *Photochemistry and Photobiology*, V. 93, No. 4, 2017, pp. 912–9.

71. Quintero, B., and Miranda, M. “Mechanisms of photosensitization induced by drugs: A general survey,”*Ars Pharmaceutica*, V. 41, No. 1, 1999, pp. 27-46.

69. Bartusik-Aebisher, D., Ożóg, Ł., and Aebisher, D. “Alternative methods of photodynamic therapy and oxygen consumption measurements—A review,” *Biomedicine & Pharmacotherapy*, V. 134, 2021, pp. 111095.

73. Schweitzer, V. G., and Somers, M. L. “Photofrin-mediated photodynamic therapy for treatment of early stage (Tis-T2N0M0) SqCCa of oral cavity and oropharynx,” *Lasers in Surgery and Medicine*, V. 42, No. 1, 2010, pp. 1–8.

71. Mateos Pujante, A. “Evaluación del potencial fotoquímico y fotobiológico de los inhibidores de la poli (ADP-ribosa) polimerasa.” Universitat Politècnica de València, Valencia (Spain), 2023.

72. Romiszewska, A., and Nowak-Stępniowska, A. “[Photodynamic reaction and oxidative stress - influence of the photodynamic effect on the activity antioxidant enzymes],” *Postepy biochemii*, V. 60, 2014, pp. 355–64.

73. Therond, P. “Dommages créés aux biomolécules (lipides, protéines, ADN) par le stress oxydant,” *Annales Pharmaceutiques Françaises*, V. 64, No. 6, 2006, pp. 383–9.

74. Juan, C. A., Pérez De La Lastra, J. M., Plou, F. J., et al. “The Chemistry of Reactive Oxygen Species (ROS) Revisited: Outlining Their Role in Biological Macromolecules (DNA, Lipids and Proteins) and Induced Pathologies,” *International Journal of Molecular Sciences*, V. 22, No. 9, 2021, pp. 4642.

75. Su, L.-J., Zhang, J.-H., Gomez, H., et al. “Reactive Oxygen Species-Induced Lipid Peroxidation in Apoptosis, Autophagy, and Ferroptosis,” *Oxidative Medicine and Cellular Longevity*, V. 2019, 2019, pp. 1–13.

76. Zhang, W., Xiao, S., and Ahn, D. U. “Protein Oxidation: Basic Principles and Implications for Meat Quality,” *Critical Reviews in Food Science and Nutrition*, V. 53, No. 11, 2013, pp. 1191–201.

77. Cadet, J., and Wagner, J. R. “DNA Base Damage by Reactive Oxygen Species, Oxidizing Agents, and UV Radiation,” *Cold Spring Harbor Perspectives in Biology*, V. 5, No. 2, 2013, pp. a012559–a012559.

78. Srinivas, U. S., Tan, B. W. Q., Vellayappan, B. A., et al. “ROS and the DNA damage response in cancer,” *Redox Biology*, V. 25, 2019, pp. 101084.

79. Martin, L. J. “DNA Damage and Repair: Relevance to Mechanisms of Neurodegeneration,” *Journal of Neuropathology & Experimental Neurology*, V. 67, No. 5, 2008, pp. 377–87.

80. Giglia-Mari, G., Zotter, A., and Vermeulen, W. “DNA Damage Response,” *Cold Spring Harbor Perspectives in Biology*, V. 3, No. 1, 2011, pp. a000745–a000745.

81. Vechtomova, Y., Telegina, T., Buglak, A., et al. “UV Radiation in DNA Damage and Repair Involving DNA-Photolyases and Cryptochromes,” *Biomedicines*, V. 9, No. 11, 2021, pp. 1564.

82. Kciuk, M., Marciniak, B., Mojzych, M., et al. “Focus on UV-Induced DNA Damage and Repair—Disease Relevance and Protective Strategies,” *International Journal of Molecular Sciences*, V. 21, No. 19, 2020, pp. 7264.

83. Yokoyama, H., and Mizutani, R. “Structural Biology of DNA (6-4) Photoproducts Formed by Ultraviolet Radiation and Interactions with Their Binding Proteins,” *International Journal of Molecular Sciences*, V. 15, No. 11, 2014, pp. 20321–38.

84. Cadet, J., Mouret, S., Ravanat, J., et al. “Photoinduced Damage to Cellular DNA: Direct and Photosensitized Reactions,” *Photochemistry and Photobiology*, V. 88, No. 5, 2012, pp. 1048–65.

85. Sies, H., and Menck, C. F. M. “Singlet oxygen induced DNA damage,” *Mutation Research/DNAging*, V. 275, Nos. 3–6, 1992, pp. 367–75.

86. Hu, J., De Souza-Pinto, N. C., Haraguchi, K., et al. “Repair of Formamidopyrimidines in DNA Involves Different Glycosylases,” *Journal of Biological Chemistry*, V. 280, No. 49, 2005, pp. 40544–51.

87. Mori, T., Nakane, H., Iwamoto, T., et al. “High levels of oxidatively generated DNA damage 8,5′-cyclo-2′-deoxyadenosine accumulate in the brain tissues of xeroderma pigmentosum group A gene-knockout mice,” *DNA Repair*, V. 80, 2019, pp. 52–8.

88. Chatgilialoglu, C., Krokidis, M. G., Papadopoulos, K., et al. “Purine 5′,8-cyclo-2′-deoxynucleoside lesions in irradiated DNA,” *Radiation Physics and Chemistry*, V. 128, 2016, pp. 75–81.

89. Douki, T., Bérard, I., Wack, A., et al. “Contribution of Cytosine-Containing Cyclobutane Dimers to DNA Damage Produced by Photosensitized Triplet–Triplet Energy Transfer,” *Chemistry – A European Journal*, V. 20, No. 19, 2014, pp. 5787–94.

90. Lu, C., Gutierrez-Bayona, N. E., and Taylor, J.-S. “The effect of flanking bases on direct and triplet sensitized cyclobutane pyrimidine dimer formation in DNA depends on the dipyrimidine, wavelength and the photosensitizer,” *Nucleic Acids Research*, V. 49, No. 8, 2021, pp. 4266–80.

92. Sharma, A., Singh, K., and Almasan, A. “Histone H2AX Phosphorylation: A Marker for DNA Damage”. DNA Repair Protocols, vol. 920. Totowa, NJ, Humana Press, 2012. pp. 613–26.

92. Cannan, W. J., and Pederson, D. S. “Mechanisms and Consequences of Double-Strand DNA Break Formation in Chromatin,” *Journal of Cellular Physiology*, V. 231, No. 1, 2016, pp. 3–14.

93. Mah, L.-J., El-Osta, A., and Karagiannis, T. C. “γH2AX: a sensitive molecular marker of DNA damage and repair,” *Leukemia*, V. 24, No. 4, 2010, pp. 679–86.

94. Noubissi, F. K., McBride, A. A., Leppert, H. G., et al. “Detection and quantification of γ-H2AX using a dissociation enhanced lanthanide fluorescence immunoassay,” *Scientific Reports*, V. 11, No. 1, 2021, pp. 8945.

95. Galluzzi, L., Vitale, I., Aaronson, S. A., et al. “Molecular mechanisms of cell death: recommendations of the Nomenclature Committee on Cell Death 2018,” *Cell Death & Differentiation*, V. 25, No. 3, 2018, pp. 486–541.

97. Tang, D., and Kang, R. “Cell death.” Mechanisms of Cell Death and Opportunities for Therapeutic Development. *Elsevier*, 2022. pp. 47–64.

97. D’Arcy, M. S. “Cell death: a review of the major forms of apoptosis, necrosis and autophagy,” *Cell Biology International*, V. 43, No. 6, 2019, pp. 582–92.

98. Yan, G., Elbadawi, M., and Efferth, T. “Multiple cell death modalities and their key features (Review),” *World Academy of Sciences Journal*, 2020.

99. Lossi, L. “The concept of intrinsic versus extrinsic apoptosis,” *Biochemical Journal*, V. 479, No. 3, 2022, pp. 357–84.

100. Lindblad, A., Johansson, C., Persson, K., et al. “The role of caspase-1, caspase-4 and NLRP3 in regulating the host cell response evoked by uropathogenic Escherichia coli,” *Scientific Reports*, V. 12, No. 1, 2022, pp. 2005.

101. Proskuryakov, S. Y. a., Konoplyannikov, A. G., and Gabai, V. L. “Necrosis: a specific form of programmed cell death?,” *Experimental Cell Research*, V. 283, No. 1, 2003, pp. 1–16.

102. Festjens, N., Vanden Berghe, T., and Vandenabeele, P. “Necrosis, a well-orchestrated form of cell demise: Signalling cascades, important mediators and concomitant immune response,” *Biochimica et Biophysica Acta (BBA) - Bioenergetics*, V. 1757, Nos. 9–10, 2006, pp. 1371–87.

103. Chan, F. K.-M., Moriwaki, K., and De Rosa, M. J. “Detection of Necrosis by Release of Lactate Dehydrogenase Activity.” In: Snow, A. L., Lenardo, M. J., eds. Immune Homeostasis, vol. 979. Totowa, NJ, Humana Press, 2013. pp. 65–70.

104. Oelgemöller, M., and Hoffmann, N. “Studies in organic and physical photochemistry – an interdisciplinary approach,” *Organic & Biomolecular Chemistry*, V. 14, No. 31, 2016, pp. 7392–442.

105. Mai, S., and González, L. “Molecular Photochemistry: Recent Developments in Theory,” *Angewandte Chemie International Edition*, V. 59, No. 39, 2020, pp. 16832–46.

106. Kowalska, J., Rok, J., Rzepka, Z., et al. “Drug-Induced Photosensitivity—From Light and Chemistry to Biological Reactions and Clinical Symptoms,” *Pharmaceuticals*, V. 14, No. 8, 2021, pp. 723.

107. Nau, W. “Modern Molecular Photochemistry of Organic Molecules. by N. J. Turro, V. Ramamurthy, J. C. Scaiano.,” *ChemPhysChem*, V. 12, No. 13, 2011, pp. 2496–7.

108. Wittig, C. “Photochemistry, Molecular.” Encyclopedia of Physical Science and Technology. Elsevier, 2003. pp. 29–47.

110. Turro, N. J., Ramamurthy, V., Scaiano, J. C., et al. “Modern molecular photochemistry of organic molecules,” Sausalito, California, *University Science Books*, 2010, 1084 pp.

111. Van Loon, J. C., and Van Loon, J. C. “Analytical atomic absorption spectroscopy: selected methods,” *New York, Academic Press,* 1980.

112. Montalti, M., Credi, A., Prodi, L., et al. “Handbook of photochemistry,” Third edition, Boca Raton, C*RC/Taylor & Francis*, 2006.

112. Nilapwar, S. M., Nardelli, M., Westerhoff, H. V., et al. “Absorption Spectroscopy.” Methods in Enzymology, vol. 500. Elsevier, 2011. pp. 59–75.

114. Jameson, D. M. “Introduction to fluorescence,” Boca Raton, *CRC Press Taylor & Francis*, 2014, 295 pp.

115. Jameson, D. M., Croney, J. C., and Moens, P. D. J. “[1] Fluorescence: Basic concepts, practical aspects, and some anecdotes.” *Methods in Enzymology*, vol. 360. Elsevier, 2003. pp. 1–43.

116. Lakowicz, J. R. “Principles of fluorescence spectroscopy,” Third edition, corrected at 4. printing, *New York, NY, Springer*, 2010, 954 pp.

117. Rendell, D., and Mowthorpe, D. J. “Fluorescence and phosphorescence spectroscopy,” *ACOL, London by Wiley*, 1987, 419 pp.

118. Garcia-Revilla, M. A., and Vargas-Rodríguez, I. “Photochemistry: A topological perspective.” *Advances in Quantum Chemical Topology Beyond QTAIM*, 2023. pp. 515–40.

119. Schulman, S. G. “Fluorescence and phosphorescence spectroscopy: physicochemical principles and practice,” *1st ed, Oxford, England, Pergamon Press*, 1979.

120. Guinn, V. P. “Radioactivity.” *Encyclopedia of Physical Science and Technology. Elsevier*, 2003. pp. 661–74.

120. Penfold, T. J., Gindensperger, E., Daniel, C., et al. “Spin-Vibronic Mechanism for Intersystem Crossing,” *Chemical Reviews*, V. 118, No. 15, 2018, pp. 6975–7025.

121. Baptista, M. S., Cadet, J., Greer, A., et al. “Photosensitization Reactions of Biomolecules: Definition, Targets and Mechanisms,” *Photochemistry and Photobiology*, V. 97, No. 6, 2021, pp. 1456–83.

122. Fahmy, S. A., Azzazy, H. M. E.-S., and Schaefer, J. “Liposome Photosensitizer Formulations for Effective Cancer Photodynamic Therapy,” *Pharmaceutics*, V. 13, No. 9, 2021, pp. 1345.

124. Bregnhøj, M. “The electronic transitions of molecular oxygen,” *Cham, Springe*r, 2019, 151 pp.

124. Crous, A., and Abrahamse, H. “Targeted Photodynamic Therapy for Improved Lung Cancer Treatment.” In: Torres, A. F. C., ed. Lung Cancer - Strategies for Diagnosis and Treatment. InTech, 2018.

126. Nonell, S., and Flors, C., eds. “Singlet oxygen: applications in biosciences and nanosciences,” *Cambridge, Royal Society of Chemistry*, 2016, 2 pp.

127. “Singlet oxygen. volume 2,” *Cambridge, UK, Royal Society of Chemistry*, 2016.

127. Mao, F., Ni, W., Xu, X., et al. “Chemical Structure-Related Drug-Like Criteria of Global Approved Drugs,” *Molecules*, V. 21, No. 1, 2016, pp. 75.

128. Selvam, T. P., and Palanirajan, V. K. “Quinazoline Marketed drugs - A Review.” 2011.

129. Luu, M., Lai, S. E., Patel, J., et al. “Photosensitive rash due to the epidermal growth factor receptor inhibitor erlotinib,” *Photodermatology, Photoimmunology & Photomedicine*, V. 23, No. 1, 2007, pp. 42–5.

130. Kozuki, T. “Skin problems and EGFR-tyrosine kinase inhibitor,” *Japanese Journal of Clinical Oncology*, V. 46, No. 4, 2016, pp. 291–8.

131. García-Lainez, G., Vayá, I., Marín, M. P., et al. “In vitro assessment of the photo(geno)toxicity associated with Lapatinib, a Tyrosine Kinase inhibitor,” *Archives of Toxicology*, V. 95, No. 1, 2021, pp. 169–78.

132. Vayá, I., Andreu, I., Lence, E., et al. “Characterization of Locally Excited and Charge-Transfer States of the Anticancer Drug Lapatinib by Ultrafast Spectroscopy and Computational Studies,” *Chemistry – A European Journal*, V. 26, No. 68, 2020, pp. 15922–30.

133. Andreu, I., Lence, E., González-Bello, C., et al. “Protein Binding of Lapatinib and Its N- and O-Dealkylated Metabolites Interrogated by Fluorescence, Ultrafast Spectroscopy and Molecular Dynamics Simulations,” *Frontiers in Pharmacology*, V. 11, 2020, pp. 576495.

134. Nardi, G., Lhiaubet-Vallet, V., and Miranda, M. A. “Photosensitization by Imatinib. A Photochemical and Photobiological Study of the Drug and Its Substructures,” *Chemical Research in Toxicology*, V. 27, No. 11, 2014, pp. 1990–5.

135. Sun, W., Kajimoto, Y., Inoue, H., et al. “Gefitinib enhances the efficacy of photodynamic therapy using 5-aminolevulinic acid in malignant brain tumor cells,” *Photodiagnosis and Photodynamic Therapy*, V. 10, No. 1, 2013, pp. 42–50.

136. Liu, W., Baer, M. R., Bowman, M. J., et al. “The Tyrosine Kinase Inhibitor Imatinib Mesylate Enhances the Efficacy of Photodynamic Therapy by Inhibiting ABCG2,” *Clinical Cancer Research*, V. 13, No. 8, 2007, pp. 2463–70.

137. Hua, J., Wu, P., Gan, L., et al. “Current Strategies for Tumor Photodynamic Therapy Combined With Immunotherapy,” *Frontiers in Oncology*, V. 11, 2021, pp. 738323.

138. Yamamoto, S., Fukuhara, H., Lai, H. W., et al. “Photosensitizers in Urology and Potential of Sunitinib, a Tyrosine Kinase Inhibitor, as a Photosensitizer through Drug Repositioning,” *The Journal of Japan Society for Laser Surgery and Medicine*, V. 44, No. 1, 2023, pp. 47–52.

139. Xu, W., Yang, M., Du, X., et al. “Multifunctional Nanoplatform Based on Sunitinib for Synergistic Phototherapy and Molecular Targeted Therapy of Hepatocellular Carcinoma,” *Micromachines*, V. 14, No. 3, 2023, pp. 613.

140. Huang, F., Li, Y., Zhang, X.-J., et al. “Novel chlorin e6-based conjugates of tyrosine kinase inhibitors: Synthesis and photobiological evaluation as potent photosensitizers for photodynamic therapy,” *European Journal of Medicinal Chemistry*, V. 261, 2023, pp. 115787.

141. Andreu, I., Neshchadin, D., Rico, E., et al. “Probing Lipid Peroxidation by Using Linoleic Acid and Benzophenone,” *Chemistry – A European Journal*, V. 17, No. 36, 2011, pp. 10089–96.

142. Edinburgh Instruments Ltd “What is a Spectrometer?” Available at: https://www.edinst.com/blog/what-is-a-spectrometer/.

144. Slavin, W., and Slavin, M. “Atomic absorption spectroscopy,” *New York, Wiley*, 1968, 307 pp.

145. Knowles, A., and Burgess, C. “Practical Absorption Spectrometry: Ultraviolet Spectrometry Group,” Dordrecht, *Springer Netherlands*, 1984.

146. Melhuish, W. H. “Quantum efficiences of organic substances: effect of solvent and concentration of the fluorescent solute [1],” *The Journal of Physical Chemistry*, V. 65, No. 2, 1961, pp. 229–35.

249. De La Peña, D., Martí, C., Noneil, S., et al. “Time-Resolved Near Infrared Studies on Singlet Oxygen Production by the Photosensitizing 2-Arylpropionic Acids,” *Photochemistry and Photobiology*, V. 65, No. 5, 1997, pp. 828–32.

147. Strober, W. “Trypan Blue Exclusion Test of Cell Viability,” *Current Protocols in Immunology*, V. 111, No. 1, 2015.

148. Wassie, A. T., Zhao, Y., and Boyden, E. S. “Expansion microscopy: principles and uses in biological research,” *Nature Methods*, V. 16, No. 1, 2019, pp. 33–41.

149. Chozinski, T. J., Halpern, A. R., Okawa, H., et al. “Expansion microscopy with conventional antibodies and fluorescent proteins,” *Nature Methods*, V. 13, No. 6, 2016, pp. 485–8.

150. Strack, R. “Expansion microscopy,” *Nature Methods*, V. 14, No. 1, 2017, pp. 32–32.

151. Zhuang, Y., and Shi, X. “Expansion microscopy: A chemical approach for super-resolution microscopy,” *Current Opinion in Structural Biology*, V. 81, 2023, pp. 102614.

153. OECD “Test No. 432: In Vitro 3T3 NRU Phototoxicity Test,” *OECD*, 2019.

153. Garcia-Lainez, G., Martínez-Reig, A. M., Limones-Herrero, D., et al. “Photo(geno)toxicity changes associated with hydroxylation of the aromatic chromophores during diclofenac metabolism,” *Toxicology and Applied Pharmacology*, V. 341, 2018, pp. 51–5.

154. Svobodová, A. R., Ulrichová, J., and Vostálová, J. “Human keratinocyte cell line as a suitable alternative model for in vitro phototoxicity testing,” *Anais Brasileiros de Dermatologia*, V. 94, No. 1, 2019, pp. 105–6.

155. Palumbo, F., Garcia-Lainez, G., Limones-Herrero, D., et al. “Enhanced photo(geno)toxicity of demethylated chlorpromazine metabolites,” *Toxicology and Applied Pharmacology*, V. 313, 2016, pp. 131–7.

156. Yang, X., Daifallah, A. E. M., Shankar, S., et al. “Topical kinase inhibitors induce regression of cutaneous squamous cell carcinoma,” *Experimental Dermatology*, V. 28, No. 5, 2019, pp. 609–13.

157. Donthi, M. R., Saha, R. N., Singhvi, G., et al. “Dasatinib-Loaded Topical Nano-Emulgel for Rheumatoid Arthritis: Formulation Design and Optimization by QbD, In Vitro, Ex Vivo, and In Vivo Evaluation,” *Pharmaceutics*, V. 15, No. 3, 2023, pp. 736.

158. Wichaiyo, S., Svasti, S., Maiuthed, A., et al. “Dasatinib Ointment Promotes Healing of Murine Excisional Skin Wound,” *ACS Pharmacology & Translational Science*, V. 6, No. 7, 2023, pp. 1015–27.

160. AEMPS. “Emulsion elaboration PN/L/FF/002/00.” *Spanish National Formulary*. 2023.

161. OECD “Test No. 498: In vitro Phototoxicity - Reconstructed Human Epidermis Phototoxicity test method,” *OECD*, 2023.

161. Seto, Y., Inoue, R., Kato, M., et al. “Photosafety assessments on pirfenidone: Photochemical, photobiological, and pharmacokinetic characterization,” *Journal of Photochemistry and Photobiology B: Biology*, V. 120, 2013, pp. 44–51.

162. Zeb, A., and Ullah, F. “A Simple Spectrophotometric Method for the Determination of Thiobarbituric Acid Reactive Substances in Fried Fast Foods,” *Journal of Analytical Methods in Chemistry*, V. 2016, 2016, pp. 1–5.

163. Bacellar, I. O. L., and Baptista, M. S. “Mechanisms of Photosensitized Lipid Oxidation and Membrane Permeabilization,” *ACS Omega*, V. 4, No. 26, 2019, pp. 21636–46.

164. Colombo, G., Clerici, M., Garavaglia, M. E., et al. “A step-by-step protocol for assaying protein carbonylation in biological samples,” *Journal of Chromatography B*, V. 1019, 2016, pp. 178–90.

165. Ostling, O., and Johanson, K. J. “Microelectrophoretic study of radiation-induced DNA damages in individual mammalian cells,” *Biochemical and Biophysical Research Communications*, V. 123, No. 1, 1984, pp. 291–8.

166. Singh, N. P., McCoy, M. T., Tice, R. R., et al. “A simple technique for quantitation of low levels of DNA damage in individual cells,” *Experimental Cell Research*, V. 175, No. 1, 1988, pp. 184–91.

167. Garcia-Lainez, G., El Ouardi, M., Moreno, A., et al. “Singlet oxygen and radical-mediated mechanisms in the oxidative cellular damage photosensitized by the protease inhibitor simeprevir,” *Free Radical Biology and Medicine*, V. 194, 2023, pp. 42–51.

168. Podhorecka, M., Skladanowski, A., and Bozko, P. “H2AX Phosphorylation: Its Role in DNA Damage Response and Cancer Therapy,” *Journal of Nucleic Acids*, V. 2010, 2010, pp. 1–9.

169. Ruprecht, N., Hungerbühler, M. N., Böhm, I. B., et al. “Improved identification of DNA double strand breaks: γ-H2AX-epitope visualization by confocal microscopy and 3D reconstructed images,” *Radiation and Environmental Biophysics*, V. 58, No. 2, 2019, pp. 295–302.

170. Kumar, S. “Caspase function in programmed cell death,” *Cell Death & Differentiation*, V. 14, No. 1, 2007, pp. 32–43.

171. Kaja, S., Payne, A. J., Singh, T., et al. “An optimized lactate dehydrogenase release assay for screening of drug candidates in neuroscience,” *Journal of Pharmacological and Toxicological Methods*, V. 73, 2015, pp. 1–6.

172. Parhamifar, L., Andersen, H., and Moghimi, S. M. “Lactate Dehydrogenase Assay for Assessment of Polycation Cytotoxicity.” In: Ogris, M., Oupicky, D., eds. Nanotechnology for Nucleic Acid Delivery, vol. 948. Totowa, NJ, Humana Press, 2013. pp. 13–22.

173. Das, A., Sil, A., Khan, I. A., et al. “Dermatological adverse drug reactions to tyrosine kinase inhibitors: a narrative review,” *Clinical and Experimental Dermatology*, V. 48, No. 6, 2023, pp. 599–608.

174. Delgado, L., Giraudier, S., Ortonne, N., et al. “Adverse cutaneous reactions to the new second-generation tyrosine kinase inhibitors (dasatinib, nilotinib) in chronic myeloid leukemia,” *Journal of the American Academy of Dermatology*, V. 69, No. 5, 2013, pp. 839–40.

176. Castell, J. V., Gomez-Lechon, M. J., Hernandez, D., et al. “Molecular basis of phototoxicity: photosensitized cell damage by the major photoproduct of tiaprofenic acid,” *Photochemistry and Photobiology*, V. 60, No. 6, 1994, pp. 586–90.

176. Kazandjian, D., Blumenthal, G. M., Yuan, W., et al. “FDA Approval of Gefitinib for the Treatment of Patients with Metastatic *EGFR* Mutation–

Positive Non–Small Cell Lung Cancer," *Clinical Cancer Research*, V. 22, No. 6, 2016, pp. 1307–12.

177. Cohen, M. H., Williams, G. A., Sridhara, R., et al. "FDA Drug Approval Summary: Gefitinib (ZD1839) (Iressa®) Tablets," *The Oncologist*, V. 8, No. 4, 2003, pp. 303–6.

178. Kobayashi, S., Boggon, T. J., Dayaram, T., et al. "*EGFR* Mutation and Resistance of Non–Small-Cell Lung Cancer to Gefitinib," *New England Journal of Medicine*, V. 352, No. 8, 2005, pp. 786–92.

179. Sordella, R., Bell, D. W., Haber, D. A., et al. "Gefitinib-Sensitizing *EGFR* Mutations in Lung Cancer Activate Anti-Apoptotic Pathways," *Science*, V. 305, No. 5687, 2004, pp. 1163–7.

180. Janjigian, Y. Y., Park, B. J., Zakowski, M. F., et al. "Impact on Disease-Free Survival of Adjuvant Erlotinib or Gefitinib in Patients with Resected Lung Adenocarcinomas that Harbor EGFR Mutations," *Journal of Thoracic Oncology*, V. 6, No. 3, 2011, pp. 569–75.

181. Yang, J. J., Zhou, Q., Yan, H. H., et al. "A phase III randomised controlled trial of erlotinib vs gefitinib in advanced non-small cell lung cancer with EGFR mutations," *British Journal of Cancer*, V. 116, No. 5, 2017, pp. 568–74.

182. Araki, T., Yashima, H., Shimizu, K., et al. "Review of the Treatment of Non-Small Cell Lung Cancer with Gefitinib," *Clinical Medicine Insights: Oncology*, V. 6, 2012, pp. CMO.S7340.

183. Segovia-Mendoza, M., González-González, M. E., Barrera, D., et al. "Efficacy and mechanism of action of the tyrosine kinase inhibitors gefitinib, lapatinib and neratinib in the treatment of HER2-positive breast cancer: preclinical and clinical evidence," *American Journal of Cancer Research*, V. 5, No. 9, 2015, pp. 2531–61.

184. Li, J., Brahmer, J., Messersmith, W., et al. "Binding of gefitinib, an inhibitor of epidermal growth factor receptor-tyrosine kinase, to plasma proteins and blood cells: in vitro and in cancer patients," *Investigational New Drugs*, V. 24, No. 4, 2006, pp. 291–7.

185. Frampton, J. E., and Easthope, S. E. "Gefitinib: A Review of its Use in the Management of Advanced Non-Small-Cell Lung Cancer," *Drugs*, V. 64, No. 21, 2004, pp. 2475–92.

186. Mckillop, D., Mccormick, A. D., Miles, G. S., et al. "*In vitro* metabolism of gefitinib in human liver microsomes," *Xenobiotica*, V. 34, Nos. 11–12, 2004, pp. 983–1000.

187. Li, J., Zhao, M., He, P., et al. "Differential Metabolism of Gefitinib and Erlotinib by Human Cytochrome P450 Enzymes," *Clinical Cancer Research*, V. 13, No. 12, 2007, pp. 3731–7.

188. Tan, W. K., Tan, A. R. Y., Sivanandam, P., et al. "In Vitro Inhibition of Human Aldehyde Oxidase Activity by Clinically Relevant Concentrations of Gefitinib and Erlotinib: Comparison with Select Metabolites, Molecular Docking Analysis, and Impact on Hepatic Metabolism of Zaleplon and Methotrexate," *Journal of Pharmacology and Experimental Therapeutics*, V. 374, No. 2, 2020, pp. 295–307.

189. Herbst, R. S., LoRusso, P. M., Purdom, M., et al. "Dermatologic Side Effects Associated with Gefitinib Therapy: Clinical Experience and Management," *Clinical Lung Cancer*, V. 4, No. 6, 2003, pp. 366–9.

190. Dhillon, S. "Gefitinib: a review of its use in adults with advanced non-small cell lung cancer," *Targeted Oncology*, V. 10, No. 1, 2015, pp. 153–70.

191. European Medicines Agency. "Iressa, INN-gefitinib," 2023.

192. Agúndez, J. A. G., García-Martín, E., García-Lainez, G., et al. "Photomutagenicity of chlorpromazine and its N-demethylated metabolites assessed by NGS," *Scientific Reports*, V. 10, No. 1, 2020, pp. 6879.

193. Onoue, S., and Tsuda, Y. "Analytical Studies on the Prediction of Photosensitive/Phototoxic Potential of Pharmaceutical Substances," *Pharmaceutical Research*, V. 23, No. 1, 2006, pp. 156–64.

194. Tamarit, L., El Ouardi, M., Andreu, I., et al. "Photoprocesses of the tyrosine kinase inhibitor gefitinib: from femtoseconds to microseconds and from solution to cells," *Chemical Science*, V. 12, No. 36, 2021, pp. 12027–35.

195. Tamura, M., Kondo, M., Horio, M., et al. "Genetic polymorphisms of the adenosine triphosphate-binding cassette transporters (ABCG2, ABCB1) and gefitinib toxicity," *Nagoya Journal of Medical Science*, V. 74, Nos. 1–2, 2012, pp. 133–40.

196. Kabir, Md. Z., Tee, W.-V., Mohamad, S. B., et al. "Interaction of an anticancer drug, gefitinib with human serum albumin: insights from fluorescence

spectroscopy and computational modeling analysis," *RSC Advances*, V. 6, No. 94, 2016, pp. 91756–67.

197. Moller, P. "Assessment of reference values for DNA damage detected by the comet assay in human blood cell DNA," *Mutation Research/Reviews in Mutation Research*, V. 612, No. 2, 2006, pp. 84–104.

198. Morgan, M. J., and Thorburn, A. "Measurement of caspase activity in individual cells reveals differences in the kinetics of caspase activation between cells," *Cell Death & Differentiation*, V. 8, No. 1, 2001, pp. 38–43.

199. Gross-Goupil, M., Françlois, L., Quivy, A., et al. "Axitinib: A Review of its Safety and Efficacy in the Treatment of Adults with Advanced Renal Cell Carcinoma," *Clinical Medicine Insights: Oncology*, V. 7, 2013, pp. CMO.S10594.

200. Ehrhardt, M., Craveiro, R. B., Velz, J., et al. "The FDA approved PI 3K inhibitor GDC -0941 enhances *in vitro* the anti-neoplastic efficacy of Axitinib against c-myc-amplified high-risk medulloblastoma," *Journal of Cellular and Molecular Medicine*, V. 22, No. 4, 2018, pp. 2153–61.

201. Smith, B. J., Pithavala, Y., Bu, H.-Z., et al. "Pharmacokinetics, Metabolism, and Excretion of [^{14} C]Axitinib, a Vascular Endothelial Growth Factor Receptor Tyrosine Kinase Inhibitor, in Humans," *Drug Metabolism and Disposition*, V. 42, No. 5, 2014, pp. 918–31.

202. Chen, Y., Tortorici, M. A., Garrett, M., et al. "Clinical Pharmacology of Axitinib," *Clinical Pharmacokinetics*, V. 52, No. 9, 2013, pp. 713–25.

203. Zakharia, Y., Huynh, L., Du, S., et al. "Impact of Therapy Management on Axitinib-Related Adverse Events in Patients With Advanced Renal Cell Carcinoma Receiving First-Line Axitinib + Checkpoint Inhibitor," *Clinical Genitourinary Cancer*, V. 21, No. 5, 2023, pp. e343–51.

204. Parekh, H., Griswold, J., and Rini, B. "Axitinib for the treatment of metastatic renal cell carcinoma," *Future Oncology*, V. 12, No. 3, 2016, pp. 303–11.

205. Rini, B. I., Atkins, M. B., Choueiri, T. K., et al. "Time to Resolution of Axitinib-Related Adverse Events After Treatment Interruption in Patients With Advanced Renal Cell Carcinoma," *Clinical Genitourinary Cancer*, V. 19, No. 5, 2021, pp. e306–12.

206. Sedef, A. M., Köse, F., Rişvanoğlu, E. E., et al. “Unexpected skin lesions after axitinib treatment,” *Journal of Oncological Sciences*, V. 3, No. 2, 2017, pp. 89–91.

207. European Medicines Agency “CHMP assessment report-Inylta.” 2012.

208. Sparidans, R. W., Iusuf, D., Schinkel, A. H., et al. “Liquid chromatography-tandem mass spectrometric assay for the light sensitive tyrosine kinase inhibitor axitinib in human plasma,” *Journal of Chromatography B*, V. 877, No. 32, 2009, pp. 4090–6.

209. Campeta, A. M., Chekal, B. P., Abramov, Y. A., et al. “Development of a Targeted Polymorph Screening Approach for a Complex Polymorphic and Highly Solvating API,” *Journal of Pharmaceutical Sciences*, V. 99, No. 9, 2010, pp. 3874–86.

210. Pithavala, Y. K., Tong, W., Mount, J., et al. “Effect of ketoconazole on the pharmacokinetics of axitinib in healthy volunteers,” *Investigational New Drugs*, V. 30, No. 1, 2012, pp. 273–81.

211. Wei, N., Liang, J., Peng, S., et al. “Design, Synthesis, and Biological Evaluation of Axitinib Derivatives,” *Molecules*, V. 23, No. 4, 2018, pp. 747.

212. Schmidt, D., Rodat, T., Heintze, L., et al. “Axitinib: A Photoswitchable Approved Tyrosine Kinase Inhibitor,” *ChemMedChem*, V. 13, No. 22, 2018, pp. 2415–26.

213. Verimer, T., Long, J. P., Rusterholz, D. R., et al. “Dopaminergic activity of cis-trans isomers of benzhydro[f]quinoline analogs,” *European Journal of Pharmacology*, V. 64, No. 4, 1980, pp. 271–7.

214. Geiger, J.-M., and Brindley, C. J. “*Cis-trans* Intelconversion of Acitretin in Man,” *Skin Pharmacology and Physiology*, V. 1, No. 4, 1988, pp. 230–6.

215. Mirzaei, M. S., and Taherpour, A. A. “Tautomeric preferences of the cis and trans isomers of axitinib,” *Chemical Physics*, V. 507, 2018, pp. 10–8.

216. Kuo, L. J., and Yang, L.-X. “Gamma-H2AX - a novel biomarker for DNA double-strand breaks,” *In Vivo (Athens, Greece)*, V. 22, No. 3, 2008, pp. 305–9.

217. European Medicines Agency “Sprycel, INN - Dasatinib,” 2006.

218. Tsimberidou, A.-M. “Dasatinib in chronic myeloid leukemia: a review,” *Therapeutics and Clinical Risk Management*, 2009, pp. 281.

219. Nam, S., Kim, D., Cheng, J. Q., et al. “Action of the Src Family Kinase Inhibitor, Dasatinib (BMS-354825), on Human Prostate Cancer Cells,” *Cancer Research*, V. 65, No. 20, 2005, pp. 9185–9.

220. Kang, B., Kim, Y., Park, T. J., et al. “Dasatinib, a second-generation tyrosine kinase inhibitor, induces melanogenesis via ERK-CREB-MITF-tyrosinase signaling in normal human melanocytes,” *Biochemical and Biophysical Research Communications*, V. 523, No. 4, 2020, pp. 1034–9.

221. Maiti, A., Cortes, J. E., Patel, K. P., et al. “Long-term results of frontline dasatinib in chronic myeloid leukemia,” *Cancer*, V. 126, No. 7, 2020, pp. 1502–11.

222. “Dasatinib.” Meyler’s Side Effects of Drugs. Elsevier, 2016. pp. 835.

223. Scholar, E. “Dasatinib.” xPharm: The Comprehensive Pharmacology Reference. Elsevier, 2009. pp. 1–5.

234. Boudadi, K. “Diffuse Hypopigmentation Followed by Hyperpigmentation in an African American Woman with Hemangiopericytoma Treated with Dasatinib,” *Journal of clinical and diagnostic research*, 2014.

225. Tarantini, F., Anelli, L., Ingravallo, G., et al. “Skin lesions in chronic myeloid leukemia patients during dasatinib treatment,” *Cancer Management and Research*, V. Volume 11, 2019, pp. 7991–6.

226. Ratushny, V., Gober, M. D., Hick, R., et al. “From keratinocyte to cancer: the pathogenesis and modeling of cutaneous squamous cell carcinoma,” *Journal of Clinical Investigation*, V. 122, No. 2, 2012, pp. 464–72.

227. Bos, J. D., and Meinardi, M. M. H. M. “The 500 Dalton rule for the skin penetration of chemical compounds and drugs,” *Experimental Dermatology*, V. 9, No. 3, 2000, pp. 165–9.

228. Jung, S. H., Sun, X., Ryu, W.-S., et al. “Topical administration of the pan-Src kinase inhibitors, dasatinib and LCB 03-0110, prevents allergic contact dermatitis in mice: Suppression of ACD by dasatinib and LCB 03-0110,” *British Journal of Dermatology*, V. 168, No. 1, 2013, pp. 112–9.

229. Bilkis, I., Silman, I., and Weiner, L. “Generation of Reactive Oxygen Species by Photosensitizers and their Modes of Action on Proteins,” *Current Medicinal Chemistry*, V. 25, No. 40, 2019, pp. 5528–39.

230. Nakai, K., and Tsuruta, D. “What Are Reactive Oxygen Species, Free Radicals, and Oxidative Stress in Skin Diseases?,” *International Journal of Molecular Sciences*, V. 22, No. 19, 2021, pp. 10799.

231. Martínez, L. J., and Scaiano, J. C. “Characterization of the Transient Intermediates Generated from the Photoexcitation of Nabumetone: A Comparison with Naproxen,” *Photochemistry and Photobiology*, V. 68, No. 5, 1998, pp. 646–51.

232. Hackbarth, S., Schlothauer, J., Preuß, A., et al. “New insights to primary photodynamic effects – Singlet oxygen kinetics in living cells,” *Journal of Photochemistry and Photobiology B: Biology*, V. 98, No. 3, 2010, pp. 173–9.

233. Pap, E. H. W., Drummen, G. P. C., Winter, V. J., et al. “Ratio-fluorescence microscopy of lipid oxidation in living cells using C11-BODIPY $^{581/591}$,” *FEBS Letters*, V. 453, No. 3, 1999, pp. 278–82.

234. Davies, M. J. “Singlet oxygen-mediated damage to proteins and its consequences,” *Biochemical and Biophysical Research Communications*, V. 305, No. 3, 2003, pp. 761–70.

235. Insińska-Rak, M., Golczak, A., Gierszewski, M., et al. “5-Deazaalloxazine as photosensitizer of singlet oxygen and potential redox-sensitive agent,” *Photochemical & Photobiological Sciences*, V. 22, No. 7, 2023, pp. 1655–71.

236. Sousa, C., Rego, A. M. B. D., and Sá E Melo, T. “Singlet oxygen reactivity in water-rich solvent mixtures,” *Química Nova*, V. 31, No. 6, 2008, pp. 1392–9.

237. Shlyapintokh, V. Y., and Ivanov, V. B. “The Quenching of Singlet Oxygen,” *Russian Chemical Reviews*, V. 45, No. 2, 1976, pp. 99–110.

238. Oliveros, E., Suardi-Murasecco, P., Aminian-Saghafi, T., et al. “1 *H* - Phenalen-1-one: Photophysical Properties and Singlet-Oxygen Production,” *Helvetica Chimica Acta*, V. 74, No. 1, 1991, pp. 79–90.

239. Azqueta, A., and Collins, A. R. “The essential comet assay: a comprehensive guide to measuring DNA damage and repair,” *Archives of Toxicology*, V. 87, No. 6, 2013, pp. 949–68.

240. Sylvester, P. W. “Optimization of the Tetrazolium Dye (MTT) Colorimetric Assay for Cellular Growth and Viability.” In: Satyanarayanajois, S. D., ed. Drug Design and Discovery, vol. 716. Totowa, NJ, Humana Press, 2011. pp. 157–68.

241. Gotlib, J., Reiter, A., and DeAngelo, D. J. “Avapritinib for advanced systemic mastocytosis,” *Blood*, V. 140, No. 15, 2022, pp. 1667–73.

242. Reiter, A., Schwaab, J., DeAngelo, D. J., et al. “Efficacy and safety of avapritinib in previously treated patients with advanced systemic mastocytosis,” *Blood Advances*, V. 6, No. 21, 2022, pp. 5750–62.

243. Giannetti, M. P. “Treatment of systemic mastocytosis,” *Annals of Allergy, Asthma & Immunology*, V. 127, No. 4, 2021, pp. 412–9.

256. Papke, D., and Doyle, L. “Gastrointestinal Mesenchymal Tumors.” *Gastrointestinal and Liver Pathology. Elsevier*, 2024. pp. 169–210.

245. European Medicines Agency “Ayvakyt INN.” 2020.

246. US Food and Drug Administration “AYVAKIT™ (avapritinib) tablets, for oral use.” 2021.

247. Dadrass, F., Han, J., Gaddis, K. J., et al. “Avapritinib-induced photo-aggravated cutaneous reaction,” *JAAD Case Reports*, V. 21, 2022, pp. 43–5.

248. European Medicines Agency “Avapritinib: summary of product characteristics.” 2022.

249. Swanson, H. I. “Cytochrome P450 expression in human keratinocytes: an aryl hydrocarbon receptor perspective,” *Chemico-Biological Interactions*, V. 149, Nos. 2–3, 2004, pp. 69–79.

250. Ahmad, N., and Mukhtar, H. “Cytochrome P450: A Target for Drug Development for Skin Diseases,” *Journal of Investigative Dermatology*, V. 123, No. 3, 2004, pp. 417–25.

251. Gonzalez, M.-C., Marteau, C., Franchi, J., et al. “Cytochrome P450 4A11 expression in human keratinocytes: effects of ultraviolet irradiation.,” *British Journal of Dermatology*, V. 145, No. 5, 2001, pp. 749–57.

SCIENTIFIC CONTRIBUTIONS

Publications

Publications related to this doctoral thesis

1. **El Ouardi M**, Tamarit L, Vayá I, Miranda MA, Andreu I. "Cellular photo(geno)toxicity of gefitinib after biotransformation," *Frontiers in Pharmacology*, V. 14, 2023, pp. 1208075.
2. Tamarit L, **El Ouardi M**, Andreu I, Vayá I, Miranda MA. "Photoprocesses of the tyrosine kinase inhibitor gefitinib: from femtoseconds to microseconds and from solution to cells*," Chemical Science*, V. 12, No. 36, 2021, pp. 12027–35.
3. **El Ouardi M**, Tamarit L, Vayá I, Miranda MA, Andreu I. "Cellular damage photosensitized by dasatinib, radical-mediated mechanisms and photoprotection in reconstructed epidermis," *Free Radical Biology and Medicine,* 2024 (submitted).

Other publications

1. Tamarit L, **El Ouardi M**, Lence E, Andreu I, González-Bello C, Vayá I, Miranda MA. "Switching from ultrafast electron transfer to proton transfer in excited drug–protein complexes upon biotransformation," *Chemical Science*, V. 13, No. 33, 2022, pp. 9644–54.
2. Garcia-Lainez G, **El Ouardi M**, Moreno A, Lence E, González-Bello C, Miranda MA, Andreu I. "Singlet oxygen and radical-mediated mechanisms in the oxidative cellular damage photosensitized by the protease inhibitor simeprevir," *Free Radical Biology and Medicine*, V. 194, 2023, pp. 42–51.
3. Tamarit L, **El Ouardi M**, Lence E, Andreu I, González-Bello C, Miranda MA, Vayá I. "Modulation of the photobehavior of gefitinib and its phenolic metabolites by human transport proteins," *Frontiers in Pharmacology*, V. 15, 2024.

Congress presentations

Poster communications

1. **El Ouardi M**, Tamarit L, Vayá I, Miranda MA, Andreu I. "In vitro photo(geno)toxicity assessment of gefitinib and its metabolites," *19th Congress of the European Society for Photobiology (ESP)*, V. 35, 2021, pp. 323–324.
2. **El Ouardi M**, Tamarit L, Vayá I, Miranda MA, Andreu I. "Evaluation of the photo(geno)toxicity associated with Tyrosine Kinase inhibitors," *XXXVIII Reunión Bienal de la Real Sociedad Española de Química (RSEQ)*, V. 14, 2022, pp. 1208075.

Oral communications

1. **El Ouardi M**, Tamarit L, Vayá I, Miranda MA, Andreu I. "Evaluación de la foto(geno)toxicidad de gefitinib y sus metabolitos," *4th Winter Meeting Instituto de Tecnología Química (ITQ)*, 2022, pp. 323–324.
2. **El Ouardi M**, Garcia-Lainez G, Moreno A, Lence E, González-Bello C, Miranda MA, Andreu I. "Photophysical and Photobiological Study of the Viral NS3/A4 Protease Inhibitor Simeprevir," *X Reunión de Química Orgánica del Mediterráneo (REQOMED)*, 2022, pp. 45.
3. **El Ouardi M**, Garcia-Lainez G, Moreno A, Lence E, González-Bello C, Miranda MA, Andreu I. "Simeprevir, a viral NS3/A4 protease inhibitor, causes oxidative cellular photodamage after exposure to UVA Light," *PhDay Health Research Institute Hospital La Fe (IIS La Fe)*, 2022.

frontiers | Frontiers in Pharmacology

TYPE Original Research
PUBLISHED 07 June 2023
DOI 10.3389/fphar.2023.1208075

Check for updates

OPEN ACCESS

EDITED BY
Albert P. Li,
In Vitro ADMET Laboratories,
United States

REVIEWED BY
Sankha Bhattacharya,
SVKM's Narsee Moonjee Institute of Management and Studies (NMIMS), India
Chararen Pourzand,
University of Bath, United Kingdom

*CORRESPONDENCE
Miguel A. Miranda,
mmiranda@qim.upv.es
Inmaculada Andreu,
iandreur@qim.upv.es

RECEIVED 18 April 2023
ACCEPTED 23 May 2023
PUBLISHED 07 June 2023

CITATION
El Ouardi M, Tamarit L, Vayá I, Miranda MA and Andreu I (2023), Cellular photo(geno)toxicity of gefitinib after biotransformation.
Front. Pharmacol. 14:1208075.
doi: 10.3389/fphar.2023.1208075

COPYRIGHT
© 2023 El Ouardi, Tamarit, Vayá, Miranda and Andreu. This is an open-access article distributed under the terms of the Creative Commons Attribution License (CC BY). The use, distribution or reproduction in other forums is permitted, provided the original author(s) and the copyright owner(s) are credited and that the original publication in this journal is cited, in accordance with accepted academic practice. No use, distribution or reproduction is permitted which does not comply with these terms.

Cellular photo(geno)toxicity of gefitinib after biotransformation

Meryem El Ouardi[1,2], Lorena Tamarit[1,2], Ignacio Vayá[1,2], Miguel A. Miranda[1,2]* and Inmaculada Andreu[1,2]*

[1]Departamento de Química-Instituto de Tecnología Química UPV-CSIC, Universitat Politècnica de València, Valencia, Spain, [2]Unidad Mixta de Investigación UPV- IIS La Fe, Hospital Universitari i Politècnic La Fe, Valencia, Spain

Gefitinib (GFT) is a selective epidermal growth factor receptor (EGFR) inhibitor clinically used for the treatment of patients with non-small cell lung cancer. Bioactivation by mainly Phase I hepatic metabolism leads to chemically reactive metabolites such as O-Demethyl gefitinib (DMT-GFT), 4-Defluoro-4-hydroxy gefitinib (DF-GFT), and O-Demorpholinopropyl gefitinib (DMOR-GFT), which display an enhanced UV-light absorption. In this context, the aim of the present study is to investigate the capability of gefitinib metabolites to induce photosensitivity disorders and to elucidate the involved mechanisms. According to the neutral red uptake (NRU) phototoxicity test, only DF-GFT metabolite can be considered non-phototoxic to cells with a photoirritation factor (PIF) close to 1. Moreover, DMOR-GFT is markedly more phototoxic than the parent drug (PIF = 48), whereas DMT-GFT is much less phototoxic (PIF = 7). Using the thiobarbituric acid reactive substances (TBARS) method as an indicator of lipid photoperoxidation, only DMOR-GFT has demonstrated the ability to photosensitize this process, resulting in a significant amount of TBARS (similar to ketoprofen, which was used as the positive control). Protein photooxidation monitored by 2,4-dinitrophenylhydrazine (DNPH) derivatization method is mainly mediated by GFT and, to a lesser extent, by DMOR-GFT; in contrast, protein oxidation associated with DMT-GFT is nearly negligible. Interestingly, the damage to cellular DNA as revealed by the comet assay, indicates that DMT-GFT has the highest photogenotoxic potential; moreover, the DNA damage induced by this metabolite is hardly repaired by the cells after a time recovery of 18 h. This could ultimately result in mutagenic and carcinogenic effects. These results could aid oncologists when prescribing TKIs to cancer patients and, thus, establish the conditions of use and recommend photoprotection guidelines.

KEYWORDS

anticancer drug, metabolism, photodamage to biomolecules, photosensitized reaction, tyrosine kinase inhibitor

1 Introduction

Significant medical advances in cancer treatment have been made during the past few decades. However, the drugs used for this cure have a limited therapeutic index, and often the responses are only just palliative and unpredictable (Chai et al., 2021; Sapio and Naviglio, 2022). In contrast, targeted therapy introduced more recently has less non-specific toxicities since it interferes with a specific molecular target, generally a protein with a crucial role in tumor growth or progression (Baudino, 2015; Zhong et al., 2021).

The epidermal growth factor receptors (EGFRs) are transmembrane glycoproteins consisting of an extracellular ligand-binding domain, a transmembrane domain, and an

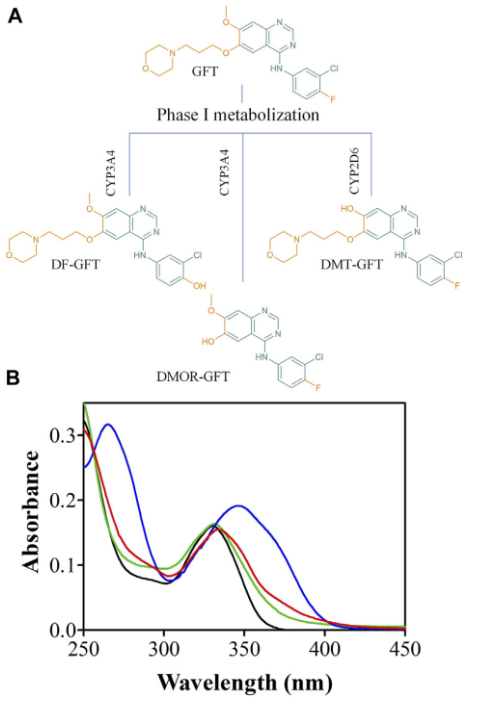

FIGURE 1
(A) Chemical structure of gefitinib (GFT), 4-Defluoro-4-hydroxy gefitinib (DF-GFT), O-Demethyl gefitinib (DMT-GFT) and O-Demorpholinopropyl gefitinib (DMOR-GFT); **(B)** Absorption spectra of GFT (black), DF-GFT (green), DMT-GFT (blue) and DMOR-GFT (red) in PBS at 10 μM.

intracellular domain with tyrosine kinase activity. They regulate the cell signaling pathways, including cell growth, survival, migration, and differentiation (Normanno et al., 2006). Pathological alterations of EGFRs, including kinase-activating mutation or overexpression, may result in the appearance of different types of cancers and may promote solid tumor growth. Therefore, they are major targets for the design of anticancer agents (Normanno et al., 2006; da Cunha Santos et al., 2011; Teng et al., 2011). In this regard, tyrosine kinase inhibitors (TKIs) are of high interest due to their ability to block the kinase activity of these receptors (Hartmann et al., 2009; Yamaoka et al., 2018). They are orally active small molecules that have a favorable safety profile and can be easily combined with other forms of chemotherapy or radiation therapy (Hartmann et al., 2009; Yamaoka et al., 2018; Zhong et al., 2021).

In this context, it is interesting to note that TKIs are an important new class of drugs in cancer remedies (considered smart drugs) that interfere with specific cell signaling pathways and thus allow target-specific treatment for selected malignancies (Pottier et al., 2020). These anticancer drugs have significantly improved the quality of life and the survival rate of oncologic patients. Generally, they are well tolerated by patients; however, cutaneous reactions are very common, and, in most cases, enhanced by sunlight exposure (Lembo et al., 2020). Hence, although TKIs have revolutionized oncology practice over the past 20 years, very little is known about their photosensitizing potential. These side effects can be associated with damage to biomolecules mediated by radicals or reactive oxygen species arising from excited states (Salvador et al., 2014). In this context, we have previously established a good correlation between the photophysical behavior of the TKIs lapatinib and gefitinib and their photobiological properties (Vayá et al., 2020; García-Lainez et al., 2021; Tamarit et al., 2021). Gefitinib (GFT) is a selective EGFR inhibitor clinically used for the treatment of patients with non-small cell lung cancer (NSCLC) (Rawluk and WallerGefitinib, 2018). In humans, GFT undergoes metabolic bioactivation by mainly Phase I hepatic metabolism (cytochromes CYP3A4 and CYP2D6) resulting in chemically reactive metabolites such as O-Demethyl gefitinib (DMT-GFT), 4-Defluoro-4-hydroxy gefitinib (DF-GFT), and O-Demorpholinopropyl gefitinib (DMOR-GFT) (Figure 1A) (McKillop et al., 2004; Li et al., 2007; Tan et al., 2020). This chemical change generates non-negligible modifications in the quinazoline chromophore, leading to a more efficient UV-light absorption (Figure 1B). Thus, although drug biotransformation is usually regarded to a decreased toxicity, in some cases metabolites may display more phototoxicity and photoreactivity than the parent drug (Garcia-Lainez et al., 2018; Agúndez et al., 2020). Accordingly, investigating the photo(geno)toxicity of gefitinib and its metabolites is important for assessing drug safety, evaluating the risks associated with sunlight exposure during treatment. In connection with this, we have previously reported the photo(geno)toxicity induced by one of the photoactive metabolites of lapatinib, another tyrosine kinase inhibitor (Vayá et al., 2020; García-Lainez et al., 2021).

Therefore, it appears very interesting to explore the photosensitizing potential of GFT metabolites by evaluating their photo(geno)toxicity through *in vitro* studies in human skin cells to recommend preventive health measures and thus, minimize the photosensitizing risk from TKIs. Moreover, this investigation will aid the oncologists in having a better knowledge of the photoinduced adverse effects of these drugs before prescribing TKIs to cancer patients and, thus, give them photoprotection guidelines.

2 Materials and methods

2.1 Chemicals

All solvents and chemicals were commercially available (HPLC grade) and used without additional purification. Chlorpromazine hydrochloride (CPZ; CAS 69-09-0), sodium dodecyl sulfate (SDS; CAS 151-21-3), anthracene (ANT; CAS 120-112-7) and (S)-(+)-Ketoprofen (KP; CAS 22161-81-5) were purchased from Sigma-Aldrich (Madrid, Spain). Gefitinib hydrochloride (GFT; CAS 184475-55-6) was provided by MedChemExpress (New Jersey, United States). 4-Defluoro-4-hydroxy gefitinib (DF-GFT; CAS 847949-50-2) and O-Demorpholinopropyl gefitinib (DMOR-GFT; CAS 184475-71-6) were acquired from Santa Cruz Biotechnology (Dallas, United States) and O-Demethyl gefitinib (DMT-GFT; CAS 847949-49-9) was purchased from Toronto

Research Chemicals (North York, Canada). Stock solutions were prepared in DMSO as vehicle, whereas GFT, CPZ and SDS were dissolved in ultrapure water (Milli-Q®). 1,4-dihydro-1,2-dimethylbenzoic acid (DMBA) was obtained from a Birch reduction synthesis. Dulbecco's Modified Eagle Medium (DMEM, low glucose with pyruvate and glutamine), Dulbecco's Modified Eagle Medium (DMEM, low glucose with pyruvate and without glutamine and phenol red), fetal bovine serum (FBS), penicillin–streptomycin (1.0 U/mL × 10^5 U/mL, 1.0 µg/mL × 10^5 µg/mL) and ethylenediaminetetraacetic acid (EDTA) were supplied by Honeywell Fluka (North Carolina, United States). Trypsin–EDTA (0.25%–0.02%) was provided by Cultek (Madrid, Spain). Phosphate buffered saline solution (PBS, pH 7.4), neutral red dye, human serum albumin fatty acid free (HSA), polyoxyethylenesorbitan monolaurate (TWEEN 20) and sodium hydroxide (NaOH) were purchased from Sigma-Aldrich (Madrid, Spain). Low melting point agarose was provided by Pronadisa (Madrid, Spain). Tris(hydroxymethyl)aminomethane, Linoleic acid (LA), Methyl Linoleate (ML), 1,1,3,3-Tetraethoxypropane (TEP), 2-Thiobarbituric acid (TBA) and 2,6-Di-tert-butyl-4-methylphenol (BHT) were supplied by Sigma-Aldrich (Madrid, Spain). CometAssay® Lysis Solution was purchased from R&D systems (Minneapolis, United States). 2,4-Dinitrophenylhydrazine Hydrochloride (DNPH) was acquired from Santa Cruz Biotechnology (Dallas, United States). Trichloroacetic acid (TCA) was purchased from Labbox (Barcelona, Spain). SYBR™ Gold DNA, and CellMask™ Orange Plasma membrane stains were acquired from Invitrogen (Madrid, Spain). RedDot™ Far-Red Nuclear was supplied by Biotium (California, United States). Apo-ONE® Homogeneous Caspase-3/7 assay and CytoTox-ONE™ Homogeneous Membrane Integrity Assay were received from Promega (Madison, United States). Deoxyribonucleic acid sodium salt from calf thymus was purchased from Sigma-Aldrich (Madrid, Spain).

2.2 Spectroscopic measurements

2.2.1 Absorption and emission spectra measurements

Absorption spectra were recorded in a JASCO V-760 spectrophotometer using 10 × 10 mm^2 quartz cuvettes at room temperature. For fluorescence emission experiments, solutions of GFT and metabolites in PBS were incubated in the presence of human serum albumin (HSA), methyl linoleate (ML), calf thymus DNA (ctDNA) in a ratio of 1:1 or HaCaT cells (2×10^4 cells/well) in black 96-well plates for 1 h. Fluorescence spectra (λ_{exc} = 320 nm) were recorded using a Synergy H1 multi-mode microplate reader.

2.2.2 Quenching experiments by laser flash photolysis

A pulsed Nd:YAG L52137 V LOTIS TII laser (Sp Lotis Tii, Minsk, Belarus) was used for the excitation at 355 nm. The single pulses were ~10 ns of duration, and the energy was ~12 mJ/pulse. Laser flash photolysis (LFP) equipment consisted of a pulsed laser, a 77250 Oriel monochromator, and an oscilloscope DP04054 Tektronix. The output signal from the oscilloscope was transferred to a personal computer for processing. The DMOR-GFT metabolite was dissolved in acetonitrile up to an absorbance of 0.3 at 355 nm. Solutions were deaerated by bubbling nitrogen through the solution during 15 min. The rate constant of triplet excited-state quenching by 1,4-dihydro-1,2-dimethylbenzoic acid (DMBA) was determined using the Stern–Volmer Equation:

$$1/\tau = 1/\tau_q + k_q\,[DMBA]$$

Where τ and τ_q are the lifetime of transient species in the presence and absence of DMBA, respectively. Concentrations between 0.1 and 10 mM were used for DMBA. This compound was prepared through Birch reduction following standard procedures (Andreu et al., 2011).

2.3 Cell culture conditions

Human keratinocytes cells (HaCaT) were grown in 75 cm^2 plastic flasks in DMEM supplemented with 10% FBS and penicillin/streptomycin (100 U/mL, and 100 µg/mL) in a humidified incubator (100% relative humidity) at 37°C with 5% CO_2 atmosphere. Cells were routinely passed twice a week for maintenance (1:5 splitting ratio) and a trypan blue exclusion test was used to ensure that the cultures were viable before each experiment.

2.4 Cellular localization by confocal microscopy

HaCaT cells were seeded on sterile round glass coverslips and incubated in 24-well plates (2.5×10^4 cells/well). After 24 h of incubation, DMEM medium was replaced with 1 mL of fresh medium containing drugs (GFT, DMT-GFT or DMOR-GFT) at 15 µM followed by staining with CellMask™ Orange Plasma membrane and RedDot™ Far-Red nuclear stains (1:10,000 and 1:200 dilutions, respectively). Cells treated with the compounds were incubated for 1 h whereas CellMask™ Orange Plasma membrane and RedDot™ Far-Red nuclear stains were incubated for 30 and 10 min respectively at 37°C. Then, coverslips were washed three times for 5 min with PBS and finally mounted in glass slides using a solution of mowiol. Through sequential mode, a Leica SP5 confocal microscope was used for cell imaging. The excitation wavelengths were 405 nm for GFT, DMT-GFT and DMOR-GFT. For CellMask™ Orange Plasma membrane and RedDot™ Far-Red nuclear stains, the excitation wavelengths were 543 nm and 662 nm, respectively. The maxima emission wavelengths were 450, 567, and 694 nm for the drug and its metabolites, plasma membrane and nuclear stains, respectively.

2.5 Irradiation equipment

Irradiations under UVA light conditions were performed with an LCZ-4 photoreactor equipped with six top and eight sides Hitachi lamps (λ_{max} = 350 nm, Gaussian distribution; Luzchem, Canada), which emit 94% UVA and 2% UVB radiation, respectively. The samples for *in vitro* HaCaT NRU phototoxicity assay were irradiated

in 96-well transparent plates, for comet assay 24-well transparent plates were used while in both protein and lipid photooxidation assay irradiations were performed in 6-well transparent wells. All irradiations were carried out through the lid of the plates which does not absorb beyond 310 nm for the purpose of reducing the direct effect of UVB radiation over the cell cultures. Since cell viability after irradiation was higher than 90%, the UV dose selected was suitable for the photogenotoxicity experiments, therefore, false-positive results triggered by DNA fragmentation as a result of cell death were avoided. Moreover, in order to prevent overheating, plates were kept on ice during the irradiation process and the temperature was controlled by ventilation.

2.6 *In Vitro* neutral red uptake (NRU) phototoxicity test

Neutral red uptake phototoxicity test (NRU) was assessed according to the OECD Guideline 432 (OECD, 2019) in keratinocyte cells (HaCaT) with additional minor modifications (Garcia-Lainez et al., 2018). Chlorpromazine (CPZ) and sodium dodecyl sulfate (SDS) served as the positive phototoxic and negative non-phototoxic controls, respectively. CPZ is a widely used typical antipsychotic drug with well-known phototoxic properties as already reported (Palumbo et al., 2016). In our recent study, GFT has shown a very significant phototoxic potential in HaCaT cells (Tamarit et al., 2021). Therefore, the phototoxicity behavior of the metabolites was studied in parallel with the parent drug.

Concisely, for each compound, two 96-well plates were seeded at a density of 2.0×10^4 cells/well. Next day, HaCaT cells in a fresh DMEM medium without phenol red were treated with the compounds (GFT, DF-GFT, DMT-GFT and DMOR-GFT) at eight concentrations ranging from 2.5 to 500 µM except for DMOR-GFT which was added in a concentration range from 125 to 0.625 µM. Additional plates were processed with CPZ (from 1.57 to 500 µM) and SDS (from 3.13 to 500 µM). All plates were incubated for 1 h in dark conditions. Then, for each sample, in the presence of ice, one plate was irradiated with a non-cytotoxic dose of 5 J/cm^2 UVA (UVA Light), whereas the other was kept in a dark box (Dark). Next, drug solutions were replaced with fresh DMEM medium, and plates were further incubated overnight. Next day, neutral red solution (50 µg/mL) was added into the wells and incubated for 2 h at 37°C. Later, cells were washed once with PBS and neutral red was recovered from lysosomes in 100 µL of the extraction buffer [distilled water 50% (v/v), ethanol 49.5% (v/v) and acetic acid 0.5% (v/v)]. Lastly, the absorbance of the plates was read at 550 nm on a Synergy H1 microplate reader. For each compound, dose–response curves were performed to establish the concentration causing a reduction of 50% of neutral red uptake (IC_{50}) in dark and UVA light conditions. Afterwards, photoirritation factor (PIF) values were calculated using the following equation:

$$PIF = IC_{50}\,(Dark) \,/\, IC_{50}\,(UVA\ Light)$$

Conforming to OECD Guideline 432 (OECD, 2019), a substance is labelled as "non-phototoxic" when PIF is <2, "probably phototoxic" if PIF is between 2 and 5 and "phototoxic" if PIF is >5.

2.7 Photosensitized lipid peroxidation

Linoleic acid photosensitized oxidation assay was performed as described previously (Seto et al., 2013) with minor adjustments exposed in prior studies (Zeb and Ullah, 2016). For this, a solution of linoleic acid (1 mM) in 20 mM PBS (pH 7.4) containing 0.05% Tween 20 was prepared and irradiated in the presence of GFT or its metabolites (DMT-GFT or DMOR-GFT) in a concentration of 100 µM. KP 200 µM was taken as a positive control (Seto et al., 2013). Lipid peroxidation was monitored with TBA-reactive substances assay (TBARS) (Zeb and Ullah, 2016) adding 4 mM TBA and 10 µL BHT solution in glacial acetic acid to the irradiated samples (500 µL). Then, samples were heated at 95 °C for 60 min. After 10 min of cooling, the absorbance of the samples was measured at 532 nm for the determination of TBARS. A standard curve of TEP was used to determine the total of malondialdehyde (MDA) produced. The data was analyzed statistically using a Two-way ANOVA (Analysis of Variance) technique.

2.8 Photoinduced protein oxidation assay

Protein photooxidation assay was assessed according to Colombo et al. (2016) with minor modifications as explained below. The photooxidative activity of GFT has already been evaluated in our previous study (Tamarit et al., 2021), which has proved its protein photooxidation capability. Briefly, a solution of HSA (5 mg/mL, 1 mg protein/sample) was prepared in PBS and irradiated alone or in the presence of 100 µM of GFT, DMT-GFT or DMOR-GFT with a UVA dose of 15 J/cm^2. The amount of HSA oxidation in each sample was determined immediately after irradiation by incubating the samples for 60 min at room temperature with 200 µL of 2,4-dinitrophenylhydrazine (DNPH) 10 mM to create stable protein-DNP hydrazone adducts. After incubation, proteins were precipitated with 20% TCA solution and incubated on ice for 15 min. Next, samples were washed twice with ethanol/ethyl acetate 1:1 (v/v) containing 20% TCA, in order to reduce the protein loss, followed by its resolubilization in 100 µL guanidine buffer (6 M). Finally, absorbance at 375 nm was registered using the Synergy H1 microplate reader and the HSA oxidation degree was expressed as nmol of carbonyl per mg protein as displayed in the next equation:

$$Carbonyl\ content\ (nmol/mg\ protein) = \frac{(A_{375}/\varepsilon^{mM})}{P} \times 100$$

Where A_{375} is the absorbance of the sample at 375 nm, ε^{mM} is the corrected millimolar extinction coefficient (6.364) and P the amount of protein from standard well.

The statistical analysis of the data was conducted using a Two-way ANOVA (Analysis of Variance) method.

2.9 Nuclear DNA damage by single cell gel electrophoresis (comet) assay

The comet assay (single-cell gel electrophoresis) was performed as already detailed in Garcia-Lainez et al. (2018) in order to detect both single and double strand breaks and alkaline labile sites on

TABLE 1 ***In vitro*** **HaCaT NRU phototoxicity assay of GFT and its metabolites[a].**

Compound	IC_{50} dark (μM)	IC_{50} UVA light (μM)	Photoirritant factor (PIF)[b]
CPZ	80 ± 17	4 ± 0.9	20
GFT[c]	64 ± 3	5 ± 1.7	13
DF-GFT	1,015 ± 222	1,099 ± 406	1
DMT-GFT	34 ± 3	5 ± 0.1	7
DMOR-GFT	144 ± 6	3 ± 0.6	48
SDS	133 ± 31	136 ± 23	1

[a]Data represent the mean ± SD from 4 independent dose-response curves. CPZ and SDS were selected as positive and negative controls of phototoxicity, respectively.
[b]According to the OECD 432 Guide (OECD, 2019), PIF <2 means "no phototoxicity", 2< PIF <5 means "probable phototoxicity" and PIF >5 means "phototoxicity."
[c]The PIF value of GFT was taken from the literature (Tamarit et al., 2021).

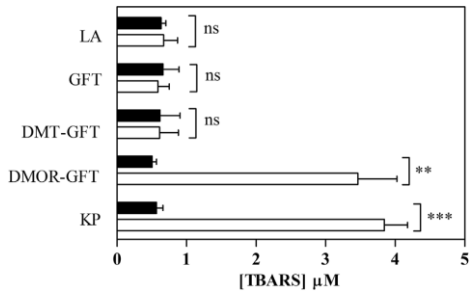

FIGURE 2
Photosensitized lipid peroxidation. Solutions of linoleic acid (LA) in PBS alone or with GFT/metabolites (100 μM) were kept in darkness (■ Dark) or exposed to a UVA dose of 15 J/cm² (□ UVA Light), and TBARS content was monitored with TBA method. Ketoprofen (KP) 200 μM was selected as a reference. Data represent mean ± SD of at least 4 independent experiments. Asterisks indicate significant changes in relation to TBARS formation under darkness by the Student's t-test (**p < 0.01, ***p < 0.001 and ns: non-significant).

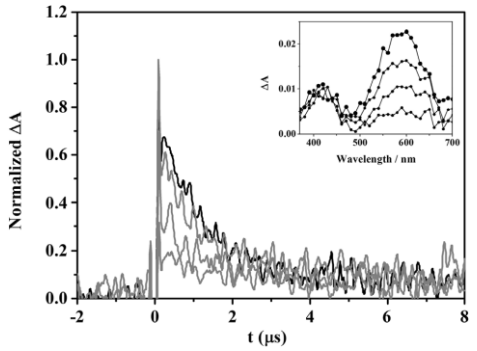

FIGURE 3
Decays at 610 nm for DMOR-GFT alone (black) or in the presence of an increasing amount of DMBA (0.1–10 mM) (gray) in deaerated acetonitrile solution after the 355 nm laser excitation. Inset: triplet-triplet absorption spectra of DMOR-GFT (from 0.2 to 3 μs).

nuclear DNA. Briefly, HaCaT cells in exponential growth were harvested by trypsinization and kept in ice-cold PBS for 2 h to neutralize any DNA damage produced during trypsinization step, as has been previously demonstrated in FSK cells (Agúndez et al., 2020). Then, 24-wells plates (1.0×10^4 cells/well) were seeded and treated with 100 μM of GFT or its metabolites (DMT-GFT or DMOR-GFT) for 30 min at 4°C in darkness to minimize cell aggregation and inhibit DNA repair. The reference photogenotoxic control of this assay was CPZ (10 μM). Afterwards, one plate was irradiated under 2 J/cm² UVA light dose (4 J/cm² for DMT-GFT and DMOR-GFT) while the other one was kept in darkness as the negative control. Later, both irradiated and non-irradiated cells were detached from the plates and 100 μL of cell suspension was mixed with 100 μL 1% low melting point agarose solution and loaded onto FLARE® slides. Then, slides were incubated on ice to allow drop jellification. Finally, slides were embedded in a box with lysis buffer to initiate the lysis of cells and incubated overnight at 4°C. Next day, slides were placed in electrophoresis tank filled with 1 L of cold alkaline electrophoresis buffer (0.2 M NaOH, 1 mM EDTA in distilled water and pH ≥ 13). The electrophoresis was run at 21 V (1 V/cm) for 30 min and kept at 4°C. Then, slides were washed twice with MilliQ water and DNA fixation accomplished by a serial dehydration with 70% ethanol and 100% ethanol solutions during 5 min and followed by drying for 2 h at 37°C. Nuclear DNA was stained with a SYBR Gold® bath (1:10,000 in Tris-EDTA buffer) for 30 min at 4°C and slides were kept in darkness until its visualization. Comets (nucleoids and tails) were visualized using a fluorescence microscope (Leica DMI 4000B). DNA damage was quantified by counting and analyzing at least 100 DNA comets. Finally, total comet score (TCS) was obtained with the classification of six DNA damage types (Møller, 2006) applying the formula:

$$[(Cl.0 \times 0) + (Cl.1 \times 1) + (Cl.2 \times 2) + (Cl.3 \times 3) + [(Cl.4 \times 4) + (Cl.5 \times 5) + (Cl.6 \times 6)]]/6$$

Where Cl. is the class of DNA damage according to the visual scoring.

10.3389/fphar.2023.1208075

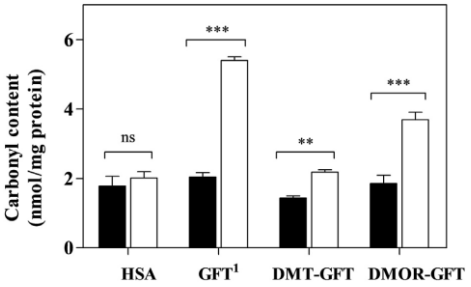

FIGURE 4
Protein carbonyl content assay. HSA solutions in PBS (5 mg/mL), alone (HSA) or in the presence of 100 μM of GFT, DMT-GFT and DMOR-GFT were irradiated with a UVA dose of 15 J/cm^2 (□ UVA Light) or kept in dark conditions (■ Dark). Protein oxidation was spectrophotometrically evaluated by the determination of carbonyl content with 2,4-dinitrophenylhydrazine (DNPH) derivatization assay. Data are the mean ± SD of 4 independent determinations. Asterisks indicate significant changes in relation to the carbonyl content of HSA under darkness by the Student's t-test (**$p < 0.01$, ***$p < 0.001$ and ns: non-significant). 1, Carbonyl content value of GFT was taken from the literature (Tamarit et al., 2021).

The results are expressed in 1–100 arbitrary units, where class 0 comets are comets with no DNA damage while class 6 comets represent comets with maximum DNA damage. Two-way ANOVA (Analysis of Variance) method was used for the statistical analysis of the data.

2.10 Measurement of cell death

2.10.1 Caspase 3/7 activity assay

HaCaT cells were seeded in 96-well plates at a concentration of 2×10^5 cell/mL. The next day, cells, in fresh DMEM medium without phenol red, were treated with the compounds at two different concentrations representing 100% and 50% of cell viability according to NRU dose-response curves. After 1 h incubation at 37°C, one plate was irradiated with UVA light (5 J/cm^2) and the other one was kept in dark conditions. Later, plates were incubated for another 24 h at 37°C with fresh DMEM medium. Then, samples were analyzed by the Apo-ONE Homogeneous Caspase-3/7 assay according to the manufacturer's instructions. Immediately after, the fluorescence was monitored at 0 h and 4 h after the addition of the substrate using Synergy H1 multi-mode microplate reader (excitation at 499 nm and emission at 521 nm). The data was subjected to statistical analysis using the Two-way ANOVA (Analysis of Variance).

2.10.2 Lactate Dehydrogenase release assay

Lactate Dehydrogenase activity assay was performed according to the manufacturer´s protocol. Briefly, HaCaT cells were seeded in 96-well plates (2×10^5 cell/mL) and incubated for 24 h. Then, after replacement of the medium with fresh no-phenol red DMEM, cells were incubated for 1 h with the compounds in two different concentrations representing 100% and 50% of cell viability according to NRU dose-response curves. Next, one plate was irradiated with UVA light (5 J/cm^2) while the other one was kept in dark conditions. Next day, samples were analyzed by CytoTox-ONE™ Homogeneous Membrane Integrity Assay and a lysis solution (9% weight/volume solution of Triton X-100 in water)

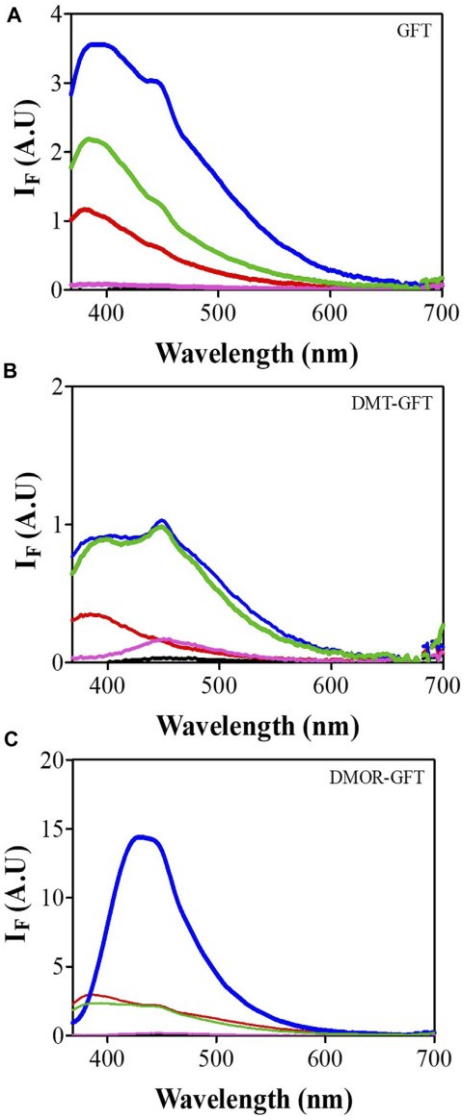

FIGURE 5
Emission spectra (λ_{exc} = 320 nm) of GFT **(A)**, DMT-GFT **(B)** and DMOR-GFT **(C)** alone (black) or in the presence of methyl linoleate (red), HSA (blue), ctDNA (magenta), or inside HaCaT cells (green).

10.3389/fphar.2023.1208075

TABLE 2 Emission maximum wavelength of GFT and metabolites in different media[a].

Media	Emission (λ_{max})		
	GFT	DMT-GFT	DMOR-GFT
ML[b]	380	384	384
HSA	386	394, 448	432
ctDNA[c]	390	450	448
HaCaT cells	388	392, 448	392, 448

[a]Excitation at 320 nm.
[b]Methyl linoleate (ML).
[c]Calf thymus DNA (ctDNA).

was used to determine the maximum amount of LDH present. The fluorescence was measured 10 min after the addition of the substrate using Synergy H1 multi-mode microplate reader (excitation at 560 nm and emission at 590 nm). The percent of LDH release was determined following the following equation:

$$\%\ \boldsymbol{LDH\ release} = \frac{\boldsymbol{Experimental\ LDH\ release}}{\boldsymbol{Maximum\ LDH\ release}}\ \boldsymbol{x}\ \mathbf{100}$$

The data was analyzed statistically employing the Two-way ANOVA (Analysis of Variance) method.

2.11 Data analysis and statistics

Results are presented as mean ± standard deviation retrieved from the results of at least three independent experiments. Data were analyzed and regression methods were developed using either GraphPad or OriginLab software. Statistical significance was obtained from the Student's t-test and p values lower than 0.05 were considered significant ($^{*}p < 0.05$; $^{**}p < 0.01$; $^{***}p < 0.001$).

3 Results and discussion

3.1 Phototoxicity of gefitinib metabolites

In vitro phototoxicity testing enables the early detection and screening of substances or compounds that may exhibit phototoxic properties. Thus, in a first stage, *in vitro* neutral red uptake (NRU) phototoxicity studies were performed with HaCaT cells to determine the phototoxic potential of GFT and its metabolites upon exposure to UVA light (5 J/cm^2).

3.1.1 *In vitro* neutral red uptake phototoxicity test

Viability of HaCaT cells was measured after treatment with the compounds employing as vital dye the neutral red, both in darkness and in the presence of UVA light. Non-linear regression dose-response curves were obtained and IC_{50} values were determined (Supplementary Figure S1). Then, the photoirritation factor (PIF) value was calculated as a ratio between the IC_{50} with and without UVA irradiation for GFT and its metabolites. The obtained values are collected in Table 1. As already found in our previous study, GFT is undoubtedly phototoxic with a PIF value of 13. The demethylated metabolite (DMT-GFT) showed a decrease in the phototoxic potential; however, following the OECD 432 Guide (OECD, 2019), DMT-GFT can still be considered phototoxic. Conversely,

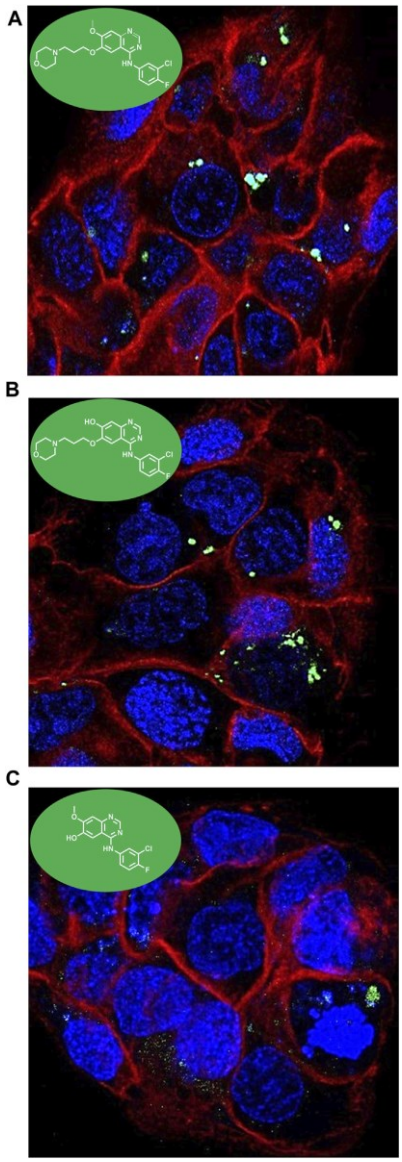

FIGURE 6
Intracellular colocalization of **(A)** GFT; **(B)** DMT-GFT and **(C)** DMOR-GFT 15 μM in HaCaT cells by confocal microscopy. A cytoplasmic distribution is observed for both drug and metabolites.

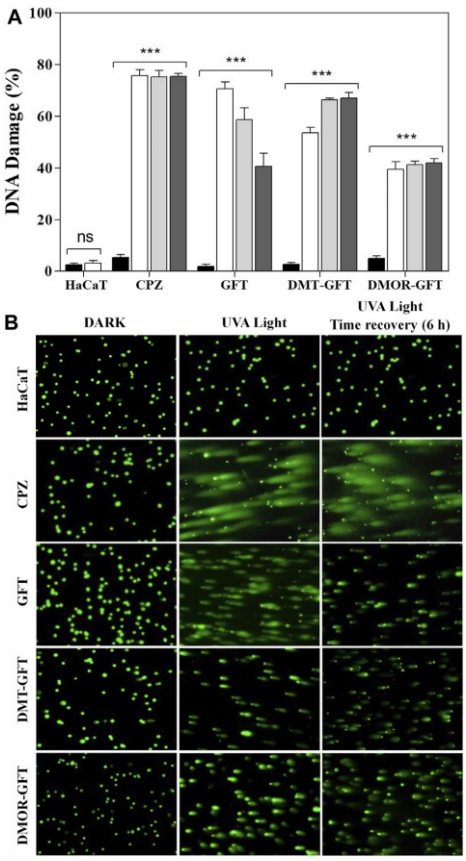

FIGURE 7
(A) Alkaline comet assay and DNA damage repair ability of HaCaT cells treated with 100 μM of GFT or metabolites. Cells were irradiated with UVA light at 2 J/cm^2 dose, 4 J/cm^2 for DMT-GFT and DMOR-GFT (□), followed by 6 h (▨) or 18 h (■) of cell recovery, or kept in the dark (■). Data are displayed as the percentage of DNA damage calculated following the six visual scoring categories. Data represent the mean ± SD of 3 independent experiments. Asterisks indicate significant differences by the Student's t-test (***$p < 0.001$, ns: non-significant). **(B)** Representative microscopy images of irradiated (UVA Light) or non-irradiated (Dark) cells non-treated or treated with GFT, DMT-GFT or DMOR-GFT and followed by 6 h of cell recovery (UVA Light + Time recovery 6 h).

replacement of the fluorine substituent with OH (DF-GFT) resulted in a negligible phototoxic activity. Surprisingly, dealkylation of the propoxy-morpholine side chain (DMOR-GFT) led to a notable enhancement of the phototoxic potential with a PIF value as high as 48.

3.1.2 Lipid photoperoxidation

Photoinduced lipid peroxidation can be one of the processes involved in cellular phototoxicity. A previous investigation has confirmed that various phototoxic drugs induce the peroxidation of linoleic acid, leading to high levels of thiobarbituric acid reactive substances (TBARS) (Onoue and Tsuda, 2006). Herein, photosensitized lipid peroxidation properties were studied for GFT and its metabolites upon UVA light irradiation in the presence of linoleic acid (1 mM). Results are given in Figure 2. According to expectations, KP (200 μM) generated a significant amount of TBARS, which confirms the suitability of this compound as a reference for photo induced peroxidation of linoleic acid. On the contrary, neither GFT nor DMT-GFT showed detectable changes in the amount of TBARS, whereas irradiation with DMOR-GFT produced a remarkable enhancement in photosensitized lipid peroxidation comparable to the reference.

In principle, photodynamic lipid peroxidation may occur via Type I (radical-mediated) or Type II (trough singlet oxygen, $^1O_2$) mechanisms, where a common intermediate is the triplet excited state of the photosensitizer. In the case of GFT and DMOR-GFT, the triplet states (^{3}GFT* and ^{3}DMOR-GFT*) have been previously identified and characterized by means of their transient absorption at ca. 600 nm. The capability of these species to produce $^1O_2$ was studied by time-resolved NIR emission at 1,270 nm, and the quantum yields ($\Phi_\Delta \leq 0.1$) were found to be very low. This indicates a marginal participation of Type II process and suggests that it would be interesting to investigate the possible involvement of the Type I oxidative mechanism in the lipid peroxidation photosensitized by DMOR-GFT. For this purpose, ^{3}DMOR-GFT* quenching experiments were performed using 1,4-dihydro-1,2-dimethylbenzoic (DMBA) as a lipid model, which contains double allylic hydrogens and is a suitable probe for studying the reactivity of lipids with photosensitizing drugs (Andreu et al., 2011). Thus, using the laser flash photolysis (LFP) technique, triplet decay traces were obtained in deaerated acetonitrile solutions of DMOR-GFT after the addition of increasing quencher concentration. As shown in Figure 3, the DMOR-GFT triplet species was efficiently quenched by DMBA with a rate constant (k_q) of $1.96\ M^{-1}{\cdot}s^{-1} \times 10^9\ M^{-1}{\cdot}s^{-1}$ (Supplementary Figure S2). This is consistent with the photoreaction between DMOR-GFT metabolite and DMBA model system proceeding by a Type I mechanism.

3.1.3 Protein photooxidation

The pharmacological target of GFT, as a tyrosine kinase inhibitor, is the ATP-rich site of plasmatic membrane receptor EGFR in cancer cells. It is known that GFT is highly protein bound in human plasma, specially to human serum albumin (HSA) (Li et al., 2006). Thus, the protein oxidation photoinduced by GFT, DMT-GFT and DMOR-GFT was studied using HSA as a model. To this end, PBS solutions of HSA and GFT, DMT-GFT or DMOR-GFT were irradiated, and then the carbonyl content, as an early biomarker of oxidative damage, was determined by the 2,4-dinitrophenylhydrazine (DNPH) derivatization method. As illustrated in Figure 4, no significant differences were found between irradiated and non-irradiated HSA, indicating the suitability of the UVA dose selected for this assay. In accordance with NRU phototoxicity results, GFT and DMOR-GFT displayed a significant oxidative effect towards HSA, although GFT showed a higher activity than the metabolite. It is interesting to recall that DMOR-GFT showed the highest PIF value among the compounds

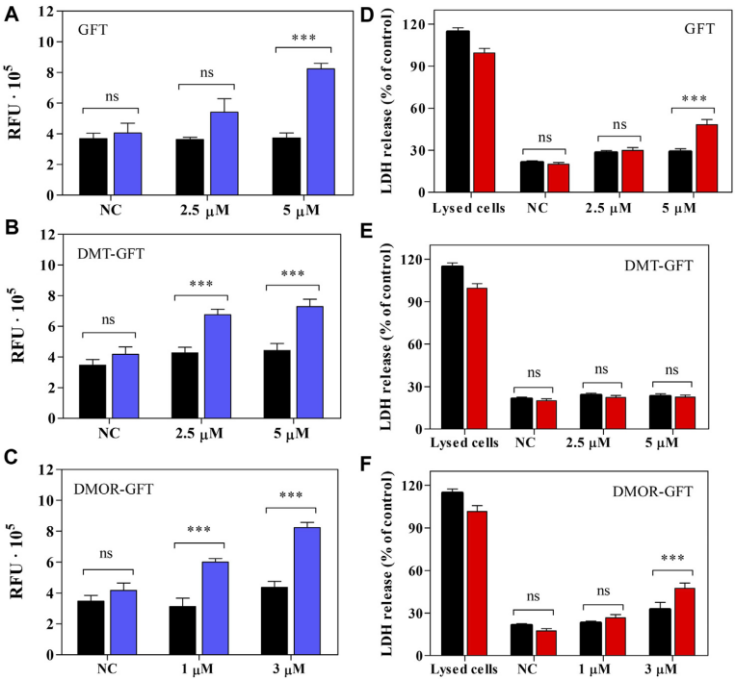

FIGURE 8
(A–C) The effect of GFT and its metabolites on caspase-3/7 activity in HaCaT cells before (■) and after UVA light exposure at 5 J/cm^2 dose (■). **(D–F)** Lactate dehydrogenase (LDH) release in HaCaT cells treated with GFT and metabolites before (■) and after UVA light exposure at 5 J/cm^2 dose (■). Data represent the mean ± SD of 3 independent experiments. Asterisks indicate significant differences by the Student's t-test (***p < 0.001, ns, non-significant).

evaluated; hence, the phototoxic potential seems to be better correlated with lipid peroxidation than with protein oxidation. Lastly, DMT-GFT did not exhibit any lipid or protein oxidative damage, consistent with the NRU phototoxicity assay outcome.

3.2 Fluorescence properties and *in vitro* cellular uptake of GFT and its metabolites

Having established the phototoxic potential of GFT (Tamarit et al., 2021), DMT-GFT and DMOR-GFT (Table 1), the fluorescence spectral characteristics of these compounds were analyzed in order to investigate the photophysical differences between GFT and its metabolites in different biological media. Thus, the emission spectra (λ_{exc} = 320 nm) were recorded in PBS solution and in the presence of different biomolecules (lipids, protein and DNA) or inside keratinocyte cells. As displayed in Figure 5 and Table 2, an evident red shift in the emission maximum occurred for the metabolites in all models, probably due to emission from the phenolate form. Expectedly, in terms of fluorescence intensity, the protein environment increased fluorescence emission in all cases, especially for the DMOR-GFT metabolite, which was markedly enhanced. On this basis, it can be foreseen that this effect is also observed once the compounds are inside keratinocyte cells (Figure 5).

In parallel, fluorescence quantum yield (Φ_F) of the internalized compounds were also determined, by comparison with anthracene as standard (Φ_F = 0.27 in ethanol) [26]. Hence, both GFT and DMT-GFT showed similar values, Φ_F = 0.07 and Φ_F = 0.04, respectively. In contrast, DMOR-GFT fluorescence inside the cells revealed a measurable enhancement of the quantum yield (Φ_F = 0.1) (Supplementary Figure S3).

Considering the intrinsic fluorescence properties stated above, confocal microscopy was used to define the intracellular colocalization of the compounds. Keratinocytes were seeded in coverslips and treated with GFT 15 µM, DMT-GFT 25 µM and DMOR-GFT 15 µM and further labeled with both RedDot™ Far-Red Nuclear (far red fluorescence) and CellMask™ Orange Plasma membrane stains (red fluorescence). After 1 h incubation, the uptake was efficiently observed in all compounds. A cytoplasmic distribution was shown in all cases without a predominant specific localization in any organelle (Figure 6).

3.3 Photogenotoxicity

Single-cell gel electrophoresis (comet assay) under alkaline conditions was carried out to disclose DNA damage as a result of single strand and double strand breaks as well as alkali-labile sites on chromosomic DNA of individual human keratinocytes. Hence, HaCaT cells were embedded in low melting point agarose on a slide and incubated with the compounds for 1 h. Then, samples were exposed to UVA light for 5 min (10 min for DMT-GFT and DMOR-GFT) and alkaline electrophoresis was performed after cell lysis. During electrophoresis, damaged DNA migrates from the nucleus yielding to formation of comet nucleoids and tails, which were visualized by fluorescence after SYBR Gold staining. Percentage of DNA damage was calculated following the classification of the images in six different classes. As shown in Figure 7, GFT displayed a significant damage (around 72%) after 5 min of UVA light irradiation. Likewise, DMT-GFT generated high percentage of DNA damage (around 54%). In contrast, irradiation of DMOR-GFT for 5 min did not promote DNA damage given that the nucleoids remained intact compared to control cells. Further irradiation of DMOR-GFT up to 10 min led to a significant degree of DNA damage (around 45%).

Generally, cells have evolved a number of repair mechanisms to reduce DNA damage; however, if the repair is faulty, DNA lesions can result in long-term mutations that can ultimately result in carcinogenic effects. For this reason, a complementary set of experiments were performed for the purpose of studying the capability of HaCaT cells to repair the nuclear DNA photodamage produced by GFT and its metabolites after UVA light irradiation. In brief, HaCaT cells containing GFT, DMT-GFT or DMOR-GFT were irradiated and processed for comet assay with two different incubation time (6 h and 18 h) before cell lysis was performed. Finally, DNA damage was monitored as mentioned earlier. Apparently, cells treated with GFT recovered considerably from the initial DNA damage although a residual damage was still remanent even when the recovery time reached 18 h (41%) (Figure 7). This trend was not found either with DMT-GFT or with DMOR-GFT treated cells, which maintained the initial damage intact (Figure 7). More details are provided in the supplementary information (Supplementary Figure S4).

3.4 Cell death mechanisms (apoptosis vs. necrosis)

Apoptosis, frequently referred to as programmed cell death, plays a crucial role in the regulation of the cellular lifecycle (Kumar, 2007), however; excessive activation of this process can lead to critical diseases (Kam and Ferch, 2000). The apoptosis event involves, in most cases, the activation of the so-called zymogens, which are evidenced to be the precursors of the well-known caspase enzymes (Kumar, 2007). Upon apoptotic signals, caspases are activated and, through their proteolytic activity, initiate protein digest inducing cell death (Morgan and Thorburn, 2001). The key effector caspases in mammals are caspase-3, -6 and -7, being caspase-3 the most frequently involved in apoptosis (Kumar, 2007). Based on these facts, the contribution of GFT or its metabolites to apoptosis upon UVA light exposure was investigated in HaCaT cells using Apo-ONE homogeneous caspase-3/7 assay. The kit contains a profluorescent Rhodamine 110 (Z-DEVD-R110), which serves as a substrate for both caspase-3 and caspase-7. Consequent to the cleavage and removal of the DEVD peptide by caspase-3/7, Rhodamine 110 (the leaving group) becomes intensely fluorescent. Considering this, caspase-3/7 activity was monitored by fluorescence and represented as a relative change, indicating the level of apoptosis activation inside the cells. Thus, both GFT and DMOR-GFT induce a concentration dependent activation of caspase-3/7 after UVA light exposure, as shown in Figures 8A, C, specially at the concentration close to the IC_{50} value (5 μM and 3 μM, respectively). In the case of DMT-GFT (Figure 8B), caspase-3/7 activity was similar between the concentration of 2.5 μM and the concentration corresponding to IC_{50} (5 μM).

L-Lactate dehydrogenase (LDH) is a stable cytoplasmic enzyme that catalyzes the conversion of lactate to pyruvate, as it converts NAD^+ to NADH during glycolysis (Kaja et al., 2015). LDH-release assay is used to assess the level of plasma membrane damage since the permeabilization of the membrane cause the leakage of this enzyme out of the cells (Chan et al., 2013). Bearing in mind that the key factor for necrotic cells is the permeabilization of the plasma membrane, the measurement of LDH-release can be considered an indicator for necrosis. However, it is interesting to highlight that the leakage of LDH may also be involved in apoptotic events in late stages (Parhamifar et al., 2013). As shown in Figure 8D, a small but significant percent of LDH-release was displayed for both GFT at a concentration near the IC_{50}, respectively. Contrary, DMT-GFT (Figure 8E) did not show any effect on the LDH release. Additionally, in Figure 8F, a significant percentage of LDH-release is also observed.

In summary, gefitinib represents an important targeted therapy for certain types of cancer, offering personalized treatment options and potentially improved outcomes. However, it is crucial to carefully consider the photo(geno)toxic potential of both the parent drug and its metabolites.

4 Conclusion

Phase I biotransformation of GFT leads to reactive metabolites. This chemical event generates non-negligible modifications in the quinazoline chromophore, leading to a significant change in its light-absorbing properties. Here, it has been investigated the photobehavior of GFT and its reactive metabolites (DMT-GFT and DMOR-GFT) towards biomolecules (lipids, proteins and DNA) as well as in cellular milieu using human keratinocytes. The metabolite DMOR-GFT is markedly more phototoxic to cells than the parent drug, according to the NRU *in vitro* studies, whereas DMT-GFT is much less phototoxic. As regards the photosensitized lipid peroxidation, only DMOR-GFT is clearly effective in the TBARS assay; the weak production of singlet oxygen, combined with the efficient triplet excited state quenching by a lipid model containing double allylic hydrogens, support the involvement of a Type I mechanism. Protein photooxidation (monitored by carbonyl content measurements) is mainly mediated by GFT and, to a lesser extent, by DMOR-GFT; in contrast, protein oxidation associated with DMT-GFT is nearly detectable. This reaction is explained by initial electron transfer from the oxidizable amino acid residues to the quinazoline moiety. Damage to cellular DNA, as revealed by the comet assay, occurs upon irradiation in the presence of the parent GFT and its two metabolites. Interestingly, the most efficient

photosensitizer in this case is DMT-GFT; moreover, the DNA damage induced by this metabolite is hardly repaired by the cells after several hours.

Overall, the observed cellular phototoxicity can be satisfactorily correlated with the results from the mechanistic studies. Thus, DMOR-GFT, which displays the highest phototoxicity, produces the most remarkable lipid photoperoxidation and is also significantly active in the protein oxidation and DNA damage studies. Conversely, DMT-GFT is the weakest phototoxic, but it shows the highest photogenotoxicity in the comet assay. The parent drug GFT constitutes an intermediate case. Hence, cellular phototoxicity seems to be rather related to photooxidation of membrane components through a Type I (radical-mediated) mechanism. These findings highlight that the biotransformation of the anticancer drug gefitinib leads to a double-edged sword cellular photo(geno)toxicity. This knowledge is crucial for the development of new TKIs to anticipate and mitigate potential phototoxic side effects. All these considerations have to be taken into account by oncologists when prescribing TKIs to cancer patients, in order to establish the conditions of use and to recommend photoprotection guidelines.

Data availability statement

The original contributions presented in the study are included in the article/Supplementary Material, further inquiries can be directed to the corresponding authors.

Author contributions

MM and IA conceived this work. Experiments were performed by ME and LT under the supervision of IV and IA. The manuscript was written by IV, MM and IA. ME and LT contributed to the preparation of figures and ESI. All authors contributed to the article and approved the submitted version.

Funding

This research was funded by the MICINN (Grant PID2020-115010RB-I00 funded by MCIN/AEI/10.13039/501100011033, RYC-2015-17737 and FPU predoctoral fellowship for ME.).

Acknowledgments

The authors would like to acknowledge IIS La Fe Microscopy Unit for technical assistance.

Conflict of interest

The authors declare that the research was conducted in the absence of any commercial or financial relationships that could be construed as a potential conflict of interest.

Publisher's note

All claims expressed in this article are solely those of the authors and do not necessarily represent those of their affiliated organizations, or those of the publisher, the editors and the reviewers. Any product that may be evaluated in this article, or claim that may be made by its manufacturer, is not guaranteed or endorsed by the publisher.

Supplementary material

The Supplementary Material for this article can be found online at: https://www.frontiersin.org/articles/10.3389/fphar.2023.1208075/full#supplementary-material

References

Agúndez, J. A. G., García-Martín, E., García-Lainez, G., Miranda, M. A., and Andreu, I. (2020). Photomutagenicity of chlorpromazine and its N-demethylated metabolites assessed by NGS. *Sci. Rep.* 10 (1), 6879. doi:10.1038/s41598-020-63651-y

Andreu, I., Neshchadin, D., Rico, E., Griesser, M., Samadi, A., Morera, I. M., et al. (2011). Probing lipid peroxidation by using linoleic acid and benzophenone. *Chemistry* 17 (36), 10089–10096. doi:10.1002/chem.201100983

Baudino, T. A. (2015). Targeted cancer therapy: The next generation of cancer treatment. *Curr. Drug Discov. Technol.* 12 (1), 3–20. doi:10.2174/1570163812666150602144310

Chai, R., Yin, Y., Cai, X., Fu, X., and Zhang, Q. (2021). Patterns of failure in patients with advanced non-small cell lung cancer treated with immune checkpoint inhibitors. *Front. Oncol.* 11, 724722. doi:10.3389/fonc.2021.724722

Chan, F. K., Moriwaki, K., and De Rosa, M. J. (2013). Detection of necrosis by release of lactate dehydrogenase activity. *Methods Mol. Biol.* 979, 65–70. doi:10.1007/978-1-62703-290-2_7

Colombo, G., Clerici, M., Garavaglia, M. E., Giustarini, D., Rossi, R., Milzani, A., et al. (2016). A step-by-step protocol for assaying protein carbonylation in biological samples. *J. Chromatogr. B Anal. Technol. Biomed. Life Sci.* 1019, 178–190. doi:10.1016/j.jchromb.2015.11.052

da Cunha Santos, G., Shepherd, F. A., and Tsao, M. S. (2011). EGFR mutations and lung cancer. *Annu. Rev. Pathol.* 6, 49–69. doi:10.1146/annurev-pathol-011110-130206

Garcia-Lainez, G., Martínez-Reig, A. M., Limones-Herrero, D., Consuelo Jiménez, M., Miranda, M. A., and Andreu, I. (2018). Photo(geno)toxicity changes associated with hydroxylation of the aromatic chromophores during diclofenac metabolism. *Toxicol. Appl. Pharmacol.* 341, 51–55. doi:10.1016/j.taap.2018.01.005

García-Lainez, G., Vayá, I., Marín, M. P., Miranda, M. A., and Andreu, I. (2021). *In vitro* assessment of the photo(geno)toxicity associated with Lapatinib, a Tyrosine Kinase inhibitor. *Arch. Toxicol.* 95 (1), 169–178. doi:10.1007/s00204-020-02880-6

Hartmann, J. T., Haap, M., Kopp, H. G., and Lipp, H. P. (2009). Tyrosine kinase inhibitors - a review on pharmacology, metabolism and side effects. *Curr. Drug Metab.* 10 (5), 470–481. doi:10.2174/138920009788897975

Kaja, S., Payne, A. J., Singh, T., Ghuman, J. K., Sieck, E. G., and Koulen, P. (2015). An optimized lactate dehydrogenase release assay for screening of drug candidates in neuroscience. *J. Pharmacol. Toxicol. Methods* 73, 1–6. doi:10.1016/j.vascn.2015.02.001

Kam, P. C., and Ferch, N. I. (2000). Apoptosis: Mechanisms and clinical implications. *Anaesthesia* 55 (11), 1081–1093. doi:10.1046/j.1365-2044.2000.01554.x

Kumar, S. (2007). Caspase function in programmed cell death. *Cell Death Differ.* 14 (1), 32–43. doi:10.1038/sj.cdd.4402060

Lembo, S., Raimondo, A., Conti, V., and Venturini, M. (2020). Photosensitivity and cancer immune-targeted therapies. *Photodermatol. Photoimmunol. Photomed.* 36 (3), 172–178. doi:10.1111/phpp.12533

Li, J., Brahmer, J., Messersmith, W., Hidalgo, M., and Baker, S. D. (2006). Binding of gefitinib, an inhibitor of epidermal growth factor receptor-tyrosine kinase, to plasma proteins and blood cells: *In vitro* and in cancer patients. *Invest. New Drugs* 24 (4), 291–297. doi:10.1007/s10637-006-5269-2

Li, J., Zhao, M., He, P., Hidalgo, M., and Baker, S. D. (2007). Differential metabolism of gefitinib and erlotinib by human cytochrome P450 enzymes. *Clin. Cancer Res.* 13 (12), 3731–3737. doi:10.1158/1078-0432.CCR-07-0088

McKillop, D., McCormick, A. D., Miles, G. S., Phillips, P. J., Pickup, K. J., Bushby, N., et al. (2004). *In vitro* metabolism of gefitinib in human liver microsomes. *Xenobiotica* 34 (11-12), 983–1000. doi:10.1080/02772240400015222

Møller, P. (2006). The alkaline comet assay: Towards validation in biomonitoring of DNA damaging exposures. *Basic Clin. Pharmacol. Toxicol.* 98 (4), 336–345. doi:10.1111/j.1742-7843.2006.pto_167.x

Morgan, M. J., and Thorburn, A. (2001). Measurement of caspase activity in individual cells reveals differences in the kinetics of caspase activation between cells. *Cell Death Differ.* 8 (1), 38–43. doi:10.1038/sj.cdd.4400800

Normanno, N., De Luca, A., Bianco, C., Strizzi, L., Mancino, M., Maiello, M. R., et al. (2006). Epidermal growth factor receptor (EGFR) signaling in cancer. *Gene* 366 (1), 2–16. doi:10.1016/j.gene.2005.10.018

OECD *Test No 432:* In vitro *3T3 NRU phototoxicity Test2019*. United States: OECD.

Onoue, S., and Tsuda, Y. (2006). Analytical studies on the prediction of photosensitive/phototoxic potential of pharmaceutical substances. *Pharm. Res.* 23 (1), 156–164. doi:10.1007/s11095-005-8497-9

Palumbo, F., Bosca, F., Morera, I. M., Andreu, I., and Miranda, M. A. (2016). Biradical vs singlet oxygen photogeneration in suprofen-cholesterol systems. *Beilstein J. Org. Chem.* 12, 1196–1202. doi:10.3762/bjoc.12.115

Parhamifar, L., Andersen, H., and Moghimi, S. M. (2013). Lactate dehydrogenase assay for assessment of polycation cytotoxicity. *Methods Mol. Biol.* 948, 13–22. doi:10.1007/978-1-62703-140-0_2

Pottier, C., Fresnais, M., Gilon, M., Jérusalem, G., Longuespée, R., and Sounni, N. E. (2020). Tyrosine kinase inhibitors in cancer: Breakthrough and challenges of targeted therapy. *Cancers (Basel)* 12 (3), 731. doi:10.3390/cancers12030731

Rawluk, J., and WallerGefitinib, C. F. (2018). Gefitinib. *Recent Results Cancer Res.* 211, 235–246. doi:10.1007/978-3-319-91442-8_16

Salvador, A., Vedaldi, D., Brun, P., and Dall'Acqua, S. (2014). Vandetanib-induced phototoxicity in human keratinocytes NCTC-2544. *Toxicol Vitro* 28 (5), 803–811. doi:10.1016/j.tiv.2014.03.007

Sapio, L., and Naviglio, S. (2022). Innovation through tradition: The current challenges in cancer treatment. *Int. J. Mol. Sci.* 23 (10), 5296. doi:10.3390/ijms23105296

Seto, Y., Inoue, R., Kato, M., Yamada, S., and Onoue, S. (2013). Photosafety assessments on pirfenidone: Photochemical, photobiological, and pharmacokinetic characterization. *J. Photochem Photobiol. B* 120, 44–51. doi:10.1016/j.jphotobiol.2013.01.010

Tamarit, L., El Ouardi, M., Andreu, I., Vayá, I., and Miranda, M. A. (2021). Photoprocesses of the tyrosine kinase inhibitor gefitinib: From femtoseconds to microseconds and from solution to cells. *Chem. Sci.* 12 (36), 12027–12035. doi:10.1039/d1sc03154f

Tan, W. K., Tan, A. R. Y., Sivanandam, P., Goh, E. J. H., Yap, Z. P., Saburulla, N. F., et al. (2020). *In vitro* inhibition of human aldehyde oxidase activity by clinically relevant concentrations of gefitinib and erlotinib: Comparison with select metabolites, molecular docking analysis, and impact on hepatic metabolism of zaleplon and methotrexate. *J. Pharmacol. Exp. Ther.* 374 (2), 295–307. doi:10.1124/jpet.120.265249

Teng, Y. H., Tan, W. J., Thike, A. A., Cheok, P. Y., Tse, G. M., Wong, N. S., et al. (2011). Mutations in the epidermal growth factor receptor (EGFR) gene in triple negative breast cancer: Possible implications for targeted therapy. *Breast Cancer Res.* 13 (2), R35. doi:10.1186/bcr2857

Vayá, I., Andreu, I., Lence, E., González-Bello, C., Consuelo Cuquerella, M., Navarrete-Miguel, M., et al. (2020). Characterization of locally excited and charge-transfer states of the anticancer drug lapatinib by ultrafast spectroscopy and computational studies. *Chem. Eur. J.* 26 (68), 15922–15930. doi:10.1002/chem.202001336

Yamaoka, T., Kusumoto, S., Ando, K., Ohba, M., and Ohmori, T. (2018). Receptor tyrosine kinase-targeted cancer therapy. *Int. J. Mol. Sci.* 19 (11), 3491. doi:10.3390/ijms19113491

Zeb, A., and Ullah, F. (2016). A simple spectrophotometric method for the determination of thiobarbituric acid reactive substances in fried fast foods. *J. Anal. Methods Chem.* 2016, 9412767. doi:10.1155/2016/9412767

Zhong, L., Li, Y., Xiong, L., Wang, W., Wu, M., Yuan, T., et al. (2021). Small molecules in targeted cancer therapy: Advances, challenges, and future perspectives. *Signal Transduct. Target Ther.* 6 (1), 201. doi:10.1038/s41392-021-00572-w

Chemical Science

ROYAL SOCIETY OF CHEMISTRY

EDGE ARTICLE

Check for updates

Cite this: Chem. Sci., 2021, 12, 12027

All publication charges for this article have been paid for by the Royal Society of Chemistry

Photoprocesses of the tyrosine kinase inhibitor gefitinib: from femtoseconds to microseconds and from solution to cells†

Lorena Tamarit, [ab] Meryem El Ouardi, [ab] Inmaculada Andreu, [ab] Ignacio Vaya *[ab] and Miguel A. Miranda *[ab]

Received 10th June 2021
Accepted 13th July 2021

DOI: 10.1039/d1sc03154f

rsc.li/chemical-science

Gefitinib (GFT) is a tyrosine kinase inhibitor currently used for the treatment of metastatic non-small cell lung cancer. Although it has been suggested that GFT can be phototoxic, there are no systematic studies on this issue. Here, the photosensitizing potential of GFT has been assessed by means of NRU assays and protein photooxidation. In addition, a thorough photophysical study is presented based on ultrafast transient absorption spectroscopy, fluorescence and laser flash photolysis. Transient species generated after excitation of GFT have been characterized in solution and in biological environments (i.e. HSA and HaCaT cells) to gain insight into the mechanisms involved in photodamage. The photobehavior of GFT was strongly medium-dependent. Excitation of the drug resulted in the formation of locally excited (LE) singlet states (^{1}GFT*), which were found to be the main emissive species in non-polar solvents and also within HSA and HaCaT cells. By contrast, in polar solvents, LE states rapidly evolved (~1 ps) towards the formation of longer-lived intramolecular charge transfer (ICT) states. The triplet excited state of GFT (^{3}GFT*) can be formed through intersystem crossing from ^{1}GFT* in non-polar solvents and from ICT states in the polar ones, or in the particular case of ethanol, by photosensitization using 2-methoxyacetophenone as an energy donor. In the HSA environment, ^{3}GFT* was hardly detected due to quenching of its LE ^{1}GFT* precursor by Trp through an electron transfer process. Accordingly, HSA photooxidation by GFT was demonstrated using the protein carbonylation method. In summary, a good correlation is established between the photophysical behavior and the photobiological properties of GFT, which provides a mechanistic basis for the observed phototoxicity.

Introduction

The epidermal growth factor receptor (EGFR) family is composed of four members (HER1–4), which are transmembrane glycoproteins with tyrosine kinase activity. They are able to regulate a number of signaling pathways within cells including cell proliferation, migration, differentiation, tissue repair and wound healing.[1,2] Mutations and overexpression of tyrosine kinase receptors, especially HER1 and HER2, may result in the appearance of different types of cancers and may promote solid tumor growth.[3] Therefore, EGFRs are major targets for the design of anticancer agents. In this regard, tyrosine kinase inhibitors (TKIs) are of high interest due to their ability to block the kinase activity of these receptors.[4–8]

Ge□tinib (GFT) is an orally active □rst-generation TKI.[9] It is clinically used for patients with locally advanced or metastatic non-small cell lung cancer; the mode of action involves speci□c binding of GFT to the ATP site of HER1 preventing autophosphorylation in tumor cells.[10] Although the bene□ts of this drug are evident, it can also induce adverse effects, which are normally associated with rash, diarrhea, dry skin, nausea and vomiting.[11]

Many drugs are known to absorb solar radiation and can induce photosensitivity reactions, such as phototoxicity or photoallergy, but also photoaging, weakening of the immune system and skin cancer.[12] These side effects can be associated with damage to biomolecules (lipids, proteins and DNA) caused by radicals or reactive oxygen species (ROS) arising from excited singlet or triplet states.[13–15] Interestingly, drugs containing the quinazoline moiety are known to produce photodermatosis.[16] In this regard, it has recently been reported that lapatinib (LAP), a TKI used for the treatment of breast and lung cancer, can induce protein photooxidation and phototoxicity.[17] The excited states arising from irradiation of LAP with UV light have been investigated by means of spectroscopic techniques in solution and in the presence of

[a]Departamento de Química/Instituto de Tecnología Química UPV-CSIC, Universitat Politècnica de València, Camino de Vera s/n, 46022 València, Spain. E-mail: mmiranda@qim.upv.es; igvapre@qim.upv.es

[b]Unidad Mixta de Investigación, Universitat Politècnica de València, Instituto de Investigación Sanitaria (IIS) La Fe, Hospital Universitari i Politècnic La Fe, Avenida de Fernando Abril Martorell 106, 46026, València, Spain

† Electronic supplementary information (ESI) available. See DOI: 10.1039/d1sc03154f

© 2021 The Author(s). Published by the Royal Society of Chemistry

human serum albumin (HSA).[18,19] It has been shown that short-lived (ps scale) intramolecular charge transfer states (ICT) are formed in the bulk solution, while longer-lived locally excited (LE) states predominate in the protein-bound LAP; these states must be related to the photosensitizing potential of the drug.

In this context, preliminary *in vitro* studies suggest that GFT may be phototoxic,[20] although there are no reports about the involved photochemical mechanisms. In the present work, the photobiological response of GFT is investigated; thus, its phototoxic potential is evaluated by means of the NRU assay, while its photooxidation activity is assessed towards HSA, the main transport protein in human serum.[21] Besides, fluorescence and transient absorption spectroscopies from the femtosecond to the microsecond time-scale are used to investigate the photobehavior of GFT in solution and in the presence of HSA, in addition to human keratinocytes (HaCaT) cells. As a result, it has been observed that the excited state properties of the drug are strongly affected by the environment: LE states are mainly formed in organic non-polar solvents and within HSA or HaCaT cells, while ICT sates are predominant in organic polar solvents. The triplet excited state of gefitinib (^{3}GFT*) has been identified and completely characterized for the first time, and its potential to generate ROS has been assessed. All these features are of key importance in connection with the photosensitizing potential of this drug.

Experimental

Chemicals and reagents

Gefitinib was purchased from Quimigen. Chlorpromazine hydrochloride (CPZ), sodium dodecyl sulphate (SDS), anthracene, human serum albumin (HSA) were purchased from Sigma-Aldrich. For cell culture experiments, HaCaT cells and Dulbecco's Modified Eagle Medium (DMEM), fetal bovine serum (FBS), and penicillin–streptomycin (1.0×10^5 U mL^{-1}, 1.0×10^5 μg mL^{-1}) were supplied by invitrogen. Trypsin–EDTA (0.25–0.02%) and glutamine solutions were provided by Cultek. 2,4-Dinitrophenylhydrazine hydrochloride (DNPH) was purchased from Santa Cruz Biotechnology (Dallas, USA). PBS buffer was prepared by dissolving phosphate-buffered saline tablets (Sigma) using ultrapure water from a Millipore (Milli-Q Synthesis) system. Spectrophotometric HPLC solvents were obtained from Scharlab and used without further purification.

Irradiation equipment

Irradiations were performed using a LCZ-4 photoreactor fitted with six top and eight side Hitachi lamps (λ_{max} = 350 nm, Gaussian distribution; Luzchem, Canada). Irradiation for *in vitro* NRU assay was performed in 96-well transparent plates while 6-well transparent plates were used for photooxidation assay. All experiments were performed keeping the plates on ice inside the photoreactor to avoid overheating.

Spectroscopic measurements

Steady-state absorption spectra were recorded in a JASCO V-760 spectrophotometer. Steady-state fluorescence spectra were obtained using a JASCO spectrofluorometer system provided with a monochromator in the wavelength range 200–900 nm, with an excitation wavelength of 340 nm at 25 °C. Measurements on drug@protein complexes were performed in aerated PBS of 1 : 1 molar ratio mixtures at 10 μM. The absorbance of the samples at the excitation wavelength was kept below 0.1. Phosphorescence measurements were performed in a Photon Technology International (PTI, TimeMaster TM-2/2003) spectrophotometer equipped with a pulsed Xe lamp, operating in a time-resolved mode with a delay time of 0.5 ms. The sample was dissolved in ethanol, introduced in a quartz tube of 5 mm of diameter and cooled with liquid N_2 (77 K).

Time-resolved fluorescence measurements were performed using an EasyLife X system containing a sample compartment composed of an automated peltier cuvette holder to control the temperature, a pulsed LED excitation source and a lifetime detector. The employed LED excitation source was 340 nm, with an emission filter of WG370.

Laser Flash Photolysis (LFP) measurements were performed using a pulsed Nd:YAG L52137 V LOTIS TII at an excitation wavelength of 355 nm. The single pulses were *ca.* 10 ns duration, and the energy was ∼12 mJ per pulse. The laser flash photolysis system consisted of the pulsed laser, a 77250 Oriel monochromator and an oscilloscope DP04054 Tektronix. The output signal from the oscilloscope was transferred to a personal computer. The absorbances of all solutions were adjusted at ∼0.20 at 355 nm. All UV, fluorescence and LFP measurements were performed using 10×10 mm^2 quartz cuvettes at room temperature under deaerated conditions (25 min N_2 bubbling), or in the case of the protein complexes and/or singlet oxygen detection in an aerated atmosphere. Control experiments indicated that the degree of decomposition of the samples after photolysis was lower than 5%.

Femtosecond transient absorption experiments were performed using a typical pump-probe system. The femtosecond pulses were generated with a compact regenerative amplifier that produces pulses centered at 800 nm (τ_{pulse} 100 fs approx., 1 mJ per pulse). The output of the laser was split into two parts to generate the pump and the probe beams. Thus, tunable femtosecond pump pulses were obtained by directing the 800 nm light into an optical parametric amplifier. In the present case, the pump was set at 330 nm and passed through a chopper prior to focusing onto a rotating cell (1 mm optical path) containing the samples in organic or aqueous solution. The white light used as a probe was produced after part of the 800 nm light from the amplifier travelled through a computer controlled 8 ns variable optical delay line and impinged on a CaF_2 rotating crystal. This white light was in turn split in two identical portions to generate reference and probe beams that then are focused on the rotating cell containing the sample. The pump and the probe were made to coincide to probe the sample. The power of the pump beam was set to 180 μW. Under these conditions, the degree of photodegradation of the samples was lower than 5%. A computer-controlled imaging spectrometer was placed after this path to measure the probe and the reference pulses to obtain the transient absorption decays/spectra.

© 2021 The Author(s). Published by the Royal Society of Chemistry

The experimental data were treated and compensated by the chirp using the ExciPro program.

Phototoxicity assay

A neutral Red Uptake phototoxicity test (NRU) was selected for the study of the cellular phototoxic properties of GFT. The assay was performed in accordance with the OECD Guideline 432 (OECD 2019) in HaCaT cells instead of the 3T3 cell line from BALB/c, the standard method, due to the similarity with human skin cells.[22]

The positive and negative phototoxic controls were CPZ and SDS, respectively. Chlorpromazine is a commonly used antipsychotic drug which has demonstrated relevant phototoxic properties.[23] Briefly, two 96-well plates were seeded at a density of 2.0×10^4 cells per well, and cells were treated the next day with GFT at eight concentrations ranging from 2.5 to 500 μM. Additional plates were treated with CPZ (from 1.57 μM to 500 μM) and SDS (from 3.13 μM to 500 μM) as the references for this experiment. Then, one plate was irradiated with 5 J cm^{-2} UVA dose (UVA light) whereas the other plate was kept in a dark box (DARK). The next day, cells were incubated with neutral red solution (50 μg mL^{-1}) and further dye extraction from lysosomes was accomplished with a mix buffer [distilled water 50% (v/v), ethanol 49.5% (v/v) and acetic acid 0.5% (v/v)]. Afterwards, the absorbance of the plates was read at 540 nm on a Synergy H1 microplate reader. Dose–response curves for GFT and controls were obtained to determine the concentration causing a reduction of 50% of the neutral red uptake (IC_{50}) under dark and UVA light conditions. Lastly, the photoirritation factor (PIF) values were calculated using the following equation:

$$\mathrm{PIF} = \frac{\mathrm{IC_{50}DARK}}{\mathrm{IC_{50}UVA\ light}}$$

Conforming to OECD guideline 432, a substance is labelled as "non-phototoxic" when PIF is <2, "probably phototoxic" if PIF is between 2 and 5 and "phototoxic" if PIF is >5.

Protein carbonyl content assay

Protein carbonyl content assay was carried out following the protocol described elsewhere,[24] but with minor modifications. Briefly, a solution of HSA (5 mg mL^{-1}, 1 mg protein/sample) was prepared in PBS and irradiated alone or in the presence of 100 μM of GFT followed by the exposure to UVA light at doses of 5, 10 and 15 J cm^{-2}. Then, the amount of HSA oxidation was monitored spectrophotometrically after incubation of the samples with 2,4-dinitrophenylhydrazine (DNPH) 10 mM in order to generate quantifiable DNPH adducts. Later, proteins were precipitated with 20% trichloroacetic acid solution and a sequence of two washes was performed with ethanol/ethyl acetate 1 : 1 (v/v) containing 20% trichloroacetic acid. Finally, dried protein pellets were resolubilized with guanidine buffer (6 M) and absorbance was registered at 375 nm using a Synergy H1 microplate reader. Conclusively, the potential of protein oxidation was measured based on the content of carbonyl generated (nmol of carbonyl per mg protein) in the presence of GFT.

Results and discussion

As mentioned in the introduction, TKIs can exhibit photosensitizing potential in combination with sunlight.[17] Hence, it appeared interesting to assess the phototoxicity of GFT *in vitro* based on the established neutral red uptake (NRU) method. Thus, human keratinocytes were incubated with GFT and irradiated with a UVA light dose of 5 J cm^{-2}. The cytotoxic profiles were determined by measurements of the irradiated samples in comparison with those kept in the dark, using neutral red as a vital dye. Thus, from the obtained dose–response curves (see Fig. S1 in the ESI†), IC_{50} was determined, and the photoirritation factor was calculated as the ratio of IC_{50} between dark and UVA conditions (see the Experimental section). The PIF value of GFT was found to be 13. Therefore, following the OECD 432 guide (OECD 2019), GFT can be considered a phototoxic drug (Fig. 1 and 2).

In view of the phototoxic potential of GFT, its photobehavior was studied by means of fluorescence and transient absorption spectroscopies. The photophysical properties of the drug were first investigated in organic solvents of different polarities. The UV absorption spectra barely varied from acetonitrile to

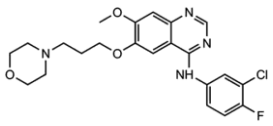

Fig. 1 Chemical structure of GFT.

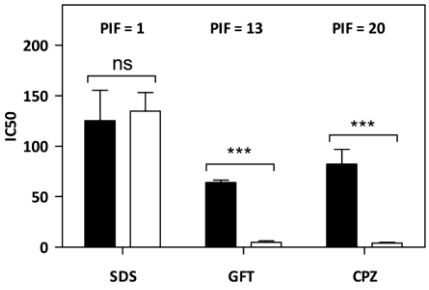

Fig. 2 *In vitro* phototoxicity of GFT in the NRU assay. The concentration causing a reduction of 50% of the neutral red uptake (IC_{50}) was calculated both in the dark (filled bars) and under UVA light conditions (empty bars). The represented data correspond to the mean ± SD from 4 independent dose–response curves. Chlorpromazine (CPZ) and sodium dodecyl sulfate (SDS) represent the selected positive and negative phototoxicity controls, respectively. The PIF value was determined from the ratio between IC_{50} dark and IC_{50} UVA for each compound. According to the OECD 432 guide (2019), PIF < 2 means "non-phototoxic"; 2 < PIF < 5 means "probable phototoxicity" and PIF > 5 means "phototoxicity". Asterisks indicate significant differences by the *t*-Student test (ns: non-significant, ***$p < 0.001$).

© 2021 The Author(s). Published by the Royal Society of Chemistry

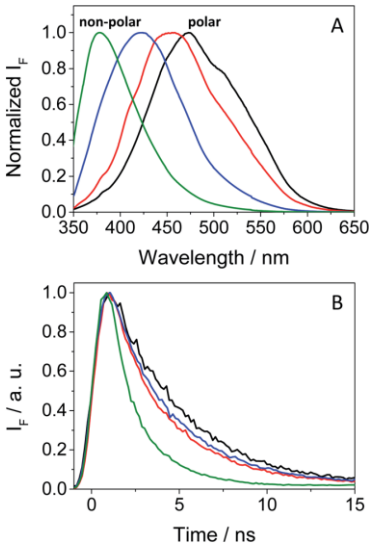

Fig. 3 Normalized fluorescence spectra (A) and decays (B) under aerated conditions for GFT in acetonitrile (black), 1,4-dioxane (red), toluene (blue) and cyclohexane (green) after excitation at 340 nm.

cyclohexane (see Fig. S2 in the ESI†) while the fluorescence properties were strongly affected by the polarity. This is in agreement with previous observations in *n*-hexane, chloroform or in alcohol solutions, where no detailed explanation was given.[25,26] The results show that the emission spectra of GFT were broad and unstructured in polar solvents (see Fig. 3A), displaying low quantum yield (ϕ_F) and peaking at long wavelengths (λ_{max} > 450 nm). By contrast, ϕ_F values were much higher in non-polar solvents, and emission occurred at much shorter wavelengths with a lower fwhm (see Table 1). To give a comparison, the fluorescence quantum yield of GFT in acetonitrile was 0.05, with $\lambda_{max} \sim 473$ nm and a fwhm of about 118 nm, while in cyclohexane ϕ_F was 0.19, and the spectrum showed a fwhm of *ca.* 71 nm and $\lambda_{max} \sim 378$ nm. In addition, the fluorescence decay kinetics (see Fig. 3B) showed the longest lifetime for the emitting species in acetonitrile, while the shortest one was detected in cyclohexane. Due to the short fluorescence lifetimes (1–3 ns), the presence or absence of oxygen had only a marginal effect (see Fig. S3 in the ESI†).

Table 1 Fluorescence properties of GFT in solvents of different polarities and within HSA and HaCaT cells at $\lambda_{exc} = 340$ nm

	λ_{max}/nm	fwhm/nm	ϕ_F[a]	τ_F/ns
MeCN	473	118	0.05	3.4
1,4-Dioxane	458	116	0.09	2.5
Toluene	421	101	0.18	2.6
Cyclohexane	378	71	0.19	1.3
HSA	390	95	0.02	1.3
HaCaT cells	390	70	0.05	—

[a] ϕ_F were determined using anthracene in ethanol as ref. 27.

The combined results from both steady-state and time-resolved measurements can be interpreted as emission from locally excited (LE) singlet states in non-polar solvents or from intramolecular charge transfer (ICT) states in the polar ones. The energy of LE in cyclohexane, determined from the crossing point between the normalized excitation and emission spectra (see Fig. S4 in the ESI†), was ~82 kcal mol^{-1}, while that of ICT in MeCN was roughly estimated to be of about 64 kcal mol^{-1} from the bathochromic shift between the maxima spectra of cyclohexane and MeCN. At low temperatures, the fluorescence signal of GFT in a solid cyclohexane matrix at 77 K was very similar to that found in solution at 298 K. For acetonitrile, it was not possible to record the spectrum of a solid sample. Hence, low temperature measurements in a polar medium were performed in frozen ethanol, where two components were clearly distinguished in the 350–425 and 430–550 nm regions (see Fig. S5 in the ESI†), attributed to the LE and ICT states, respectively. From the wavelength corresponding to the first maximum of the ICT emission, a value of 65 kcal mol^{-1} was obtained for the energy of this state, which is compatible with the 64 kcal mol^{-1} estimated in MeCN from the bathochromic shift of the maximum (see above). In ethanol solution, at room temperature, the emission was very weak and no clear spectrum was recorded.

In order to get more insight into the formation of both LE and ICT states, femtosecond transient absorption measurements were performed on GFT in toluene, acetonitrile and ethanol (cyclohexane was not used due to solubility limitations). This is a highly sensitive technique which allows studying the formation of transient species in terms of spectral shape and kinetics resolution, and provides direct information on processes such as intersystem crossing (ISC), energy or electron transfer (ET) and charge separation.[28–30] Thus, excitation of the drug at 330 nm in toluene gave rise to an absorption band peaking at $\lambda_{max} \sim 460$ nm. It evolved through two nearly isosbestic points (415 and 560 nm) towards the formation of a new band with two maxima *ca.* 605 and 410 nm (see Fig. 4A), which became clearly defined on the nanosecond scale. This band, mostly formed in about 10 ps (see Fig. S6 in the ESI†), can be tentatively ascribed to the triplet excited state of gefitinib (^{3}GFT*). By contrast, in acetonitrile, the band at around 460 nm evolved in about 1 ps towards other species with a maximum *ca.* 430 nm, which persisted up to the nanosecond scale (see Fig. 4B). This behavior is comparable to that previously observed for LAP in MeCN, where LE was the precursor species of the ICT state, formed in about 1.5 ps and decayed in the nanosecond time-scale.[18] Accordingly, a similar interpretation can be done for GFT in MeCN; thus, the band at 460 nm is associated with LE, while that at 430 nm to a ICT state. Interestingly, the transient absorption band at ~605 nm was again visible on the ns scale, coexisting with that of ICT. A similar photobehavior was detected in ethanol; so, LE rapidly evolved (*ca.* 1.4 ps) towards the formation of ICT, which disappeared in about 700 ps (see Fig. 4C). Surprisingly, the long-lived band associated to ^{3}GFT* with maxima around 410 and 605 nm was not detected.

In order to further characterize the excited species of the drug at longer time scales, nanosecond LFP measurements were

© 2021 The Author(s). Published by the Royal Society of Chemistry

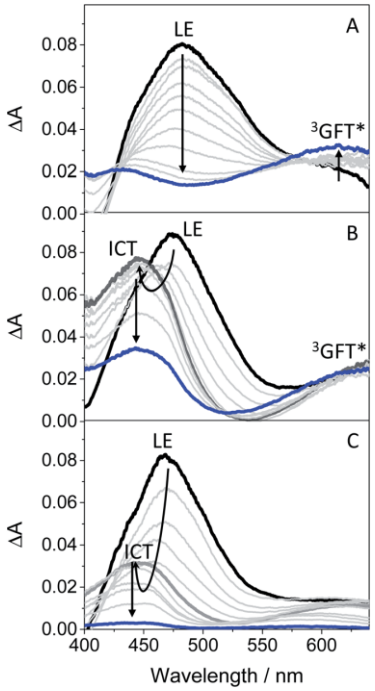

Fig. 4 Femtosecond transient absorption spectra of GFT in (A) toluene, (B) acetonitrile and (C) ethanol, after excitation at 330 nm. The spectra were recorded from 0.5 ps (black line) to 2 ns (blue line) in (A) and (B), and from 0.5 ps (black line) to 0.7 ns (blue line) in (C).

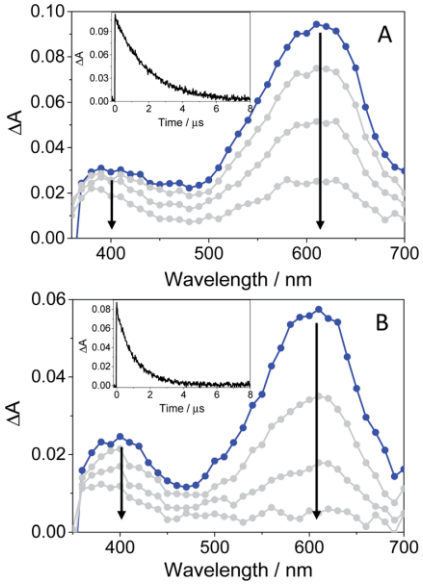

Fig. 5 LFP spectra (from 0.2 to 3 μs) and decay traces at 600 nm of GFT in toluene (A) and MeCN (B), after excitation at 355 nm under deaerated conditions.

performed at $\lambda_{exc} = 355$ nm. The transient spectra obtained in toluene showed two maxima around 400 and 600 nm (see Fig. 5A), very similar to those detected in the ns window from ultrafast spectroscopy; the two bands decayed in a similar manner (*ca.* 2 μs), indicating that both are associated with the same species in the excited state. The photobehavior in acetonitrile (see Fig. 5B) was very similar to that observed in toluene, but with slightly lower efficiency and the excited species displaying shorter lifetimes (~1.7 μs).

The signal at 600 nm, assigned to ^{3}GFT*, was strongly quenched by oxygen ($k_Q \sim 5.6 \times 10^9$ M^{-1} s^{-1}). In order to better characterize its triplet nature, photosensitization LFP measurements using naproxen (NPX) as an acceptor were performed. The energy of ^{3}NPX* is 62 kcal mol^{-1},[31] while that of ^{3}GFT*, determined from the 4% rise of its phosphorescence spectrum in a solid matrix of ethanol at 77 K (see Fig. S7 in the ESI†), was of about 69 kcal mol^{-1}. Selective excitation of GFT at 355 nm in the presence of NPX resulted in a strong quenching of the signal at 600 nm with a concomitant formation of ^{3}NPX* ($\lambda_{max} \sim 430$ nm) through a triplet–triplet energy transfer process from GFT to NPX (see Fig. S8 in the ESI†). Therefore, the transient band peaking at ~600 nm can be undoubtedly assigned to the first triplet excited state of the drug. It is worth noting that ^{3}GFT* was much lower in ethanol (see Fig. S9 in the ESI†); all these results are in agreement with those obtained from ultrafast spectroscopy.

In this context, an interesting point of discussion is the formation of ^{3}GFT* in both non-polar and polar solvents, as it can arise from different precursors (LE and/or ICT states, respectively). Interestingly, excitation of the drug in non-polar solvents such as toluene gives rise to LE states, which would evolve towards the formation of ^{3}GFT* in *ca.* 10 ps through ISC. In contrast, ICT predominates in polar solvents such as acetonitrile; therefore, in this case, ^{3}GFT* would be mainly formed from ICT rather than from LE states, as the latter disappear in a few ps. The minor formation of ^{3}GFT* in ethanol might be due to an enhanced stabilization of the ICT species, whose energy becomes lower than that of ^{3}GFT* (65 *vs.* 69 kcal mol^{-1}), resulting in an endothermic ISC. However, markedly higher formation of triplet gefitinib was accomplished through triplet–triplet energy transfer from 2-methoxyacetophenone (MAP) as the photosensitizer.[32] Thus, excitation of a mixture containing GFT and MAP in deaerated ethanol resulted in enhanced formation of ^{3}GFT* (see the difference spectrum in the inset in Fig. 6A). The growth and decay of this species at its absorption maximum (*ca.* 600 nm) are clearly shown in Fig. 6B.

From a photobiological point of view, triplet excited species are key intermediates that can induce damage to proteins and other biological targets.[33] This can involve radical pathways initiated by electron transfer or hydrogen abstraction (type I mechanism), and/or energy transfer from a photosensitizer to molecular oxygen, leading to singlet oxygen ($^1O_2$ type II mechanism).[34,35] In this context, it has been observed by means of LFP ($\lambda_{exc} = 355$ nm) that GFT can induce formation of $^1O_2$, which has been detected by time-resolved NIR emission at 1270 nm. In

© 2021 The Author(s). Published by the Royal Society of Chemistry

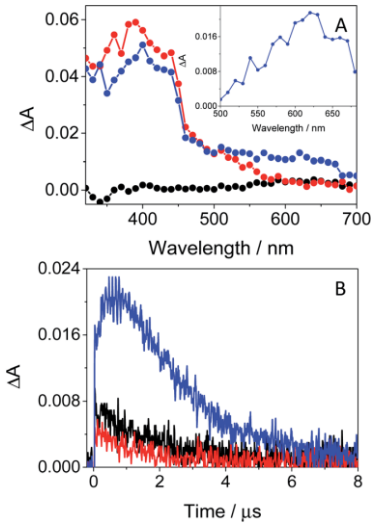

Fig. 6 (A) Transient absorption spectra of GFT (black), MAP (red) and a mixture of GFT/MAP (blue). The inset shows the spectrum obtained from subtraction of the MAP spectrum to that of the GFT/MAP spectrum 0.6 μs after the laser pulse. (B) LFP decay traces at 610 nm for GFT (black), MAP (red) and a mixture of GFT/MAP. All measurements were performed in deaerated ethanol at $\lambda_{exc} = 355$ nm at concentrations of 40 μM for GFT and 30 mM for MAP.

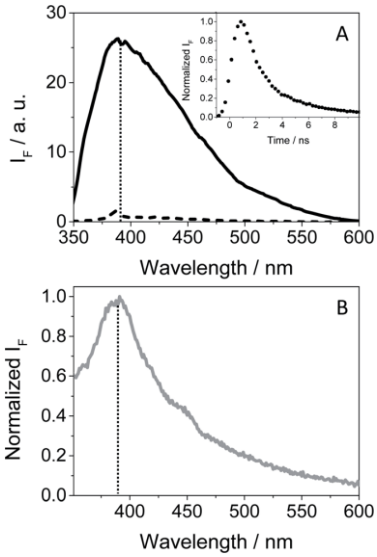

Fig. 7 (A) Fluorescence spectra of isoabsorptive solutions at the excitation wavelength for GFT in the bulk aqueous solution (dashed line) and GFT@HSA at 1 : 1 molar ratio (solid line). The inset shows the normalized fluorescence decay for GFT@HSA at 1 : 1 molar ratio (10 μM) in PBS. (B) Normalized fluorescence spectra of GFT within HaCaT cells. All measurements were performed at $\lambda_{exc} = 340$ nm. The vertical dotted line marks the maximum emission at *ca.* 390 nm.

the case of GFT, the singlet oxygen quantum yields, determined using ketoprofen as a reference,[36] were of about 0.17 and 0.1 in aerated toluene and MeCN, respectively; this agrees with the enhanced triplet formation in the former.

As GFT is phototoxic to cells (see above) and membrane proteins are major targets for photosensitized oxidation,[37,38] the photobehavior of GFT was investigated in the presence of human serum albumin, a model protein which is the most abundant in plasma.[21] It is known that GFT highly binds to HSA.[39] Selective excitation of the protein-bound gefitinib at 340 nm (see Fig. S10 in the ESI†) evidenced a significant enhancement of its fluorescence compared with the drug free in aqueous solution, which is insignificant (see Fig. 7A). The stronger emission of complexed gefitinib may result from the higher restrictions in its degrees of freedom for conformational relaxation within HSA. Interestingly, the spectrum profile displays its maximum at ~390 nm, and decays with a lifetime of about 1.3 ns, showing a very similar behavior to that observed in cyclohexane (see Table 1). Accordingly, the excited species detected for GFT@HSA can again be associated with LE singlet states. However, the lower fluorescence quantum yield of the drug within the protein compared with cyclohexane (0.02 *vs.* 0.19) is worth noting; this decrease can be the result of an electron transfer process to GFT in its excited state from appropriate donors, for instance the only tryptophan (Trp) residue of HSA.[40] A similar process was previously observed for other drug@HSA systems.[41,42] In order to check this possibility, application of the Weller equation,[43] considering the singlet energy of GFT and the corresponding redox potentials,[27] agrees with an exergonic electron transfer from Trp to the excited drug ($\Delta G = -18.5$ kcal mol^{-1}). As a matter of fact, the feasibility of this process was confirmed experimentally from fluorescence measurements. Thus, decay kinetics of ^{1}GFT* was recorded in the non-polar solvent cyclohexane in the presence of increasing amounts of 3-methylindole, the chromophore present in the Trp residue (see Fig. S11 in the ESI†); a quenching rate constant of $\sim 4.3 \times 10^{10}$ M^{-1} s^{-1} was determined. Therefore, the low ϕ_F observed for gefitinib within HSA can be explained as a result of an electron transfer from Trp to the LE ^{1}GFT*.

An interesting point to highlight is the similarity of the emission spectra detected for GFT within HSA and HaCaT cells after selective excitation of the drug at 340 nm. As it can be observed, the emission of the drug in a cellular milieu (see Fig. 7B) was centered at the same position as in the protein (~390 nm), showing a slightly higher quantum yield of about 0.05 (see Table 1). This may suggest that the photobehavior of GFT in the protein environment is similar to what could be expected in cells.

In order to obtain further information about the early processes occurring inside HSA, femtosecond transient absorption measurements were performed upon selective excitation of the protein-bound gefitinib at 330 nm. This resulted in the formation of a single transient band with a maximum at ~460 nm (see Fig. 8A), assigned to LE ^{1}GFT*. This species decays following a multi-exponential law (see Fig. 8B), which

© 2021 The Author(s). Published by the Royal Society of Chemistry

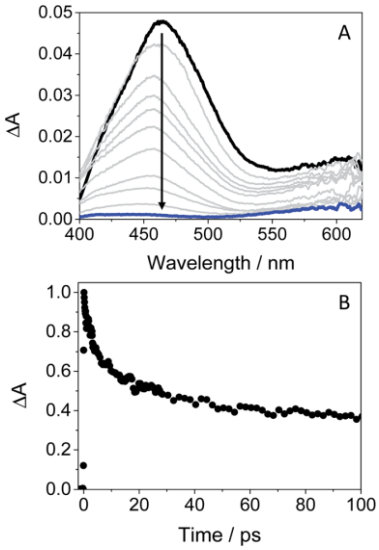

Fig. 8 Femtosecond transient absorption spectra from 0.5 ps (black line) to 2 ns (blue line) (A), and decay trace at 460 nm (B) for GFT@HSA at 1 : 1 molar ratio in aerated PBS at $\lambda_{exc} = 330$ nm.

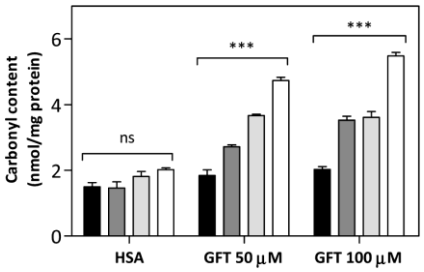

Fig. 9 Protein photooxidation by GFT. Solutions of HSA (5 mg mL^{-1}) in the presence or absence of 50 μM or 100 μM of GFT were irradiated at 5 J cm^{-2} UVA dose (dark gray bar), 10 J cm^{-2} (light gray bar) and 15 J cm^{-2} (empty bar) of UVA dose or kept under dark conditions (black bar). The carbonyl content was quantified spectrophotometrically after derivatization with 2,4-dinitrophenylhydrazine (DNPH). Data represent the mean ± SD of 4 independent experiments. Asterisks indicate significant differences relative to the carbonyl content in HSA in darkness by the *t*-Student test (*$p < 0.05$, **$p < 0.01$, ***$p < 0.001$, ns: non-significant).

can be associated with parallel processes arising from the drug located in different binding sites of HSA. Thus, the shortest component, of *ca.* 5 ps, can be related to the binding of GFT in a site close to the Trp residue, where the electron transfer process from the amino acid to ^{1}GFT* might take place. By contrast, the longest component, which persists up to the nanosecond time-scale, could correspond to the location of GFT in another site far from Trp, where the electron transfer process cannot occur.

It should be emphasized that ^{3}GFT* was hardly detectable in the protein medium, where the band at ~600 nm is marginal. In this regard, nanosecond LFP measurements on GFT@HSA at $\lambda_{exc} = 355$ nm indicated a very weak absorption around 600 nm compared with MeCN (see Fig. S12 in the ESI†). This may be the result of the LE ^{1}GFT* quenching through electron transfer from the Trp residue of HSA. As stated above, this process might occur in about 5 ps, which is faster than ISC (~10 ps); consequently, the yield of ^{3}GFT* within HSA is greatly decreased. This has clear biological implications, since the photosensitization of GFT in biological media could involve the participation of LE singlet states rather than ^{3}GFT*.

In this context, as the electron transfer process from Trp to ^{1}GFT* has been detected not only in solution but also in the HSA-bound drug, it appeared interesting to evaluate the capability of GFT to induce protein photooxidation, since this process could be the origin of the above mentioned GFT-photosensitized damage occurring in HaCaT cells. To this end, the protein carbonylation method was used, which represents the most frequent irreversible oxidative modification affecting proteins. In this regard, PBS solutions containing HSA and GFT were irradiated at different UVA light doses (5, 10 and 15 J cm^{-2}), and the carbonyl content, as an early biomarker of oxidative damage, was quantified using 2,4-dinitrophenylhydrazine (DNPH). The results shown in Fig. 9 revealed that GFT promotes a consistent photooxidative effect towards HSA, which agrees with the results obtained from the phototoxicity NRU assay.

Scheme 1 summarizes the main species generated upon excitation of the drug in different media. In all cases, an instantaneous formation of LE ^{1}GFT* is observed. In non-polar solvents, this species emits light at wavelengths around 380 nm within *ca.* 1 ns; in addition, LE ^{1}GFT* undergoes ISC to the triplet excited state (~10 ps), which displays a maximum at *ca.* 600 nm. By contrast, in polar solvents, LE rapidly evolves (~1 ps) towards the formation of ICT states, which emit at longer wavelengths (~470 nm) with much lower yields. In these media, ^{3}GFT* is mainly populated from ICT states; surprisingly, it is formed in very low efficiency in ethanol solution, where conversion of ICT ^{1}GFT* to ^{3}GFT* is thermodynamically disfavored. Finally, in the biological environment, *i.e.* HSA and HaCaT cells, LE ^{1}GFT* is the only detected species; its lifetime is significantly decreased through ET-quenching by electron donors.

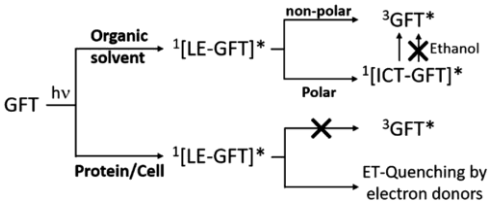

Scheme 1 Schematic representation of the main species arising from the excited gefitinib in different environments: non-polar or polar organic solvents, and biological media such as protein or cells.

© 2021 The Author(s). Published by the Royal Society of Chemistry

Conclusions

The photophysical behavior of GFT has been investigated in solution and in biological environments, from the femtosecond to the microsecond time-scales, whereas the photosensitizing properties of the drug have been studied by means of the NRU and protein carbonylation methods. *In vitro* NRU assay using human keratinocytes (HaCaT) has proven the phototoxic potential of GFT. The main excited species arising from selective irradiation of the drug are the locally excited (LE) and intramolecular charge transfer (ICT) singlet states, as well as the triplet state. In general, the LE singlet is the only emitting species both in organic non-polar solution and in biological media (*i.e.* HSA and HaCaT cells). In the former, intersystem crossing to the triplet excited state of GFT occurs in the picosecond scale. By contrast, in organic polar solvents, LE states rapidly evolve towards the formation of ICT states. This species emits at longer wavelengths and shows higher lifetimes than LE states; they are also able to populate ^{3}GFT* in acetonitrile. Surprisingly, ISC is not observed in ethanol, since ICT states are rapidly deactivated (in about 0.7 ns); however, ^{3}GFT* is generated in this solvent by photosensitization with 2-methoxyacetophenone as an energy donor. In the HSA binding sites, formation of ^{3}GFT* is hardly detected; instead, quenching of its LE singlet precursor by Trp through an electron transfer mechanism is observed. Accordingly, GFT photosensitized oxidation of HSA is demonstrated using the protein carbonylation method. In summary, a good correlation is established between the photophysical behavior and the photobiological properties of GFT, which provides a mechanistic basis for the observed phototoxicity.

Author contributions

Research was conceived by all authors. Experiments were performed by L. T. and M. O., with the aid of I. A. and I. V. The research was supervised by I. A., I. V. and M. A. M. All authors contributed to the writing of the manuscript and ESI.†

Conflicts of interest

There are no conflicts to declare.

Acknowledgements

Financial support from the Spanish Government (RYC-2015-17737, CTQ2017-89416-R, BEAGAL 18/00211, FPU19/00048 and PID2020-115010RB-I00; the Carlos III Institute (ISCIII) of Health, grants: PI16/01877, and CPII16/00052) and Conselleria d'Educació, Cultura i Esport (PROMETEO/2017/075) is gratefully acknowledged.

References

1 S. R. Hubbard and J. H. Till, *Annu. Rev. Biochem.*, 2000, **69**, 373–398.
2 M. J. Wieduwilt and M. M. Moasser, *Cell. Mol. Life Sci.*, 2008, **65**, 1566–1584.
3 R. I. Nicholson, J. M. W. Gee and M. E. Harper, *Eur. J. Cancer*, 2001, **37**, S9–S15.
4 L. Huang, S. Jiang and Y. Shi, *J. Hematol. Oncol.*, 2020, **13**, 143.
5 J. Mendelsohn and J. Baselga, *Oncogene*, 2000, **19**, 6550–6565.
6 C. Pottier, M. Fresnais, M. Gilon, G. Jerusalem, R. Longuespee and N. E. Sounni, *Cancers*, 2020, **12**, 731.
7 T. Yamaoka, S. Kusumoto, K. Ando, M. Ohba and T. Ohmori, *Int. J. Mol. Sci.*, 2018, **19**, 3491.
8 N. E. Hynes and H. A. Lane, *Nat. Rev. Cancer*, 2005, **5**, 341–354.
9 M. H. Cohen, G. A. Williams, R. Sridhara, G. Chen and R. Pazdur, *Oncologist*, 2003, **8**, 303–306.
10 A. Arora and E. M. Scholar, *J. Pharmacol. Exp. Ther.*, 2005, **315**, 971–979.
11 R. J. Cersosimo, *Expert Opin. Drug Saf.*, 2006, **5**, 469–479.
12 B. L. Diffey and I. E. Kochevar, in *Photodermatology*, ed. H. W. Lim, H. H. Hönigsmann and J. L. M. Hawk, Informa Healthcare, USA, 1st edn, 2007.
13 M. Gonçalo, in *Contact Dermatitis*, ed. J. D. Johansen, Springer-Verlag, Berlin, 2011, ch. 18, pp. 361–376.
14 S. Lembo, A. Raimondo, V. Conti and M. Venturini, *Photodermatol., Photoimmunol. Photomed.*, 2020, **36**, 172–178.
15 K. R. Stein and N. S. Scheinfeld, *Expert Opin. Drug Saf.*, 2007, **6**, 431–443.
16 T. P. Selvam and P. V. Kumar, *Res. Pharm.*, 2011, **1**, 1–21.
17 G. García-Laínez, I. Vayá, M. P. Marín, M. A. Miranda and I. Andreu, *Arch. Toxicol.*, 2021, **95**, 169–178.
18 I. Vayá, I. Andreu, E. Lence, C. González-Bello, M. C. Cuquerella, M. Navarrete-Miguel, D. Roca-Sanjuan and M. A. Miranda, *Chem.–Eur. J.*, 2020, **26**, 15922–15930.
19 I. Andreu, E. Lence, C. Gonzalez-Bello, C. Mayorga, M. C. Cuquerella, I. Vayá and M. A. Miranda, *Front. Pharmacol.*, 2020, **11**, 576495.
20 https://ec.europa.eu/health/documents/community-register/2009/2009062459389/anx_59389_en.pdf.
21 T. Peters, in *All About Albumin - Biochemistry, Genetics, and Medical Applications*, ed. Elsevier, Academic Press, San Diego, 1995, ch. 3, pp. 76–132.
22 A. R. Svobodova, J. Ulrichova and J. Vostalova, *An. Bras. Dermatol.*, 2019, **94**, 105–106.
23 F. Palumbo, G. Garcia-Lainez, D. Limones-Herrero, M. D. Coloma, J. Escobar, M. C. Jimenez, M. A. Miranda and I. Andreu, *Toxicol. Appl. Pharmacol.*, 2016, **313**, 131–137.
24 G. Colombo, M. Clerici, M. E. Garavaglia, D. Giustarini, R. Rossi, A. Milzani and I. Dalle-Donne, *J. Chromatogr. B: Anal. Technol. Biomed. Life Sci.*, 2016, **1019**, 178–190.
25 B. J. Trummer, V. Iyer, S. V. Balu-Iyer, R. O'Connor and R. M. Straubinger, *J. Pharm. Sci.*, 2012, **101**, 2763–2776.
26 O. Domotor, K. Pelivan, A. Borics, B. K. Keppler, C. R. Kowol and E. A. Enyedy, *J. Pharm. Biomed. Anal.*, 2018, **154**, 321–331.

© 2021 The Author(s). Published by the Royal Society of Chemistry

27 M. Montalti, A. Credi, L. Prodi and M. T. Gandolfi, *Handbook of Photochemistry*, CRC Press, Taylor and Francis Group, Boca Raton, FL, 2006.
28 G. Cosa and J. C. Scaiano, *Photochem. Photobiol.*, 2004, **80**, 159–174.
29 C. Ruckebusch, M. Sliwa, P. Pernot, A. de Juan and R. Tauler, *J. Photochem. Photobiol., C*, 2012, **13**, 1–27.
30 I. Vayá, V. Lhiaubet-Vallet, M. C. Jimenez and M. A. Miranda, *Chem. Soc. Rev.*, 2014, **43**, 4102–4122.
31 L. J. Martínez and J. C. Scaiano, *Photochem. Photobiol.*, 1998, **68**, 646–651.
32 O. R. Alzueta, M. C. Cuquerella and M. A. Miranda, *Spectrochim. Acta, Part A*, 2019, **218**, 191–195.
33 M. J. Davies, *Photochem. Photobiol. Sci.*, 2004, **3**, 17–25.
34 M. S. Baptista, J. Cadet, P. Di Mascio, A. A. Ghogare, A. Greer, M. R. Hamblin, C. Lorente, S. C. Nunez, M. S. Ribeiro, A. H. Thomas, M. Vignoni and T. M. Yoshimura, *Photochem. Photobiol.*, 2017, **93**, 912–919.
35 C. S. Foote, *Photochem. Photobiol.*, 1991, **54**, 659.
36 D. de la Peña, C. Martí, S. Nonell, L. A. Martínez and M. A. Miranda, *Photochem. Photobiol.*, 1997, **65**, 828–832.
37 M. J. Davies and R. J. W. Truscott, in *Sun Protection in Man*, ed. P. U. Giacomoni, Elsevier, 2001, ch. 12, pp. 251–275.
38 D. I. Pattison, A. S. Rahmanto and M. J. Davies, *Photochem. Photobiol. Sci.*, 2012, **11**, 38–53.
39 J. Li, J. Brahmer, W. Messersmith, M. Hidalgo and S. D. Baker, *Invest. New Drugs*, 2006, **24**, 291–297.
40 G. Sudlow, D. J. Birkett and D. N. Wade, *Mol. Pharmacol.*, 1976, **12**, 1052–1061.
41 I. Vayá, M. C. Jimenez and M. A. Miranda, *J. Phys. Chem. B*, 2007, **111**, 9363–9371.
42 I. Vayá, P. Bonancia, M. C. Jimenez, D. Markovitsi, T. Gustavsson and M. A. Miranda, *Phys. Chem. Chem. Phys.*, 2013, **15**, 4727–4734.
43 A. Z. Weller, *Phys. Chem.*, 1982, **133**, 93–98.

© 2021 The Author(s). Published by the Royal Society of Chemistry

Contents lists available at ScienceDirect

Free Radical Biology and Medicine

journal homepage: www.elsevier.com/locate/freeradbiomed

Cellular damage photosensitized by dasatinib, radical-mediated mechanisms and photoprotection in reconstructed epidermis

Meryem El Ouardi [a,b], Lorena Tamarit [a,b], Ignacio Vayá [a,b], Miguel A. Miranda[a,b,**], Inmaculada Andreu [a,b,*]

[a]Departamento de Química-Instituto de Tecnología Química UPV-CSIC. Universitat Politècnica de València, Camino de Vera s/n, 46022, Valencia, Spain

bUnidad Mixta de Investigación UPV-Instituto de Investigación Sanitaria (IIS) La Fe, Hospital Universitari i Politècnic La Fe, Avenida de Fernando Abril Martorell 106, 46026, Valencia, Spain.

Abstract

Dasatinib (DAS) is an anticancer drug employed in the treatment of certain hematological malignancies, such as chronic myeloid leukemia and Philadelphia chromosome-positive acute lymphoblastic leukemia. Although DAS has been mainly developed for oral administration, it has recently garnered attention for its potential application in topical dermatological formulations. However, the use of topical drugs is far from innocuous, introducing a noteworthy consideration such as photosensitivity, which is not listed as an adverse reaction for DAS. Thus, considering that DAS has a UVA-absorbing chromophore, it could induce photosensitivity reactions such as phototoxicity. In these phenomena oxidative damage to cellular targets, such as lipids, proteins, and DNA, may occur through Type I (via free radical intermediates) or Type II (singlet oxygen-mediated) mechanisms. With this background, the aim of the present study is to investigate whether DAS exhibits phototoxic reactions on primary cellular targets, not only in solution, but also in artificial skin, to emulate the topical administration of the drug. In addition, the potential to generate highly reactive intermediates like organic radicals and reactive oxygen species (ROS) has also been investigated, since these intermediates could be responsible for triggering photosensitivity reactions. As a matter of fact, the first transient species detected upon DAS irradiation in the UVA region was the diradicaloid triplet excited state (^{3}DAS*), with an absorption maximum at ca. 490, which was subsequently quenched by oxygen, yielding singlet oxygen. The latter species is capable to induce Type II photooxidative reactions in biomolecules. Independent triplet quenching experiments using linoleic acid and 3-methylindole as models for lipids and proteins, respectively, revealed that radical-mediated (Type I) photosensitized damage to membrane components is also feasible.

Keywords:

Artificial skin, phototoxicity, singlet oxygen, tyrosine kinase inhibitor, triplet excited state, ultraviolet filter.

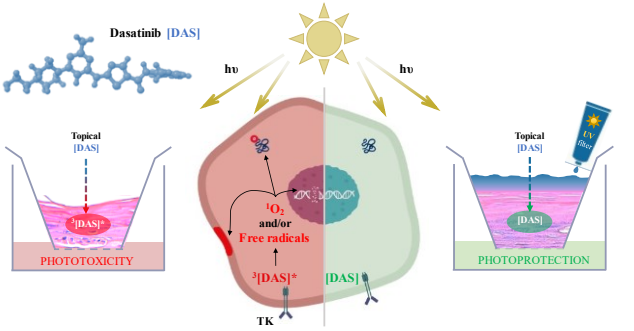

Accordingly, the neutral red uptake (NRU) phototoxicity test (photoirritation factor of 5) and the comet assay, revealed that this drug is phototoxic and photogenotoxic to keratinocyte cells (HaCaT). Further investigations were performed on lipid photoperoxidation in fibroblast cells (FSK), using a lipid-soluble fluorescent marker C11-Bodipy581/591, as well as on protein photooxidation, by means of carbonyl content measurements. The obtained results suggest that cellular membranes are likely

targets for DAS phototoxicity. Regarding its potential application in topical dermatological formulations, an O/W emulsion of DAS was prepared and tested in reconstructed human epidermis, using the cell viability MTT assay. As anticipated from the results obtained in NRU experiments, a significant phototoxicity was demonstrated. Fortunately, this undesired side effect disappeared upon formulation of DAS along with a sunscreen (tinosorb S). Thus, for topical treatments, the photosensitivity reactions induced by DAS can be prevented by using formulations including appropriate UVA filters.

Introduction

Dasatinib (DAS), a potent tyrosine kinase inhibitor, has become a significant player in targeted cancer therapy [1]. It is particularly efficacious in the treatment of certain hematological malignancies, such as chronic myeloid leukemia (CML) and Philadelphia chromosome-positive acute lymphoblastic leukemia (Ph+ ALL) [2–5]. Like any medication, it is associated with potential adverse events, and the commonly reported for DAS include headache, fatigue, nausea, diarrhea, fluid retention, muscle pain, and skin rash [6,7].

Although DAS has been mainly developed for oral administration, it has recently garnered attention for its potential application in topical dermatological formulations. The unique properties of DAS, including its ability to target specific signaling pathways implicated in various skin conditions, make it a compelling candidate for novel topical treatments [8–10]. This shift in focus from systemic to localized application opens pathways for exploring DAS therapeutic benefits in dermatology, presenting opportunities for developing innovative topical formulations for skin disorders. However, the use of topical drugs is far from innocuous, introducing a noteworthy consideration such as photosensitivity, which is not listed as a specific dermal response [11]. As shown in Fig. 1, DAS chromophore, highlighted in violet, exhibits absorption in the UVA region and is therefore capable to induce photosensitivity reactions such as phototoxicity. These reactions occur when a drug absorbs light and undergoes a chemical change, potentially leading to skin reactions or other adverse effects upon exposure to sunlight [12,13]. In phototoxicity, oxidative damage to cellular targets, such as lipids, proteins, and DNA, may occur through Type I or Type II mechanisms. The former involves radical pathways (generally initiated through electron transfer or hydrogen abstraction), and the latter entails energy transfer from a photosensitizer to molecular oxygen, leading to singlet oxygen. Thus, understanding this type of adverse reaction will help implement photoprotection strategies to minimize photosensitivity disorders phenomena and to reduce the risk of suffering skin cancer.

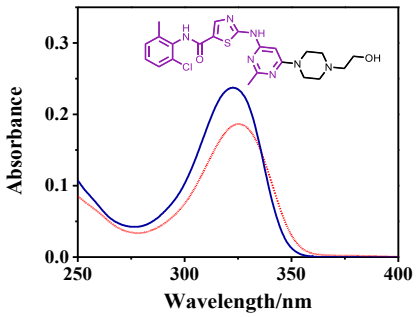

Fig. 1. Absorption spectra of DAS in PBS (**red**) and ethanol (**blue**) (4 µM). Inset: Chemical structure of DAS.

Considering all the above-mentioned, this study aims to investigate whether DAS exhibits phototoxic reactions on the primary cellular

targets, both in solution and artificial skin to emulate the topical administration of the drug. Moreover, following the absorption of sunlight by DAS, the potential exists to generate highly reactive intermediates like organic radicals and reactive oxygen species (ROS). Thus, we have also investigated these transient species that could potentially underlie the photosensitivity reactions. In addition, to prevent these side effects, drug formulations containing a sunscreen have been prepared and tested on a skin model in an attempt to mitigate the negative impact of the sun.

Material and methods

Chemicals and reagents

Dasatinib (DAS; CAS 302962-49-8) was provided by TargetMol (Boston, USA), and stock solutions were prepared in DMSO as vehicle. (*S*)-(+)-Ketoprofen (KP; CAS 22161-81-5), guanosine (Guo; CAS 118-00-3), 3-methylindole (CAS; 83-34-1), linoleic acid (LA; CAS 60-33-3), 1H-phenalen-1-one (PN; CAS 548-39-0), anthracene (ANT; CAS 120-112-7), (3-(4,5-dimethylthiazol-2-yl)-2,5-diphenyl-tetrazolium bromide (MTT) and trypan blue (CAS 72-57-1) were retrieved from Sigma-Aldrich (Madrid, Spain). Spectrophotometric HPLC solvents were commercially available and used without additional purification. Dulbecco's Modified Eagle Medium (DMEM, low glucose with pyruvate and glutamine), Dulbecco's Modified Eagle Medium (DMEM, low glucose with pyruvate and without glutamine and phenol red), penicillin-streptomycin ($1.0 \cdot 10^5$ U/mL, 1.0 10^5 µg/mL) and ethylenediaminetetraacetic acid (EDTA) were obtained from Honeywell Fluka (North Carolina, U.S.). Fetal bovine serum (FBS) and Trypsin–EDTA (0.25–0.02 %) were supplied by Cultek (Madrid, Spain). Fetal bovine serum (FBS) and Trypsin–EDTA (0.25–0.02 %) were provided by Cultek (Madrid, Spain). Reconstructed human epidermis (Epi-200-PHO kit) was acquired from MatTek (Bratislava, Slovakia), and cultures were shipped every Monday and received on the following Tuesday for immediate utilization. Decyl oleate, glycerol monostearate 40-55 and propyleneglycol were purchased from Guinama (Valencia, Spain). Ceteareth-12 was obtained from PCC Group (Brzeg Dolny, Poland). Bemotrizinol (tinosorb S) was retrieved from TCI (Zwijndrecht, Belgium).

Cell culture conditions

Keratinocyte cells (HaCaT) and human skin fibroblast cell line (FSK) were retrieved from CLS (Eppelheim, Germany) and cultured in a CO_2 incubator (100 % relative humidity, 5 % CO_2) at 37 ºC, using DMEM supplemented with 10 % FBS, 4 mM L-glutamine, and penicillin/streptomycin (100 U/mL and 100 µg/mL). The cells were grown in 75 cm^2 plastic flasks and split at 90 % confluence. To ensure cell viability, trypan blue exclusion assay was regularly performed.

Irradiation conditions

Irradiation was performed in a Luzchem multi-lamp LCZ-4 photoreactor fitted with six top and

eight side Hitachi lamps (λ_{max} = 350 nm, Gaussian distribution; Luzchem, Canada). The plates were placed on ice during the irradiation process to prevent overheating.

Spectroscopic techniques

Absorption measurements

The UV-1800 UV/Vis spectrophotometer (Shimadzu, Kyoto, Japan) was used to record the absorption spectra of DAS in both PBS and ethanol (EtOH). The measurements were performed using 1 cm Suprasil quartz cells (Hellma Analytics, Müllheim, Germany) with a capacity of 3.5 mL, at room temperature.

Fluorescence experiments

A spectrofluorometer FP-8500 (JASCO, Tokyo, Japan) was used to record the fluorescence spectra with an excitation wavelength of 325 nm, using both PBS and EtOH. As regards the quantification of the fluorescence quantum yield (Φ_F) in keratinocyte cells, the area under the emission curve (λ_{exc} = 320 nm) between DAS and anthracene (ANT) was compared. ANT was used as fluorescence standard with a quantum yield (Φ_F) of 0.27 in EtOH [14]. Isoabsorptive samples ($A_{320nm} \sim 0.2$) were used in the measurements.

Phosphorescence experiments

Phosphorescence emission spectrum was measured using Edinburg instruments spectrofluorometer FS5, which was outfitted with a 150 W CW Ozone-free xenon arc lamp and a SC-70 module with liquid nitrogen EPR Dewar. DAS was dissolved in EtOH, then placed in a 5 mm diameter quartz tube, and a solid matrix was formed by cooling it with liquid nitrogen (77 K).

Laser Flash Photolysis

Laser flash photolysis (LFP) experiments were conducted as described elsewhere by a pulsed Nd:YAG L52137 V LOTIS TII laser at an excitation wavelength of 355 nm (Sp Lotis Tii, Minsk, Belarus) [15–17]. The single pulses were approximately 10 ns in duration, with each pulse having an energy of less than 30 mJ. The detecting light source used was a pulsed Lo255 Oriel Xenon lamp. Additionally, the LFP setup included a pulsed Lo255 Oriel Xe lamp (Newport, Irvine, CA, USA), a 77,200 Oriel monochromator, a photomultiplier (Oriel, model 70705PMT) system, and a TDS-640A Tektronix oscilloscope (Betashire, UK). A customized Luzchem Research LFP-111 system was used to collect and transfer the output signal from the oscilloscope to a personal computer for data processing. All the measurements were taken in a 1 cm Suprasil quartz cells and deareated atmosphere was achieved by bubbling DAS solution for 15 min with nitrogen gas. The absorbance of the samples was adjusted to approximately 0.30 at 355 nm, and the rate constant for the quenching of the triplet excited state (kq) upon the addition of quencher was determined using the Stern-Volmer equation (eq.1).

$$\frac{1}{\tau} = \frac{1}{\tau_0} + \mathrm{kq}\,[\mathrm{quencher}] \qquad \mathrm{eq.1}$$

Where τ and τ_0 are the lifetime of transient species with and without quencher, respectively.

The detection of singlet oxygen ($^1O_2$, $^1\Delta g$) species was accomplished through near-infrared emission using the same LFP equipment previously described, with a single pulse energy of 15 mJ per pulse and laser excitation at 355 nm. The emission of the generated $^1O_2$ was measured at 1275 nm using a Hamamatsu NIR emission detector (Shizuoka, Japan), which was peltier cooled at -62.8 ºC and operated at 800 V, coupled with a grating monochromator. The absorbance of the samples was adjusted to approximately 0.55 at 355 nm and decay traces were recorded in a 1 cm Suprasil quartz cells and aerated atmosphere. The rate constant for the quenching of $^1O_2$ (kq_Δ) generated upon the excitation of 1H-phenalen-1-one (PN) after the addition of DAS was determined using the Stern-Volmer equation (eq.2).

$$\frac{1}{\tau_\Delta} = \frac{1}{\tau_{\Delta_0}} + kq_\Delta\,[DAS] \qquad eq.\,2$$

Where τ_Δ and τ_{Δ_0} are the lifetime of $^1O_2$ species with and without DAS, respectively.

To determine the quantum yield (Φ_Δ) of singlet oxygen, ketoprofen (KP) was used as a standard with a Φ_Δ value of approximately 0.39 in acetonitrile (MeCN) [18]. The Φ_Δ value of DAS was calculated using equation 3, which considers the Φ_Δ value of the standard, as well as the emission intensity of DAS and KP, and the refractive index of the solvent used for the measurement.

$$\Phi_\Delta^{DAS} = \Phi_\Delta^{KP} \times \frac{I_{DAS}}{I_{KP}} \times \frac{n_{MeCN}}{n_i} \qquad eq.\,3$$

Where Φ_Δ^{KP} is the quantum yield of the standard (KP), I_{DAS} and I_{KP} are the emission intensity of DAS and KP, n_{MeCN} and n_i the refractive index of standard solvent (MeCN) and the sample solvent, respectively.

In vitro neutral red uptake (NRU)

Phototoxicity assay was carried out in compliance with the OECD Guideline 432 [19] and using human keratinocyte cells (HaCaT cells) instead of 3T3 fibroblast cells as explained in detail in previous studies [15,20]. Chlorpromazine (CPZ) and sodium dodecyl sulfate (SDS) were chosen as positive and negative controls, respectively. Concisely, two 96-well plates were seeded with HaCaT cells at a density of 2 x 10^4 cells/well and serial dilutions of DAS were added to each plate, ranging from 500 to 2.5 µM. After incubation at 37 ºC in the dark for 1 h, one plate was irradiated with a non-cytotoxic UVA light dose of 5 J/cm^2, while the other plate was kept in the dark. The next day, a neutral red solution with a concentration of 50 µg/mL was added to each well and incubated for 2 h at 37 ºC. Neutral red was extracted from lysosomes and the absorbance was measured at 550 nm. Dose-response curves were established for each compound to determine the concentration producing a 50 % decrease in the neutral red uptake (IC50) under both dark and

UVA light conditions, using non-linear regression methods with GraphPad 5.0 software. Finally, the photoirritant factor (PIF) values were calculated using equation 4.

$$PIF = \frac{IC50\ DARK}{IC50\ UVA\ LIGHT} \quad \text{eq. 4}$$

Lipid photoperoxidation

C11-Bodipy$^{581/591}$, is a fatty acid analogue which serves as a fluorescent reporter molecule used to evaluate lipid peroxidation in living cells [15,21]. This sensor undergoes a fluorescence shift from red to green when it is oxidized [22,23]. Thus, in this study, human skin fibroblast cells (FSK) were seeded in two 12-well plates with a density of 6.0×10^4 cells/well. The following day, the cells were treated with 20 or 50 μM of DAS solutions and incubated in the dark for 30 min. One plate was then exposed to irradiation (5 J/cm^2) while the other plate was kept in the dark as a negative control. After incubation, the cells were labeled with C11-Bodipy$^{581/591}$ (10 μM) for 30 min at 37 ºC. The cultures were then examined by fluorescence microscope to detect both non-oxidized (red fluorescence, λ_{exc} 535 nm) and oxidized (green fluorescence, λ_{exc} 490 nm) forms of the probe. To determine the extent of lipid peroxidation in each condition, the fluorescence intensity ratio (FIR) was calculated using equation 5.

$$FIR = \frac{I\ red\ fluorescence}{I\ green\ fluorescence} \quad \text{eq. 5}$$

Protein photooxidation

The extent of protein oxidation induced by DAS through photoirradiation was assessed using human serum albumin (HSA) as a model, and by a method similar to as previously described [15,24]. Briefly, 5 mg/mL solutions of HSA in PBS were treated with different concentrations of DAS (20 and 50 μM) at room temperature for 1 h. Following the incubation, the samples were either exposed to a UVA dose ranging from 5 to 15 J/cm^2 or kept in the dark as a control. After irradiation, the degree of HSA oxidation was measured using spectrophotometry through derivatization with 2,4-dinitrophenylhydrazine (DNPH). The extent of HSA oxidation was determined by measuring the absorbance at 375 nm and the results were expressed as nmol of carbonyl moiety per mg protein.

DNA photodamage

Single cell gel electrophoresis technique, also called comet assay, was conducted in accordance with the method described previously [15,25]. The purpose of this study was to identify any strand breaks or alkaline labile sites present in the nuclear DNA after the exposure to a UVA light source. HaCaT cells, suspended in cold PBS, were seeded in two 24-well plates with 5.0×10^4 cells/well and treated with 50 μM DAS solution for 30 min at 4 ºC. CPZ was used as the reference compound for photogenotoxicity at a concentration of 5 μM. After the incubation period, one plate was placed in the photoreactor to irradiate the cells (5 J/cm^2), while the other was kept in the dark as a negative control. After

irradiation, drops containing 1.0×10^5 cells/agarose gel were placed onto treated slides on a tray cooled with ice to permit solidification. Slides were then immersed in a lysis buffer and incubated overnight at 4 ºC. In the DNA recovery experiments slides were maintained in DMEM medium at 37ºC for 18 h and then lysing as above. Then, electrophoresis was carried out in a cold alkaline buffer at 21 V for 30 min to allow for DNA unwinding. Finally, after fixation and staining with SYBR Gold, comet nucleoids and tails were visualized using a fluorescence microscope. The percentage of DNA damage was calculated using a formula based on visual scoring of at least 100 DNA comets: [(Nclass 0 comets × 0) + (Nclass 1 comets × 1) + (Nclass 2 comets × 2) + (Nclass 3 comets × 3) + [(Nclass 4 comets × 4) + (Nclass 5 comets × 5) + (Nclass 6 comets × 6)]/6, where class 0 comets indicate comets with no DNA damage and class 6 comets indicate comets with maximum DNA damage.

Pharmaceutical formulations

DAS 0.45 % cream was chosen as the test material by formulating an oil-in-water (O/W) emulsion. DAS emulsion was prepared according to the Spanish Pharmacopeia and the National Formulary [26] consisting of a non-ionic O/W emulsion in which the drug was incorporated in the inner oil phase because of its lipophilic nature. Parallelly, a formulation of DAS combined with bemotrizinol (tinosorb S), as a broad-spectrum UV filter, was also prepared. Similarly, tinosorb S was added in the oil phase of the O/W emulsion at a concentration of 3 %. Both formulations were applied topically on the top of the tissue inserts and covering the surface completely. Due to the opacity of the cream samples, residues remaining on top of the emulsion were removed minutes before irradiation to avoid the blockage of the UVA light.

Reconstructed human epidermis (RhE) phototoxicity test

The EpiDerm System is composed of human-derived epidermal keratinocytes which have been cultured to create a complex, multi-layered, and highly differentiated model of the human epidermis. The model consists of well-organized basal, spinous, and granular layers, as well as a multi-layered stratum corneum that contains intercellular lamellar lipid layers arranged in patterns in a cell culture insert (Milicells, 10 mm) similar to those found in living tissues. Upon receipt, the RHE tissue samples were incubated for 1 h (100 % relative humidity, 5 % CO_2) at 37 ºC in 6-well plates containing assay medium. After the equilibration period, the medium was exchanged with fresh medium, and plates were incubated overnight according to the instructions provided by the supplier. The next day, test materials were applied to the surface of the epidermis. Chlorpromazine (CPZ) and the vehicle (EtOH) served as the positive and negative control for phototoxicity, respectively. Subsequently, CPZ, as a water-soluble substance, was incorporated in a volume of 50 µL, whereas DAS in both EtOH (10 mM) and O/W emulsion (0.45 %) was added in a volume of 25 µL.

Tissues were incubated for another 24 h (100 % relative humidity, 5 % CO_2) at 37 ºC to allow the compounds to penetrate through the epidermis layers. Then, one set of tissues was exposed to 7 J/cm^2 UVA and the other set was kept in the dark for the same period. Culture inserts were then rinsed with DPBS buffered solution until the compounds were completely removed. Afterwards, tissues were transferred to new 6-well plates with fresh medium and incubated overnight. Next day, assay medium was replaced by MTT solution (1 mg/mL), and inserts were incubated for 3 h in the same conditions. After the incubation is complete, the formazan was extracted with isopropanol for at least 2 h at room temperature, then small aliquots of the final solution were transferred to a 96-well plate. The optical density of the blue formazan was determined at 540/570 nm using isopropanol as a blank. The cell viability for each tissue was determined as the percentage of the corresponding vehicle control (EtOH). Mean values were obtained and then the results of irradiated or non-irradiated samples were compared. Thus, according to the OECD guidelines [27], a substance is predicted to be phototoxic when the tissues treated with one or more test concentrations and subsequently exposed to irradiation, show a decrease in relative viability of ≥ 30 % compared to the relative viability values of the same concentrations without irradiation.

Histological analysis

For histological observation, RhE tissues were fixed overnight in 10 % formalin at room temperature, dehydrated in an EtOH gradient prior to vitrification by xylene. Then, tissue membranes were embedded in paraffin wax and sections 5 µm thick were cut using a Leica rotary microtome (RM2235, Germany). Slices were, then, stained with hematoxylin and eosin (H&E), mounted in covered slides, and examined under light microscopy (Leica DMD108 optical microscope).

Data analysis and statistics

Results are expressed as mean ± standard deviation (SD) and are based on at least three independent experiments. GraphPad 5.0 software was used for the regression methods, while Image-J software was used to quantify the fluorescence intensity. Statistical significance was determined using the Student's t-test, and p values less than 0.05 were considered statistically significant (*$p<0.05$; **$p<0.01$; ***$p<0.001$).

Results and discussion

Photophysical studies

The ability of a drug to induce photosensitization damage to biomolecules can be linked to the formation of reactive oxygen species (ROS) or radicals arising from excited states of the molecule [28,29]. Accordingly, to predict the phototoxicity of dasatinib, preliminary investigations on its photobehavior were conducted using several photophysical techniques such as fluorescence, transient

absorption, and near-infrared luminescence spectroscopy.

Emission spectra

The fluorescence spectra of DAS, in PBS and within cells, displayed a maximum centered at 374 nm (Fig. 2). Similar findings were observed when employing EtOH as solvent, emulating the lipophilic environment present in the cellular milieu (Fig. S1A). Additionally, the fluorescence quantum yield (Φ_F) of DAS in keratinocyte cells (HaCaT) was determined using ANT in EtOH as a reference (Φ_F = 0.27) [14] and it was found to be around 0.001 (Fig. S1B). Furthermore, the energy of the singlet excited state (Es) was calculated from the intersection point between the normalized excitation and emission spectra (Fig. S2), yielding a value of *ca.* 343 kJ/mol for both PBS and EtOH solution.

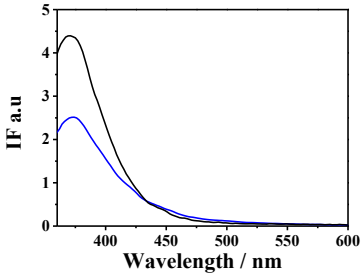

Fig. 2. Fluorescence emission spectra of DAS. Emission spectra of DAS recorded at an excitation wavelength of 350 nm in PBS (**black**) or within HaCaT cells (**blue**).

Laser flash photolysis

Laser flash photolysis (LFP) technique was employed to investigate, in the microsecond timescale, the transient species generated upon excitation of DAS. Thus, the excitation of DAS, in deareated EtOH solution, with a nanosecond laser pulse at 355 nm resulted in a transient absorption with a maximum exhibited at 490 nm (Fig. 3A and Table S1). Furthermore, this transient species displayed a lifetime *ca.* 2 µs in deareated atmosphere. Similar results were found in aprotic solvents such as MeCN, dichloromethane (DCM) and 1,4-dioxane (DX) (Fig. S3 and Table S1). Moreover, as presented in Fig. 3B and Table S1, the detected species displayed effective quenching by molecular oxygen with a rate constant (kq) of 6.9×10^{10} M^{-1} s^{-1}, determined by a mono-exponential decay function (Fig. S4). Hence, the results strongly suggest that the transient species corresponds to a triplet excited state of DAS ($^3DAS^*$).

A

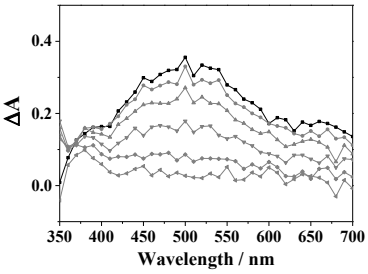

B

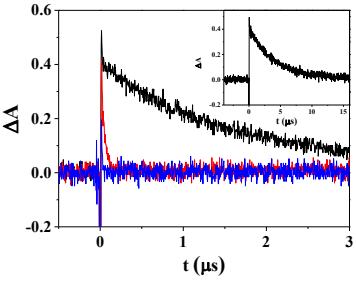

C

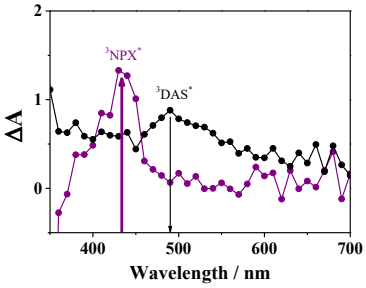

D

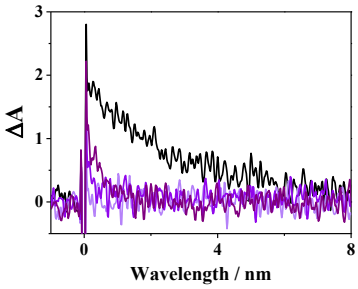

Fig. 3. Transient absorption experiments (λ_{exc} = 355 nm, EtOH). (A) Normalized transient absorption spectra (from 1 to 16 µs) for DAS in deareated conditions. (B) Decay kinetics of ^{3}DAS* monitored at 490 nm in deareated (**black**), aerated (**red**) and oxygen saturated atmosphere (**blue**). Inset: Decay trace of DAS in deareated solution on a longer timescale. (C) Transient absorption spectra of DAS (**black**) and for a mixture containing DAS and NPX 10 mM (**violet**). (D) Decay traces at 490 nm for DAS (**black**) and for a mixture containing DAS and increasing amounts of NPX (1-10 mM) (**violet**).

Moreover, to better characterize the triplet nature of DAS excited species, photosensitization LFP measurements were conducted using naproxen (NPX) as an acceptor. The energy level of ^{3}NPX* is 259.4 kJ/mol [30], whereas that of ^{3}DAS*, determined through a 15 % increase in its phosphorescence emission recorded in an EtOH solid matrix at 77 K (Fig. S5), was approximately 274.5 kJ/mol. Thus, selective excitation of DAS at 355 nm in the presence of NPX resulted in significant quenching of the signal at 490 nm (kq = 1.02×10^{10} M^{-1} s^{-1}) (Fig. 3C, Fig. 3D and Fig. S6), accompanied by the generation of ^{3}NPX* (λ_{max} ~430 nm) through a triplet–triplet energy transfer process from DAS to NPX (Fig. 3C). Hence, the transient band with a maximum at ~490 nm can unambiguously be assigned to the triplet excited state of the drug.

It is well known that the interaction between triplet excited species and molecular oxygen mainly leads to the generation of singlet oxygen ($^1O_2$ or $^1\Delta g$), typically known as Type II oxidative reaction [31]. Moreover, $^1O_2$ species can induce significant oxidative damage to cellular targets. This includes the formation of lipid hydroperoxides through lipid peroxidation [22,23], oxidation of proteins [32], and DNA nucleosides oxidation [33]. Thus, to investigate Type II photodamage to biomolecules, time-resolved near-infrared spectra of DAS aerated solution were recorded upon excitation at 355 nm. Consequently, a luminescence signal indicative of $^1O_2$ was detected at 1270 nm, which displayed a quantum yield (Φ_Δ) *ca.* 0.1 in EtOH solution. Similar Φ_Δ was obtained for MeCN, while in DCM and DX, the values were enhanced (Φ_Δ *ca.* 0.2) (Fig. 4A and Table S1). All Φ_Δ were calculated considering ketoprofen (KP) in MeCN as the standard (Φ_Δ = 0.39) [18]. Surprisingly, the $^1O_2$ lifetimes (τ_Δ) for DAS (Fig. 4A and Table S1) were lower than those expected for organic solvents [34–36]. This can be associated with the reaction $^1O_2$ with tertiary aliphatic amines that

are typical $^1O_2$ quenching agents. In this case, DAS contains a piperazine moiety in its structure, which exhibits a $^1O_2$ quenching rate of around 1.0 × 10^6 M^{-1} s^{-1} [37]. To confirm this observation, the quenching of the luminescence emitted by 1H-phenalen-1-one, also known as perinaphthenone (PN), upon the addition of DAS was conducted. It is considered as one of the most effective $^1O_2$ sensitizers in both polar and non-polar environments, exhibiting a Φ_Δ close to unity [38]. Therefore, $^1O_2$ NIR-luminescence signal for PN at 1270 nm was recorded upon increasing amounts of DAS. As illustrated in Fig. 4B, $^1O_2$ generated from PN was quenched by DAS (0.2-4 mM), displaying a rate constant (kq_Δ) of approximately 1.20 × 10^7 M^{-1} s^{-1} in aerated DCM. Similar result was shown in MeCN solution (kq_Δ *ca.* 9.2 × 10^6 M^{-1} s^{-1}) (Fig. S7 and Fig. S8). Thus, it was evidenced that DAS exerts a $^1O_2$ quenching effect, likely attributed to the interaction between piperazine and $^1O_2$, which might constitute the primary mechanism underlying the observed low τ_Δ values.

Overall, DAS demonstrated its ability to photogenerate $^1O_2$ species, which can subsequently initiate Type II photooxidative reactions towards biomolecules. Additionally, the potential involvement of Type I oxidative mechanism was also investigated using linoleic acid (LA), 3-methylindole (in lieu of tryptophan), and guanosine (Guo) as models for lipids, proteins, and DNA, respectively. Hence, transient absorption decays for DAS were registered at 490 nm in deareated EtOH solution with increasing concentrations of quencher.

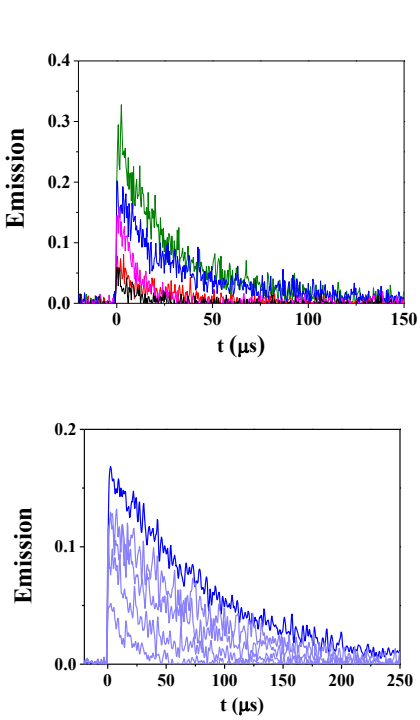

Fig. 5. Singlet oxygen emission measurements (λ_{exc} = 355 nm). (A) Kinetic traces for DAS in aerated EtOH (**black**), MeCN (**red**), dichloromethane (**blue**) and dioxane (**magenta**) solutions. Ketoprofen (KP) in MeCN (**green**) was used as reference (Φ_Δ *ca.* 0.39) [18]. (B) Kinetic traces of singlet oxygen emission quenching for PN in the presence of DAS (0.2-4 mM) in aerated DCM.

As illustrated in Fig. 5, a significant quenching of the triplet excited species by LA and 3-methylindole becomes evident, displaying a kq around 1.7 × 10^8 M^{-1} s^{-1} and 4.3 × 10^7 M^{-1} s^{-1}, respectively. This suggests the potential implication of radical formation photoinduced by DAS in the photodamage to lipids and proteins (Type I mechanism). Conversely, Guo did not exhibit the ability to quench $^3DAS^*$ species (Fig. S9), and therefore, Type I mechanism

involvement in the photooxidation of guanine bases was not evidenced.

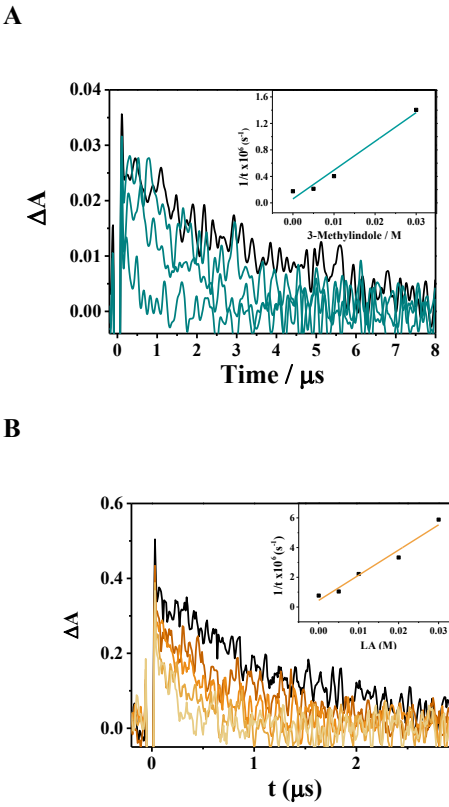

Fig. 5. Decays at 490 nm for DAS in deareated EtOH in the presence of increasing concentrations of A) 3-methylindole or B) linoleic acid, LA (5-30 mM). Insert: Stern-Volmer plots.

Phototoxicity assessment

In the initial stage, phototoxicity of DAS in HaCaT cells was evaluated using the *in vitro* neutral red uptake (NRU) phototoxicity test according to the OECD Guideline 432 [19]. For this aim, cell viability was analyzed with DAS treated cells before and after UVA irradiation. From the dose-response curves obtained, the IC50 values were estimated for both dark and UVA light conditions (Fig. 6). Finally, the photoirritant factor (PIF) was calculated, which corresponds to the ratio of the IC50 values obtained under both light and dark conditions ($IC50_{Dark}$ = 55 ± 8 μM, $IC50_{UVA\ light}$ = 12 ± 3 μM), and it was approximately 5, therefore, DAS can be considered a phototoxic compound.

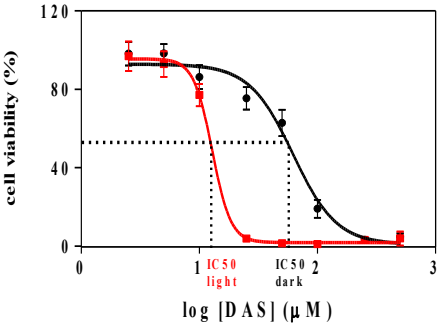

Fig. 6. Dose-response curves obtained by NRU phototoxicity assay using HaCaT cells, after treatment with DAS in Dark (●) and UVA light conditions (5 J/cm^2, ■). Data are the mean ± SD from four independent experiments.

Photoamage to biomolecules

Given the significant lipophilic properties and the high affinity to plasma proteins exhibited by DAS, its phototoxicity may potentially target membrane components such as proteins and lipids. To confirm this hypothesis, both lipid and protein photooxidation were investigated. In this context, the detection of lipid peroxidation was carried out using a lipid-soluble fluorescent marker C11-Bodipy$^{581/591}$, which is designed to penetrate the plasmatic membrane and exhibits a notable distinction in the spectral range between the non-oxidized (595 nm) and oxidized forms (520 nm) [15,22,23]. Thus, upon oxidation, the reporter shifts the fluorescence emission from red (λ_{exc} 535 nm), corresponding to the native structure of the probe, to green (λ_{exc} 490 nm),

which is attributed to the oxidized products. For this purpose, human skin fibroblast cells (FSK) were exposed to DAS (50 µM), followed by irradiation (dose: 5 J/cm^2), or were maintained in darkness as a control. Then, images of cells labelled with C11-Bodipy$^{581/591}$ were obtained using a fluorescence microscope and the rate of lipid peroxidation was expressed as the ratio between red and green fluorescence intensity. The images displayed in Fig. 7A and Fig. S10 A show a significant increase in the green fluorescence intensity after the exposure of fibroblasts to UVA light, specially at a concentration of 50 µM. Likewise, results from the quantitative analysis indicate a substantial decrease in the ratio of red to green fluorescence intensity in treated FSK cells (Fig. S10 B). These findings suggest that the lipid membrane could be a feasible target for DAS phototoxicity.

In addition, photoinduced protein oxidation was assessed by carbonyl content quantification using the 2,4-dinitrophenylhydrazine (DNPH) derivatization method as described elsewhere [15,24]. Human serum albumin (HSA) was selected as a protein model. Thus, HSA incubated in the presence of DAS (20 or 50 µM) was exposed to 15 J/cm^2 UVA radiation and labelled with DNPH which reacts with the carbonyl groups from the inner core of the protein to form HSA-bound hydrazones measurable by UV/Vis spectrophotometer. As revealed by this method, DAS triggered a dose-dependent carbonylation in HSA protein, reaching *ca.* 3-fold increase at 50 µM (Fig. 7B). As for non-treated HSA control, carbonyl content remained unchanged after irradiation, thereby the selected UVA dose was suitable for this experiment.

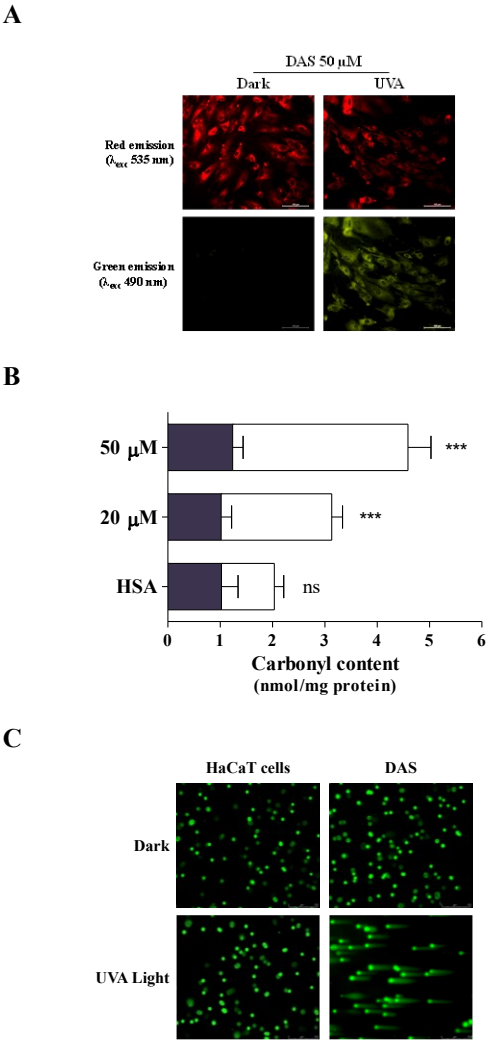

Fig. 7. Evaluation of the photo(geno)toxicity profile of DAS. (A) Photosensitized lipid peroxidation. Human fibroblast cells (FSK) were treated with DAS 50 µM, and either kept under darkness conditions or UVA irradiation at a dose of 5 J/cm^2. Subsequently, cells were stained with 10 µM C11-Bodipy$^{581/591}$, and the degree of lipid peroxidation was determined based on the intensity of the oxidized Bodipy fluorescence (green). Scale bar: 100 µm. Images are representative of three independent experiments. (B) Photooxidation of HSA protein. Samples were treated either with 20 or 50 µM DAS in the presence (10 J/cm^2, □) or absence of UVA light (■), and carbonyl content was monitored

by 2,4-dinitrophenylhydrazine derivatization method (λ = 375 nm). Data represent the mean ± SD of three independent experiments. Asterisks show significant differences between irradiated and non-irradiated samples by the Student's t-test (***$p < 0.001$, ns: non-significant). (C) Alkaline comet assay experiment. Keratinocyte cells (HaCaT) were kept in dark conditions or exposed to UVA light at a dose of 5 J/cm^2, either alone or after treatment with DAS (50 µM). Scale bar: 250 µm. Images are representative of three independent experiments.

The alkaline comet assay is a commonly used method for measuring various forms of DNA damage, including single-strand breaks (SSB), double-strand breaks (DSB), and alkali labile sites (ALS), although particularly prevalent in detecting SSB [39]. In this experiment, keratinocyte cells were subjected to a 1 h incubation with DAS followed by the exposure to UVA radiation. Agarose embedded cells were lysed, and electrophoresis was performed in order to facilitate the migration of damaged DNA fragments out of the cell nucleus, thereby resulting in the formation of comet nucleoids and tails. After staining with SYBR Gold, the comets were observed under a fluorescence microscope, and a visual scoring system comprising six different categories was used to calculate the extent of nuclear DNA damage [40]. Chlorpromazine (CPZ) was selected as the positive control based on its well described photogenotoxic profile [41]. As reflected in Fig. 7C and Fig. S11, the level of DNA damage photoinduced by DAS was significant (around 55 %) and as revealed by recovery experiments, the extent of damaging DNA remained persistent after a time period of 18 h. It is well established that deficient DNA repair can lead to genomic instability, apoptosis, or senescence and ultimately, carcinogenesis.

All in all, the phototoxicity of DAS in skin cell culture was successfully proven by the *in vitro* NRU assay and the approach on the biomolecular damage mechanisms revealed that DAS could trigger oxidative reactions targeting lipids, proteins, and genomic DNA.

Phototoxicity evaluation of dasatinib formulations in reconstructed human epidermis (RhE)

Evaluating percutaneous permeation and ensuring safety are pivotal aspects when assessing dermal or transdermal delivery systems to successfully develop new drug formulations intended for human use. Accordingly, the neutral red uptake assay in keratinocytes provided a clear determination of DAS phototoxic potential, however, this current approach relies on a monolayer cell culture and might not be suitable for topically applied chemicals. Given the evolving regulations on animal testing, artificial skin models are increasingly recognized as viable alternatives for evaluating drug formulations [42–44]. Thus, a 3D human skin model, which better reflect the penetration and barrier function of the stratum corneum, is more appropriate for testing the phototoxicity of drugs with topical application.

In this study, DAS was tested in both EtOH solution (10 mM) and O/W emulsion (0.45 %) using MTT assay on reconstructed epidermis [45]. The UVA light dose was 7 J/cm^2 and the positive control was CPZ as previously used for

the initial NRU experiments. The Fig. 8A depicts the effect of different formulations of DAS on EpiDerm tissues. Thus, compared to non-photoexposed tissues, DAS applied topically as a solution (10 mM in EtOH) caused a reduction in the tissue viability of 41%. This result is in good agreement with the aforementioned phototoxic potential revealed by the *in vitro* NRU experiments. Moreover, DAS formulated in a O/W emulsion at similar concentration (0.45 %) displayed a comparable reduction in the tissue viability (~ 45 %) upon UVA radiation. Additionally, as expected, DAS emulsion combined with tinosorb S 3 %, a photostable UV broad-spectrum filter (Fig. S12), showed lower reduction in the tissue viability (20 %) compared to the original emulsion, thus, demonstrating the protection effect of tinosorb S against UVA radiation.

In order to get insight into the phototoxicity effect of DAS, the characterization of the histological sections of the reconstructed epidermis by hematoxylin and eosin staining was performed. As displayed in Fig. 8B, no significant alterations in the morphology were observed for the untreated skin tissues. Similarly, non-irradiated samples treated with DAS emulsion 0.45 % showed no major modification of the epidermis histology. Conversely, some disorders in the basal layers became visible after the exposure of the tissue to a UVA dose of 7 J/cm^2. Specifically, disorganization of the epidermal layer, vacuoles/spongiosis and parakeratosis (retention of nuclei in the stratum corneum).

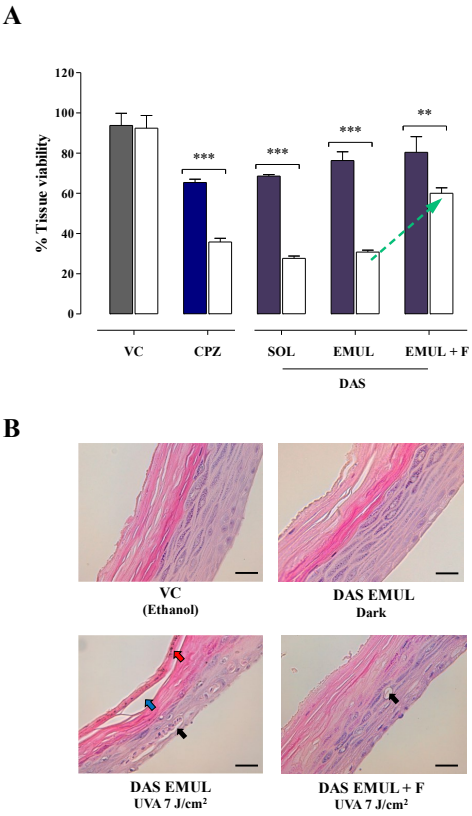

Fig. 8. Phototoxicity of DAS in the reconstructed human skin model. (A) Tissue viability after treatment with different formulations of DAS; SOL (10 mM of DAS in EtOH), EMUL (DAS 0.45 % O/W emulsion), or EMUL + F (DAS 0.45 % O/W emulsion combined with 3 % UV filter, tinosorb S). Tissues where either kept in dark conditions (filled bar) or exposed to UVA dose of 7 J/cm^2 (empty bar). Chlorpromazine 300 µM was used as the positive control. (B) Histological examination of the reconstructed skin model by hematoxylin and eosin (H&E) staining. Tissues were treated with vehicle (EtOH) or DAS 0.45 % O/W emulsion alone (EMUL) or combined with UVA filter (tinosorb S) 3 % (EMUL + F) in the presence or absence of UVA radiation 7 J/cm^2, and paraffin embedded sections were processed for hematoxylin and eosin staining. Represented alterations: spongiosis (**black** arrow), parakeratosis (**red** arrow) and disorganization in the epidermal layers (**blue** arrow). Scale bar: 50 µm. Images are representative of three independent experiments.

Altogether, these alterations indicate morphological disfunction which compromises the skin barrier integrity and resistance. Finally, as expected, the incorporation of a UV filter was associated with a protective effect against the photosensitization reaction upon DAS treatment.

Conclusions

Dasatinib (DAS) exhibits a significant absorption band in the active region of sunlight, and therefore, it has the potential to induce photosensitivity reactions. As a matter of fact, *in vitro* NRU and comet cellular assays have revealed that DAS is both phototoxic and photogenotoxic to HaCaT cells. Moreover, studies focused on lipid photoperoxidation in FSK cells, using a lipid-soluble fluorescent marker C11-Bodipy581/591, as well as on protein photooxidation, by means of carbonyl content measurements, strongly support that cellular membranes are potential targets for DAS-induced phototoxicity.

The main transient species generated upon DAS irradiation in the UVA region is the diradicaloid triplet excited state (^{3}DAS*). This species presents an absorption maximum at 490 and is efficiently quenched by oxygen, generating singlet oxygen. The latter is a proven Type II photooxidative reagent towards biomolecules. Likewise, triplet quenching experiments using linoleic acid and 3-methylindole as models of lipids and proteins, respectively, have revealed that radical-mediated (Type I) photosensitized membrane damage may also be operating.

Finally, in connection with the introduction of DAS for topical application, topical O/W emulsions of the drug have been prepared and tested in reconstructed human epidermis. Although a significant drug phototoxicity has been demonstrated in the cell viability MTT assay, this side effect has been markedly mitigated by including a broad-spectrum UV filter (tinosorb S) in the formulation. Thus, the present work has proven that triggering of DAS-mediated photosensitivity reactions may be prevented by including UVA filters in topical formulations, thus providing a photoprotection strategy that should be considered in topical treatments.

Acknowledgments

Financial support from the Spanish Ministry of Science and Innovation [PID2020-115010RB-I00/AEI/10.13039/501100011033, and FPU predoctoral fellowship for M. El O.] and from Generalitat Valenciana [CIAICO/2021/061]

References

1.Olivieri A, Manzione L. Dasatinib: a new step in molecular target therapy. Ann Oncol. 2007 Jun;18:vi42–6.

2.Kang B, Kim Y, Park TJ, Kang HY. Dasatinib, a second-generation tyrosine kinase inhibitor, induces melanogenesis via ERK-CREB-MITF-tyrosinase signaling in normal human melanocytes. Biochem Biophys Res Commun. 2020 Mar;523(4):1034–9.

3.Maiti A, Cortes JE, Patel KP, Masarova L, Borthakur G, Ravandi F, et al. Long-term results of frontline dasatinib in chronic myeloid leukemia. Cancer. 2020 Apr;126(7):1502–11.

4.Scholar E. Dasatinib. In: xPharm: The Comprehensive Pharmacology Reference [Internet]. Elsevier; 2009 [cited 2023 Nov 14]. p. 1–5.Available from:https://linkinghub.elsevier.com/retrieve/pii/B9780080552323640917

5.Tsimberidou AM. Dasatinib in chronic myeloid leukemia: a review. Ther Clin Risk Manag. 2009 Mar;281.

6.Lindauer M, Hochhaus A. Dasatinib. In: Martens UM, editor. Small Molecules in Hematology [Internet]. Cham: Springer International Publishing; 2018 [cited 2024 Jan 26]. p. 29–68. (Recent Results in Cancer Research; vol. 212). Available from: http://link.springer.com/10.1007/978-3-319-91439-8_2

7.Suh KJ, Lee JY, Shin DY, Koh Y, Bang SM, Yoon SS, et al. Analysis of adverse events associated with dasatinib and nilotinib treatments in chronic-phase chronic myeloid leukemia patients outside clinical trials. Int J Hematol. 2017 Aug;106(2):229–39.

8.Donthi MR, Saha RN, Singhvi G, Dubey SK. Dasatinib-Loaded Topical Nano-Emulgel for Rheumatoid Arthritis: Formulation Design and Optimization by QbD, In Vitro, Ex Vivo, and In Vivo Evaluation. Pharmaceutics. 2023 Feb 22;15(3):736.

9.Jung SH, Sun X, Ryu WS, Yang BS. Topical administration of the pan-Src kinase inhibitors, dasatinib and LCB 03-0110, prevents allergic contact dermatitis in mice: Suppression of ACD by dasatinib and LCB 03-0110. Br J Dermatol. 2013 Jan;168(1):112–9.

10.Yang X, Daifallah AEM, Shankar S, Beer J, Marshall C, Dentchev T, et al. Topical kinase inhibitors induce regression of cutaneous squamous cell carcinoma. Exp Dermatol. 2019 May;28(5):609–13.

11.Monteiro AF, Rato M, Martins C. Drug-induced photosensitivity: Photoallergic and phototoxic reactions. Clin Dermatol. 2016 Sep;34(5):571–81.

12.Kowalska J, Rok J, Rzepka Z, Wrześniok D. Drug-Induced Photosensitivity—From Light and Chemistry to Biological Reactions and Clinical Symptoms. Pharmaceuticals. 2021 Jul 26;14(8):723.

13.Tarantini F, Anelli L, Ingravallo G, Attolico I, Zagaria A, Russo Rossi A, et al. Skin lesions in chronic myeloid leukemia patients during dasatinib treatment. Cancer Manag Res. 2019 Aug;Volume 11:7991–6.

14.Melhuish WH. Quantum efficiencies of fluorescence of organic substances: effect of solvent and concentration of the fluorescent solute. J Phys Chem. 1961;65(2):229-235. doi:10.1021/j100820a009

15.Garcia-Lainez G, El Ouardi M, Moreno A, Lence E, González-Bello C, Miranda MA, et al. Singlet oxygen and radical-mediated mechanisms in the oxidative cellular damage photosensitized by the protease inhibitor simeprevir. Free Radic Biol Med. 2023 Jan;194:42–51.

16.Tamarit L, El Ouardi M, Lence E, Andreu I, González-Bello C, Vayá I, et al. Switching from ultrafast electron transfer to proton transfer in excited drug–protein complexes upon biotransformation. Chem Sci. 2022;13(33):9644–54.

17.Tamarit L, El Ouardi M, Andreu I, Vayá I, Miranda MA. Photoprocesses of the tyrosine kinase inhibitor gefitinib: from femtoseconds to microseconds and from solution to cells. Chem Sci. 2021;12(36):12027–35.

18.De La Peña D, Martí C, Noneil S, Martínez LA, Miranda MA. Time-Resolved Near Infrared Studies on Singlet Oxygen Production by the Photosensitizing 2-Arylpropionic Acids*. Photochem Photobiol. 1997 May;65(5):828–32.

19.OECD. Test No. 432: In Vitro 3T3 NRU Phototoxicity Test [Internet]. OECD; 2019 [cited 2023 Oct 31]. (OECD Guidelines for the Testing of Chemicals, Section 4). Available from: https://www.oecd-ilibrary.org/environment/test-no-432-in-vitro-3t3-nru-phototoxicity-test_9789264071162-en

20.Svobodová AR, Ulrichová J, Vostálová J. Human keratinocyte cell line as a suitable

alternative model for in vitro phototoxicity testing. An Bras Dermatol. 2019 Feb;94(1):105–6.

21.Drummen GPC, Van Liebergen LCM, Op Den Kamp JAF, Post JA. C11-BODIPY581/591, an oxidation-sensitive fluorescent lipid peroxidation probe: (micro)spectroscopic characterization and validation of methodology. Free Radic Biol Med. 2002 Aug;33(4):473–90.

22.Pap EHW, Drummen GPC, Winter VJ, Kooij TWA, Rijken P, Wirtz KWA, et al. Ratio-fluorescence microscopy of lipid oxidation in living cells using C11-BODIPY 581/591. FEBS Lett. 1999 Jun 25;453(3):278–82.

23.Bacellar IOL, Baptista MS. Mechanisms of Photosensitized Lipid Oxidation and Membrane Permeabilization. ACS Omega. 2019 Dec 24;4(26):21636–46.

24.Colombo G, Clerici M, Garavaglia ME, Giustarini D, Rossi R, Milzani A, et al. A step-by-step protocol for assaying protein carbonylation in biological samples. J Chromatogr B. 2016 Apr;1019:178–90.

25.García-Lainez G, Vayá I, Marín MP, Miranda MA, Andreu I. In vitro assessment of the photo(geno)toxicity associated with Lapatinib, a Tyrosine Kinase inhibitor. Arch Toxicol. 2021 Jan;95(1):169–78.

26.AEMPS. Emulsion elaboration PN/L/FF/002/00. In: Spanish National Formulary. 2023.

27. OECD. Test No. 498: In vitro Phototoxicity - Reconstructed Human Epidermis Phototoxicity test method [Internet]. OECD; 2023 [cited 2023 Oct 31]. (OECD Guidelines for the Testing of Chemicals, Section 4). Available from:https://www.oecd-ilibrary.org/environment/test-no-498-in-vitro-phototoxicityreconstructed-human-epidermis-phototoxicity-test-method_7b2f9ea0-en

28.Nakai K, Tsuruta D. What Are Reactive Oxygen Species, Free Radicals, and Oxidative Stress in Skin Diseases? Int J Mol Sci. 2021 Oct 6;22(19):10799.

29.Bilkis I, Silman I, Weiner L. Generation of Reactive Oxygen Species by Photosensitizers and their Modes of Action on Proteins. Curr Med Chem. 2019 Jan 21;25(40):5528–39.

30.Martínez LJ, Scaiano JC. Characterization of the Transient Intermediates Generated from the Photoexcitation of Nabumetone: A Comparison with Naproxen. Photochem Photobiol. 1998 Nov;68(5):646–51.

31.Hackbarth S, Schlothauer J, Preuß A, Röder B. New insights to primary photodynamic effects – Singlet oxygen kinetics in living cells. J Photochem Photobiol B. 2010 Mar;98(3):173–9.

32.Davies MJ. Singlet oxygen-mediated damage to proteins and its consequences. Biochem Biophys Res Commun. 2003 Jun;305(3):761–70.

33.Baptista MS, Cadet J, Di Mascio P, Ghogare AA, Greer A, Hamblin MR, et al. Type I and Type II Photosensitized Oxidation Reactions: Guidelines and Mechanistic Pathways. Photochem Photobiol. 2017 Jul;93(4):912–9.

34.Bregnhøj M, Westberg M, Jensen F, Ogilby PR. Solvent-dependent singlet oxygen lifetimes: temperature effects implicate tunneling and charge-transfer interactions. Phys Chem Chem Phys. 2016;18(33):22946–61.

35.Insińska-Rak M, Golczak A, Gierszewski M, Anwar Z, Cherkas V, Kwiatek D, et al. 5-Deazaalloxazine as photosensitizer of singlet oxygen and potential redox-sensitive agent. Photochem Photobiol Sci. 2023 Jul;22(7):1655–71.

36.Sousa C, Rego AMBD, Sá E Melo T. Singlet oxygen reactivity in water-rich solvent mixtures. Quím Nova. 2008;31(6):1392–9.

37.Shlyapintokh VY, Ivanov VB. The Quenching of Singlet Oxygen. Russ Chem Rev. 1976 Feb 28;45(2):99–110.

38.Oliveros E, Suardi-Murasecco P, Aminian-Saghafi T, Braun AM, Hansen H. 1 H -Phenalen-1-one: Photophysical Properties and Singlet-Oxygen Production. Helv Chim Acta. 1991 Jan 30;74(1):79–90.

39.Azqueta A, Collins AR. The essential comet assay: a comprehensive guide to measuring DNA damage and repair. Arch Toxicol. 2013 Jun;87(6):949–68.

40.Moller P. Assessment of reference values for DNA damage detected by the comet assay in human blood cell DNA. Mutat Res Mutat Res. 2006 Mar;612(2):84–104.

41.Palumbo F, Garcia-Lainez G, Limones-Herrero D, Coloma MD, Escobar J, Jiménez MC, et al. Enhanced photo(geno)toxicity of demethylated chlorpromazine metabolites. Toxicol Appl Pharmacol. 2016 Dec;313:131–7.

42.Eberlin S, Silva MSD, Facchini G, Silva GHD, Pinheiro ALTA, Eberlin S, et al. The Ex Vivo Skin Model as an Alternative Tool for the Efficacy and Safety Evaluation of Topical Products. Altern Lab Anim. 2020 Jan;48(1):10–22.

43.Mertsching H, Weimer M, Kersen S, Brunner H. Human skin equivalent as an alternative to animal testing. GMS Krankenhaushygiene Interdiszip. 2008 Mar 11;3(1):Doc11.

44.Suhail S, Sardashti N, Jaiswal D, Rudraiah S, Misra M, Kumbar SG. Engineered Skin Tissue Equivalents for Product Evaluation and Therapeutic Applications. Biotechnol J. 2019 Jul;14(7):1900022.

45.Sylvester PW. Optimization of the Tetrazolium Dye (MTT) Colorimetric Assay for Cellular Growth and Viability. In: Satyanarayanajois SD, editor. Drug Design and Discovery [Internet]. Totowa, NJ: Humana Press; 2011 [cited 2024 Mar 1]. p. 157–68. (Methods in Molecular Biology; vol. 716). Available from: http://link.springer.com/10.1007/978-1-61779-012-6_9

Chemical Science

ROYAL SOCIETY OF CHEMISTRY

EDGE ARTICLE

View Article Online
View Journal | View Issue

Check for updates

Cite this: *Chem. Sci.*, 2022, **13**, 9644

All publication charges for this article have been paid for by the Royal Society of Chemistry

Switching from ultrafast electron transfer to proton transfer in excited drug–protein complexes upon biotransformation†

Lorena Tamarit, [ab] Meryem El Ouardi,[ab] Emilio Lence, [c] Inmaculada Andreu, [ab] Concepción González-Bello, *[c] Ignacio Vayá *[ab] and Miguel A. Miranda *[ab]

Photosensitization by drugs is directly related with the excited species and the photoinduced processes arising from interaction with UVA light. In this context, the ability of gefitinib (GFT), a tyrosine kinase inhibitor (TKI) used for the treatment of a variety of cancers, to induce phototoxicity and photooxidation of proteins has recently been demonstrated. In principle, photodamage can be generated not only by a given drug but also by its photoactive metabolites that maintain the relevant chromophore. In the present work, a complete study of *O*-desmorpholinopropyl gefitinib (GFT-MB) has been performed by means of fluorescence and ultrafast transient absorption spectroscopies, in addition to molecular dynamics (MD) simulations. The photobehavior of the GFT-MB metabolite in solution is similar to that of GFT. However, when the drug or its metabolite are in a constrained environment, *i.e.* within a protein, their behavior and the photoinduced processes that arise from their interaction with UVA light are completely different. For GFT in complex with human serum albumin (HSA), locally excited (LE) singlet states are mainly formed; these species undergo photoinduced electron transfer with Tyr and Trp. By contrast, since GFT-MB is a phenol, excited state proton transfer (ESPT) to form phenolate-like excited species might become an alternative deactivation pathway. As a matter of fact, the protein-bound metabolite exhibits higher fluorescence yields and longer emission wavelengths and lifetimes than GFT@HSA. Ultrafast transient absorption measurements support direct ESPT deprotonation of LE states (rather than ICT), to form phenolate-like species. This is explained by MD simulations, which reveal a close interaction between the phenolic OH group of GFT-MB and Val116 within site 3 (subdomain IB) of HSA. The reported findings are relevant to understand the photosensitizing properties of TKIs and the role of biotransformation in this type of adverse side effects.

Received 10th June 2022
Accepted 2nd August 2022

DOI: 10.1039/d2sc03257k

rsc.li/chemical-science

CC BY-NC

Introduction

The photosensitizing potential of a drug is directly related with the excited species that can be formed upon its interaction with UVA light. In this regard, photo(geno)toxicity or photoallergy are associated with damage to biomolecules such as proteins, lipids or DNA caused by radicals or reactive oxygen species (ROS), which can be generated from excited singlet or triplet states.[1–3] Therefore, investigation of the transient species of an excited drug in different media is crucial to better understand the mechanism leading to photodamage, since either their yields of formation, spectral profile and kinetic evolution may be strongly affected by the surroundings. To this end, fluorescence and transient absorption spectroscopies are suitable techniques that allow studying in depth the photophysical properties of a drug, in addition to getting a better understanding of fundamental photoinduced processes such as energy or electron transfer, charge separation, proton transfer, *etc.*[4]

In this context, gefitinib (GFT) is a tyrosine kinase inhibitor (TKI) clinically used for the treatment of different types of cancer, including lung cancer and locally advanced or metastatic non-small cell lung cancer.[5,6] The mechanism of action of this drug involves targeting the ATP binding pocket of the epidermal growth factor receptor to block its kinase activity preventing autophosphorylation.[7–11] The photosensitizing potential of GFT has recently been demonstrated by *in vitro* neutral red uptake (NRU) assays and protein photooxidation.[12] This drug is administered orally, and the main route of its

[a]*Departamento de Química/Instituto de Tecnología Química UPV-CSIC, Universitat Politècnica de València, Camino de Vera s/n, 46022 València, Spain. E-mail: mmiranda@qim.upv.es; igvapre@qim.upv.es*

[b]*Instituto de Investigación Sanitaria La Fe, Hospital Universitari i Politècnic La Fe, Avenida de Fernando Abril Martorell 106, 46026 Valencia, Spain*

[c]*Centro Singular de Investigación en Química Biolóxica e Materiais Moleculares (CiQUS), Departamento de Química Orgánica, Universidade de Santiago de Compostela, Jenaro de la Fuente s/n, 15782 Santiago de Compostela, Spain. E-mail: concepcion.gonzalez.bello@usc.es*

† Electronic supplementary information (ESI) available. See https://doi.org/10.1039/d2sc03257k

© 2022 The Author(s). Published by the Royal Society of Chemistry

elimination is through hepatic metabolism *via* CYP3A4 and biliary excretion.[13] One of its metabolites is shown in Fig. 1: *O*-desmorpholinopropyl gefitinib (GFT-MB). As it can be observed, both the drug and its metabolite maintain the quinazoline moiety in its structure; drugs containing this chromophore are known to induce photodermatosis.[14] Besides, the ability of other TKIs to mediate photodamage has also been proven with lapatinib (LAP),[15] a drug currently used for the treatment of lung and breast cancer. Interestingly, not only LAP is phototoxic and photogenotoxic, but also one of its photoactive metabolites, the *N*-dealkylated derivative (*N*-LAP).

Previous studies on the photobehavior of LAP and its metabolites by means of spectroscopic techniques have shown that their photophysical properties are strongly medium-dependent.[16,17] A similar result was recently obtained for the parent drug GFT.[12] Thus, excitation of these anticancer drugs in organic non-polar solvents or in biological media leads to the formation of locally excited (LE) singlet states. By contrast, in organic polar solvents LE states rapidly evolve to the formation of longer-lived intramolecular charge transfer (ICT) singlet states. Actually, LE species have been proposed to be responsible for the photoinduced biological damage mediated by GFT, LAP and its metabolite *N*-LAP.[12,15]

With this background, the aim of the present work is to compare the photobehavior of GFT with that of GFT-MB in solution and in the presence of human serum albumin (HSA)[18] using fluorescence and transient absorption spectroscopies, from the femtosecond to the microsecond time-scales. Besides, molecular dynamics (MD) simulations have been used to investigate in atomic detail the binding of this drug and its metabolite to the protein, in order to achieve a better understanding of the experimental results.[19] In this context, MD simulation has proven to be a powerful tool for studying the strength and characteristics of the interactions of a drug with the amino acids of the protein binding sites.[16,20] All these features are relevant as they can be directly connected with the photosensitizing properties of GFT and its metabolite.

Experimental

Chemicals and reagents

Gefitinib (GFT) was purchased from Quimigen. *O*-Desmorpholinopropyl gefitinib (GFT-MB) was purchased from Fluorochem. *N*-Acetyl-L-tyrosine methyl ester (NAc-TyrMe), *N*-acetyl-L-tryptophan methyl ester (NAc-TrpMe), anthracene, 3-methylindole, ibuprofen, warfarin and human serum albumin (HSA) were purchased from Sigma-Aldrich. PBS buffer was prepared by dissolving phosphate-buffered saline tablets (Sigma) using ultrapure water from a Millipore (Milli-Q Synthesis) system. Spectrophotometric HPLC solvents were obtained from Scharlab and used without further purification.

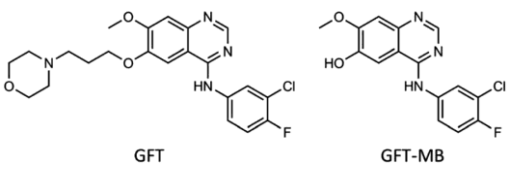

Fig. 1 Chemical structure of gefitinib (GFT) and its *O*-desmorpholinopropyl metabolite GFT-MB.

Spectroscopic measurements

Steady-state absorption spectra were recorded in a JASCO V-760 spectrophotometer. Steady-state fluorescence spectra were obtained using a JASCO spectrofluorometer system provided with a monochromator in the wavelength range 200–900 nm, with an excitation wavelength of 340 nm at 25 °C. Measurements on ligand@protein complexes were performed of 1 : 1 molar ratio mixtures at 10 μM in aerated PBS. The absorbance of the samples at the excitation wavelength was kept below 0.1. Phosphorescence measurements were performed in a Photon Technology International (PTI, TimeMaster TM-2/2003) spectrophotometer equipped with a pulsed Xe lamp, operating in a time-resolved mode with a delay time of 0.5 ms. The sample was dissolved in ethanol, introduced in a quartz tube of 5 mm of diameter and cooled with liquid nitrogen (77 K).

Time-resolved fluorescence measurements were done using an EasyLife X system containing a sample compartment composed of an automated Peltier cuvette holder to control the temperature at 24 °C, a pulsed LED excitation source and a lifetime detector. The employed LED excitation source was 340 nm, with emission filter of WG370.

Laser flash photolysis (LFP) measurements were performed using a pulsed Nd:YAG L52137 V LOTIS TII at the excitation wavelength of 355 nm. The single pulses were *ca.* 10 ns duration, and the energy was ~12 mJ per pulse. The laser flash photolysis system consisted of the pulsed laser, a 77250 Oriel monochromator and an oscilloscope DP04054 Tektronix. The output signal from the oscilloscope was transferred to a personal computer. Absorbances of all solutions were adjusted at ~0.20 at 355 nm. All UV, fluorescence and LFP measurements were recorded using 10 × 10 mm^2 quartz cuvettes at room temperature in deaerated conditions (25 min N_2 bubbling), or in the case of the protein complexes in aerated atmosphere. Control experiments indicated that the degree of decomposition of the samples after photolysis was lower than 5%.

Femtosecond transient absorption experiments were performed using a typical pump-probe system. The femtosecond pulses were generated with a compact regenerative amplifier that produces pulses centered at 800 nm (τ_{pulse} ~ 100 fs, 1 mJ per pulse). The output of the laser was split into two parts to generate the pump and the probe beams. Thus, tunable femtosecond pump pulses were obtained by directing the 800 nm light into an optical parametric amplifier. In the present case, the pump was set at 330 nm and passed through a chopper prior to focus onto a rotating cell (1 mm optical path) containing the samples in organic or aqueous solution. The white light used as probe was produced after part of the 800 nm light from the amplifier travelled through a computer controlled 8 ns variable optical delay line and impinge on a CaF_2 rotating

© 2022 The Author(s). Published by the Royal Society of Chemistry

crystal. This white light was in turn split in two identical portions to generate reference and probe beams that then are focused on the rotating cell containing the sample. The pump and the probe were made to coincide to interrogate the sample. The power of the pump beam was set to 180 μW. Under these conditions, the degree of photodegradation of the samples was lower than 5%. A computer-controlled imaging spectrometer was placed after this path to measure the probe and the reference pulses to obtain the transient absorption decays/spectra. The experimental data were treated and compensated by the chirp using the ExciPro program.

Molecular docking

These calculations were performed using GOLD program version 2020.2.0,[21] and the protein coordinates were taken from the crystal structure of HSA in complex with hemin and myristic acid (PDB entry 1O9X).[22] The experimental procedure was similar to that described for LAP, *N*-LAP and *O*-LAP in HSA.[17]

Molecular dynamics simulation studies

The highest score solution obtained by docking was subjected to 100 ns of dynamic simulation. The experimental protocol involved: (i) the minimization of the ligands (GFT, GFT-MB); (ii) the generation and minimization of the binary GFT@HSA and GFT-MB@HSA complexes using the poses obtained by docking; and (iii) simulations of the resulting minimized ligand@HSA complexes. The protocol was performed as described for LAP, *N*-LAP and *O*-LAP in HSA.[17] The cpptraj module in AMBER 17 was used to analyze the trajectories and to calculate the rmsd of the protein and the ligand during the simulation.[23] The molecular graphics program PyMOL[24] was employed for visualization and depicting enzyme structures. For figures related to HSA, the amino acid numbering described in PDB entry 1O9X was employed.

Binding free energies

The binding free energy for GFT and GFT-MB was calculated by the MM/PBSA approach as implemented in Amber.[25] The ante-MMPBSA.py module was used to create topology files for the complexes, protein and ligands, while the binding free energies were calculated with the MMPBSA.py module. Only the last 80 ns of the 100 ns MD trajectories were used to calculate binding free energies. The Poisson–Boltzmann (PB) and generalized Born (GB) implicit solvation models were employed. Both models provided similar results.

Results and discussion

In view of the photosensitizing potential recently demonstrated for GFT,[12] which is assumed to arise from the excited species formed upon interaction with UVA light, it seemed relevant to study the photophysical properties of GFT-MB, since this metabolite maintains the quinazoline moiety and is structurally similar to the parent drug. To this end, the species formed after excitation of GFT-MB with UVA light were first explored in organic solvents of different polarities by means of fluorescence and ultrafast transient absorption spectroscopies.

The UV absorption spectra of GFT-MB hardly changed with the polarity of the organic solvent, while the fluorescence properties (Table 1 and Fig. 2) were strongly affected. This behavior is similar to that previously observed for GFT.[12] Accordingly, a similar interpretation can be done for the metabolite and its parent drug: emission from intramolecular charge transfer (ICT) states is detected in polar solvents such as acetonitrile, while locally excited (LE) states are formed in the non-polar ones, *i.e.* cyclohexane. The latter emit at shorter wavelengths and display higher yields (ϕ_F) than ICT states. In addition, the fluorescence lifetimes (τ_F) were found to be much shorter for LE (*ca.* 1.2 ns) than for ICT states (~3 ns).

In order to investigate the formation of LE and ICT states in more detail, femtosecond transient absorption experiments were performed for GFT-MB in acetonitrile. This is a very sensitive and precise technique that allows investigating processes occurring at the very early steps after excitation, such as photoinduced energy and electron transfer, charge separation, photoinduced proton transfer and intersystem crossing (ISC).[27] Hence, excitation of GFT-MB at 330 nm in acetonitrile gave rise to the instantaneous formation of a band centered at 480 nm (Fig. 3A, black line). In line with the behavior previously observed for GFT,[12] this species was assigned to LE states, which rapidly evolved towards the formation of a band with maximum at ~435 nm (Fig. 3A, dark gray line), associated to ICT states. This process took place in *ca.* 2.4 ps: as it can be deduced from the kinetic traces of Fig. 3B, the decay at 480 nm (black line) is directly associated with the formation of the trace at 435 nm (dark gray line). Once ICT states were formed, they disappeared in a temporal scale reaching the nanosecond time profile. These results are in line with the observations from the fluorescence experiments. Finally, it is worth to mention that a new absorption band displaying a maximum ~610 nm (blue line), remained in the ns timescale; this species was assigned to the triplet–triplet absorption of GFT-MB (^{3}GFT-MB*).

As ^{3}GFT-MB* was detected from ultrafast transient absorption spectroscopy, and triplet species normally survive up to the microsecond time scale, it seemed relevant to use the laser flash photolysis (LFP) technique to study in more detail not only their

Table 1 Fluorescence properties (λ_{exc} = 340 nm) of GFT-MB in organic solvents of different polarity and within HSA, compared with those of GFT

	GFT[a]			GFT-MB		
	λ_{max}/nm	ϕ_F[b]	τ_F/ns	λ_{max}/nm	ϕ_F[b]	τ_F/ns
MeCN	473	0.05	3.4	468	0.03	3.2
1,4-Dioxane	458	0.09	2.5	456	0.08	3.1
Toluene	421	0.18	2.6	442	0.14	2.9
Cyclohexane	378	0.19	1.3	375[c]	0.16[c]	1.2[c]
HSA	390	0.02	1.3	432	0.15	2.5

[a] Data from ref. 12. [b] ϕ_F were determined using anthracene in ethanol as ref. 26. [c] Due to solubility requirements, 10% of toluene was needed to solubilize GFT-MB in cyclohexane.

© 2022 The Author(s). Published by the Royal Society of Chemistry

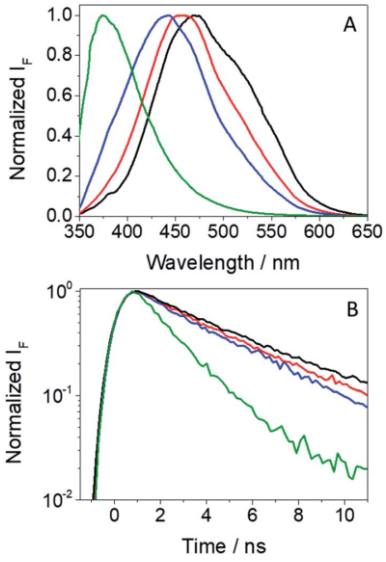

Fig. 2 Normalized fluorescence spectra (A) and decay traces (B) for GFT-MB in acetonitrile (black), 1,4-dioxane (red), toluene (blue) and cyclohexane (green) after excitation at 340 nm.

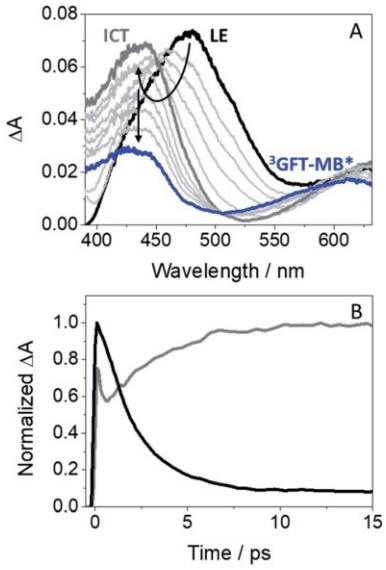

Fig. 3 (A) Femtosecond transient absorption spectra from 0.5 ps (black) to 2 ns (blue) for GFT-MB. (B) Kinetic traces monitored at 480 (black) and 435 nm (dark gray). Measurements were performed in acetonitrile after excitation at 330 nm.

formation but also the reactive species that may arise from triplets, *i.e.* radicals and/or ROS,[28] since they can be responsible for the photosensitized damage to biomolecules (lipids, proteins or DNA).[1–3] In this context, it is known that light-absorbing drugs are able to induce photodamage to biomolecules through two different mechanisms: type I, involving formation of radicals *via* electron transfer and/or hydrogen abstraction, or type II mechanism occurring through energy transfer from the excited drug to molecular oxygen, yielding formation of the highly reactive singlet oxygen ($^1O_2$) species.[29,30]

The main transients arising from excitation of GFT-MB in deaerated MeCN upon LFP at λ_{exc} = 355 nm are shown in Fig. 4A. In agreement with previous observations from the parent drug GFT, triplets were the main excited species detected for the metabolite. Hence, ^{3}GFT-MB* displayed a maximum absorption band at *ca.* 600 nm, which disappeared in about 1.3 μs. A similar trend was also observed in the less polar solvent toluene (Fig. 4B), but displaying slightly higher triplet yields and decaying with similar lifetimes as in MeCN. The energy value of ^{3}GFT-MB*, determined from the phosphorescence spectra in a solid matrix of ethanol at 77 K (Fig. S1†), was 67 kcal mol^{-1}, similar to that of GFT (69 kcal mol^{-1}).[12]

As stated above, from a photobiological point of view, formation of triplet excited species is important since they can induce a cascade of reactions that could finally result in damage to biomolecules (*e.g.* proteins). In this regard, since a type I mechanism may operate in the photobiological damage, the ability of both the drug and its metabolite to photoinduce formation of radical species was also investigated in the presence of tyrosine (Tyr) and tryptophan (Trp). These are key amino acids located in different binding sites of transport proteins, which play a significant role in drug@protein interactions.[31] In

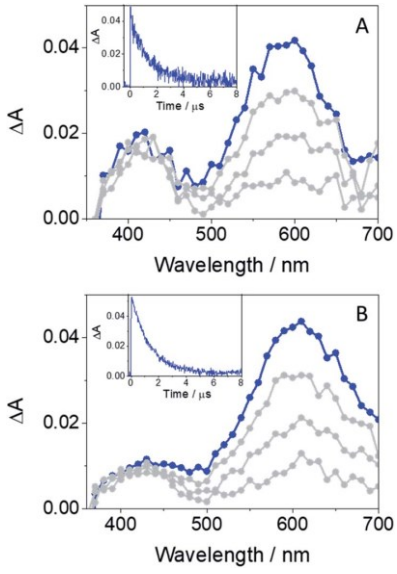

Fig. 4 LFP spectra (from 0.2 to 3 μs) and decay traces at 600 nm for GFT-MB in MeCN (A) and toluene (B) under deaerated conditions after excitation at 355 nm.

© 2022 The Author(s). Published by the Royal Society of Chemistry

order to check this possibility, application of the Weller equation,[32] considering the triplet energy of the drug (or metabolite) and the redox potentials of model compounds such as quinazoline, phenol and 3-methylindole,[26,33] agrees with an exergonic electron transfer from the amino acid to the excited drug (ΔG *ca.* −6 kcal mol^{-1} for Tyr, and ΔG *ca.* −4 kcal mol^{-1} for Trp). As the energies of the singlet excited states are markedly higher, the electron transfer from these states would be even more favorable. In fact, the feasibility of this process was confirmed experimentally as explained below.

Laser flash photolysis measurements at $\lambda_{exc} = 355$ nm were performed in deaerated MeCN on mixtures containing the drug (or its metabolite) and increasing amounts of the corresponding amino acid (due to solubility requirements, the *N*-acetyl methyl ester amino acid derivatives, namely NAc-TyrMe or NAc-TrpMe, were used). Thus, selective excitation of GFT in the presence of Tyr or Trp induced deactivation of its triplet excited state with $\lambda_{max} \sim 600$ nm (Fig. S2†); quenching rate constants (k_Q) of *ca.* 1.4×10^8 M^{-1} s^{-1} and 1.5×10^7 M^{-1} s^{-1} were determined for Tyr and Trp, respectively. This quenching is attributed to a photoinduced electron transfer (PET) process, since energy transfer from the excited drug to the amino acid is energetically disfavored, as the triplet energies of Tyr and Trp (82 and 71 kcal mol^{-1}, respectively)[26] are higher than that of GFT (69 kcal mol^{-1}). Interestingly, formation of the Tyr radical at ~400 nm (ref. 34) was detected for GFT/Tyr mixtures (Fig. 5). PET processes have previously been observed for other drug/Tyr and drug/Trp systems.[35]

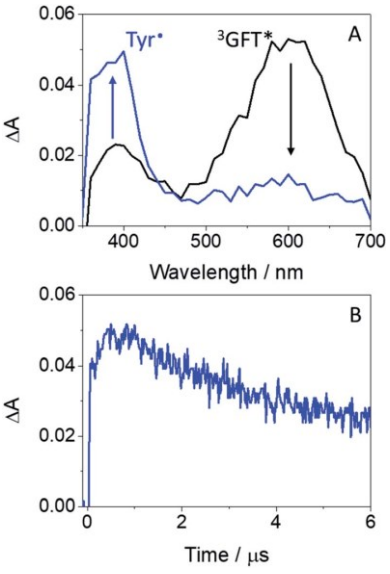

Fig. 5 (A) LFP spectra monitored 0.08 μs after the laser pulse for GFT (black) and a mixture of GFT/NAc-TyrMe in a molar ratio of 1 : 200 (blue); the concentration of GFT was 120 μM. (B) Kinetic trace at 400 nm. Measurements were performed in deaerated MeCN after excitation at 355 nm.

A similar behavior was observed for GFT-MB. Hence, quenching of its triplet excited state was observed upon addition of increasing amounts of the Tyr and Trp derivatives. In this case, k_Q values of *ca.* 6.0×10^7 M^{-1} s^{-1} and 2.5×10^8 M^{-1} s^{-1} were determined, respectively. Again, as shown above for GFT, formation of the Tyr radical was also detected (Fig. S3†). As stated above, electron transfer processes can also occur from singlet excited states. In fact, this was previously observed for ^{1}GFT* in toluene in the presence of increasing amounts of 3-methylindole, the chromophore of the Trp residue; a k_Q value of $\sim 4.3 \times 10^{10}$ M^{-1} s^{-1} was determined.[12] A similar result has also been obtained here using NAc-TyrMe (Fig. S4A†), with a quenching rate constant of *ca.* 6.3×10^9 M^{-1} s^{-1}. As expected, quenching of ^{1}GFT-MB* through electron transfer from 3-methylindole or NAc-TyrMe takes actually place, displaying k_Q values of *ca.* 8.7×10^9 M^{-1} s^{-1} and 5.8×10^9 M^{-1} s^{-1} (Fig. S4B and C†), respectively, which are slightly lower than those observed for ^{1}GFT*.

So far, the results have only been discussed in organic solvents, where both GFT and GFT-MB are in their neutral forms. However, the scenario may change in aqueous solution, since the quinazoline and morpholine moieties can be protonated at sufficiently low pH; moreover, in the case of the metabolite, the –OH group can be deprotonated leading to phenolate-like species. In this context, the pK_a values for the quinazoline moiety and the morpholine side chain of GFT are 5.4 and 7.2, respectively.[36] By contrast, for the main chromophore of GFT-MB, 6-hydroxyquinazoline, these values are 3.2 and 8.2, which are associated with deprotonation of the quinazoline moiety and the –OH group, respectively.[37] In view of the above pK_a values, GFT should be fully protonated at pH 2. However, at physiological pH 7.4, the protonated amino group of the morpholine moiety should be in equilibrium with its neutral form while the quinazoline moiety should be deprotonated. Besides, in basic media GFT would be fully deprotonated, and its absorption band at *ca.* 330 nm peaks at lower wavelengths compared with the acidic medium (Fig. S5A†). As regards GFT-MB, it should also be fully protonated at pH 2, while at physiological pH its neutral form would predominate. By contrast, at basic pH the metabolite starts to deprotonate to form phenolate-like species, whose UV absorption band appears at longer wavelengths (Fig. S5B†).

Considering the capability of both the drug and its metabolite to participate in photoinduced electron transfer with Tyr and Trp, which could finally result in damage to biomolecules, it seemed appropriate to investigate their interactions with human serum albumin (HSA) in aqueous PBS solution. This is the most abundant protein in human plasma, and it is responsible for a number of relevant processes including transport of endogenous and exogenous agents (*e.g.* drugs, metabolites, fatty acids, *etc.*) for their selective delivery to specific targets.[38] In this regard, the binding of drugs to transport proteins is important since it regulates drug solubility in plasma, susceptibility to oxidation, toxicity and *in vivo* half-life.[31]

The stoichiometry of the protein-bound drug or metabolite has been determined by means of Job's plot analysis,[39] which

© 2022 The Author(s). Published by the Royal Society of Chemistry

provides evidence for the formation of a 1 : 1 complex; this has been further confirmed by MD simulations, where only a single molecule of GFT (or GFT-MB) can bind within HSA (Fig. S6†).

The photophysical properties of GFT interacting with HSA have been recently investigated.[12] In this case, emission from LE singlet states (LE ^{1}GFT*) with $\lambda_{max} \sim 390$ nm is predominantly observed. However, the photobehavior of GFT-MB bound to HSA remains unexplored. Thus, fluorescence and transient absorption spectroscopies were used to study in detail the photobehavior of the protein-bound metabolite upon its selective excitation with UVA light ($\lambda_{exc} = 340$ nm); this excitation wavelength is relevant from a photobiological point of view since HSA does not absorb light at 340 nm and, therefore, the photoinduced processes would only arise from the excited metabolite.

The fluorescence spectra of GFT@HSA and GFT-MB@HSA are compared in Fig. 6. Emission from the drug or the metabolite free in solution is almost negligible; however, it is strongly enhanced within the protein cavities as a result of the higher restrictions in their degrees of freedom for conformational relaxation. Interestingly, this effect is more important for GFT-MB@HSA, which displays a much higher ϕ_F value than GFT@HSA (~0.15 *vs.* ~0.02, respectively; Table 1). The strength and preferential site of interaction for GFT-MB within HSA has been studied using displacement probes for site 1 (warfarin, WRF),[40] site 2 (ibuprofen, IBP).[41] In the case of GFT, it was previously reported that it interacts with site 3 of HSA with a binding constant (k_a) of 1.7×10^4 M^{-1}.[42] Under physiological conditions, *ca.* 97% of GFT is bound to plasma proteins, namely HSA.[43] For GFT-MB@HSA at 1 : 1 molar ratio, addition of IBP or WRF did not result in its displacement from the binding site; instead, a slight fluorescence enhancement was observed due to an allosteric effect. By contrast, addition of GFT induced a clear displacement of the metabolite from its binding site (Fig. S7†). These results are consistent with site 3 as the preferred site for GFT-MB@HSA, with a binding constant in the order of that of GFT@HSA. This was further confirmed by theoretical studies. The binding free energies of GFT and GFT-MB to site 3 of HSA were calculated using the MM/PBSA method in explicit water (generalized Born, GB) as implemented in Amber.[25] The affinity of GFT-MB to HSA proved to be slightly weaker (13.1 kcal mol^{-1}) than that of the parent drug.

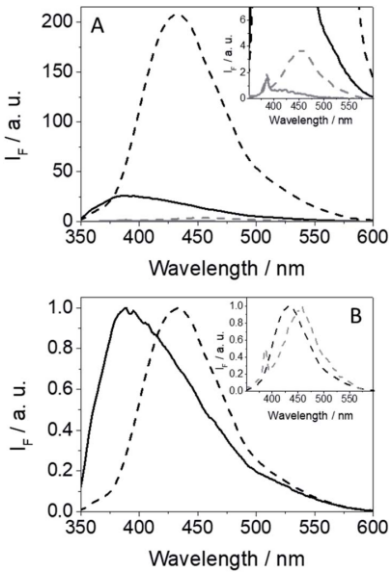

Fig. 6 Fluorescence spectra (A) and normalized spectra (B) for GFT (gray line), GFT-MB (dashed gray line), GFT@HSA (black line) and GFT-MB@HSA (black dashed line) after excitation at 340 nm in aqueous PBS under air. For the protein complexes, mixtures were at 1 : 1 ligand@HSA molar ratio, using isoabsorptive solutions at the excitation wavelength. The inset in (A) shows a zoom of the weakly emitting species, while in (B) shows the normalized fluorescence spectra for GFT-MB@HSA and GFT-MB in PBS.

An interesting point to discuss is the bathochromic shift of the emission band of the protein-bound metabolite ($\lambda_{max} \sim 432$ nm) compared with that of GFT@HSA ($\lambda_{max} \sim 390$ nm, Fig. 6B), whose emission arises from LE states. These results point to the occurrence of different photoinduced processes for the drug and the metabolite within HSA upon interaction with UV light. In this context, and as stated above, photoinduced electron transfer from electron donors (Tyr and/or Trp) to the excited drug might occur in GFT@HSA, which explains its low fluorescence yield.[12] By contrast, since the metabolite is a phenol, although electron transfer might also occur, as it has been observed for GFT-MB/Tyr (or Trp) mixtures in organic solvent, excited state proton transfer (ESPT) to form phenolate-like excited species might be a competitive process within the protein; these species are known to absorb and emit at wavelengths longer than phenols.[44–46] In this regard, not only emission from GFT-MB@HSA was shifted to longer wavelengths, but also its absorption spectrum revealed a red-shifted shoulder at *ca.* 375 nm compared to GFT-MB in the bulk aqueous solution (Fig. 7A). In fact, the UV absorption spectra of GFT@HSA was hardly affected for aqueous solutions with pH above 6, in contrast to what was observed for GFT-MB@HSA, whose maximum shifted progressively towards longer wavelengths at increasing pH (Fig. S8†). This strongly suggests that phenolate-like species predominate in the GFT-MB@HSA complex; indeed, the shoulder at *ca.* 375 nm became more important at low GFT-MB/HSA ratios, supporting the prevalence of phenolate species within the protein (Fig. S9†). As it can be anticipated, this effect was not observed for GFT@HSA, since ESPT is not possible (Fig. 7B and S9A†). In this connection, fluorescence of GFT in the bulk solution was negligibly affected by the pH, while it was increased only slightly within HSA in aqueous solutions from pH 6 to 10 (Fig. S10A and C†); this is probably associated with the protonation–deprotonation equilibrium of the morpholine's nitrogen. By contrast, emission from GFT-MB was highly affected by the pH; this effect was even greater in the presence of HSA (Fig. S10B and D†), which is related with the formation of phenolate-like species within the protein. The small differences in the fluorescence maxima for GFT-MB in the bulk basic solution or within HSA (inset in Fig. 6B) arise from

(cc) BY-NC

© 2022 The Author(s). Published by the Royal Society of Chemistry

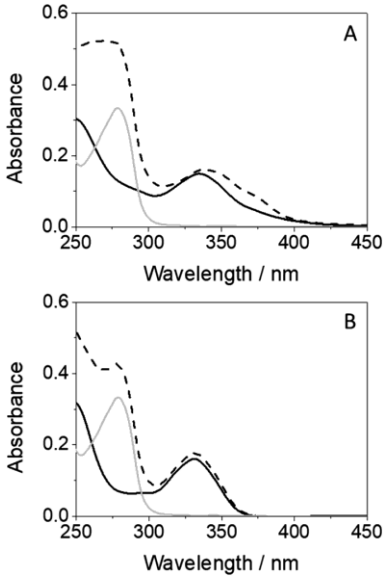

Fig. 7 (A) Absorption spectra for GFT-MB (black line), HSA (gray line) and GFT-MB@HSA (dashed black line). (B) Absorption spectra for GFT (black line), HSA (gray line) and GFT@HSA (dashed black line). All solutions were prepared at 10 μM in aqueous PBS. For the protein complexes, mixtures were at 1 : 1 ligand@HSA molar ratio.

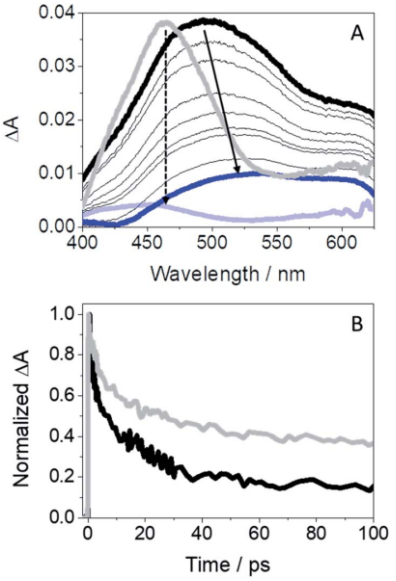

Fig. 8 (A) Femtosecond transient absorption spectra from 1 ps (black) to 0.5 ns (blue) for GFT-MB@HSA; the absorption spectra of GFT@HSA[12] from 1 ps (light gray) to 1 ns (light blue) is also shown for comparison. (B) Kinetic traces for GFT-MB@HSA at 500 nm (black) and for GFT@HSA at 460 nm (light gray) after excitation at 330 nm of a 1 : 1 molar ratio ligand@protein complexes in aerated aqueous PBS solution.

the constrained environment provided by the protein, but in both cases this emission is associated to phenolate-like species.

The high ϕ_F value for GFT-MB@HSA may have implications in connection with its photosensitizing potential. Accordingly, fluorescence for the protein-bound metabolite decays at times longer than that observed for GFT@HSA (2.8 *vs.* 0.8 ns, respectively; Fig. S11†).

Since diverging photoinduced processes may arise from GFT@HSA or GFT-MB@HSA, *i.e.* electron or proton transfer, respectively, it seemed appropriate to study the photobehavior of the protein-bound metabolite by means of ultrafast spectroscopy upon excitation with UVA light ($\lambda_{exc} = 330$ nm). Thus, the transient absorption spectra for GFT-MB@HSA from 1 ps to 0.5 ns are shown in Fig. 8A. For comparison, the spectra of GFT@HSA have also been included; in the latter case, formation of a single transient with maximum at 460 nm is assigned to LE ^{1}GFT* states. It decays following a multi-exponential law (Fig. 8B); the shortest component is associated to electron transfer from appropriate donors to gefitinib.[12] By contrast, a broad absorption band (410–600 nm) centered at ~500 nm was instantaneously formed for GFT-MB@HSA. We assign this species to phenol-like LE ^{1}GFT-MB* states. The absorption maximum shifted over time to longer wavelengths (from 500 to *ca.* 530 nm). This process can be related to intermolecular ESPT from LE ^{1}GFT-MB to a proper acceptor located in the protein cavity to form phenolate-like excited species. Such assignment is consistent with the ultrafast transient absorption spectra previously observed for phenolate anions.[47] The kinetic trace for GFT-MB@HSA can be satisfactorily fitted using a multi-exponential function; the shortest component, on the ps time scale, is associated to the proton transfer process, while the longer one, on the ns scale, is assigned to the decay of the phenolate-like excited species. This agrees with the UV and steady-state fluorescence results, where a bathochromic shift is observed. It is worth to mention that ^{3}GFT-MB* was practically not observed in the protein medium, since the signal at *ca.* 600 nm is insignificant; this species was not even detected at longer time scales by means of LFP measurements (Fig. S12†). This result agrees with the formation of phenolate-like species within HSA, which hinders the formation of triplet excited species through ISC.

Finally, to get an insight in atomic detail into the ligand@-protein interactions responsible for the photophysical properties experimentally observed, the binding mode of GFT and GFT-MB to HSA was explored by molecular docking using the GOLD program version 2020.2.0 (ref. 21) and further studied by molecular dynamics (MD) simulation studies. It should be noted that HSA is a large protein (60 kDa) that contains three main domains, namely I (residues 1–195), II (196–383) and III (384–585) (Fig. 9A). Each domain is divided into two sub-domains, namely A and B, with different recognition patterns, which explains the huge capacity of this protein to transport a large variety of endogenous and exogenous compounds.[48] HSA employs three main binding sites for recognition: site 1

© 2022 The Author(s). Published by the Royal Society of Chemistry

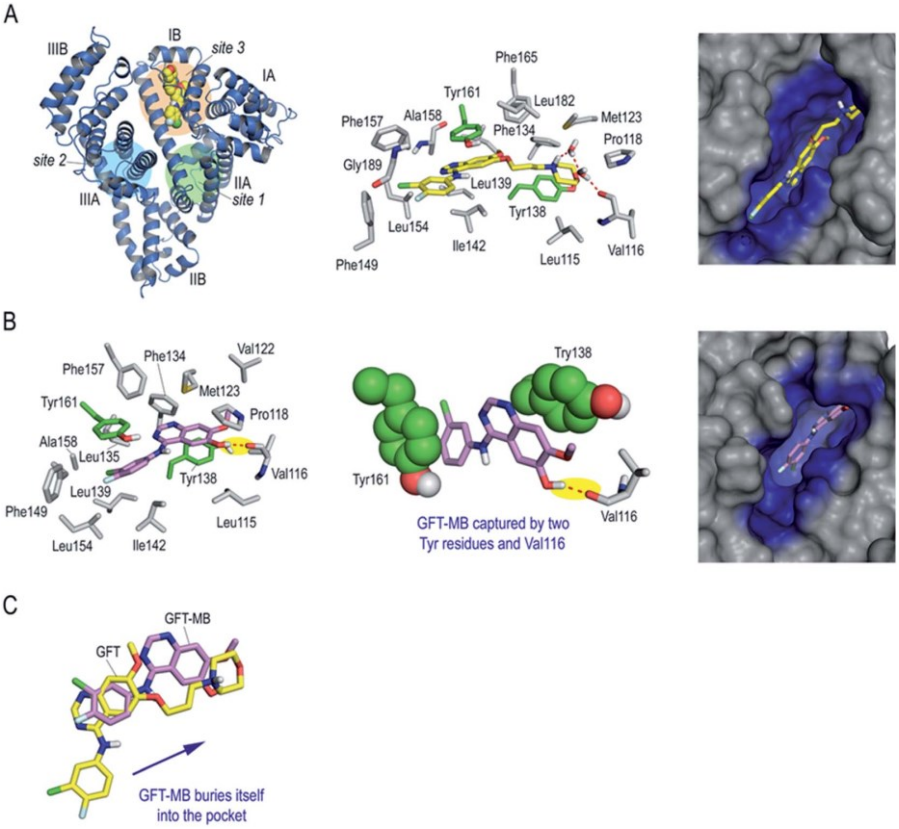

Fig. 9 Binding mode of GFT and GFT-MB with subdomain IB (site 3) of HSA obtained by MD simulation studies. (A) Overall and detailed views of GFT (yellow) binding mode. Snapshot after 100 ns is shown. Protein subdomains and main binding sites 1–3 of HSA are labelled and highlighted in the overall view. (B) Detailed view of GFT-MB (violet) binding mode. Snapshot after 90 ns is shown. Note how GFT-MB is anchored in the pocket thanks to a strong hydrogen bonding interaction with Val116 (yellow shadow) and a double π–π stacking interaction with two tyrosine residues (green spheres), which are located on both sides of the aromatic ring. (C) Superposition of the arrangements of GFT and GFT-MB with subdomain IB of HSA. Note the different arrangements of GFT and GFT-MB, which is more buried in the pocket. Hydrogen bonding interactions between the ligands and the protein are shown as red dashed lines. Relevant side chain residues are shown and labelled. The tyrosine residues Tyr161 and Tyr138 are highlighted in green color.

(subdomain IIA), site 2 (subdomain IIIA) and site 3 (subdomain IB). Based on the structural similarity of the basic core of GFT (*N*-phenylquinazolin-4-amine moiety) with lapatinib, which was reported to bind to site 3,[17] this region was selected for docking. The protein coordinates found in the crystal structure of HSA in complex with hemin (PDB entry 1O9X),[22] which also binds to subdomain IB, was used for these studies. The GFT@HSA and GFT-MB@HSA complexes obtained by docking were immersed in a truncated octahedron box of water molecules and then subjected to 100 ns of dynamic simulation for validation using the molecular mechanics force field AMBER ff14SB and GAFF.[49,50]

The results of these MD simulation studies revealed the significant differences in the binding mode of GFT and GFT-MB with HSA (Fig. 9A *vs.* Fig. 9B). For GFT@HSA, the existence of a flexible side chain with a terminal morpholine group determines the arrangement of the compounds within the pocket. Thus, the most relevant interaction with the protein is the hydrogen bond between the quaternary amino group in its morpholine moiety and the side chain residues in the vicinity (Val116, Asp183), mainly through a network of water molecules (Fig. 9A). In this case, no direct polar contacts with protein residues were observed. Although the side chain of GFT is flexible and some motion is observed, the position of the quinazoline moiety is frozen within the pocket. Thus, the analysis of the root-mean-square deviation (rmsd) of the quinazoline core in GFT during the whole simulation revealed average values of 1.9 Å (Fig. S13†). This is due to the interaction of its quinazoline ring with the side chain of Tyr161, which is located on top, establishing a strong π–π stacking between them. The analysis of the variation of the relative distance between the mass center of the phenol group in Tyr161 and the quinazoline

© 2022 The Author(s). Published by the Royal Society of Chemistry

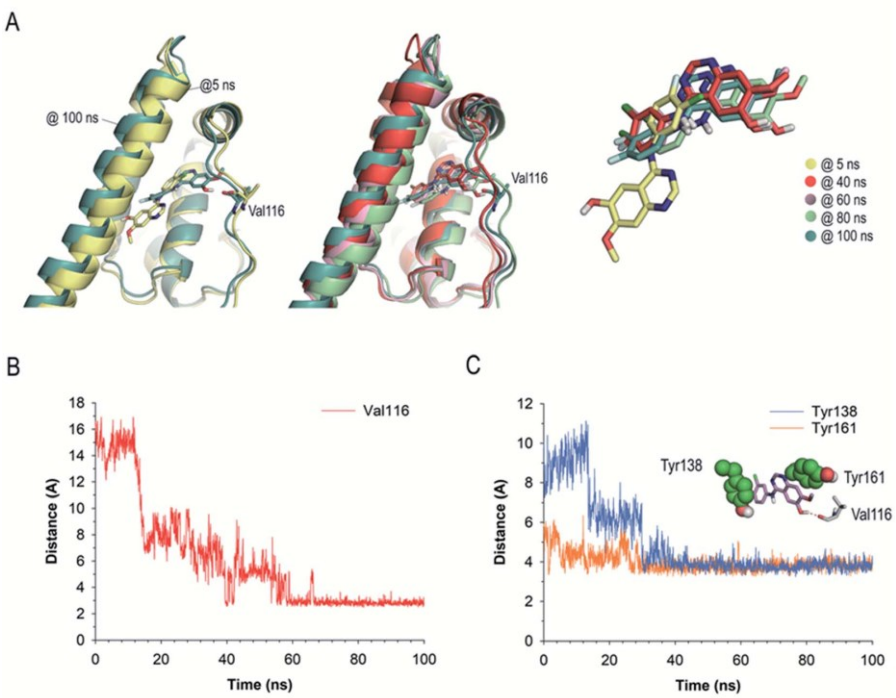

Fig. 10 (A) Comparison of several snapshots of GFT-MB@HSA during 100 ns of MD simulation. GFT-MB and Val116 are shown as sticks. Note that during the simulation GFT-MB was displaced towards the bottom part of the pocket to locate its hydroxyl group pointing towards the main carbonyl group of Val116, remaining in this arrangement after ~15 ns of simulation. (B) Variation of the relative distance between the oxygen atom (OH group) of the quinazoline moiety in GFT-MB and the oxygen atom of the main carbonyl group of Val116 in the GFT-MB@HSA protein complex during whole simulation. (C) Variation of the relative distance between the mass center of the phenol groups in Tyr138 and Tyr161 and GFT-MB in the GFT-MB@HSA protein complex during whole simulation. Note how, after stabilization, both residues remain in close contact with the ligand during the simulation.

moiety of GFT in the complex during the whole simulation showed average distances of 3.7 Å (Fig. S14†). In addition, the arrangement of GFT in subdomain IB of HSA is further stabilized by numerous lipophilic interactions with the non-polar residues within the pocket, specifically Leu115, Pro118, Met123, Phe134, Tyr138, Leu139, Ile142, Phe149, Leu154, Phe157, Ala158, Phe165, Leu182, and Gly189.

The binding mode of GFT-MB was clearly different from that observed for GFT, since the lack of the flexible chain allows it to bury itself in the pocket, stabilizing its arrangement through a strong hydrogen bonding interaction with the protein, specifically between its hydroxyl group and the main carbonyl group in Val116 (Fig. 9B). In fact, after ~15 ns of simulation, GFT-MB moved away from the position identified by docking (like GFT) towards the bottom of the pocket to establish a direct contact with Val116, remaining fixed in this arrangement during the rest of the simulation (Fig. 10A). The average distance of the latter interaction during the last 50 ns of simulation was 3.2 Å (Fig. 10B). The position of GFT-MB is also frozen through strong π–π stacking with the phenol groups of Tyr161 and Tyr138, which are located on both faces of the ligand. The average distance between the mass center of the phenol groups and the quinazoline moiety in GFT-MB during the last 50 ns of simulation was 3.8 Å (Fig. 10C). As for GFT, diverse lipophilic interactions with the non-polar residues of the pocket, specifically Leu115, Pro118, Met123, Phe134, Leu135, Ile142, Phe149, Leu154, Phe157, and Ala158, were also identified.

Conclusions

The photobehavior of GFT-MB, a photoactive GFT metabolite, has been compared with that of its parent drug in different media, *i.e.* in solution and within HSA. To this end, fluorescence and transient absorption spectroscopies, from the femtosecond to the microsecond time scales have been used. Besides, MD simulations have been performed to explain in atomic detail the experimental results. The main excited species detected for both GFT and GFT-MB in solution are very similar. Thus, locally excited (LE) states are mainly formed in non-polar solvents, whereas intramolecular charge transfer (ICT) species predominate in polar solvents. Triplet excited states are detected in both

© 2022 The Author(s). Published by the Royal Society of Chemistry

polar and non-polar organic solvents; from this species, a type I mechanism seems to operate in the photodamage to biomolecules, since the resulting radicals have been detected by means of LFP. By contrast, significant differences are observed in the photobehavior of both the drug or the metabolite within the constrained environment provided by HSA. Thus, for GFT@HSA, LE species are instantaneously formed, which can photoinduce electron transfer with appropriate donors (*e.g.* Tyr or Trp residues). On the contrary, since the metabolite is a phenol, excited state proton transfer to form phenolate-like excited species occurs in GFT-MB@HSA. MD simulations have confirmed the occurrence of this process, which might hinder the formation of triplet species in the protein-bound metabolite. Since phenolate-like excited species exhibit much higher fluorescence yields and longer lifetimes than GFT@HSA, this might have consequences in the photosensitizing potential of GFT-MB, which can be anticipated to be higher than that of GFT.

Data availability

All details about the experimental and computational data related with this article are included in the Experimental Section of this manuscript. Additional spectroscopic and theoretical results are provided in the ESI.†

Author contributions

Research was conceived by all authors. Experiments were performed by L. T., M. O and E. L., with the aid of C. G.-B., I. A and I. V. The research was supervised by C. G.-B., I. A., I. V. and M. A. M. All authors contributed to the writing of the manuscript and ESI.†

Conflicts of interest

There are no conflicts to declare.

Acknowledgements

Financial support from the Spanish Ministry of Science and Innovation (RYC-2015-17737, BEAGAL 18/00211, PID2020-115010RB-I00/AEI/10.13039/501100011033, FPU19/00048, PID2019-105512RB-I00/AEI/10.13039/501100011033), the Xunta de Galicia (ED431C 2021/29), the Centro singular de investigación de Galicia accreditation 2019–2022 (ED431G 2019/03), and the European Regional Development Fund (ERDF) is gratefully acknowledged. All authors are grateful to the Centro de Supercomputación de Galicia (CESGA) for use of the Finis Terrae computer.

References

1 M. Gonçalo, in *Contact Dermatitis*, ed. J. D. Johansen, Springer-Verlag, Berlin, 2011, ch. 18, pp. 361–376.
2 K. R. Stein and N. S. Scheinfeld, *Expert Opin. Drug Saf.*, 2007, **6**, 431–443.
3 J. Kowalska, J. Rok, Z. Rzepka and D. Wrzesniok, *Pharmaceuticals*, 2021, **14**, 723.
4 I. Vayá, V. Lhiaubet-Vallet, M. C. Jimenez and M. A. Miranda, *Chem. Soc. Rev.*, 2014, **43**, 4102–4122.
5 M. H. Cohen, G. A. Williams, R. Sridhara, G. Chen and R. Pazdur, *Oncologist*, 2003, **8**, 303–306.
6 J. G. Paez, P. A. Jänne, J. C. Lee, S. Tracy, H. Greulich, S. Gabriel, P. Herman, F. J. Kaye, N. Lindeman, T. J. Boggon, K. Naoki, H. Sasaki, Y. Fujii, M. J. Eck, W. R. Sellers, B. E. Johnson and M. Meyerson, *Science*, 2004, **304**, 1497–1500.
7 P. Cohen, D. Cross and P. A. Janne, *Nat. Rev. Drug Discovery*, 2021, **20**, 551–569.
8 L. Huang, S. Jiang and Y. Shi, *J. Hematol. Oncol.*, 2020, **13**, 143.
9 C. Pottier, M. Fresnais, M. Gilon, G. Jerusalem, R. Longuespee and N. E. Sounni, *Cancers*, 2020, **12**, 731.
10 R. Thomas and Z. Weihua, *Front. Oncol.*, 2019, **9**, 800.
11 D. Veale, T. Ashcroft, C. Marsh, G. J. Gibson and A. L. Harris, *Br. J. Cancer*, 1987, **55**, 513–516.
12 L. Tamarit, M. El Ouardi, I. Andreu, I. Vayá and M. A. Miranda, *Chem. Sci.*, 2021, **12**, 12027–12035.
13 J. T. Hartmann, M. Haap, H.-G. Kopp and H.-P. Lipp, *Curr. Drug Metab.*, 2009, **10**, 470–481.
14 T. P. Selvam and P. V. Kumar, *Res. Pharm.*, 2011, **1**, 1–21.
15 G. García-Laínez, I. Vayá, M. P. Marín, M. A. Miranda and I. Andreu, *Arch. Toxicol.*, 2021, **95**, 169–178.
16 I. Vayá, I. Andreu, E. Lence, C. González-Bello, M. C. Cuquerella, M. Navarrete-Miguel, D. Roca-Sanjuan and M. A. Miranda, *Chem.–Eur. J.*, 2020, **26**, 15922–15930.
17 I. Andreu, E. Lence, C. Gonzalez-Bello, C. Mayorga, M. C. Cuquerella, I. Vayá and M. A. Miranda, *Front. Pharmacol.*, 2020, **11**, 576495.
18 Y. Toyama, J. Ueyama, H. Nomura, I. Tsukiyama, H. Saito, T. Hisada, K. Matsuura and T. Hasegawa, *Anticancer Res.*, 2014, **34**, 2283–2290.
19 A. Spitaleri and W. Rocchia, in *Biomolecular Simulations in Structure-Based Drug Discovery*, ed. F. L. Gervasio and V. Spiwok, Wiley-VCH, Weinheim, Germany, 2019, pp. 29–39.
20 R. Pérez-Ruiz, E. Lence, I. Andreu, D. Limones-Herrero, C. González-Bello, M. A. Miranda and M. C. Jiménez, *Chem.–Eur. J.*, 2017, **23**, 13986–13994.
21 G. Jones, P. Willett, R. C. Glen and R. Taylor, *J. Mol. Biol.*, 1997, **267**, 727–748.
22 P. A. Zunszain, J. Ghuman, T. Komatsu, E. Tsuchida and S. Curry, *BMC Struct. Biol.*, 2003, **3**, 6.
23 D. A. Case, R. M. Betz, D. S. Cerutti, T. E. Cheatham, T. A. Darden, R. E. Duke, T. J. Giese, H. Gohlke, A. W. Goetz, N. Homeyer, S. Izadi, P. Janowski, J. J. Kaus, A. Kovalenko, T. S. Lee, S. LeGrand, P. Li, C. Lin, T. Luchko, R. Luo, B. Madej, D. Mermelstein, K. M. M. Merz, G. Monard, H. Nguyen, H. Nguyen, I. Omelyan, A. Onufriev, D. R. R. Roe, A. Roitberg, C. Sagui, C. L. Simmerling, W. M. Botello-Smith, J. Swails, R. Walker, J. Wang, R. M. Wolf, X. Wu, L. Xiao and P. A. Kollman, *Amber*, University of California, San Francisco, CA, USA, 2016.

© 2022 The Author(s). Published by the Royal Society of Chemistry

24 W. L. DeLano, *The PyMOL Molecular Graphics System*, DeLano Scientific LLC, Palo Alto, CA, 2008, 2021, **http://www.pymol.org/**.
25 B. R. Miller 3rd, T. D. McGee Jr, J. M. Swails, N. Homeyer, H. Gohlke and A. E. Roitberg, *J. Chem. Theory Comput.*, 2012, **8**, 3314–3321.
26 M. Montalti, A. Credi, L. Prodi and M. T. Gandolfi, *Handbook of Photochemistry*, CRC Press, Taylor and Francis Group, Boca Raton, FL, 2006.
27 C. Ruckebusch, M. Sliwa, P. Pernot, A. de Juan and R. Tauler, *J. Photochem. Photobiol., C*, 2012, **13**, 1–27.
28 G. Cosa and J. C. Scaiano, *Photochem. Photobiol.*, 2004, **80**, 159–174.
29 M. S. Baptista, J. Cadet, P. Di Mascio, A. A. Ghogare, A. Greer, M. R. Hamblin, C. Lorente, S. C. Nunez, M. S. Ribeiro, A. H. Thomas, M. Vignoni and T. M. Yoshimura, *Photochem. Photobiol.*, 2017, **93**, 912–919.
30 D. I. Pattison, A. S. Rahmanto and M. J. Davies, *Photochem. Photobiol. Sci.*, 2012, **11**, 38–53.
31 T. Peters, in *All about Albumin - Biochemistry, Genetics, and Medical Applications*, Elsevier, Academic Press, San Diego, 1995, ch. 3, pp. 76–132.
32 A. Z. Weller, *Phys. Chem.*, 1982, **133**, 93–98.
33 A. Harriman, *J. Phys. Chem.*, 1987, **91**, 6102–6104.
34 C.-Y. Lu and Y.-Y. Liu, *Biochim. Biophys. Acta*, 2002, **1571**, 71–76.
35 I. Vayá, I. Andreu, V. T. Monje, M. C. Jimenez and M. A. Miranda, *Chem. Res. Toxicol.*, 2016, **29**, 40–46.
36 **https://pubchem.ncbi.nlm.nih.gov/compound/Gefitinib**.
37 A. Albert and J. N. Phillips, *J. Chem. Soc.*, 1956, 1294–1304.
38 T. Peters, in *Advances in Protein Chemistry*, Academic Press, New York, 1985, vol. 37, pp. 161–245.
39 C. Y. Huang, *Methods Enzymol.*, 1982, **87**, 509–525.
40 T. Wybranowski, M. Cyrankiewicz, B. Ziomkowska and S. Kruszewski, *Biosystems*, 2008, **94**, 258–262.
41 T. Itoh, Y. Saura, Y. Tsuda and H. Yamada, *Chirality*, 1997, **9**, 643–649.
42 M. Z. Kabir, W.-V. Tee, S. B. Mohamad, Z. Alias and S. Tayyab, *RSC Adv.*, 2016, **6**, 91756–91767.
43 J. Li, J. Brahmer, W. Messersmith, M. Hidalgo and S. D. Baker, *Invest. New Drugs*, 2006, **24**, 291–297.
44 J. R. Lakowicz, *Principles of Fluorescence Spectroscopy*, Plenum Press, New York, 3rd edn, 2006.
45 M. Lukeman and P. Wan, *J. Am. Chem. Soc.*, 2002, **124**, 9458–9464.
46 P. Bonancia, I. Vayá, D. Markovitsi, T. Gustavsson, M. C. Jimenez and M. A. Miranda, *Org. Biomol. Chem.*, 2013, **11**, 1958–1963.
47 X. Chen, D. S. Larsen, S. E. Bradforth and I. H. van Stokkum, *J. Phys. Chem. A*, 2011, **115**, 3807–3819.
48 G. Rabbani and S. N. Ahn, *Int. J. Biol. Macromol.*, 2019, **123**, 979–990.
49 J. Wang, W. Wang, P. A. Kollman and D. A. Case, *J. Mol. Graphics Modell.*, 2006, **25**, 247–260.
50 J. Wang, R. M. Wolf, J. W. Caldwell, P. A. Kollman and D. A. Case, *J. Comput. Chem.*, 2004, **25**, 1157–1174.

(cc) BY-NC

© 2022 The Author(s). Published by the Royal Society of Chemistry

Free Radical Biology and Medicine 194 (2023) 42–51

Contents lists available at ScienceDirect

Free Radical Biology and Medicine

journal homepage: www.elsevier.com/locate/freeradbiomed

Singlet oxygen and radical-mediated mechanisms in the oxidative cellular damage photosensitized by the protease inhibitor simeprevir

Guillermo Garcia-Lainez [a,1], Meryem El Ouardi [b,c,1], Alejandro Moreno [a], Emilio Lence [d], Concepción González-Bello [d], Miguel A. Miranda [b,c,**], Inmaculada Andreu [b,c,*]

[a] Instituto de Investigación Sanitaria (IIS) La Fe, Hospital Universitari i Politècnic La Fe, Avenida de Fernando Abril Martorell 106, 46026, Valencia, Spain
[b] Departamento de Química-Instituto de Tecnología Química UPV-CSIC. Universitat Politècnica de València, Camino de Vera s/n, 46022, Valencia, Spain
[c] Unidad Mixta de Investigación UPV- IIS La Fe, Hospital Universitari i Politècnic La Fe, Avenida de Fernando Abril Martorell 106, 46026, Valencia, Spain
[d] Centro Singular de Investigación en Química Biolóxica e Materiais Moleculares (CiQUS), Departamento de Química Orgánica, Universidade de Santiago de Compostela, Jenaro de la Fuente s/n, 15782, Santiago de Compostela, Spain

ARTICLE INFO

Keywords:
Antiviral agent
Binding to proteins
Cellular photo(geno)toxicity
Photodamage to biomolecules
Triplet excited state

ABSTRACT

Hepatitis C, a liver inflammation caused by the hepatitis C virus (HCV), is treated with antiviral drugs. In this context, simeprevir (SIM) is an NS3/4A protease inhibitor used in HCV genotypes 1 and 4. It is orally administered and achieves high virological cure rates. Among adverse reactions associated with SIM treatment, photosensitivity reactions have been reported. In the present work, it is clearly shown that SIM is markedly phototoxic, according to the *in vitro* NRU assay using BALB/c 3T3 mouse fibroblast. This result sheds light on the nature of the photosensitivity reactions induced by SIM in HCV patients, suggesting that porphyrin elevation in patients treated with SIM may not be the only mechanism responsible for SIM-associated photosensitivity. Moreover, lipid photoperoxidation and protein photooxidation assays, using human skin fibroblasts (FSK) and human serum albumin (HSA), respectively, reveal the capability of this drug to promote photodamage to cellular membranes. Also, DNA photo lesions induced by SIM are noticed through comet assay in FSK cells. Photochemical and photobiological studies on the mechanism of SIM-mediated photodamage to biomolecules indicate that the key transient species generated upon SIM irradiation is the triplet excited state. This species is efficiently quenched by oxygen giving rise to singlet oxygen, which is responsible for the oxidation of lipids and DNA (Type II mechanism). In the presence of HSA, the photobehavior is dominated by binding to site 3 of the protein, to give a stable SIM@HSA complex. Inside the complex, quenching of the triplet excited state is less efficient, which results in a longer triplet lifetime and in a decreased singlet oxygen formation. Hence, SIM-mediated photooxidation of the protein is better explained through a radical (Type I) mechanism.

1. Introduction

Hepatitis C virus (HCV) infection is a health service problem of the first magnitude in Europe and especially in the Mediterranean countries, where prevalence rates are in the range 1–3% [1–3]. Moreover, hepatitis C can lead to liver cirrhosis and liver cancer, being a leading cause of liver transplantation [4].

Simeprevir (SIM) is an NS3/4A protease inhibitor for use in HCV genotypes 1 and 4. It is orally administered and achieves high virological cure rates. Moreover, it has a favorable tolerability profile when used in combination with peginterferon-alfa plus ribavirin or with sofosbuvir [5–8].

Recently, it has been reported that SIM is an especially promising drug for treating COVID-19 because it potently reduces SARS-CoV-2 viral load by multiple orders of magnitude [9,10]. In this context, the viral protease inhibitors nelfinavir and simeprevir revealed good plasma exposures and based on their described mode of action, they may inhibit SARS-CoV-2 directly [11]. Therefore, SIM could prevent coronavirus

* Corresponding author. Departamento de Química-Instituto de Tecnología Química UPV-CSIC. Universitat Politècnica de València, Camino de Vera s/n, 46022, Valencia, Spain.
** Corresponding author. Departamento de Química-Instituto de Tecnología Química UPV-CSIC. Universitat Politècnica de València, Camino de Vera s/n, 46022, Valencia, Spain.
E-mail addresses: mmiranda@qim.upv.es (M.A. Miranda), iandreur@qim.upv.es (I. Andreu).
[1] These authors equally contributed to the work.

https://doi.org/10.1016/j.freeradbiomed.2022.11.006
Received 29 July 2022; Received in revised form 4 October 2022; Accepted 6 November 2022
Available online 12 November 2022
0891-5849/© 2022 The Author(s). Published by Elsevier Inc. This is an open access article under the CC BY-NC license (http://creativecommons.org/licenses/by-nc/4.0/).

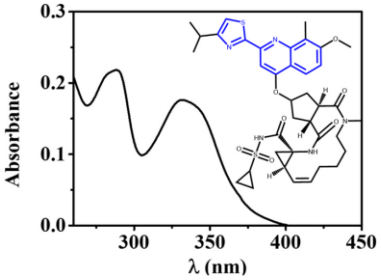

Fig. 1. Absorption spectrum of SIM in PBS. Inset: Chemical structure of SIM.

from replicating and might help in Covid-19 treatment.

The most commonly occurring adverse events associated with SIM treatment are rash, itching, sun sensitivity, muscle pain, shortness of breath, and nausea [5,12–14]. In particular, photosensitivity reactions have been reported in phase III studies [15]. Moreover, dermatological side-effects could be a problem in the management of SIM administration, and pharmacokinetic analysis is a valuable tool in a "real-life" clinical setting. In a previous study, it has been evaluated a possible relationship between plasma levels and the onset of skin complaints. With regard to this, SIM plasma concentrations were significantly related to dermatological side effects at early time points and the best predictive factor for skin symptoms was simeprevir concentrations at one week. Photosensitive condition (grade-1 sunburn) was found after the first month [16].

In this context, SIM is associated with phototoxicity, but there is no clear evidence for an increased risk of keratinocyte carcinoma [17]. Thus, SIM would act as a light-activated photosensitizer triggering a cascade of chemical events that may finally result in important biological disorders. This damage would occur by direct modification of biomolecules (isomerization, bond breaking, oxidation, etc.) or through the involvement of free radical intermediates, including singlet oxygen. As a result, cell constituents such as unsaturated lipids, proteins, or bases of nucleic acids can be altered. In this situation, if the repair mechanisms are not efficient, there can be irreversible lesions.

Given the above, a better understanding of the photodermatologic adverse reactions of SIM, based on a thorough photochemical and photobiological mechanistic study is necessary.

With this background, the aim of the present work is to investigate the direct photodamage to cells induced by SIM itself, using a methodology previously set up in our group to study photosensitivity reactions [18–21]. This makes sense since SIM displays a significant absorption band in the UVA region, which is an active fraction of solar light able to produce photosensitivity disorders. As shown in Fig. 1, the spectrum has two maxima centered at 288 nm and 332 nm that correspond to the thiazole-quinoline chromophore (Fig. 1). After light absorption by SIM, highly reactive intermediates could be formed including organic radicals and reactive oxygen species (ROS). Short-lived transients of these types could be in the origin of the clinically observed photosensitivity reactions.

2. Material and methods

2.1. General

Experimental descriptions such as chemicals and reagents, irradiation equipment, spectroscopic measurements, cell culture conditions, data analysis and statistics are provided in the supplementary material.

2.2. Laser flash photolysis

Laser flash photolysis (LFP) measurements were performed using a pulsed Nd:YAG L52137 V LOTIS TII laser at 355 nm as the excitation wavelength (Sp Lotis Tii, Minsk, Belarus). The LFP equipment consisted of a pulsed laser, a 77 250 Oriel monochromator, and an oscilloscope DP04054 Tektronix. The single pulses were ~10 ns of duration, and the energy was ~12 mJ/pulse. For processing, the output signal from the oscilloscope was transferred to a personal computer. The measurements were recorded under aerated atmosphere, or in the case of triplet excited state decays, the solutions were deaerated by bubbling nitrogen (15 min). The absorbance of the samples was adjusted at ~0.30 at 355 nm and the rate constant of triplet excited state quenching by oxygen (k_q) was determined using the Stern–Volmer equation (eq. (1)).

$$\frac{1}{\tau}=\frac{1}{\tau_0}+k_q\,[O_2] \qquad \text{eq.1}$$

Where τ and τ_0 are the lifetime of transient species with and without quencher (O_2), respectively.

For the rate constant of triplet excited state quenching by 2-methyl-cyclohexa-2,5-dienecarboxyl acid (MBA), the following Stern–Volmer equation (eq. (2)) was used:

$$\frac{1}{\tau}=\frac{1}{\tau_q}+k_q\,[MBA] \qquad \text{eq.2}$$

Where τ and τ_q are the lifetime of transient species in the presence and absence of MBA, respectively. Concentrations between 0.1 and 3 mM were used for MBA.

The rate constant of triplet excited state quenching by lapatinib (LAP) was calculated using the next Stern–Volmer equation (eq. (3)):

$$\frac{1}{\tau}=\frac{1}{\tau_q}+k_q\,[LAP] \qquad \text{eq.3}$$

Where τ and τ_q are the lifetime of transient species in the presence and absence of LAP, respectively. Concentrations up to 3 mM were used for the quencher.

Singlet oxygen ($^1O_2$, $^1\Delta g$) species was detected by NIR emission upon excitation with the Nd:YAG L52137 V LOTIS TII laser at 355 nm in aerated atmosphere. The absorbance of samples was adjusted at ~0.55 at 355 nm and decay traces were recorded at 1274 nm. Tetramethyl-*p*-benzoquinone (DQ) was used as a standard with a $^1O_2$ quantum yield (Φ_Δ) in MeCN, *ca.* 0.89 [22]. The Φ_Δ of SIM was calculated following equation (4).

$$\Phi_\Delta^{SIM}=\Phi_\Delta^{DQ}\times\frac{A_{SIM}}{A_{DQ}}\times\frac{I_{MeCN}}{I_i} \qquad \text{eq.4}$$

Where Φ_Δ^{DQ} is the quantum yield of the standard (DQ), A_{SIM} and A_{DQ} are the absorbances of SIM and DQ, I_{MeCN} and I_i the refractive index of acetonitrile and the sample solvent, respectively.

All transient absorption experiments were performed in PBS, MeOH or MeCN at room temperature.

2.3. *In vitro* 3T3 neutral red uptake (NRU) phototoxicity test

The *in vitro* 3T3 NRU phototoxicity assay was basically performed according to the OECD Guideline 432 [23] as described in Garcia-Lainez et al. [19]. As positive and negative control were selected chlorpromazine (CPZ) and sodium dodecyl sulphate (SDS), respectively. In brief, two 96-well plates were seeded at a density of 2.5×10^4 cells/well. Then, serial dilutions of the drug ranging from 100 μM to 0.25 μM were added to each plate. After 1 h incubation at 37 °C in dark conditions, one plate was irradiated with a non-cytotoxic UVA light dose of 5 J/cm^2 whereas the other one was kept in the dark. Once UVA irradiation finished, culture medium was replaced, and plates were incubated overnight. Next day, 50 μg/mL neutral red solution was added into each well and incubated for 2 h at 37 °C. Cells were then washed once with PBS. In order to extract neutral red from lysosomes, 100 μL of desorption

solution (50% distilled water, 49.5% absolute ethanol and 0.5% acetic acid) was added per well. Absorbance was measured at 550 nm on a Synergy H1 microplate reader. Dose-response curves were established for each compound to determine the concentration producing a 50% decrease in the neutral red uptake (IC50) in dark and UVA light conditions by non-lineal regression methods using the Graph Pad 5.0 software. Finally, photoirritant factor (PIF) values were calculated according to equation (5).

$$PIF = \frac{IC50\ DARK}{IC50\ UVA\ LIGHT} \quad \text{eq.5}$$

As stated in the OECD Guideline 432, a compound is labeled as "non-phototoxic" when PIF is < 2, "probably phototoxic" if PIF is between 2 and 5 and "phototoxic" if PIF is > 5.

2.4. Photoinduced lipid peroxidation assay

The compound 4,4-difluoro-5-(4-phenyl-1,3-butadienyl)-4-bora-3a,4a-diaza-*s*-indacene-3-undecanoic acid, also known as C11-Bodipy 581/591 is a molecular probe to assess lipid peroxidation in living cells that shifts its fluorescence from red to green when the molecule is oxidized [24,25]. To this end, human skin fibroblast cells (FSK) were seeded in two 12-well-plates at a density of 6.0×10^4 cells/well. Next day, the cells were treated with 5 μM of SIM solutions and incubated for 30 min in dark conditions. After incubation, one plate was irradiated (2.5 J/cm^2) and the other one was kept in dark conditions as negative control. Cells were labeled with the lipid peroxidation sensor C11 Bodipy 581/591 (10 μM) for 30 min at 37 °C. Finally, the cultures were visualized using a Leica DMI 4000B fluorescence microscope in sequential mode to detect both the non-oxidized (red fluorescence, λ_{exc} 535 nm) and the oxidized (green fluorescence, λ_{exc} 490 nm) forms of the probe. To determine the extent of lipid peroxidation in each condition, the fluorescence intensity ratio (FIR) was calculated following equation (6) using the Image-J software image analyzer (NIH).

$$FIR = \frac{I\ red\ fluorescence}{I\ green\ fluorescence} \quad \text{eq.6}$$

2.5. Protein photooxidation assay

Protein oxidation photoinduced by SIM, using human serum albumin (HSA) as model, was evaluated as previously described [26] with minor modifications. In brief, HSA solutions in PBS were prepared (5 mg/mL, 1 mg/sample) and incubated with increasing concentrations of SIM (1 μM, 2.5 μM and 5 μM) at room temperature for 1 h. Then, mixtures were irradiated with a UVA dose of 10 J/cm^2 or maintained in dark conditions as control of the assay. Immediately after irradiation, the extent of HSA oxidation was measured in all experimental conditions spectrophotometrically by derivatization with 2,4-dinitrophenylhydrazine (DNPH). Thus, 200 μL of DNPH (10 mM) was added and incubated at room temperature for 1 h to form stable dinitrophenyl hydrazone adducts. Proteins were then precipitated with a 20% (v/v) trichloroacetic (TCA) solution and incubated on ice for 15 min. Afterwards, pellets were washed twice with ethanol/ethyl acetate 1:1 (v/v) containing 20% TCA to remove the unbound DNPH and dried at 60 °C. The adducts were resolubilized in 100 μL of 6 M guanidine-hydrochloride at 4 °C by overnight incubation. Finally, absorbance at 375 nm was recorded using the Synergy H1 microplate reader and the HSA oxidation degree was expressed as nmol of carbonyl moiety per mg protein.

2.6. Assessment of DNA photodamage

2.6.1. Plasmid DNA photosensitized damage

Samples containing 250 ng of supercoiled circular DNA (pBR322, 4361 base pairs) in the presence or absence of SIM (100 μM) in PBS supplemented with 1 mg/mL HSA were prepared. Mixtures were irradiated as described above using a UVA light dose of 15 J/cm^2 (30 min). Immediately, loading buffer (0.25% bromophenol blue and 30% glycerol, in water) was added to each sample. Moreover, to characterize chemical modifications towards DNA bases promoted by the drug, samples were digested after irradiation with an excess of Endo V, Endo III or FPG (0.5 U) at 37 °C for 1 h and then, loading buffer was added as detailed above. Afterwards, all samples were loaded on a 0.8% agarose gel containing SYBR® Safe as nucleic acid stain. Electrophoresis run was carried out in TAE Buffer (0.04 M Tris-acetate, 1 mM EDTA) at 100 V for 2 h. DNA bands were visualized with the Gel Logic 200 Imaging System (Kodak) and densitometry was quantified with the Image-J software. Thus, the relative percentage of the nicked relaxed form (Form II) of the pBR322 plasmid was calculated for each condition.

2.6.2. 8-Oxo-dG quantitation assay as a biomarker of oxidative DNA damage

FSK cells were seeded in two 24-well plates at a density of 7.5×10^5 cells/well. Next day, they were treated with 2.5 μM SIM solutions for 30 min at 4 °C in dark conditions. After incubation, one plate was irradiated (2.5 J/cm^2) and the other one was kept in darkness. Afterwards, cells were harvested from the plates and then genomic DNA extraction was performed in all samples according to the manufacturer's protocol. DNA samples were quantified using a Nanodrop 2000c (Thermo Scientific). Later, samples containing 2 μg DNA (100 ng/mL) were digested with DNase I (1 U) at 37 °C for 1 h, followed by alkaline phosphatase incubation (1 U) at 37 °C for 1 h. Lastly, 8-oxo-dG concentration was determined in all samples by a competitive Elisa assay following the manufacturer's instructions. Data were expressed in nanomoles of 8-oxo-dG formed by interpolating the sample concentrations from the standard curve.

2.6.3. Nuclear DNA photodamage by comet assay

Single cell gel electrophoresis assay (comet assay) was carried out as previously described [20] in order to detect strand breaks and alkaline labile sites on nuclear DNA. Briefly, FSK cells were trypsinized, resuspended in cold PBS and allowed to stand for 2 h at 4 °C for repairing the damage generated after detachment with trypsin. Then, two 24-well plates were seeded at a density of 1.0×10^5 cells/well and treated with 2.5 μM SIM solution for 30 min at 4 °C in dark conditions. In this assay, CPZ (10 μM) was selected as the photogenotoxic reference compound. After incubation, one plate was placed in the photoreactor to irradiate the cells (2.5 J/cm^2) and the other one was kept in dark conditions as negative control. Immediately, irradiated and non-irradiated cells were harvested from the plates. Then, 100 μL of each sample was homogenized with 100 μL of 1% low melting point agarose solution and mixtures were placed forming drops (2.0×10^4 cell/gel) onto Trevigen® treated slides, allowing their jellification. Next, slides were immediately immersed in a container filled with lysis buffer (2.5 M NaCl, 0.1 M Na_2EDTA, 0.01 M Tris, 1% Triton X-100) and incubated overnight at 4 °C. In DNA recovery experiments to promote intrinsic cellular DNA-repair mechanisms, slides were maintained in DMEM medium at 37 °C for 20 h, and then lysed as stated above. Next day, all slides were transferred to a Trevigen® comet assay electrophoresis tank and covered with cold alkaline buffer (0.2 M NaOH, 1 mM EDTA, pH $\geq$ 13) and let during 40 min for DNA unwinding at 4 °C. Afterwards, the electrophoresis was carried out at 21 V (1 V/cm) for 30 min at 4 °C. Once the electrophoresis finished, the slides were washed twice in PBS for 5 min. DNA was fixed by two subsequent incubations with 70% and 100% ethanol solutions. Then, DNA was stained with SYBR Gold® (1:10.000 dilution in TE buffer – Tris-HCl 10 mM pH 7.5, EDTA 1 mM) for 30 min at 4 °C in darkness. Finally, the slides were air-dried and kept in dark conditions. Comet nucleoids and tails were visualized using a Leica DMI 4000B fluorescence microscope (λ_{exc} 490 nm). At least 100 cells/sample were analyzed to determine DNA damage. The percentage of DNA damage of each sample was calculated with the visual scoring of at least 100 DNA comets using the subsequent formula [27]: [(Nclass 0 comets

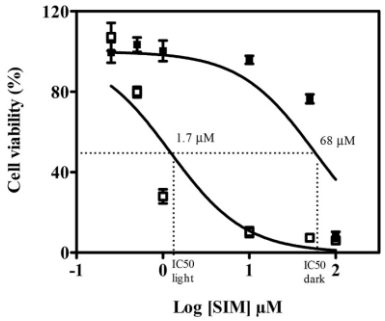

Fig. 2. 3T3 NRU phototoxicity assay. Dose-response curves for cell viability of BALB/c 3T3 mouse fibroblast cells treated with SIM in Dark (■) and UVA light conditions (5 J/cm^2, □). Data are the mean ± SD from four independent experiments.

× 0) + (Nclass 1 comets × 1) + (Nclass 2 comets × 2) + (Nclass 3 comets × 3) + [(Nclass 4 comets × 4) + (Nclass 5 comets × 5) + (Nclass 6 comets × 6)]/6, where class 0 comets indicate comets with no DNA damage and class 6 comets indicate comets with maximum DNA damage.

2.7. Molecular docking

These studies were carried out using our previously reported protocol for lapatinib against HSA [28,29]. The protein coordinates obtained in the crystal structure of HSA in complex with hemin and myristic acid (PDB entry 1O9X) [30] and the docking program GOLD version 2020.2.0 [31] were used.

2.8. Molecular dynamics simulation studies

The highest score solution obtained by docking was subjected to 100 ns of dynamic simulation, which was performed as previously described by us for trifusal [32]. The cpptraj module in AMBER 17 was used to analyze the trajectories and to calculate the rmsd of the protein and the ligand during the simulation [33]. The molecular graphics program PyMOL (DeLano) was employed for visualization and depicting enzyme structures.

3. Results and discussion

3.1. Phototoxicity of simeprevir

Sunlight activated drug can trigger a cascade of chemical events that finally result in important biological disorders including phototoxicity. This process can be evaluated through *in vitro* 3T3 NRU phototoxicity test following the OECD Guideline 432 [23].

3.1.1. In vitro 3T3 neutral red uptake (NRU) phototoxicity assay

Assessment of the phototoxicity of simeprevir (SIM) was performed according to the *in vitro* 3T3 NRU phototoxicity test [23]. To achieve this goal, BALB/c 3T3 mouse fibroblast cells were treated with increasing concentrations of SIM and cell viability was analyzed by neutral red as vital stain. From dose-response curves, half maximal inhibitory concentrations (IC50) under dark or UVA light conditions were estimated. As shown in Fig. 2, SIM displayed a cytotoxic profile in dark conditions with an IC50 in the micromolar range (68 µM). It is noteworthy that its toxicity was enhanced in combination with UVA light (IC50 = 1.7 µM). Consequently, phototoxicity was determined by the calculation of the photoirritant factor value (PIF), defined as the ratio between the IC50 under dark and light conditions. The PIF obtained was around 40, which is 8-fold higher than the cut-off value for a phototoxic compound as stated by the OECD guide [23]. Remarkably, this result sheds light on the nature of the photosensitivity reactions induced by SIM in HCV patients. So, it confirms that porphyrin elevation in patients treated with SIM may not be the only mechanism responsible for SIM-associated photosensitivity. Thus, phototoxic mechanisms usually comprise the generation of cellular oxidative stress that promotes damage to biomolecules such as lipids, proteins and DNA, leading ultimately to cell

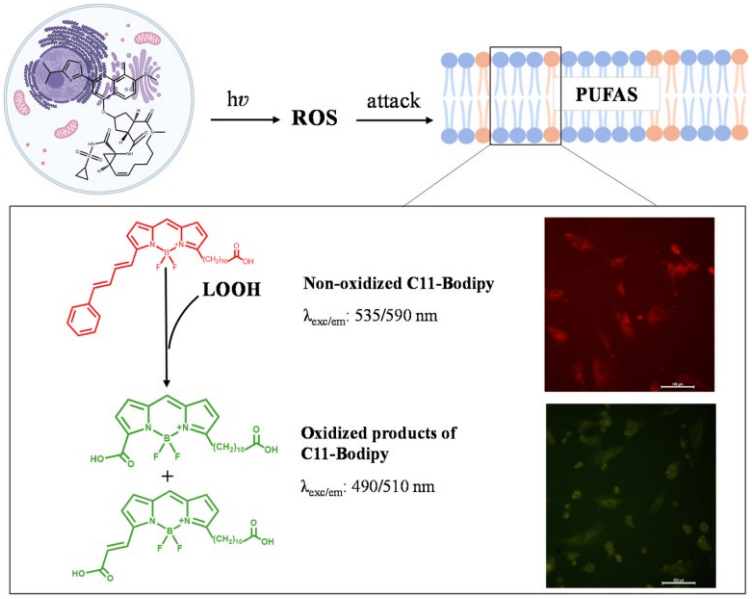

Scheme 1. Lipid photoperoxidation detection in human skin fibroblast cells (FSK) by C11-BODIPY (581/591) probe.

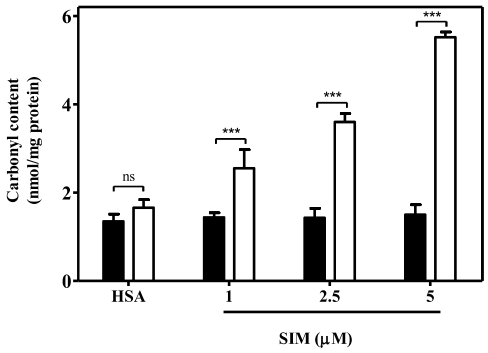

Fig. 3. Protein photooxidation promoted by SIM in human serum albumin (HSA) model. HSA was irradiated (10 J/cm^2) in the presence of SIM and the carbonyl content was evaluated spectrophotometrically by monitoring its carbonyl moiety after derivatization with 2,4-dinitrophenylhydrazine (λ = 375 nm). Non-irradiated solutions were analyzed as control (■). Data are the mean ± SD of three independent experiments. Asterisks show significant differences by the Student's t-test compared to dark conditions (***$p < 0.001$, ns: non-significant).

death [34].

3.1.2. Lipid and protein photooxidation

As SIM displays highly lipophilic properties, membrane components (lipids and proteins) could be the targets for its phototoxicity. To confirm this hypothesis, first, lipid photoperoxidation was investigated using the fluorescent reporter C11-Bodipy 581/591, which consists of a boron dipyrromethene difluoride core attached to a fatty acid tail and a phenyl moiety connected by a diene bond (Scheme 1). This assay is based on the capability of this molecular probe to penetrate the plasmatic membrane and to shift the fluorescence emission upon its oxidation from red (λ_{exc} 535 nm), which corresponds to the native structure of the probe, to green (λ_{exc} 490 nm), attributed to its oxidation products. As it is described in the literature, the Bodipy is exclusively sensitive to free radical species generated from hydroperoxides, but not to hydroperoxides *per se* [35,36]. With this aim, FSK cells were treated with SIM (5 μM) and subsequently irradiated (2.5 J/cm^2) or maintained in darkness as control. Then, cells were stained with the C11-Bodipy 581/591 after irradiation to rule out direct photochemical reactions between the drug and the probe, and finally, they were visualized under the fluorescent microscope. The images shown in Scheme 1 and Fig. S1 revealed an increase in the green fluorescence intensity (oxidized product) in UVA light conditions in comparison with non-irradiated treated cells, indicating a high degree of lipid peroxidation. By contrast, lipid peroxidation in non-treated cells was negligible. Accordingly, the quantitative analysis showed a significant reduction of the red to green fluorescence intensity ratio (Fig. S1). These results support that lipid membrane is indeed a potential target for SIM phototoxicity.

Moreover, protein photooxidation was investigated using the human serum albumin (HSA) as protein model. Thus, solutions of HSA containing SIM were UVA irradiated with a dose of 10 J/cm^2 and afterwards, the carbonyl moiety, as a biomarker of protein oxidation, was quantified by the derivatization method using 2,4-dinitropheynlhydrazine (DNPH). According to Fig. 3, irradiated HSA without treatment showed similar concentration of carbonyl moiety as non-irradiated HSA, indicating the suitability of the dose selected. Interestingly, for SIM, a dose-dependent enhancement of the carbonyl content of HSA was observed after irradiation in comparison with non-irradiated mixtures, reaching *ca.* 3-fold increase at 5 μM. This assay confirmed the capability

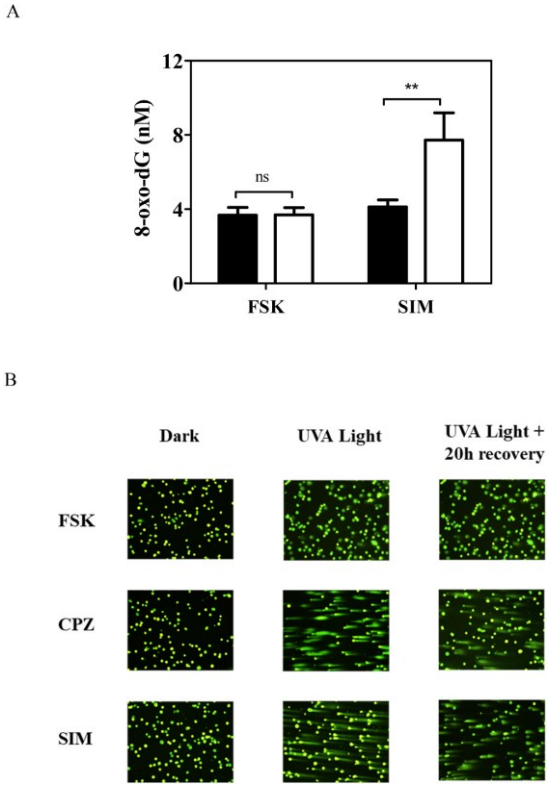

Fig. 4. Cellular photogenotoxicity. (A) 8-oxo-dG formation in human skin fibroblasts cells (FSK) upon SIM treatment. FSK cells alone (FSK) or treated with SIM (2.5 μM) were kept in Dark (■) or irradiated with a 2.5 J/cm^2 UVA dose (□). Then, genomic DNA was isolated and the oxidative biomarker 8-oxo-dG was quantified by means of colorimetric antibody Elisa assay. Asterisks indicate significant differences relative to the FSK cells in dark conditions by the Student's *t*-test (**p < 0.01; ns: non-significant). (B) Fluorescence microscopy images of SIM alkaline comet assay experiments. FSK cells alone (FSK) or treated with SIM (2.5 μM) or CPZ (10 μM) as the reference photogenotoxic compound were kept on dark conditions (Dark), irradiated with 2.5 J/cm^2 UVA dose (UVA Light) or irradiated with 2.5 J/cm^2 UVA dose followed by 20 h of cell recover (UVA Light + 20 h recovery time). Images are representative of three independent experiments.

of SIM to promote photooxidation in cellular membranes. According to our previous work on photosensitizing drugs [20,37], this type of HSA modification could involve a type I (radicals) or type II (singlet oxygen) photooxidation of the redox-active amino acid residues.

3.1.3. Photogenotoxicity

In order to evaluate whether DNA, another biomolecule target of oxidative damage, could also be involved in the SIM phototoxicity mechanism, a screening was performed using plasmid DNA alone or in combination with different repair enzymes (Endo V, Endo III and FPG). Actually, the electrophoresis agarose gel shown in Fig. S2 highlighted that SIM can indeed promote DNA photodamage mainly through purine base oxidation, as revealed using the FPG repair enzyme. Among all the oxidatively generated lesions into the cellular DNA by UVA light, one of the most frequent is the guanine residue oxidation at C8 to generate 8-oxo-7,8-dihydro-2′-deoxyguanosine (8-oxo-dG) [38]. This lesion can result highly mutagenic if it is not efficiently repaired, since this

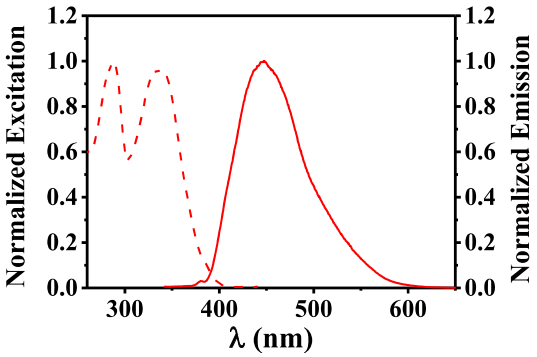

Fig. 5. Normalized fluorescence emission spectrum recorded at λ_{exc} = 332 nm (solid red) and normalized fluorescence excitation spectrum registered at λ_{max} = 447 nm (dashed red) of SIM in PBS solution. (For interpretation of the references to color in this figure legend, the reader is referred to the Web version of this article.)

modified base can pair in the double helix not only with cytosine but also with adenine. Having established the ability of SIM to induce purine oxidation in a cell-free system, in a further step, this process was also assessed in a cellular environment. Hence, the photogeneration of this biomarker in FSK cells DNA by SIM was studied. To achieve this goal, FSK were incubated with SIM and then, exposed to a UVA dose of 2.5 J/cm^2. After irradiation, genomic DNA was isolated and quantified by UV spectroscopy (λ=260 nm). Then, a competitive Elisa assay was carried out to detect the presence of 8-oxo-dG in samples. Thus, as shown in Fig. 4A, the 8-oxo-dG in SIM-treated cells was found to be twice higher than in non-treated cells. This agrees with the important role of guanine base oxidation in the photogenotoxicity of SIM.

In an attempt to describe in detail other types of DNA photolesions induced by SIM, comet assay experiments were subsequently carried out. This assay identifies combined DNA damage consisting of single-strand breaks, double-strand breaks, and alkali-labile sites on individual cells [39]. In this assay, after treatment with the drug and UVA irradiation, FSK cells were embedded in agarose mini-gels on slides and subjected to lysis. Afterwards, electrophoresis was run to allow damaged DNA fragments migrating out of the cell nucleus, forming a comet tail. Upon SYBR® Gold staining, comets and tail were examined under the fluorescence microscope and nuclear DNA damage was calculated using a visual score system of 6 different categories [27]. Moreover, chlorpromazine (CPZ), a well-known drug with photogenotoxic properties was used as positive control [18]. The results shown in Fig. 4B and Fig. S3 indicated that SIM generated significant DNA damage to cellular DNA (around 40%), to a lesser extent than CPZ. Additionally, another set of experiments were performed to investigate the capability of FSK cells to repair that DNA photodamage generated. For this purpose, cells upon treatment were incubated for different time periods up to 20 h and the remaining DNA damage was determined in the same way described above. As shown in Fig. 4B, in contrast to CPZ, it is noteworthy that photosensitized DNA was not repaired within 20 h of recovery. This is in agreement with the possibility of SIM to generate mutations in the DNA and ultimately, these could lead to photocarcinogenesis.

3.2. Photophysical studies

Drug photosensitizing potential can be associated with damage to biomolecules involving ROS or radicals arising from excited states [40]. Here, in order to gain insight into the phototoxicity of SIM, in a further step, photophysical studies combining fluorescence, transient absorption and time-resolved near-infrared luminescence spectroscopy were carried out.

3.2.1. Emission spectra

The steady-state fluorescence spectrum of SIM in PBS solution showed a maximum centered at λ_{max} = 447 nm (Fig. 5). The SIM fluorescence quantum yield (Φ_F) was determined using anthracene in ethanol as standard (Φ_F = 0.27) and it resulted to be *ca.* 0.05 [41] (Fig. S4). Similar results were obtained using MeCN and MeOH, as model solvent, mimicking lipophilic environment present in the cellular milieu (Table S1). In addition, singlet excited state energy (E_s) was calculated from the intersection between the normalized excitation and emission spectra (Fig. 5) and it was found to be 73.3 kcal/mol.

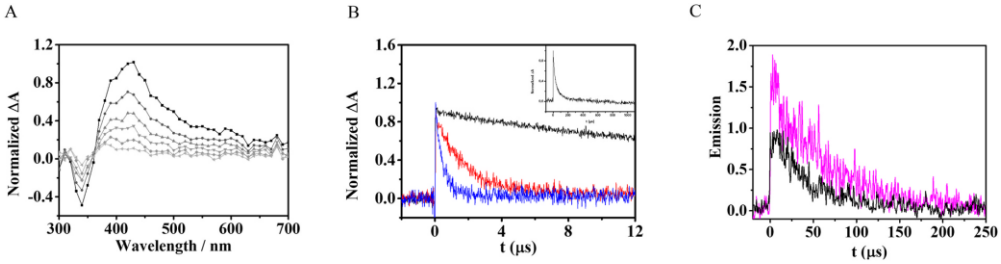

Fig. 6. Laser Flash Photolysis experiments. (A) Normalized transient absorption spectra (from 1 to 14 μs) for simeprevir in aerated PBS solution after the 355 nm laser excitation. (B) Normalized decay traces of the triplet generated in PBS solution of SIM monitored at 410 nm in deaerated (**black**), aerated (**red**) and oxygen saturated atmosphere (**blue**). Inset: normalized decay trace of SIM in deaerated PBS solution on a longer time-scale. (C) Kinetic traces for $^1O_2$ signals after laser pulse (λ_{exc} = 355 nm) for SIM in deuterated water (black). Tetramethyl-*p*-benzoquinone (DQ) in MeCN (**magenta**) was the reference of the study (Φ_Δ *ca.* 0.89). (For interpretation of the references to color in this figure legend, the reader is referred to the Web version of this article.)

3.2.2. Laser flash photolysis

To detect reactive species generated by the excitation of SIM living in the microsecond time-scale, laser flash photolysis (LFP) technique was employed. Thus, upon excitation of the drug at 355 nm in aerated PBS solution, the transient absorption spectrum exhibited a band with a maximum centered at 410 nm (Fig. 6A). In addition, from decay traces analysis at 410 nm it was determined the lifetime (τ_T) that was *ca.* 44 μs (Fig. 6B), and the triplet energy (E_T) obtained from phosphorescence measurements was approximately 59.6 kcal//mol (Fig. S5). Moreover, to characterize this transient species, oxygen quenching experiments were carried out in PBS solutions of the drug. As shown in Fig. 6B, this

species was efficiently quenched by molecular oxygen with a quenching rate constant (k_q) of 1.71 × 10^9 M^{-1} s^{-1} calculated by a mono-exponential decay function (Fig. S6). This indicates that the transient species peaking at 400 nm corresponds to a triplet excited state. For MeOH and MeCN solvents, comparable results were obtained (Fig. S7 and Table S1). Significant triplet production is indicative of potential photobiological damage since this excited state has a biradical character and is the precursor of the reactive species, including free radicals and ROS.

It is well known that a drug triplet excited state is usually regarded as the key precursor that sensitizes molecular singlet oxygen ($^1O_2$ or $^1\Delta g$) formation through an electronic energy transfer process in Type II oxidative mechanism reactions [42]. Furthermore, $^1O_2$ can promote extensive oxidative damage to biomolecules inside cells, including lipid peroxidation through hydroperoxide formation [24,25], protein oxidation [43], and DNA nucleosides (such as guanine) oxidation to obtain the final oxidized base (8-oxo-dG) [44]. Bearing in mind from cellular experiments that SIM promoted lipid photoperoxidation, protein photooxidation and 8-oxo-dG formation in DNA, the photogeneration of $^1O_2$ by this drug should be expected. To confirm this hypothesis, it is interesting to perform time-resolved near-infrared emission studies upon 355 nm excitation of SIM. Thus, formation of this species was detected by time-resolved measurements of the luminescence at 1270 nm in deuterated aqueous solution (Fig. 6C). To determine the SIM singlet oxygen quantum yield (Φ_Δ), tetramethyl-*p*-benzoquinone (DQ), was employed as reference (Φ_Δ *ca.* 0.89 in MeCN) [22]. As expected, SIM displayed ability to generate $^1O_2$ with a $\Phi_\Delta = 0.56$. The SIM Φ_Δ in organic solvents was also measured and they were found to be *ca.* 0.82 and 1 for MeOH and MeCN, respectively (Fig. S8 and Table S1). As regards the singlet oxygen lifetime (τ_Δ) in deuterated aqueous solution, it was measured using DQ as standard and was 65 μs. Likewise, the lifetime obtained for SIM was *ca.* 40 μs (Fig. 6C).

3.3. Molecular basis of simeprevir interaction with biomolecules

The photophysical studies of SIM are in good agreement with the cellular photodamage pointed out for this drug. This could be the origin of the oxidative stress to biomolecules, thus leading to undesired effects of phototoxicity and photogenotoxicity. Therefore, in view of the capability of SIM to form triplet excited species, it was considered convenient to perform additional experiments regarding SIM interaction with biomolecules, such as lipids, proteins and DNA. Thus, drug-lipid interaction studies were carried out by quenching experiments using 2-methylcyclohexa-2,5-dienecarboxylic acid (MBA) as a lipid model, which contains double allylic hydrogens and is an appropriate probe for studying the reactivity of lipids with photosensitizing drugs [43]. As a result, triplet decay traces were obtained in deaerated acetonitrile solutions of SIM after the addition of increasing amounts of MBA. As shown in Fig. 7, the SIM triplet species was quenched by MBA with a k_q of only 1.68 × 10^6 M^{-1} s^{-1} (Fig. 7, inset). Moreover, SIM-HSA (1:1) interaction did indeed occur, and the complex displayed a higher triplet lifetime ($\tau_T = 17$ μs) than the free drug in solution ($\tau_T = 1.7$ μs) under aerated atmosphere (Fig. S9 and Table S2). By contrast, τ_T of SIM in the presence of calf thymus DNA (ctDNA) remained unchanged; hence the complexation of SIM with DNA was not supported experimentally (Fig. S9 and Table S2).

Overall, the above data indicate that triplet quenching by oxygen, leading to singlet oxygen, is the predominating process in the presence of lipids and DNA; hence, photosensitized oxidation of these biomolecules occurs by a Type II mechanism. Conversely, in the presence of protein a complex is formed where the triplet state is protected from quenching by oxygen, and the formation of singlet oxygen is much less efficient (Table S2). Accordingly, under these conditions, oxidation of the proteins must proceed via a Type I mechanism. In view of the importance of SIM complexation to proteins, a detailed docking and molecular dynamics simulation study was performed on the binding process.

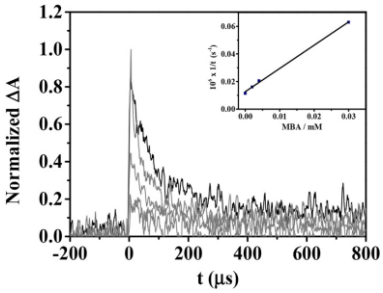

Fig. 7. Triplet decays at 410 nm for SIM alone (**black**) or in the presence of increasing amount of MBA (0–3 mM) (**gray**). Inset: Stern-Volmer plot for ^{3}SIM* quenching by MBA.

3.3.1. Binding of simeprevir to human serum albumin

To understand the underlying molecular basis of the interaction of SIM with the HSA protein, as well as its photophysical properties experimentally observed upon binding, docking and molecular dynamics (MD) simulation studies were performed.

In this context, HSA is a carrier protein with a large capacity for transporting a wide variety of endo and exogenous ligands structurally very diverse. It has three main recognition binding sites, namely domains I–III, each one divided into two sub-domains A and B, with a very different recognition pattern. Hence our first efforts were directed at identifying the SIM recognition domain of HSA, which was achieved by competition studies using three compounds whose protein binding sites are known, specifically ibuprofen (IBP) (site 1, sub-domain IIA), warfarin (WAF) (site 2, sub-domain IIIA) and lapatinib (LAP) (site 3, sub-domain IB) [45,33]. Thus, increasing amounts of the ligand were added to aerated solutions of 10 μM SIM-HSA (1:1), and transient decays were monitored at 410 nm. Under these conditions, a decrease of the transient species lifetime was only observed in parallel with the addition of LAP concomitantly with an increase of the free SIM fraction (k_q of *ca.* 5.1 × 10^9 $M^{-1}s^{-1}$), ergo, this can be correlated with the complexation of SIM to the binding site 3 of HSA (Fig. 8A and Fig. S10). Thus, to determine the binding constant of SIM to HSA, the decays monitored at 410 nm were fitted using a two-phase exponential function. Then, using the preexponential factors values, both the percentage of free and bound SIM were calculated (Fig. S10). The half-maximal effective concentration (EC50) for lapatinib was obtained by interpolation from competition displacement curve and it resulted to be 7 μM (Fig. 8B). Moreover, the binding constant of lapatinib to HSA (K_B) was taken from the literature and it was 1.24 × 10^5 M^{-1} (at 303 K) [46]. As the SIM concentration used was 10 μM, the relationship between the binding constants was found to be 0.7 and therefore the K_B of SIM resulted to be 0.87 10^5 M^{-1}.

Based on the results obtained with the afore-mentioned competition studies, through which site 3 (sub-domain IB) was identified as the SIM binding pocket, the three-dimensional structure of HSA in complex with myristic acid and hemin (PDB ID 1O9X) was selected for docking. Among the variety of HSA crystal structures available, this PDB was chosen because hemin, as well as LAP, binds to sub-domain IB. It is important to note that this protein undergoes significant conformational changes, especially in domains I and III, both located at the vertices of its general V-shaped structure, to maximize its interaction with ligands [47]. Hence, choosing a PDB with a ligand already arranged in the same pocket becomes relevant for achieving optimal docking results. In addition, performing MD simulation studies on the proposed ligand@HSA binary complex, through which the intrinsic plasticity of the protein is considered, is also relevant for achieving reliable and

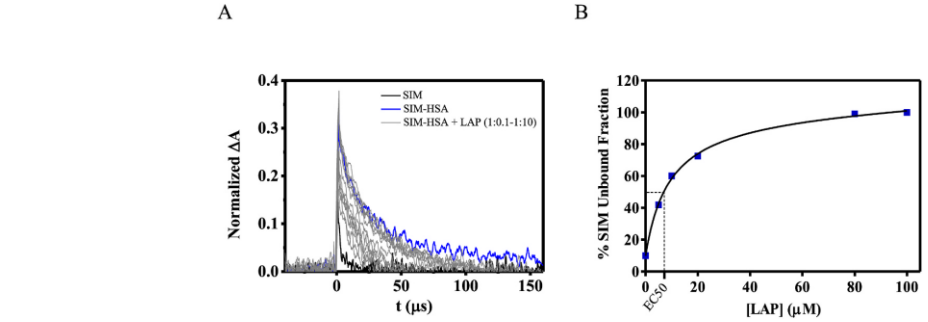

Fig. 8. A) Decays at 410 nm for SIM (**black**), SIM-HSA alone (**blue**) or in the presence of increasing amounts of LAP (**gray**). B) Percentage of unbound SIM fraction at 1:1 SIM-HSA ratio in the presence of increasing amounts of LAP. (For interpretation of the references to color in this figure legend, the reader is referred to the Web version of this article.)

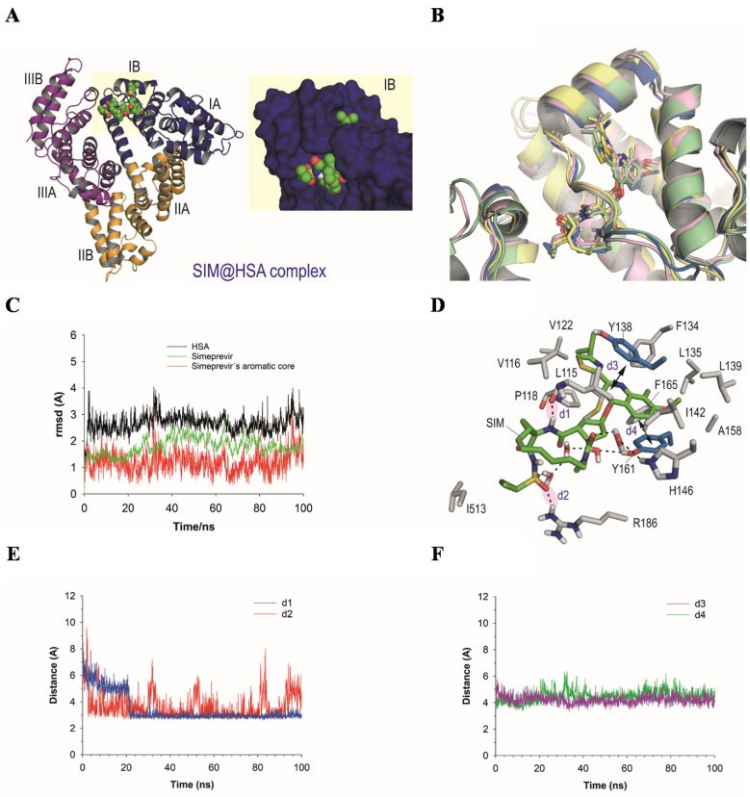

Fig. 9. SIM binding mode against HSA protein obtained by MD simulation studies. (A) General and close views of the SIM@HSA binary complex. Snapshot taken after 80 ns of simulation. The domains (I–III) and sub-domains (A, B) of the protein are shown in blue, orange, and purple colors, respectively, and labeled. Note how SIM (spheres) is deeply buried in sub-domain IB (site 3) of the protein. (B) Superposition of several snapshots taken during the whole simulation. Note how the ligand is very stable within the pocket as no relevant changes are identified. (C) RMSD plots for the protein backbone (Cα, C, O and N atoms), SIM and its quinoline core (average values of 1.8 Å, 2.7 Å and 1.2 Å, respectively). (D) Main contacts of SIM with the protein. Relevant hydrogen bonding interactions (black dashed lines) and protein residues are shown and labeled. (E) Stability of the hydrogen bonding interactions. Variation of the relative distances between the NH amide group of the ligand and the main carbonyl group of L115 (d1) and the oxygen atom of the sulfonamide group of the ligand and the guanidinium group of R186 (d2). (F) Stability of the π-π stacking interactions. Variation of the relative distances between the center of mass of quinoline ring of SIM and residues Y138 (d3, average distance of 4.2 Å) and Y161 (d4, average distance of 4.6 Å) during the whole simulation. For calculating average distances, only the last 80 ns of simulation are considered. (For interpretation of the references to color in this figure legend, the reader is referred to the Web version of this article.)

realistic results. To this end, the highest score solution obtained by docking and the protein were immersed in a truncated octahedron of water molecules obtained with the molecular mechanics force field Amber and subjected to 100 ns of simulation.

Our simulation studies revealed that SIM would be buried in sub-domain IB of the protein through its quinoline group allocating its macrocyclic moiety pointing towards the interface between domains I and III (Fig. 9A). The ligand proved to be very stable in the pocket, since no significant changes were observed, either in the binding conformation of the ligand or that of the SIM@HSA binary complex, during the whole simulation (Fig. 9B). Thus, the analysis of the root-mean-square deviation (rmsd) of the protein backbone (Cα, C, O and N atoms), the ligand and its quinoline group afforded low average values of 1.8 Å, 2.7 Å and 1.2 Å, respectively, for the whole simulation (Fig. 9C). SIM would be anchored to sub-domain IB through two hydrogen bonding interactions, one between the amide NH group in the SIM's macrocycle moiety and the main carbonyl group of L115, and the second between its sulfonamide group and the guanidinium group of

R186 (Fig. 9D). The latter interactions proved to be very stable, showing average distances during the last 80 ns of simulation of 3.0 Å and 3.5 Å, respectively (Fig. 9E). Additional hydrogen bonds are also established by the ligand through both faces of its macrocycle moiety with the side chains of residues H146 and Y161 via a network of water molecules. The arrangement of the ligand is further stabilized within the pocket by a strong sandwich-like π-π stacking interaction with residues Y138 and Y161 that trap the quinoline moiety between them. The latter interaction revealed to be strong as no significant variation of the relative distances between the center of mass of the quinoline ring and the phenol groups in Y138 and Y161 was observed during the whole simulation (Fig. 9F). Finally, the ligand is further stabilized in subdomain IB thanks to a set of hydrophobic interactions with the nonpolar residues of the pocket, specifically L115, V116, P118, V122, F134, L135, L139, I142, A158 and I513.

4. Conclusions

Comprehensive photochemical and photobiological studies reveal SIM-mediated photodamage to biomolecules, leading ultimately to cell death. This drug displays a significant absorption band in the active region of solar light, so it may trigger photosensitivity reactions. The key transient species generated upon SIM irradiation is the triplet excited state, characterized by its absorption band at 400 nm. This species is efficiently quenched by oxygen giving rise to singlet oxygen, which is responsible for the oxidation of lipids and DNA (Type II mechanism). In the presence of HSA, the photobehavior is dominated by binding to site 3 of the protein, to give a stable SIM@HSA complex. Inside the complex, quenching of the triplet excited state is less efficient, which results in a longer triplet lifetime and in a deceased singlet oxygen formation. Hence, SIM-mediated photooxidation of the protein occurs through a radical (Type I) mechanism.

In summary, the obtained results confirm that porphyrin elevation in patients treated with SIM may not be the only mechanism responsible for SIM-associated clinical photosensitivity. Instead, photochemical mechanisms may operate leading to the generation of cellular oxidative stress associated with damage to lipids, proteins and DNA, ultimately resulting in cellular photo(geno)toxicity. These considerations have to be taken into account by the doctors to have a better knowledge of the SIM photoinduced adverse effects before prescribing to patients and, thus, give them photoprotection guidelines such as the employment of sunscreens.

Acknowledgments

Financial support from the Spanish Ministry of Science and Innovation [PID2020-115010RB-I00/AEI/10.13039/501100011033 (I.A), PID2019-105512RB-I00/AEI/10.13039/501100011033 (CG-B) and FPU predoctoral fellowship for M. El O.], Axencia Galega de Innovación (2020-PG067, CG-B), the Xunta de Galicia [ED431C 2021/29 and the Centro singular de investigación de Galicia accreditation 2019–2022 (ED431G 2019/03),], and the European Regional Development Fund (ERDF) is gratefully acknowledged. All authors are grateful to the Centro de Supercomputación de Galicia (CESGA) for use of the Finis Terrae computer.

Appendix A. Supplementary data

Supplementary data to this article can be found online at https://doi.org/10.1016/j.freeradbiomed.2022.11.006.

References

[1] F. Negro, A. Alberti, The global health burden of hepatitis C virus infection, Liver Int. 31 (Suppl 2) (2011) 1–3.
[2] W.H.O. Hepatitis, C Fact Sheet No 164, 2013 [cited 2021 2 December].
[3] A. Petruzziello, et al., Global epidemiology of hepatitis C virus infection: an up-date of the distribution and circulation of hepatitis C virus genotypes, World J. Gastroenterol. 22 (34) (2016) 7824–7840.
[4] T.I. Lin, et al., In vitro activity and preclinical profile of TMC435350, a potent hepatitis C virus protease inhibitor, Antimicrob. Agents Chemother. 53 (4) (2009) 1377–1385.
[5] M. Sanford, Simeprevir: a review of its use in patients with chronic hepatitis C virus infection, Drugs 75 (2) (2015) 183–196.
[6] R. Flisiak, J. Pogorzelska, M. Flisiak-Jackiewicz, Hepatitis C: efficacy and safety in real life, Liver Int. 37 (Suppl 1) (2017) 26–32.
[7] Z. Mariño, et al., High efficacy of Sofosbuvir plus Simeprevir in a large cohort of Spanish cirrhotic patients infected with genotypes 1 and 4, Liver Int. 37 (12) (2017) 1823–1832.
[8] M.V. Lin, R. Chung, Recent FDA approval of sofosbuvir and simeprevir. Implications for current HCV treatment, Clin Liver Dis (Hoboken) 3 (3) (2014) 65–68.
[9] H.S. Lo, et al., Simeprevir potently suppresses SARS-CoV-2 replication and synergizes with remdesivir, ACS Cent. Sci. 7 (5) (2021) 792–802.
[10] F.S. Hosseini, M. Amanlou, Anti-HCV and anti-malaria agent, potential candidates to repurpose for coronavirus infection: virtual screening, molecular docking, and molecular dynamics simulation study, Life Sci. 258 (2020), 118205.
[11] M.A. Bakowski, et al., Drug repurposing screens identify chemical entities for the development of COVID-19 interventions, Nat. Commun. 12 (1) (2021) 3309.
[12] Z.W. Eyre, A.M. Secrest, J.L. Woodcock, Photo-induced drug eruption in a patient on combination simeprevir/sofosbuvir for hepatitis C, JAAD Case Rep 2 (3) (2016) 224–226.
[13] C.L. Simpson, D. McCausland, E.Y. Chu, Photo-distributed lichenoid eruption secondary to direct anti-viral therapy for hepatitis C, J. Cutan. Pathol. 42 (10) (2015) 769–773.
[14] F. Borgia, et al., Mucocutaneous toxicity during simeprevir treatment for hepatitis C. A single institution, retrospective case series, Br. J. Clin. Pharmacol. 83 (5) (2017) 1152–1154.
[15] M.P. Manns, et al., Simeprevir with peginterferon/ribavirin for treatment of chronic hepatitis C virus genotype 1 infection: pooled safety analysis from Phase IIb and III studies, J. Viral Hepat. 22 (4) (2015) 366–375.
[16] L. Boglione, et al., Role of simeprevir plasma concentrations in HCV treated patients with dermatological manifestations, Dig. Liver Dis. 49 (6) (2017) 705–708.
[17] L.D. Crow, et al., Medications associated with increased risk of keratinocyte carcinoma, Dermatol. Clin. 37 (3) (2019) 297–305.
[18] F. Palumbo, et al., Enhanced photo(geno)toxicity of demethylated chlorpromazine metabolites, Toxicol. Appl. Pharmacol. 313 (2016) 131–137.
[19] G. Garcia-Lainez, et al., Photo(geno)toxicity changes associated with hydroxylation of the aromatic chromophores during diclofenac metabolism, Toxicol. Appl. Pharmacol. 341 (2018) 51–55.
[20] G. García-Laínez, et al., In vitro assessment of the photo(geno)toxicity associated with Lapatinib, a Tyrosine Kinase inhibitor, Arch. Toxicol. 95 (1) (2021) 169–178.
[21] L. Tamarit, et al., Photoprocesses of the tyrosine kinase inhibitor gefitinib: from femtoseconds to microseconds and from solution to cells, Chem. Sci. 12 (36) (2021) 12027–12035.
[22] I. Gutiérrez, S.G. Bertolotti, M.A. Biasutti, A.T. Soltermann, N.A. García, Quinones and hydroxyquinones as generators and quenchers of singlet molecular oxygen, Can. J. Chem. 75 (4) (1997) 423–428.
[23] OECD, Test No. 432, in: Vitro 3T3 NRU Phototoxicity Test, 2019.
[24] E.H. Pap, et al., Ratio-fluorescence microscopy of lipid oxidation in living cells using C11-BODIPY(581/591), FEBS Lett. 453 (3) (1999) 278–282.
[25] I.O.L. Bacellar, M.S. Baptista, Mechanisms of photosensitized lipid oxidation and membrane permeabilization, ACS Omega 4 (26) (2019) 21636–21646.
[26] G. Colombo, et al., A step-by-step protocol for assaying protein carbonylation in biological samples, J. Chromatogr., B: Anal. Technol. Biomed. Life Sci. 1019 (2016) 178–190.
[27] P. Møller, Assessment of reference values for DNA damage detected by the comet assay in human blood cell DNA, Mutat. Res. 612 (2) (2006) 84–104.
[28] I. Vaya, et al., Characterization of locally excited and charge-transfer states of the anticancer drug lapatinib by ultrafast spectroscopy and computational studies, Chemistry 26 (68) (2020) 15922–15930.
[29] I. Andreu, et al., Protein binding of lapatinib and its N- and O-dealkylated metabolites interrogated by fluorescence, ultrafast spectroscopy and molecular dynamics simulations, Front. Pharmacol. 11 (2020), 576495.
[30] P.A. Zunszain, et al., Crystal structural analysis of human serum albumin complexed with hemin and fatty acid, BMC Struct. Biol. 3 (1) (2003) 6.
[31] G. Jones, et al., Development and validation of a genetic algorithm for flexible docking11Edited by F. E. Cohen, J. Mol. Biol. 267 (3) (1997) 727–748.
[32] O. Molins-Molina, et al., Photobinding of triflusal to human serum albumin investigated by fluorescence, proteomic analysis, and computational studies, Front. Pharmacol. 10 (2019) 1028.
[33] D. Case, et al., Amber 2017, University of California, San Francisco, 2017.
[34] J. Cadet, K.J.A. Davies, Oxidative DNA damage & repair: an introduction, Free Radic. Biol. Med. 107 (2017) 2–12.
[35] G.P. Drummen, et al., C11-BODIPY(581/591), an oxidation-sensitive fluorescent lipid peroxidation probe: (micro)spectroscopic characterization and validation of methodology, Free Radic. Biol. Med. 33 (4) (2002) 473–490.
[36] M. Laguerre, J. Lecomte, P. Villeneuve, Evaluation of the ability of antioxidants to counteract lipid oxidation: existing methods, new trends and challenges, Prog. Lipid Res. 46 (5) (2007) 244–282.

[37] L. Tamarit, et al., Photoprocesses of the tyrosine kinase inhibitor gefitinib: from femtoseconds to microseconds and from solution to cells, Chem. Sci. 12 (36) (2021) 12027–12035.
[38] J. Bai, et al., Oxidation of 8-Oxo-7,8-dihydro-2'-deoxyguanosine leads to substantial DNA-histone cross-links within nucleosome core particles, Chem. Res. Toxicol. 31 (12) (2018) 1364–1372.
[39] A. Azqueta, A.R. Collins, The essential comet assay: a comprehensive guide to measuring DNA damage and repair, Arch. Toxicol. 87 (6) (2013) 949–968.
[40] K. Nakai, D. Tsuruta, What are reactive oxygen species, free radicals, and oxidative stress in skin diseases? Int. J. Mol. Sci. 22 (19) (2021).
[41] W.H. Melhuish, Quantum efficiencies of fluorescence of organic substances: effect of solvent and concentration of the fluorescent solute1, J. Phys. Chem. 65 (2) (1961) 229–235.
[42] S. Hackbarth, et al., New insights to primary photodynamic effects–Singlet oxygen kinetics in living cells, J. Photochem. Photobiol., B 98 (3) (2010) 173–179.
[43] M.J. Davies, Singlet oxygen-mediated damage to proteins and its consequences, Biochem. Biophys. Res. Commun. 305 (3) (2003) 761–770.
[44] M.S. Baptista, et al., Type I and type II photosensitized oxidation reactions: guidelines and mechanistic pathways, Photochem. Photobiol. 93 (4) (2017) 912–919.
[45] W.L. DeLano, The PyMOL Molecular Graphics System, 2002.
[46] M.Z. Kabir, et al., Characterization of the binding of an anticancer drug, lapatinib to human serum albumin, J. Photochem. Photobiol., B 160 (2016) 229–239.
[47] S. Curry, et al., Crystal structure of human serum albumin complexed with fatty acid reveals an asymmetric distribution of binding sites, Nat. Struct. Biol. 5 (9) (1998) 827–835.

frontiers | Frontiers in Pharmacology

TYPE Original Research
PUBLISHED 16 May 2024
DOI 10.3389/fphar.2024.1387057

Check for updates

OPEN ACCESS

EDITED BY
Nico P. E. Vermeulen,
VU Amsterdam, Netherlands

REVIEWED BY
Tomasz Fraczyk,
Polish Academy of Sciences, Poland
Yolanda Vida,
University of Malaga, Spain

*CORRESPONDENCE
Miguel A. Miranda,
mmiranda@qim.upv.es
Ignacio Vayá,
igvapre@qim.upv.es
Concepcion González-Bello,
concepcion.gonzalez.bello@usc.es

RECEIVED 16 February 2024
ACCEPTED 02 May 2024
PUBLISHED 16 May 2024

CITATION
Tamarit L, El Ouardi M, Lence E, Andreu I, González-Bello C, Miranda MA and Vayá I (2024), Modulation of the photobehavior of gefitinib and its phenolic metabolites by human transport proteins.
Front. Pharmacol. 15:1387057.
doi: 10.3389/fphar.2024.1387057

COPYRIGHT
© 2024 Tamarit, El Ouardi, Lence, Andreu, González-Bello, Miranda and Vayá. This is an open-access article distributed under the terms of the Creative Commons Attribution License (CC BY). The use, distribution or reproduction in other forums is permitted, provided the original author(s) and the copyright owner(s) are credited and that the original publication in this journal is cited, in accordance with accepted academic practice. No use, distribution or reproduction is permitted which does not comply with these terms.

Modulation of the photobehavior of gefitinib and its phenolic metabolites by human transport proteins

Lorena Tamarit[1,2], Meryem El Ouardi[1,2], Emilio Lence[3], Inmaculada Andreu[1,2], Concepcion González-Bello[3]*, Miguel A. Miranda[1,2]* and Ignacio Vayá[1,2]*

[1]Departamento de Química/Instituto de Tecnología Química UPV-CSIC, Universitat Politècnica de València, Valencia, Spain, [2]Unidad Mixta de Investigación UPV-IISLaFe, Hospital Universitari i Politècnic La Fe, Valencia, Spain, [3]Centro Singular de Investigación en Química Biolóxica e Materiais Moleculares (CiQUS), Departamento de Química Orgánica, Universidade de Santiago de Compostela, Santiago de Compostela, Spain

The photobiological damage that certain drugs or their metabolites can photosensitize in proteins is generally associated with the nature of the excited species that are generated upon interaction with UVA light. In this regard, the photoinduced damage of the anticancer drug gefitinib (GFT) and its two main photoactive metabolites GFT-M1 and GFT-M2 in cellular milieu was recently investigated. With this background, the photophysical properties of both the drug and its metabolites have now been studied in the presence of the two main transport proteins of human plasma, i.e., serum albumin (HSA) and α1-acid glycoprotein (HAG) upon UVA light excitation. In general, the observed photobehavior was strongly affected by the confined environment provided by the protein. Thus, GFT-M1 (which exhibits the highest phototoxicity) showed the highest fluorescence yield arising from long-lived HSA-bound phenolate-like excited species. Conversely, locally excited (LE) states were formed within HAG, resulting in lower fluorescence yields. The reserve was true for GFT-M2, which despite being also a phenol, led mainly to formation of LE states within HSA, and phenolate-like species (with a minor contribution of LE) inside HAG. Finally, the parent drug GFT, which is known to form LE states within HSA, exhibited a parallel behavior in the two proteins. In addition, determination of the association constants by both absorption and emission spectroscopy revealed that the two metabolites bind stronger to HSA than the parent drug, whereas smaller differences were observed for HAG. This was further confirmed by studying the competing interactions between GFT or its metabolites with the two proteins using fluorescence measurements. These above experimental findings were satisfactorily correlated with the results obtained by means of molecular dynamics (MD) simulations, which revealed the high affinity binding sites, the strength of interactions and the involved amino acid residues. In general, the differences observed in the photobehavior of the drug and its two photoactive metabolites in protein media are consistent with their relative photosensitizing potentials.

KEYWORDS

anticancer drugs, fluorescence, metabolites, molecular dynamics, protein binding constants

1 Introduction

The binding of drugs to plasma proteins is involved in the modulation of relevant processes including drug pharmacokinetics (*i.e.,* absorption, distribution, metabolism and elimination) and pharmacodynamics (pharmacological effects) (Krasner, 1972; Kragh-Hansen et al., 2002; Vuignier et al., 2010). This binding is usually reversible, with an equilibrium between bound and free drug. In this regard, it is commonly stated that only unbound drugs are pharmacologically and toxicologically active since they can cross membrane barriers to be distributed to tissues (Lindup and Orme, 1981). However, photochemically active drugs can induce damage to biomolecules after absorption of solar light, which is generally associated with phototoxicity and photoallergy (Quintero and

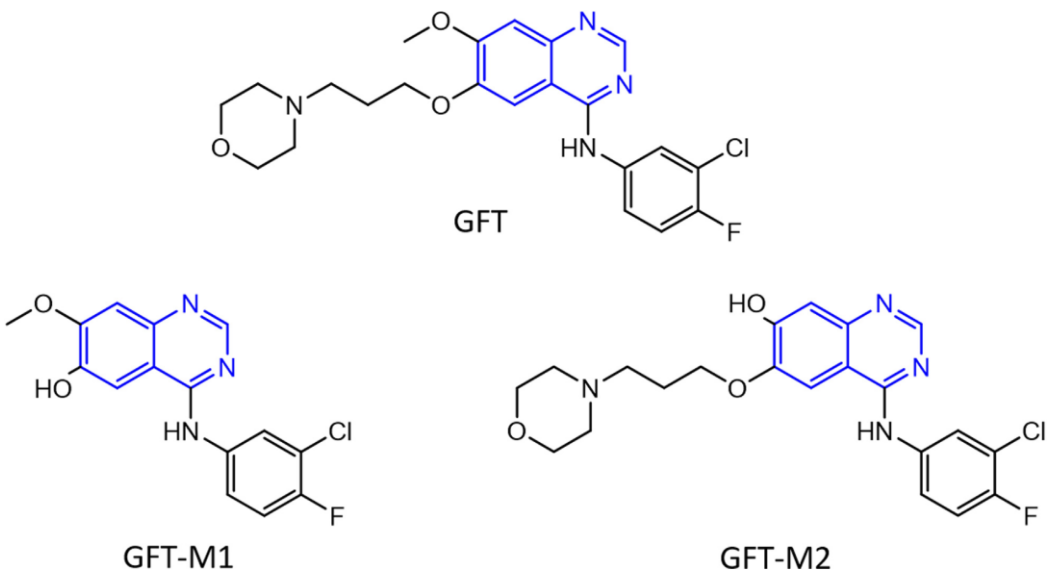

FIGURE 1
Chemical structure of gefitinib (GFT) and its *O*-desmorpholinopropyl and *O*-desmethyl metabolites GFT-M1 and GFT-M2, respectively. The quinazoline chromophore is highlighted in blue.

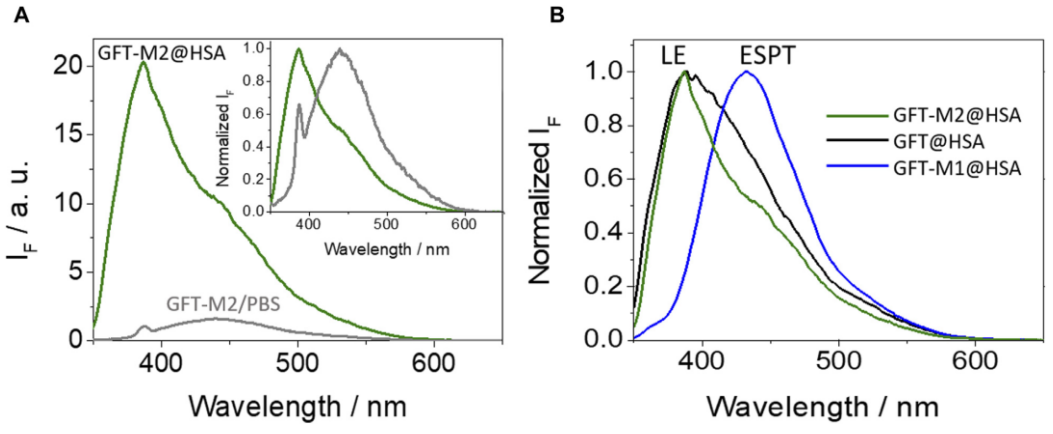

FIGURE 2
(A) Fluorescence spectra for GFT-M2 in PBS (gray) and for GFT-M2@HSA (green). The inset shows the normalized spectra. **(B)** Normalized fluorescence spectra for GFT-M2@HSA (green), GFT@HSA (black) and GFT-M1@HSA (blue). Measurements were performed at λ_{exc} = 340 nm in PBS; for ligand@HSA complexes, solutions were at 1:1 M ratio (10 μM).

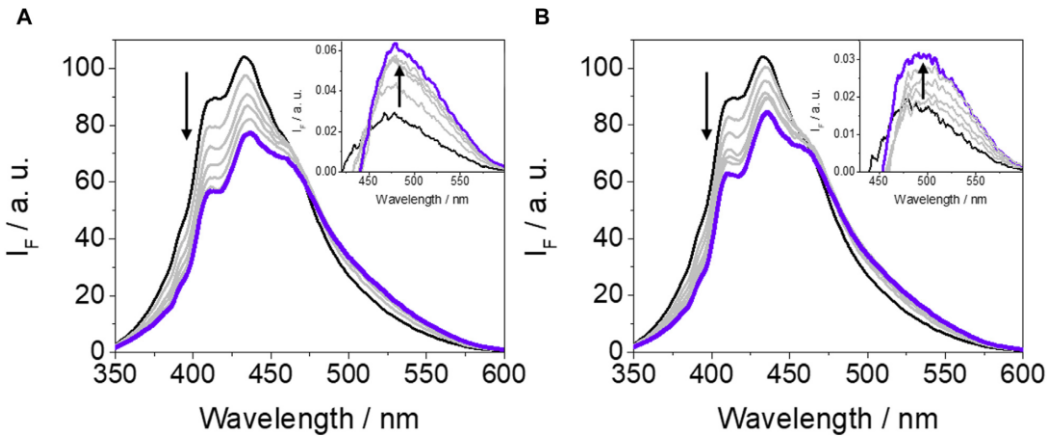

FIGURE 3
Fluorescence spectra of GFT-M2 after addition of increasing amounts of Tyr **(A)** or Trp **(B)**. All measurements were performed at metabolite:amino acid molar ratios of 1:50, 1:100, 1:150, 1:200, 1:250 and 1:300 after excitation at 340 nm in toluene. The concentration of GFT-M2 was maintained constant at 10 μM. The insets show the formation of a new band, which is associated with formation of phenolate-like species through interaction between hydrogen-bonded GFT-M2 and Tyr or Trp in the ground state; these bands were determined upon subtraction of the emission from excited GFT-M2 to those of GFT-M2/amino acid (Tyr or Trp) at the different molar ratios.

TABLE 1 Binding constants for GFT, GFT-M1 and GFT-M2 within HSA and HAG.

K_B/M^{-1}	HSA	HAG
GFT	$7.5 \pm 0.24 \times 10^4$	$1.2 \pm 0.08 \times 10^5$
GFT-M1	$1.2 \pm 0.06 \times 10^5$	$9.1 \pm 0.32 \times 10^4$
GFT-M2	$1.8 \pm 0.16 \times 10^5$	$1.5 \pm 0.05 \times 10^5$

Miranda, 2000; Stein and Scheinfeld, 2007; Vayá et al., 2014; Monteiro et al., 2016; Blakely et al., 2019; Kowalska et al., 2021). Hence, the interaction of photoactive compounds with plasma proteins must have a strong influence on drug biological effects, beyond the transport and the intrinsic photochemical properties associated with the chemical structure of the drug. In this context, drugs containing the quinazoline moiety (highlighted in blue in Figure 1) are known to produce photodermatosis (Selvam and Kumar, 2011).

The photosensitizing potential associated with this moiety is well exemplified by gefitinib (GFT), which is an orally active first-generation tyrosine kinase inhibitor (TKI) (Solassol et al., 2019; Huang et al., 2020; Pottier et al., 2020; Cohen et al., 2021) clinically used for the treatment of lung cancer and locally advanced or metastatic non-small cell lung cancer (Cohen et al., 2003; Paez et al., 2004). GFT is metabolized via CYP3A4 to form a variety of derivatives (Hartmann et al., 2009) including those shown in Figure 1, *O*-desmorpholinopropyl gefitinib (GFT-M1) and *O*-desmethyl gefitinib (GFT-M2), which have recently revealed to be biologically photoactive (El Ouardi et al., 2023). Lapatinib (LAP), which is other TKI currently used for the treatment of lung and breast cancers (Lin et al., 2008; Medina and Goodin, 2008; Lin et al., 2009), is also a relevant example. In both cases, both the parent drug and their photoactive metabolites can induce damage in cellular milieu (García-Laínez et al., 2021; Tamarit et al., 2021; El Ouardi et al., 2023); the associated mechanism is related with the excited species that are formed upon irradiation of the supramolecular drug or metabolite@protein complexes with UVA light (Andreu et al., 2020; Vayá et al., 2020; Tamarit et al., 2021; Tamarit et al., 2022).

Human serum albumin (HSA) and human α_1-acid glycoprotein (HAG) are the most abundant proteins in plasma. One of their main physiological functions is to transport a broad variety of drugs with sufficient affinity through the bloodstream for their selective delivery to specific targets (Trainor, 2007); generally, the binding affinity (K_B) is in the range of 10^4–10^6 M^{-1} (Kremer et al., 1988; Carter and Ho, 1994; Peters, 1995; Huang and Ung, 2013). In particular, HSA is the most abundant protein in blood plasma, and contains multiple binding sites, *i.e.,* stie I, II and II, where acidic, neutral, and basic drugs can interact (Sudlow et al., 1976; Zsila, 2013). As regards HAG, it is a highly glycosylated protein that contains multiple binding sites, but generally drugs bind almost exclusively to a large and flexible cavity (Kremer et al., 1988; Maruyama et al., 1990). Its concentration is much lower than that of HSA, but since it is an acute-phase protein, its serum levels can be increased in certain disease states including inflammation, depression and cancer (Kremer et al., 1988). In this context, it has been previously proposed that high concentration of HAG can affect the pharmacodynamics of some drugs *in vivo* (Yoo et al., 1996; Holladay et al., 1998; Gambacorti-Passerini et al., 2003; Trainor, 2007).

Recent publications about the photobehavior of GFT and GFT-M1 within HSA correlate their photophysical properties with their photosensitizing potential (Tamarit et al., 2021; Tamarit et al., 2022). In this regard, selective excitation of the protein-bound drug results in emission from locally excited (LE) singlet states; their main features are to display maximum fluorescence at wavelengths *ca.*

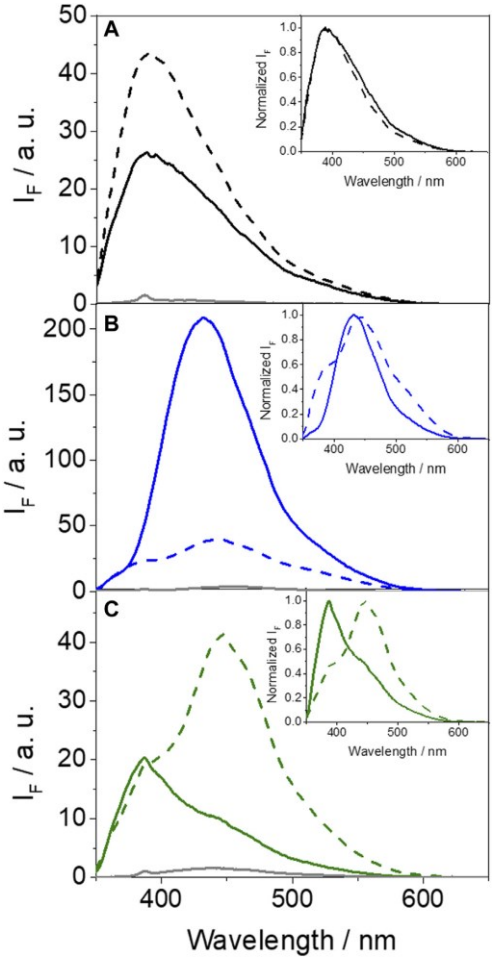

FIGURE 4
Fluorescence spectra at λ_{exc} = 340 nm in PBS for **(A)** GFT (gray), GFT@HSA (solid black) and GFT@HAG (dashed black), **(B)** GFT-M1 (gray), GFT-M1@HSA (solid blue) and GFT-M1@HAG (dashed blue), and **(C)** GFT-M2 (gray), GFT-M2@HSA (solid green) and GFT-M2@HAG (dashed green). The insets show the normalized spectra. For ligand@protein complexes, solutions were at 1:1 M ratio (10 μM).

390 nm with low quantum yields (ϕ_F ~ 0.02) and short lifetimes (τ_F ~ 1.3 ns). Noteworthy, the fluorescence profile of GFT@HSA is very similar to that observed in non-polar solvents such as cyclohexane, where formation of LE states has been demonstrated by means of ultrafast transient absorption spectroscopy. Concerning GFT-M1, although its fluorescence properties in organic solvents are comparable with those of GFT, remarkable differences are noticed after binding with HSA; here, excited state proton transfer (ESPT) to form phenolate-like species, which emit at longer wavelengths (λ_{max} ~ 430 nm) and higher τ_F values (~2.5 ns) than LE sates, is the predominant process (Tamarit et al., 2022). This result is supported by means of ultrafast spectroscopy and by molecular docking simulations. The photosensitizing damage from both GFT and GFT-M1 in the biological media is consistent with the involvement of a type I mechanism (Tamarit et al., 2021; Tamarit et al., 2022; El Ouardi et al., 2023).

In view of the importance of drug or metabolite@protein interactions, the binding of GFT and its two photoactive metabolites GFT-M1 and GFT-M2 with the main transport proteins in plasma has been investigated in the present work. To this end, spectroscopic techniques in the steady-state and time-resolved modes have been used. In this regard, fluorescence spectroscopy is a widely used analytical technique to study ligand@protein interactions due to its high sensitivity and capability to probe different microenvironments. Thus, the yield of transients formation in addition to their spectral profile and kinetics evolution may be strongly affected by the surroundings of the investigated ligand (*i.e.,* drug or metabolite) (Vayá et al., 2014). From the emission spectra and lifetimes of the excited species formed in the ligand@protein complexes, it has been possible to determine binding constants and the stoichiometry of the complex. In parallel, molecular dynamics (MD) simulations have also been done with the aim of investigating in atomic detail the binding of GFT, GFT-M1 and GFT-M2 within HSA and HAG, to achieve a better understanding of the experimental results. In this context, MD simulations has proven to be a powerful tool for studying the strength and conformational characteristics of the interactions of a drug with the amino acids located in the protein binding sites (Pérez-Ruiz et al., 2017; Spitaleri and Rocchia, 2019; Vayá et al., 2020). All these features are relevant since they can be directly connected with the photosensitizing potential recently reported for GFT and its metabolites GFT-M1 and GFT-M2 (El Ouardi et al., 2023).

2 Materials and methods

2.1 Chemicals and reagents

Gefitinib (GFT) and *O*-desmethyl gefitinib (GFT-M2) were purchased from Quimigen. *O*-Desmorpholinopropyl gefitinib (GFT-M1) was purchased from Fluorochem. *N*-Acetyl-L-tyrosine methyl ester (NAc-TyrMe), *N*-acetyl-L-tryptophan methyl ester (NAc-TrpMe), anthracene, human serum albumin (HSA) and α_1-acid glycoprotein from human plasma (HAG) were purchased from Sigma-Aldrich. PBS Buffer was prepared by dissolving phosphate-buffered saline tablets (Sigma) using ultrapure water from a Millipore (Milli-Q Synthesis) system. Spectrophotometric solvents (acetonitrile, 1,4-dioxane, toluene and cyclohexane) were obtained from Scharlab and used without further purification.

2.2 Spectroscopic measurements

UV absorption spectra were recorded in a JASCO V-760 spectrophotometer. The Job's plot analysis can be used to determine the stoichiometry of ligand@protein complexes by measuring the UV absorption spectra of mixtures containing different ligand@protein molar ratios that maintain the total

10.3389/fphar.2024.1387057

TABLE 2 Fluorescence properties of the protein-bound drug (or metabolite) complexes at λ_{exc} = 340 nm in PBS.

	HSA			HAG		
	λ_{max}/nm	ϕ_F	τ_F/ns	λ_{max}/nm	ϕ_F	τ_F/ns
GFT	390[a]	0.02[a]	1.3[a]	390	0.03	0.8
GFT-M1	432[b]	0.15[b]	2.5[b]	442 (390)[c]	0.04	1.6[d]
						τ_1 0.5 (28%)
						τ_2 3.1 (72%)
GFT-M2	388	0.01	1.0[d]	446 (388)[c]	0.03	1.7[d]
			τ_1 0.6 (75%)			τ_1 0.7 (35%)
			τ_2 4.9 (25%)			τ_2 4.1 (65%)

[a]Data from ref. 35.
[b]Data from ref. 36.
[c]Shoulders detected in the fluorescence spectra are shown between brackets. A one-exponential function was used to fit all the decay traces, except for *d*, where a mean lifetime was determined as $<\tau_F> = a_1\tau_1 + a_2\tau_2$; the τ_1 and τ_2 values, in addition with the weight of each component, are also shown.

molar concentration constant (Huang, 1982); in our case, eleven solutions with a total concentration of 20 μM in PBS were prepared varying the drug (or metabolite)@protein molar ratio: 100:0, 90:10, 80:20, 70:30, 60:40, 50:50, 40:60, 30:70, 20:80, 10:90, 0:100. Then, the maximum ligand absorbance multiplied by the corresponding HSA concentration was plotted against the corresponding protein mole fraction to obtain the binding stoichiometry of the complex from the maximum signal observed in the Job's Plot.

Steady-state fluorescence spectra were recorded on an Edinburgh FS5 spectrofluorometer, provided with a monochromator in the wavelength range of 200–900 nm using an excitation wavelength of 340 nm at room temperature. Measurements on drug@protein complexes were performed in aerated PBS of 1:1 M ratio mixtures at 10 μM. The absorbance of the samples at the excitation wavelength was kept below 0.1. The fluorescence quantum yields were determined using anthracene in ethanol as reference (Montalti et al., 2006).

A modified Scatchard analysis has been used to determine the binding constants (K_B) of GFT, GFT-M1 and GFT-M2 within HSA and HAG either from fluorescence (F) or absorption (A) measurements (Healy, 2007), following Eq. 1:

$$\frac{F_{max} - F_0}{F - F_0} = \frac{1}{K_B} \cdot [P]^{-1} + 1 \quad (1)$$

where F_{max} is the fluorescence maximum when all possible ligand is bound to the protein, F_0 is the fluorescence maximum of the free ligand, F is the fluorescence maximum observed for a given protein concentration $[P]$, and K_B is the binding constant of the ligand with the protein. To calculate the K_B values by means of UV absorption spectroscopy, the same Eq. 1 has been applied but using A instead of F.

Time-resolved fluorescence measurements were performed with an EasyLife X system containing a sample compartment composed of an automated peltier cuvette holder to control the temperature at 24°C, a pulsed LED excitation source and a lifetime detector. The employed LED excitation source was 340 nm, with emission filter of WG370. The fluorescence lifetimes (τ_F) were obtained upon fitting the decay traces by a non-linear fitting/deconvolution procedure $F(t) = \Sigma a_i \exp(-t/\tau_i)$ by means of a one- or two-exponential function, depending on the investigated system. All spectroscopic measurements were done in 10 × 10 mm^2 quartz cuvettes at room temperature.

2.3 Molecular docking

These calculations were performed using GOLD program version 2020.3.0 (Jones et al., 1997), and the protein coordinates were taken from the crystal structures of HSA in complex with hemin and myristic acid (PDB ID 1O9X) (Zunszain et al., 2003) and of HAG in the unbound form (PDB ID 3KQ0) (Schönfeld et al., 2008). The experimental procedure was similar to that described for LAP, N-LAP and O-LAP in HSA (Andreu et al., 2020). For GFT and GFT-M2, the protonated forms of the morpholine moiety were employed since they predominate at physiological pH (Domotor et al., 2018).

2.4 Molecular dynamics simulation studies

The proteins in complex with the highest score solution obtained by docking were immersed in a truncated octahedron of TIP3P water molecules and neutralized using the molecular mechanics force field ff14SB and GAFF of AMBER (Case et al., 2021). The resulting systems were submitted to 100 ns of dynamic simulation following our previously reported protocol (Andreu et al., 2020). Briefly, the experimental procedure involved: (i) minimization and charge distribution of the ligands (GFT, GFT-M1 and GFT-M2) using Gaussian 09 (Frisch et al., 2009); (ii) generation and minimization of the binary GFT@protein, GFT-M1@protein and GFT-M2@protein complexes using the poses obtained by docking; and (iii) simulations of the resulting minimized ligand@protein complexes. The cpptraj module in AMBER 20 was used to analyze the trajectories and to calculate the root-mean-square deviation (rmsd) of the protein and the ligand during the simulation (Case et al., 2021). The molecular graphics program PyMOL (DeLano, 2008) was employed for visualization and depicting enzyme structures. For Figures related to HSA and

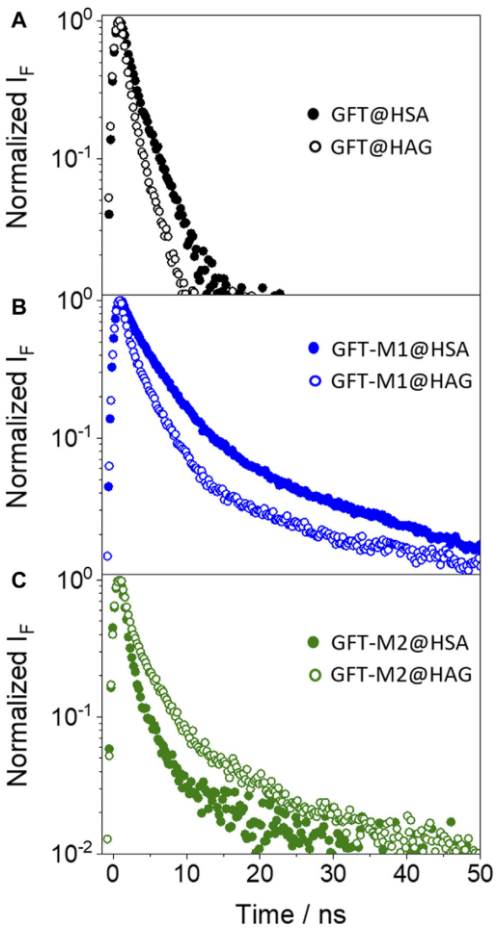

FIGURE 5
Fluorescence decays for **(A)** GFT@HSA (solid black circles) and GFT@HAG (opened black circles), **(B)** GFT-M1@HSA (solid blue circles) and GFT-M1@HAG (opened blue circles), and **(C)** GFT-M2@HSA (solid green circles) and GFT-M2@HAG (opened green circles). Measurements were performed at λ_{exc} = 340 nm for ligand@protein solutions at 1:1 M ratio (10 μM) in PBS. The fluorescence lifetimes were obtained upon fitting the decay traces by a non-linear fitting/deconvolution procedure $F(t) = \Sigma a_i \exp(-t/\tau_i)$ by means of a one- or two-exponential function, depending on the investigated system. In general, for all decay fits, the adjusted R^2 value ranged from 0.996 to 0.998.

HAG, the amino acid numbering described in PDB entries 1O9X and 3KQ0, respectively, was employed.

3 Results and discussion

As stated above, the photophysical properties of either GFT and GFT-M1 are strongly affected by the environment; hence, ICT states are detected in polar organic solvents, whereas LE species are predominantly formed in non-polar ones and in GFT@HSA; by contrast, ESPT is the main process occurring for GFT-M1 in protein medium (Tamarit et al., 2021; Tamarit et al., 2022). In view of this variability, the photobehavior of GFT-M2 was investigated here, first in organic solvents of different polarities to identify the excited species that can be formed upon irradiation with UVA light.

The UV absorption spectra of GFT-M2 were almost similar in all solvents (Supplementary Figure S1), while the fluorescence properties were strongly affected by the polarity (Supplementary Figure S2). By comparison with previous results on GFT and GFT-M1, emission from LE states was expected also for GFT-M2 in non-polar solvents. Actually, in these media, fluorescence maxima were found at λ_{max} *ca.* 390 nm with higher ϕ_F values and shorter τ_F than those detected in polar solvents, where intramolecular charge transfer (ICT) excited species are generally formed (Tamarit et al., 2021; Tamarit et al., 2022).

The photobehavior of GFT-M2 in a more complex biological environment such as that provided by the HSA binding sites has been examined. First, Job's plot analysis (Huang, 1982) allowed determination of a 1:1 stoichiometry for the protein-metabolite complex (Supplementary Figure S3). Its photophysical properties have been studied at λ_{exc} = 340 nm, where the protein does not absorb and GFT-M2 is selectively irradiated (Supplementary Figure S4). As it can be observed from Figure 2A, a noticeable fluorescence enhancement was observed upon binding with the protein. Interestingly, the emission profile of GFT-M2 strongly varied depending on the microenvironment; so, a maximum at *ca.* 440 nm was detected for GFT-M2 free in the bulk solution, while a shift towards much shorter wavelengths (~388 nm) occurred upon binding with HSA (inset in Figure 2A). Since GFT-M2 is a phenol, this can be explained as a result of a proton transfer process occurring in the bulk solution, which is hindered within the protein cavities; this is supported by UV absorption spectroscopy, where the shoulder between 370 and 400 nm (Supplementary Figure S4C), associated to phenolates, practically disappears in the supramolecular complex. This effect is even clearer at different GFT-M2/HSA ratios, where formation of phenolate-like species was lower at high protein concentrations (Supplementary Figure S5A). These results contrast with those previously observed for GFT-M1 (Supplementary Figures S4B, S5B), which is also a phenol but ESPT is the main process within HSA thanks to hydrogen bonding with Val116 (Tamarit et al., 2022). Therefore, the emission profile of GFT-M2 within HSA is comparable with that of the protein-bound GFT (Figure 2B); consequently, LE states are mainly formed in GFT-M2@HSA.

An important point to discuss is the low fluorescence yield value of GFT-M2 within the protein cavities (ϕ_F ~ 0.01) compared with that obtained in cyclohexane (ϕ_F ~ 0.13). This effect has been previously observed for GFT, where ϕ_F decreases from ~0.19 in cyclohexane to ~0.02 within HSA, and it is associated with quenching of LE states through photoinduced electron transfer from Tyr and/or Trp. It is worth to mention that this is a dynamic process that lowers τ_F values (Tamarit et al., 2021; Tamarit et al., 2022). With the aim of investigating this possibility for GFT-M2, fluorescence measurements were performed in the non-polar solvent toluene in the presence of increasing amounts of Tyr and Trp (due to solubility requirements, the *N*-acetyl methyl ester amino acid derivatives, namely, NAc-TyrMe or NAc-TrpMe, were used). Interestingly,

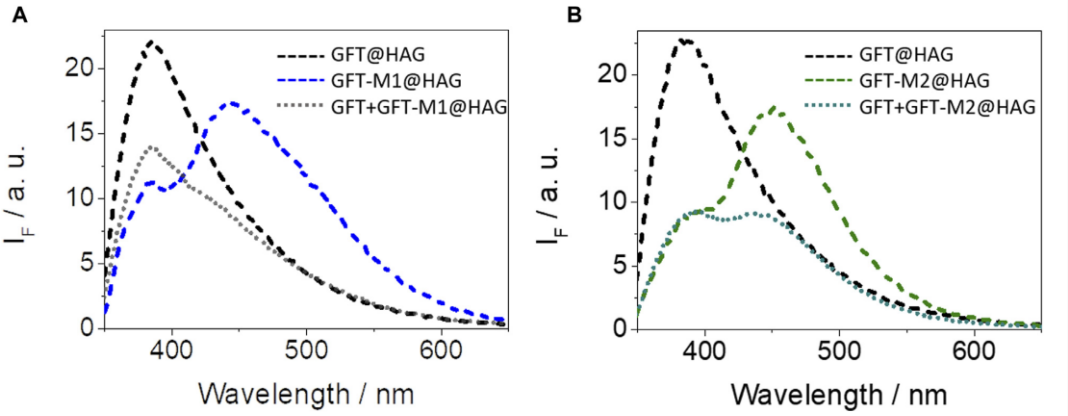

FIGURE 6
Fluorescence spectra at λ_{exc} = 340 nm for **(A)** GFT@HAG (dashed black), GFT-M1@HAG (dashed blue) and GFT + GFT-M1@HAG (dotted gray), and **(B)** GFT@HAG (dashed black), GFT-M2@HAG (dashed green) and GFT + GFT-M2@HAG (dotted dark green). All mixtures were at 1:1 M ratio (10 μM) in PBS. For drug + metabolite/HAG, equimolar 1:1:1 mixtures were used.

fluorescence quenching of the LE singlet state of the metabolite (^{1}GFT-M2*) was indeed observed upon addition of Tyr or Trp (Figure 3); however, the process was found to be static in nature since the fluorescence lifetimes were hardly affected (the lifetime of ^{1}GFT-M2* in toluene was constant at *ca.* 2.42 ns at the different GFT-M2/amino acid molar ratios: 1:50, 1:100, 1:150, 1:200, 1:250 and 1:300). It is worth to mention that using either Tyr or Trp as quenchers, a new band with λ_{max} ~ 490 nm arose at high amino acid concentrations (insets of Figure 3); this is attributed to emission from phenolate-like species involving interaction between hydrogen-bonded GFT-M2 and Tyr (or Trp) in the ground state. However, and as discussed above, these species have not been observed in the supramolecular GFT-M2@HSA complex, since LE states predominate. Therefore, it would exist an additional deactivation route for ^{1}GFT-M2* within the protein, which would be strongly affected by the conformational arrangement of the metabolite in the binding sites (see the discussion on MD simulations).

An additional point to address is the strength of interaction of the drug and its two metabolites within HSA, since it is key for their transport to the specific targets and for their toxicological activity. Although there are many analytical techniques to determine the binding constant (K_B) between a drug and a protein, fluorescence spectroscopy is a widely used one due to its high sensitivity and selectivity (Hirose, 2001; Vuignier et al., 2010; Vayá et al., 2014; Dos Santos Rodrigues et al., 2023). In this context, there are different K_B values reported for GFT within HSA, which vary in the range of 10^3–2×10^5 M^{-1} (Li et al., 2006; Kabir et al., 2016; Wu et al., 2016; Domotor et al., 2018; Tanzadehpanah et al., 2018; Tanzadehpanah et al., 2019). In view of this discrepancy, up to two-orders of magnitude, we determined the binding constants for the drug and their two metabolites within HSA by means of UV absorption and fluorescence spectroscopies. To this end, a modified Scatchard analysis was performed (Supplementary Figures S6–S8). (Healy, 2007) The K_B values obtained by the two techniques were very similar, with deviations between them lower than 10%; the obtained data are summarized in Table 1. As it can be observed, the strength of interaction of the two metabolites to HSA is slightly higher than that determined for the parent drug.

A similar study was performed for HAG, since it is another important transport protein in human plasma. In this context, fluorescence experiments were also performed at λ_{exc} = 340 nm, were the drug and/or its two metabolites are the only absorbing species (Supplementary Figure S9). As expected, a noticeable fluorescence enhancement for either GFT, GFT-M1 and GFT-M2 was observed upon binding with HAG (Figure 4). Job's plot analyses confirmed that 1:1 stoichiometry complexes are formed between the drug or its metabolites and HAG (Supplementary Figure S10).

In the case of GFT, its fluorescence profile within HAG was very similar to that observed for HSA (Tamarit et al., 2021), showing a maximum centered at *ca.* 390 nm and displaying slightly higher ϕ_F (Figure 4A; Table 2). Accordingly, emission is again associated with LE states as the only excited species; this was further supported by time-resolved fluorescence measurements, since a one-exponential law was used to get a good fitting of the kinetic traces (Figure 5A). Likewise, comparable results were obtained for GFT-M1 bound to HSA and HAG; the fluorescence bands peak at *ca.* 432 and 442 nm, respectively (Figure 4B). This is in line with emission from phenolate-like excited states, which display longer lifetimes than LE (Figure 5B; Table 2). Interestingly, a shoulder at around 390 nm was detected for GFT-M1@HAG, which might be associated with emission from LE states to a lower extent than phenolate-like species. In fact, a two-exponential function was necessary to get a good fitting for the fluorescence kinetics, where the short component (~0.5 ns) is associated to emission from LE states while the longer one (~3.1 ns) is assigned to phenolate species (Figure 5B). A completely different photobehavior was observed for the protein-bound GFT-M2. As explained above, emission from LE states predominates in HSA, whereas phenolate-like species are mainly formed in HAG (λ_{max} ~ 446 nm), although LE states also

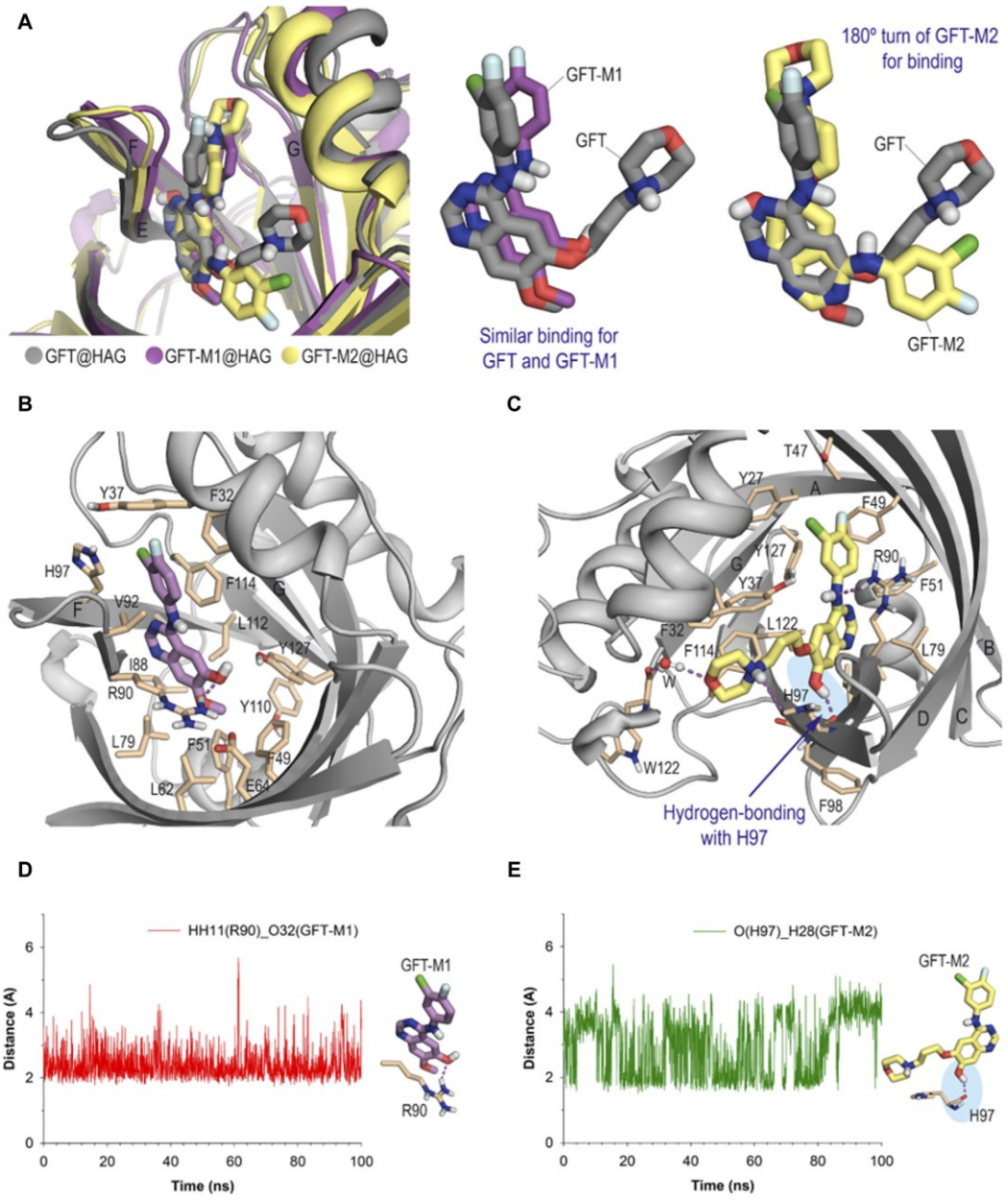

FIGURE 7
Binding mode of GFT and its metabolites with HAG obtained by MD simulation studies. **(A)** Comparison of the GFT@HAG (gray), GFT-M1@HAG (magenta) and GFT-M2@HAG (yellow) binary complexes (snapshots after 90, 90 and 80 ns, respectively, are shown) and superposition of the arrangements of GFT and GFT-M1 and GFT and GFT-M2, which are shown in sticks. Note how while GFT and GFT-M1 show a similar arrangement, GTF-M2 undergoes a 180° turn for binding. **(B, C)** Detailed views of GFT-M1 **(B)** and GFT-M2 **(C)** binding modes. Snapshots after 90 ns and 80 ns, respectively, are shown. **(C)** Detailed view of GFT-M2 binding mode. Snapshot after 80 ns is shown. Hydrogen-bonding interactions between the ligand and protein residues are shown as dashed lines (magenta). Note how the phenol moiety interacts by hydrogen-bonding with the main carbonyl group of H97 (blue shadow). A similar interaction is not observed for GFT-M1. **(D, E)** Variation of the relative distances between: **(D)** the phenol moiety (O atom) in GFT-M1 and the guanidinium group of R90 (HH11 atom) in the GFT-M1@HAG protein complex; **(E)** the phenol moiety (H atom) in GFT-M2 and the main carbonyl group of H97 (O atom) in the GFT-M2@HAG protein complex, during whole simulation. Average values of 2.9 Å and 2.4 Å, respectively.

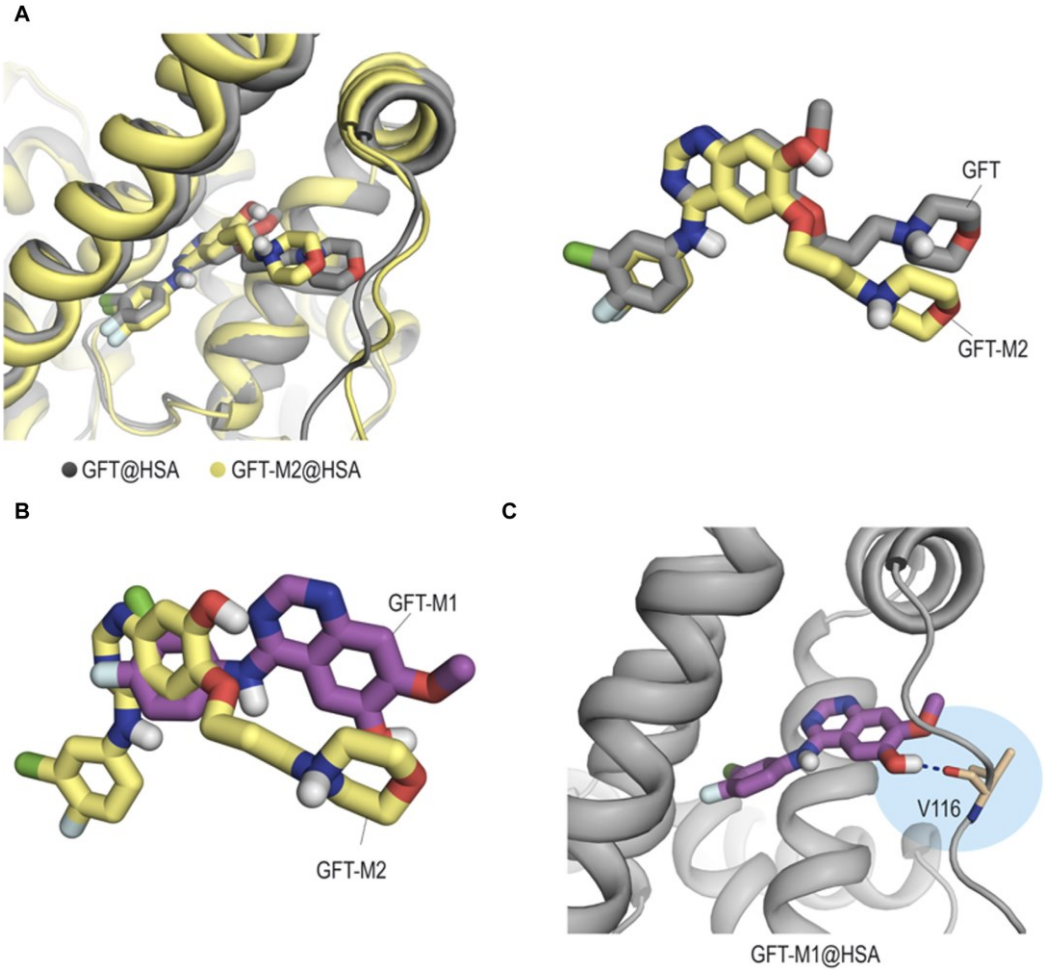

FIGURE 8
Binding mode of GFT and its metabolites with HSA obtained by MD simulation studies. **(A)** Comparison of the binary GFT@HSA (gray) and GFT-M2@HSA (yellow) complexes and overlapping of the arrangements of GFT and GFT-M2, which are shown in sticks. Snapshots after 100 ns are shown. **(B)** Superposition of the arrangements of GFT-M1 (magenta) and GFT-M2 (yellow). **(C)** Close view of GFT-M1 binding mode with HSA. Snapshot taken after 90 ns of simulation. Hydrogen-bonding interactions are shown as blue dashed lines. Contrary to what happens with GFT-M2, the phenolic proton in GFT-M1 establishes a hydrogen-bonding interaction with the protein (residue V116).

appears to a much lower extent, since a shoulder at ~ 388 nm was also detected. These results are again supported by time-resolved fluorescence measurements (Figure 5C), where a longer-lived component assigned to phenolate-like species dominates the kinetics of GFT-M2@HAG.

The strength of interactions of GFT and its two metabolites within HAG was also studied by means of spectroscopic techniques (Supplementary Figures S11–S13). The K_B values (Table 1) are on the order of those obtained for HSA, and in the case of GFT, agree well with the reported data (Li et al., 2006). Competing interactions on mixtures containing the drug and a metabolite in the presence of HAG confirmed the consistency of the determined binding constants. Hence, the emission profile of GFT + GFT-M1 in the presence of HAG resembles that of GFT@HAG, in agreement with its higher K_B value (Figure 6A). By contrast, the fluorescence spectrum for GFT + GFT-M2 in the presence of HAG might contain equal contributions from both GFT@HAG and GFT-M2@HAG (Figure 6B), which agrees with the similar strength of interactions of the two supramolecular complexes (1.2×10^5 and 1.5×10^5 M^{-1}, respectively).

Moreover, competing interactions of the drug (or its metabolites) in a mixture containing the two proteins are also in line with the K_B values obtained experimentally. In this context, the emission of GFT in the presence of an equimolar mixture of the two

proteins resembles that of GFT@HAG (Supplementary Figure S14A), confirming its higher binding constant value. A similar conclusion can be drawn for GFT-M1 and GFT-M2 in the presence of an equimolar mixture of HSA and HAG, where higher affinity to HSA was observed for the former, while similar affinity to either HSA or HAG was noticed for GFT-M2 (Supplementary Figures S14B, C, respectively).

The photobehavior herein discussed can justify the differences in the photosensitivity disorders previously observed by excitation of GFT, GFT-M1 and GFT-M2 in a biological media with UVA light (El Ouardi et al., 2023). In this regard, GFT-M1 displays the highest fluorescence yield in the protein environment, in particular in the presence of HSA. Besides, the fluorescence lifetime observed within this protein was the longest one. This can explain the highest phototoxicity detected for GFT-M1. Accordingly, GFT is also phototoxic but to a lesser extent, in line with its lower ϕ_F value and shorter τ_F, while GFT-M2 is much less phototoxic (El Ouardi et al., 2023). Interestingly, since electron and proton transfer processes are expected to occur in the protein environment, the photosensitizing damage from either the drug and its two metabolites is consistent with the involvement of a type I mechanism. Managing photosensitivity reactions involves diverse strategies, including medication adjustment, symptom monitoring and photoprotection. Since each patient can metabolize drugs yielding a personalized profile of metabolites, in the case of enhanced GFT-M1 production it might be appropriate to reduce the administered drug doses as well as avoiding Sun exposure and/or prescribing UVB plus UVA photoprotection. As a precaution, these measures would be advisable for all patients receiving GFT medication.

To provide a more in-depth understanding of the molecular bases responsible for the distinct photobehavior of the GFT metabolites, GFT-M1 and GFT-M2, relay on the protein that transport them, their binding modes were studied *in silico*. To this end, docking studies were first performed using the GOLD program version 2021.3.0 (Jones et al., 1997), followed by MD simulation studies to provide a more realistic picture of the ligand arrangement upon binding. The protein coordinates of the reported wild-type structure of HAG (PDB ID 3KQ0) and of HSA in complex with myristic acid and hemin (PDB ID 1O9X) were used for these studies (Zunszain et al., 2003; Schönfeld et al., 2008). The most plausible ligand@protein complexes obtained by docking were immersed in a truncated octahedron box of TIP3P water molecules and neutralized by addition of sodium ions, and then subjected to 100 ns of dynamic simulation using the molecular mechanics force field AMBER ff14SB and GAFF (Case et al., 2021).

As stated above, HAG contains a single large and flexible cavity to bind drugs (Kremer et al., 1988; Maruyama et al., 1990). The *in silico* results showed that GFT and its metabolites would be stable within the corresponding protein recognition sites, as revealed by the low rmsd (root-mean-square deviation) values obtained for the protein backbone and ligands during the whole simulation (Supplementary Figures S15, S16). More importantly, the two metabolites showed markedly different binding behavior depending on the transport protein used when compared with the parent drug. Thus, the interaction of GFT-M2 with HAG has been found to be much different than those of GFT and GFT-M1, which would be quite similar among them (Figure 7A). For GFT and GFT-M1, the pyrimidine ring of the quinazoline core would be located close to β-sheets F and E, and the 3-chloro-4-fluorophenyl moiety would be placed between β-sheets F and G (Figure 7B). On the contrary, GFT-M2 would undergo a 180° turn for binding, thus placing the phenyl group pointing towards β-sheets A and B and the morpholinyl moiety between β-sheets F and G (Figure 7C). Under the latter arrangement, the phenolic proton in GFT-M2 would establish a hydrogen-bonding interaction with the main carbonyl group of residue H97, which showed to be stable during most of the simulation (Figure 7E). It was also observed that when this interaction is lost as result of the rotation of OH group, a similar hydrogen-bonding interaction with the main carbonyl group of residue F98 would be established. For GFT-M1, the interaction of one of the oxygen lone pair of its OH group with the guanidinium group of R90 (average value of 2.4 Å during 100 ns-simulation) would freeze the orientation of the phenolic proton towards the bulky water solvent (Figure 7D). As a result, no interactions by hydrogen-bonding between its phenolic proton and any residue of the protein were identified.

Concerning HSA, it contains the major cavities (site I, II and III) where drugs can interact (Sudlow et al., 1976; Zsila, 2013). Previous reports show that GFT binds to site III (Tamarit et al., 2021), so that it was selected for these studies. Our computational studies revealed that unlike what happens with HAG, the interactions of GFT and its metabolites with site III (subdomain IB) of HSA does not follow the previous pattern. Thus, while GFT and GFT-M2 would achieve a similar arrangement (Figure 8A), GFT-M1 would be buried at the bottom of the pocket thanks to the lack of the morpholine moiety (Figure 8B). More importantly, this insertion into the cleft would be promoted by a hydrogen-bonding interaction between the phenolic proton in GFT-M1 and the main carbonyl group in residue V116 (Figure 8C). For GFT-M2, a similar interaction was not identified during the whole simulation.

4 Conclusion

The photobehavior of the anticancer drug GFT and its two photoactive metabolites GFT-M1 and GFT-M2 has been investigated in the presence of the most abundant transport proteins in human plasma, *i.e.,* HSA and HAG. The strength of binding and the nature of the main transient species that are formed upon irradiation of the protein-bound drug (or metabolite) with UVA have been studied by means of spectroscopic techniques. In general, the protein strongly modulates the fate of the excited species that are formed in the confined biological environment. In this regard, excitation of GFT-M2@HSA at 340 nm leads mainly to formation of locally excited states, whereas phenolate-like species predominate in HAG. By contrast, a diverging behavior is observed for GFT-M1, which forms phenolate-like species as the only excited states in HSA, while locally excited states are also formed within HAG. As regards GFT, locally excited states are primarily formed in the two proteins. These results are supported by molecular dynamics simulations, which rationalize the variability detected in the photoinduced processes and the type of excited species formed in the protein cavities based on the differences in the ligand binding mode, the type of interactions with the protein, and the arrangement of key functional groups involved in the ligand structure. Taken together, the herein reported studies highlight the relevant role of the

biomacromolecule microenvironment in the modulation of the photobiological properties of the ligand inherent to its chemical structure.

Data availability statement

The original contributions presented in the study are included in the article/Supplementary Material, further inquiries can be directed to the corresponding authors.

Author contributions

LT: Data curation, Formal Analysis, Methodology, Writing–review and editing. ME: Data curation, Formal Analysis, Methodology, Writing–review and editing. EL: Data curation, Formal Analysis, Methodology, Software, Writing–review and editing. IA: Funding acquisition, Investigation, Supervision, Writing–review and editing. CG-B: Conceptualization, Funding acquisition, Investigation, Software, Writing–review and editing. MM: Conceptualization, Investigation, Supervision, Writing–original draft, Writing–review and editing. IV: Conceptualization, Funding acquisition, Investigation, Supervision, Writing–original draft, Writing–review and editing.

Funding

The author(s) declare that financial support was received for the research, authorship, and/or publication of this article. Grants PID2020-115010RB-I00 and PID2022-136963OB-I00 funded by MCIN/AEI/10.13039/501100011033, grant CIAICO/2021/061 funded by Conselleria d'Innovació, Universitats, Ciència i Societat Digital and grant AP2022-5 funded by Programa d'Accions Preparatòries UV-La Fe. Grants from the Xunta de Galicia [ED431C 2021/29 and the Centro singular de investigación de Galicia accreditation 2019-2022 (ED431G 2019/03), CG-B], and the European Regional Development Fund (ERDF).

Acknowledgments

The Ministry of Science, Innovation and Universities of Spain, the Conselleria d'Innovació, Universitats, Ciència i Societat Digital, the University of Valencia, the Health Research Institute Hospital La Fe (IIS La Fe) and La Xunta de Galicia are gratefully acknowledged for financial support. All authors are grateful to the Centro de Supercomputación de Galicia (CESGA) for use of the Finis Terrae computer.

Conflict of interest

The authors declare that the research was conducted in the absence of any commercial or financial relationships that could be construed as a potential conflict of interest.

Publisher's note

All claims expressed in this article are solely those of the authors and do not necessarily represent those of their affiliated organizations, or those of the publisher, the editors and the reviewers. Any product that may be evaluated in this article, or claim that may be made by its manufacturer, is not guaranteed or endorsed by the publisher.

Supplementary material

The Supplementary Material for this article can be found online at: https://www.frontiersin.org/articles/10.3389/fphar.2024.1387057/full#supplementary-material

References

Andreu, I., Lence, E., Gonzalez-Bello, C., Mayorga, C., Cuquerella, M. C., Vayá, I., et al. (2020). Protein binding of lapatinib and its N- and O-dealkylated metabolites interrogated by fluorescence, ultrafast spectroscopy and molecular dynamics simulations. *Front. Pharmacol.* 11, 576495. doi:10.3389/fphar.2020.576495

Blakely, K. M., Drucker, A. M., and Rosen, C. F. (2019). Drug-Induced photosensitivity-an update: culprit drugs, prevention and management. *Drug Saf.* 42, 827–847. doi:10.1007/s40264-019-00806-5

Carter, D. C., and Ho, J. X. (1994). "Structure of serum albumin," in *Advances in protein chemistry* (New York: Academic Press), 153–203.

Case, D. A., Aktulga, H. M., Belfon, K., Ben-Shalom, I. Y., Brozell, S. R., Cerutti, D. S., et al. (2021) *Amber*. San Francisco: University of California.

Cohen, M. H., Williams, G. A., Sridhara, R., Chen, G., and Pazdur, R. (2003). FDA drug approval summary: gefitinib (ZD1839) (Iressa) tablets. *Oncologist* 8, 303–306. doi:10.1634/theoncologist.8-4-303

Cohen, P., Cross, D., and Janne, P. A. (2021). Kinase drug discovery 20 years after imatinib: progress and future directions. *Nat. Rev. Drug Discov.* 20, 551–569. doi:10.1038/s41573-021-00195-4

Delano, W. L. (2008) *The PyMOL molecular graphics system*. Palo Alto, CA: DeLano Scientific LLC. Available at: http://www.pymol.org/(2021. [Accessed].

Domotor, O., Pelivan, K., Borics, A., Keppler, B. K., Kowol, C. R., and Enyedy, E. A. (2018). Comparative studies on the human serum albumin binding of the clinically approved EGFR inhibitors gefitinib, erlotinib, afatinib, osimertinib and the investigational inhibitor KP2187. *J. Pharm. Biomed. Anal.* 154, 321–331. doi:10.1016/j.jpba.2018.03.011

Dos Santos Rodrigues, F. H., Delgado, G. G., Santana Da Costa, T., and Tasic, L. (2023). Applications of fluorescence spectroscopy in protein conformational changes and intermolecular contacts. *BBA Adv.* 3, 100091. doi:10.1016/j.bbadva.2023.100091

El Ouardi, M., Tamarit, L., Vayá, I., Miranda, M. A., and Andreu, I. (2023). Cellular photo(geno)toxicity of gefitinib after biotransformation. *Front. Pharmacol.* 14, 1208075. doi:10.3389/fphar.2023.1208075

Frisch, M. J., Trucks, G. W., Schlegel, H. B., Scuseria, G. E., Robb, M. A., Cheeseman, J. R., et al. (2009) *Gaussian 09, revision E.01*. Wallingford, CT: Gaussian, Inc.

Gambacorti-Passerini, C., Zucchetti, M., Russo, D., Frapolli, R., Verga, M., Bungaro, S., et al. (2003). Alpha1 acid glycoprotein binds to imatinib (STI571) and substantially alters its pharmacokinetics in chronic myeloid leukemia patients. *Clin. Cancer Res.* 9, 625–632.

García-Laínez, G., Vayá, I., Marín, M. P., Miranda, M. A., and Andreu, I. (2021). *In vitro* assessment of the photo(geno)toxicity associated with Lapatinib, a Tyrosine Kinase inhibitor. *Arch. Toxicol.* 95, 169–178. doi:10.1007/s00204-020-02880-6

Hartmann, J. T., Haap, M., Kopp, H.-G., and Lipp, H.-P. (2009). Tyrosine kinase inhibitors – a review on pharmacology, metabolism and side effects. *Curr. Drug Metab.* 10, 470–481. doi:10.2174/138920009788897975

Healy, E. F. (2007). Quantitative determination of DNA-ligand binding using fluorescence spectroscopy. *J. Chem. Educ.* 84, 1304–1307. doi:10.1021/ed084p1304

Hirose, K. (2001). A practical guide for the determination of binding constants. *J. Incl. Phenom. Macrocycl. Chem.* 39, 193–209. doi:10.1023/A:1011117412693

Holladay, J. W., Dewey, M. J., and Yoo, S. D. (1998). Pharmacokinetics and antidepressant activity of fluoxetine in transgenic mice with elevated serum alpha-1-acid glycoprotein levels. *Drug Metab. Dispos.* 26, 20–24.

Huang, C. Y. (1982). Determination of binding stoichiometry by the continuous variation method: the Job plot. *Methods Enzymol.* 87, 509–525. doi:10.1016/s0076-6879(82)87029-8

Huang, L., Jiang, S., and Shi, Y. (2020). Tyrosine kinase inhibitors for solid tumors in the past 20 years (2001-2020). *J. Hematol. Oncol.* 13, 143. doi:10.1186/s13045-020-00977-0

Huang, Z., and Ung, T. (2013). Effect of alpha-1-acid glycoprotein binding on pharmacokinetics and pharmacodynamics. *Curr. Drug Metab.* 14, 226–238. doi:10.2174/138920013804870709

Jones, G., Willett, P., Glen, R. C., and Taylor, R. (1997). Development and validation of a genetic algorithm for flexible docking. *J. Mol. Biol.* 267, 727–748. doi:10.1006/jmbi.1996.0897

Kabir, M. Z., Tee, W.-V., Mohamad, S. B., Alias, Z., and Tayyab, S. (2016). Interaction of an anticancer drug, gefitinib with human serum albumin: insights from fluorescence spectroscopy and computational modeling analysis. *RSC Adv.* 6, 91756–91767. doi:10.1039/c6ra12019a

Kowalska, J., Rok, J., Rzepka, Z., and Wrzesniok, D. (2021). Drug-Induced photosensitivity-from light and chemistry to biological reactions and clinical symptoms. *Pharmaceuticals* 14, 723. doi:10.3390/ph14080723

Kragh-Hansen, U., Chuang, V. T. G., and Otagiri, M. (2002). Practical aspects of the ligand-binding and enzymatic properties of human serum albumin. *Biol. Pharm. Bull.* 25, 695–704. doi:10.1248/bpb.25.695

Krasner, J. (1972). Drug-protein interaction. *Pediatr. Clin. North Am.* 19, 51–63. doi:10.1016/s0031-3955(16)32666-9

Kremer, J. M., Wilting, J., and Janssen, L. H. (1988). Drug binding to human alpha-1-acid glycoprotein in Health and disease. *Pharmacol. Rev.* 40, 1–47.

Li, J., Brahmer, J., Messersmith, W., Hidalgo, M., and Baker, S. D. (2006). Binding of gefitinib, an inhibitor of epidermal growth factor receptor-tyrosine kinase, to plasma proteins and blood cells: *in vitro* and in cancer patients. *Invest. New Drugs* 24, 291–297. doi:10.1007/s10637-006-5269-2

Lin, N. U., Carey, L. A., Liu, M. C., Younger, J., Come, S. E., Ewend, M., et al. (2008). Phase II trial of lapatinib for brain metastases in patients with human epidermal growth factor receptor 2-positive breast cancer. *J. Clin. Oncol.* 26, 1993–1999. doi:10.1200/JCO.2007.12.3588

Lin, N. U., Dieras, V., Paul, D., Lossignol, D., Christodoulou, C., Stemmler, H. J., et al. (2009). Multicenter phase II study of lapatinib in patients with brain metastases from HER2-positive breast cancer. *Clin. Cancer Res.* 15, 1452–1459. doi:10.1158/1078-0432.CCR-08-1080

Lindup, W. E., and Orme, M. C. (1981). Clinical pharmacology: plasma protein binding of drugs. *Br. Med. J.* 282, 212–214. doi:10.1136/bmj.282.6259.212

Maruyama, T., Otagiri, M., and Takadate, A. (1990). Characterization of drug binding sites on alpha 1-acid glycoprotein. *Chem. Pharm. Bull.* 38, 1688–1691. doi:10.1248/cpb.38.1688

Medina, P. J., and Goodin, S. (2008). Lapatinib: a dual inhibitor of human epidermal growth factor receptor tyrosine kinases. *Clin. Ther.* 30, 1426–1447. doi:10.1016/j.clinthera.2008.08.008

Montalti, M., Credi, A., Prodi, L., and Gandolfi, M. T. (2006) *Handbook of photochemistry*. Boca Raton, FL: CRC Press, Taylor and Francis Group.

Monteiro, A. F., Rato, M., and Martins, C. (2016). Drug-induced photosensitivity: photoallergic and phototoxic reactions. *Clin. Dermatol.* 34, 571–581. doi:10.1016/j.clindermatol.2016.05.006

Paez, J. G., Jänne, P. A., Lee, J. C., Tracy, S., Greulich, H., Gabriel, S., et al. (2004). EGFR mutations in lung cancer: correlation with clinical response to gefitinib therapy. *Science* 304, 1497–1500. doi:10.1126/science.1099314

Pérez-Ruiz, R., Lence, E., Andreu, I., Limones-Herrero, D., González-Bello, C., Miranda, M. A., et al. (2017). A new pathway for protein haptenation by β-lactams. *Chem. Eur. J.* 23, 13986–13994. doi:10.1002/chem.201702643

Peters, T. (1995). "Ligand binding by albumin," in *All about albumin - Biochemistry, genetics, and medical applications* (San Diego: Academic Press), 76–132. Elsevier.

Pottier, C., Fresnais, M., Gilon, M., Jerusalem, G., Longuespee, R., and Sounni, N. E. (2020). Tyrosine kinase inhibitors in cancer: breakthrough and challenges of targeted therapy. *Cancers* 12, 731. doi:10.3390/cancers12030731

Quintero, B., and Miranda, M. A. (2000). Mechanisms of photosensitization induced by drugs: a general survey. *Ars. Pharm.* 41, 27–46.

Schönfeld, D. L., Ravelli, R. B., Mueller, U., and Skerra, A. (2008). The 1.8-A crystal structure of alpha1-acid glycoprotein (Orosomucoid) solved by UV RIP reveals the broad drug-binding activity of this human plasma lipocalin. *J. Mol. Biol.* 384, 393–405. doi:10.1016/j.jmb.2008.09.020

Selvam, T. P., and Kumar, P. V. (2011). Quinazoline marketed drugs – a review. *Res. Pharm.* 1, 1–21.

Solassol, I., Pinguet, F., and Quantin, X. (2019). FDA- and EMA-approved tyrosine kinase inhibitors in advanced EGFR-mutated non-small cell lung cancer: safety, tolerability, plasma concentration monitoring, and management. *Biomolecules* 9, 668. doi:10.3390/biom9110668

Spitaleri, A., and Rocchia, W. (2019). "Molecular dynamics-based approaches describing protein binding," in *Biomolecular simulations in structure-based drug discovery*. Editors F. L. Gervasio and V. Spiwok (Weinheim, Germany: Wiley VCH), 29–39.

Stein, K. R., and Scheinfeld, N. S. (2007). Drug-induced photoallergic and phototoxic reactions. *Expert Opin. Drug Saf.* 6, 431–443. doi:10.1517/14740338.6.4.431

Sudlow, G., Birkett, D. J., and Wade, D. N. (1976). Further characterization of specific drug binding sites on human serum albumin. *Mol. Pharmacol.* 12, 1052–1061.

Tamarit, L., El Ouardi, M., Andreu, I., Vayá, I., and Miranda, M. A. (2021). Photoprocesses of the tyrosine kinase inhibitor gefitinib: from femtoseconds to microseconds and from solution to cells. *Chem. Sci.* 12, 12027–12035. doi:10.1039/d1sc03154f

Tamarit, L., El Ouardi, M., Lence, E., Andreu, I., González-Bello, C., Vayá, I., et al. (2022). Switching from ultrafast electron transfer to proton transfer in excited drug–protein complexes upon biotransformation. *Chem. Sci.* 13, 9644–9654. doi:10.1039/d2sc03257k

Tanzadehpanah, H., Mahaki, H., Moghadam, N. H., Salehzadeh, S., Rajabi, O., Najafi, R., et al. (2019). Binding site identification of anticancer drug gefitinib to HSA and DNA in the presence of five different probes. *J. Biomol. Struct. Dyn.* 37, 823–836. doi:10.1080/07391102.2018.1441073

Tanzadehpanah, H., Mahaki, H., Moradi, M., Afshar, S., Rajabi, O., Najafi, R., et al. (2018). Human serum albumin binding and synergistic effects of gefitinib in combination with regorafenib on colorectal cancer cell lines. *Color. Cancer* 7, CRC03. doi:10.2217/crc-2017-0018

Trainor, G. L. (2007). The importance of plasma protein binding in drug discovery. *Expert Opin. Drug Discov.* 2, 51–64. doi:10.1517/17460441.2.1.51

Vayá, I., Andreu, I., Lence, E., González-Bello, C., Cuquerella, M. C., Navarrete-Miguel, M., et al. (2020). Characterization of locally excited and charge-transfer states of the anticancer drug lapatinib by ultrafast spectroscopy and computational studies. *Chem. Eur. J.* 26, 15922–15930. doi:10.1002/chem.202001336

Vayá, I., Lhiaubet-Vallet, V., Jimenez, M. C., and Miranda, M. A. (2014). Photoactive assemblies of organic compounds and biomolecules: drug-protein supramolecular systems. *Chem. Soc. Rev.* 43, 4102–4122. doi:10.1039/c3cs60413f

Vuignier, K., Schappler, J., Veuthey, J. L., Carrupt, P. A., and Martel, S. (2010). Drug-protein binding: a critical review of analytical tools. *Anal. Bioanal. Chem.* 398, 53–66. doi:10.1007/s00216-010-3737-1

Wu, D., Yan, J., Sun, P., Xu, K., Li, S., Yang, H., et al. (2016). Comparative analysis of the interaction of capecitabine and gefitinib with human serum albumin using (19)F nuclear magnetic resonance-based approach. *J. Pharm. Biomed. Anal.* 129, 15–20. doi:10.1016/j.jpba.2016.06.034

Yoo, S. D., Holladay, J. W., Fincher, T. K., Baumann, H., and Dewey, M. J. (1996). Altered disposition and antidepressant activity of imipramine in transgenic mice with elevated alpha-1-acid glycoprotein. *J. Pharmacol. Exp. Ther.* 276, 918–922.

Zsila, F. (2013). Subdomain IB is the third major drug binding region of human serum albumin: toward the three-sites model. *Mol. Pharm.* 10, 1668–1682. doi:10.1021/mp400027q

Zunszain, P. A., Ghuman, J., Komatsu, T., Tsuchida, E., and Curry, S. (2003). Crystal structural analysis of human serum albumin complexed with hemin and fatty acid. *BMC Struct. Biol.* 3, 6. doi:10.1186/1472-6807-3-6